Numerical Modeling of Composite Systems: Composite CFT Connections and Composite Beams

José de Jesús Wilches Están

Dissertation submitted to the faculty of the Virginia Polytechnic Institute and State University in partial fulfillment of the requirements for the degree of

Doctor of Philosophy
In
Civil Engineering

Roberto T. Leon, Chair
Hernán Santa María, Co-Chair
José I. Restrepo
Eric Jacques
Ioannis Koutromanos

May 31, 2022
Blacksburg, Virginia

Keywords: Numerical modeling, Composite connections, Composite beams, Pushout tests, Concrete, Structural steel, Database.

Numerical Modeling of Composite Systems: Composite CFT Connections and Composite Beams

José de Jesús Wilches Están

ABSTRACT

The use of concrete-filled tubular composite members and composite beams has been implemented in many structural systems due to their robust structural performance, constructability, and inherent synergy when the steel and concrete components are properly designed and detailed together. While extensive research has been conducted on concrete-filled steel structural members, relatively little has been done regarding similar composite connections. Understanding how composite connections behave in structures and how they should be modeled during the design process is crucial to predict the actual structural behavior of these types of elements when subjected to different loading conditions. The goal of this research is to numerically evaluate CFTs or SRCs members and their connections subjected to axial, shear, and flexural load. Predicting composite connection behavior is exceptionally challenging due to the coupled behavior of the steel and concrete, the residual stresses in the steel, local buckling of the connection, and the sensitivity of the stress-strain response to the steel-concrete contact and confinement performance. To address these issues, a thorough literature search has been carried out and a state-of-the-art report on experimental and numerical models for composite connections is presented. The selected tests represent a range of geometries, materials, and governing failure modes. Initially, a generic connection modeling process was developed and calibrated against a classical test, then three more connections were modeled. To further the understanding of composite behavior, shear studs in steel-concrete composite beams were modeled next, taking as reference a recent experimental program that resulted in an unusual failure. Results indicate that the model can reproduce the most important behavioral aspects observed in the tests, tracking well the strength and stiffness of the samples up to ultimate. The load-deformation curves of the experimental specimens and the analytical models show very good agreement in their transitions and indicate that the behavior of the composite joints is controlled mainly by both the strength of the concrete and the confining effect of the steel tube in the joint. A data appendix containing 135 tests is described and the main characteristics of these tests are summarized in the text.

Numerical Modeling of Composite Systems: Composite CFT Connections and Composite Beams

José de Jesús Wilches Están

GENERAL AUDIENCE ABSTRACT

Every day the population increase is more evident, and the main cities of the world are densifying. This implies the accelerated construction of all types of structures, especially tall residential buildings. For the design of these structures, architects design increasingly slender structures, which must be resilient under all type of forces. The foregoing is exerting pressure on structural engineers to design structures that have the capacity to be built in the shortest possible time without losing their functionality and safety. This is where steel and concrete composite construction plays an important role. The main advantage of composite construction is the synergy of both materials. Concrete is inexpensive and provides high stiffness, mass, and fire resistance. Structural steel has high strength, ductility, lightweight, and ease of construction. Composite construction has been used for a long time in tall buildings, and experimental and numerical research has been carried out, especially on the beam and column elements. However, comparatively little research has been done on composite connection behavior and design.

This dissertation proposes a numerical evaluation of the composite connections in beams and columns under different types of loads in order to establish modeling parameters that facilitate the analysis and structural design of these elements. The important numerical models are validated with experimental investigations. The results show that the numerical models are capable of simulating the structural behavior of the tests, especially the damage mechanisms and the modeling of local behavior. This study contributes to the development of simulations of composite connections, determining modeling parameters, such as the contact resistance between steel and concrete and the distribution of shear studs in composite beams, among others.

Dedication

To God, to my wife Marcela and my children Isabella and Jacob

Acknowledgements

First and foremost, I want to thank my wife Marcela for being the pillar that supported me throughout this academic journey and my parents for teaching me the value of perseverance

Similarly, I want to thank Dr. Roberto T. León and Dr. Hernán Santa María, my advisors. They made this difficult journey possible guiding me rigorously through all academic obstacles, and by constantly encouraging me to take one more step forward. Their advice and support were a gift that I will cherish for the rest of my life. Additionally, I would like to thank the rest of the committee members, Doctors José I. Restrepo, Eric Jacques and Ioannis Koutromanos.

I want to thank my whole family for always believing in me. In particular, my grandmother Frinia Delgado (RIP), my uncles Nelson Stanp (RIP) and Buenaventura Wilches (RIP).

A special thanks to my uncle Juan Wilches and my aunts Paulina and Policarpa Wilches for motivating me and helping me become an engineer. I am very thankful with the Quinchanegua Cubides family for their continued motivation.

A special thanks to Debbie Leon and Marita Dragan for their unconditional support throughout this adventure.

I wish to acknowledge the funding provided by ANID (Chilean National Agency for Research and Development) through the ANID Doctorate Scholarship and the Research Center for Integrated Disaster Risk Management (CIGIDEN) ANID/FONDAP 15110017 and Virginia Tech who also contributed through teaching and research assistantships and through the computational facilities at the Advanced Research Center (VT-ARC). ANID and VT have funded my double doctoral studies at Pontificia Universidad Católica de Chile and Virginia Tech.

Finally, I want to thank the outstanding faculty of Virginia Tech's Department of Civil and Environmental Engineering for providing me with the tools and knowledge I needed to complete this dissertation.

CONTENTS

LIST OF TABLES

LIST OF FIGURES

Chapter 1.

1. Introduction

1.1. Background and motivation

Composite action has been implemented in many structural systems due to its robust structural performance, constructability, and economy when structural steel and concrete components are properly tied together and able to act as a unit.

The term "Composite Construction in Concrete and Steel" (Buckner and Viest, 1987) is applicable to the case of structural elements composed of structural steel and reinforced concrete in which both materials work together through connectors and/or friction in several surfaces (i.e., in concrete-filled tube connections, Figure 1.1). The term is applied also to structural systems that are composed primarily of one structural element in steel and one in concrete that work together, i.e., composite beam (Figure 1.2.a) or to situations where a composite element is used as a transition between an essentially reinforced concrete or steel system (Figure 1.2.b). These applications have been enabled by a large amount of theoretical (analytical and numerical) and practical (experimental) research. However, not all of its developments are well-known or recognized, as they come from many different countries and have not all been translated or even formally published. Thus, many parallel developments on this topic occurred in different places at essentially the same time, and it was often years before this knowledge became generally known.

Herein, the general term "composite construction" refers to the use of structural elements consisting of either concrete filled tubes (CFT) or steel encased (SRC) elements and their numerous variations; some possible configurations of these members are shown in Figure 1.3.

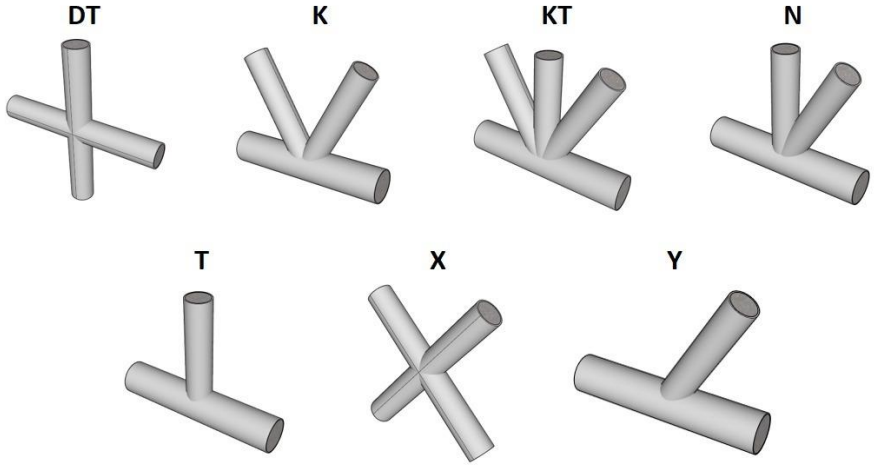

Figure 1.1 Typical configurations of concrete-filled composite connections.

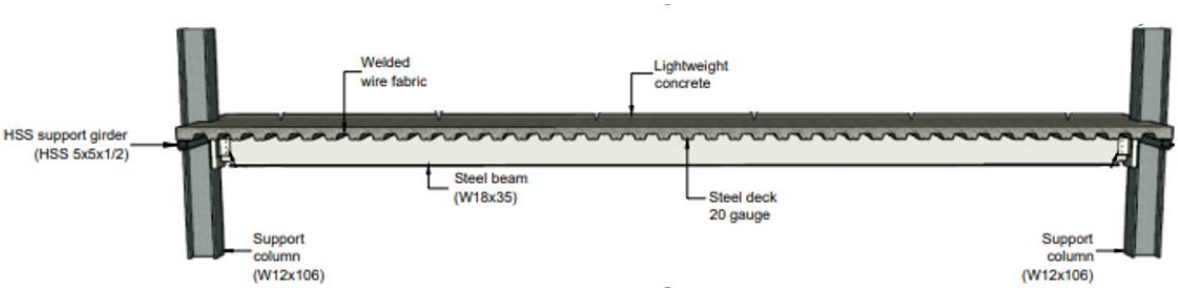

(a) Floor systems

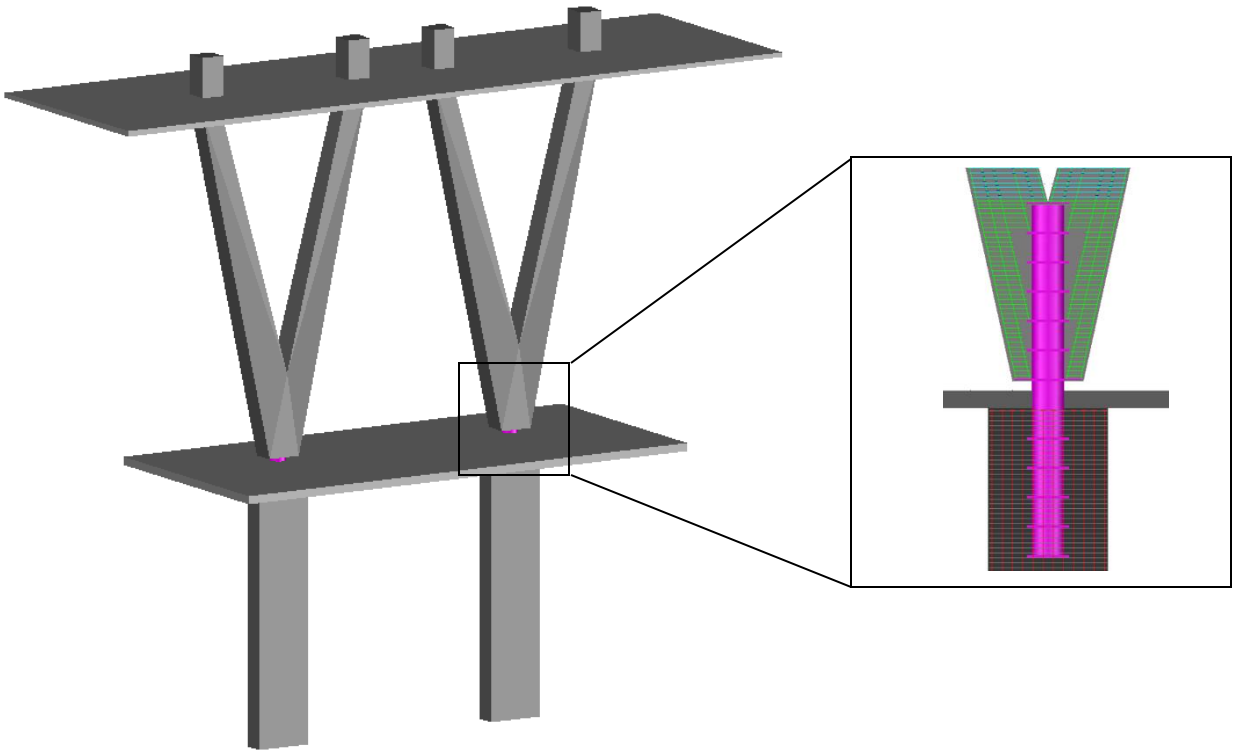

(a) Frames for West Building - 1011 Union, San Diego, CA.

Figure 1.2 Composite system applications.

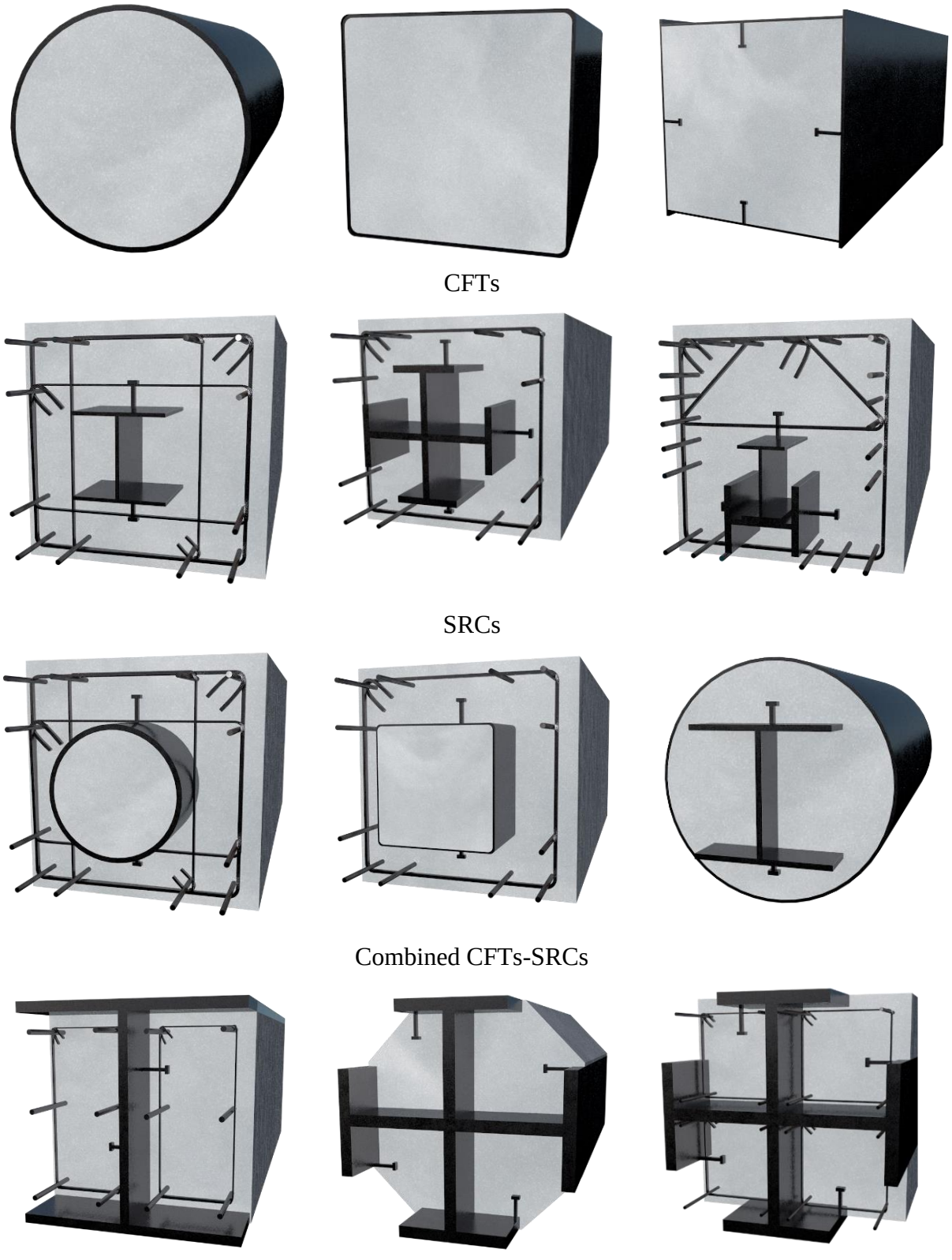

Figure 1.3 Some possible configurations of steel and concrete composite members.

The first formal research on steel-concrete composite members and their connections dates back to the late 1930s (Batho et al., 1939). However, composite construction has been used since the late 1800s in the construction of buildings (Faschan, 1992), bridges (Griffis, 1994), industrial facilities (American Petroleum Institute, 2010), as well as in retrofitting existing structures (Kim and Shinozuka, 2004).

The use of composite construction has several advantages over conventional steel or concrete construction. Among these advantages, one can mention:

- Optimal use of the material properties
- Larger free spans
- Greater resistance to corrosion
- Greater resistance to fires
- Speed of construction
- Lower construction costs.

However, composite construction has some disadvantages, such as the need:

- for special connectors (shear studs and similar anchors) resulting in additional construction and inspection cost,
- to consider two separate stages in design, before and after composite action develops,
- to address the long-term effects of creep and shrinkage of concrete for serviceability performance,
- for two construction specialties (reinforced concrete construction and steel construction) to work seamlessly, which involves careful scheduling and execution of the work.

Numerous investigations have been carried out to understand the structural behavior of composite elements, especially beam-columns (M. Denavit, 2012; Molenstra, 1990; Perea, 2010) and floor systems (Alsamsam, 1991; Johnson, 2008; Oehlers and Bradford, 1995) to name but a few. However, little has been done regarding composite connections. In this dissertation, an exhaustive review of past research on these topics is given. Because each chapter addresses different issues, each presents its own discussion of the state-of-the-art. For example, Chapter 2 presents the review of 135 test specimens available in the literature of composite connections as well as the analytical investigations carried out. Chapter 3 presents a discussion of advanced modeling for shear studs in composite beams for both the conventional pushout test and for long composite beams in buildings.

While investigations have helped to better understand the structural behavior of CFTs or SRCs-connections, there remain gaps in the modeling and understanding of the structural behavior of this type of connections. The latter has motivated this research, specifically, the need to study the structural behavior of CFTs or SRCs-connections through numerical modeling, considering particularly the effect of axial, shear, and flexural loads and the use of connectors in the form of either shear studs or bearing plates. For the connectors and plates, the emphasis will be on the influence of some parameters such as the contact modelling between steel and concrete, local buckling, residual stresses, and properties of materials on the local and overall behavior of the

connection. Where possible, existing experimental data will be utilized to assess the fidelity of the models.

1.2. Problem definition

Steel-concrete composite members are used in buildings, bridges, offshore structures, trusses, and other components and structures, mainly to promote fire protection, avoid or minimize the effect of local buckling, and increase stiffness, resistance, and ductility. The latter characteristics are, of course, of great relevance in highly seismic and wind regions, and thus this type of construction has been commonly used in countries with coastal regions (Japan, China, Europe, Australia and the Americas) or with severe seismic loading environments (Japan, China, and the USA). In China and Japan, the main application of steel-concrete composite members is in connections, floor systems and frames. These countries have specifications for analysis, design and construction that have been well documented and validated both numerically and experimentally. In Europe (Schäfer, 2019), Australia (Hicks and Uy, 2015) and America (AISC, 2010) there are design specifications for floor slabs, beams and column systems; however, it is necessary to delve deeper into the analysis and design of this type of members because the connection behavior is not explicitly included in the design of these members.

In the USA, the lack of connection design guidelines requires that a detailed numerical and/or experimental study be carried out to validate the structural behavior in each particular case to ensure that the CFTs or SRCs-connections work as envisioned in design. This leads to increased design costs, extensive peer reviews, and potential delays in the execution of projects. The main reason for this requirement is that there are significant gaps in the design provisions due to the lack of targeted comprehensive and coordinated research on CFTs or SRCs-connections. Few design codes (Architectural Institute of Japan, 2012; Han et al., 2014; Zhao et al., 2013) around the world have developed reliable provisions to design CFTs-connections based on a solid understanding of the structural behavior of their components. It is important to note that although this topic is not covered in the design regulations in the United States, specific design guidelines have been offered (Packer and Henderson, 1997; Zhao et al., 2013). Figure 1.4 illustrates some tests that have been carried out in Australia and North America to validate some composite connections. Note the relatively small scale of the specimens, mostly due to laboratory constraints.

However, some uncertainties remain in the structural behavior of such elements, such as:

- What is the actual behavior of composite connections considering axial, shear and bending interactions?

- What would be an acceptable contact resistance and associated parameters to model the concrete-structural steel interface?

- How can the use and distribution of shear connectors influence composite flooring systems?

- Could composite connections improve the seismic performance of structures?

- Are composite connections suitable when structures have irregular structural configurations?

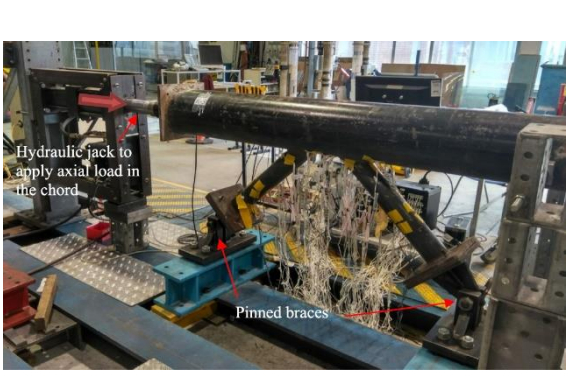

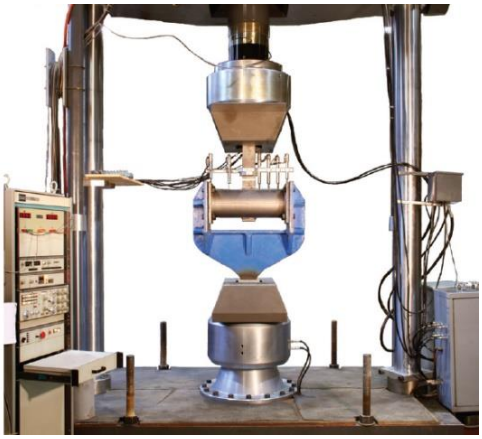

(a) Australia (Musa and Mashiri, 2019) (b) North America (Voth, 2010)

Figure 1.4 Tests performed for validation of composite connections.

This dissertation aims to address several of these problems mainly from a numerical point of view. In this study, a hypothesis will be used that the contact resistance between the concrete and the structural steel in the absence of significant normal loads is between 1% -10% of the compressive strength of concrete. It is understood that this assumption does not rest on solid fundamental principles but has some experimental justification.

1.3. Objectives and methodology

The overarching goal of this dissertation is to develop several advances in the numerical modeling of composite steel-concrete connections, considering different structural configurations and types of loads. This dissertation achieves this goal by executing two specific objectives:

1. To evaluate by means of three-dimensional nonlinear finite element models the behavior of CFTs-connections.

2. To develop three-dimensional finite elements to study the influence of shear studs on the structural behavior of composite beams with trapezoidal profiled sheets.

The dissertation methodology is presented in Table 1-1. The specific phases and specific objectives are related to the corresponding activities required to achieve the objectives described above.

Table 1.1 Investigation methodology.

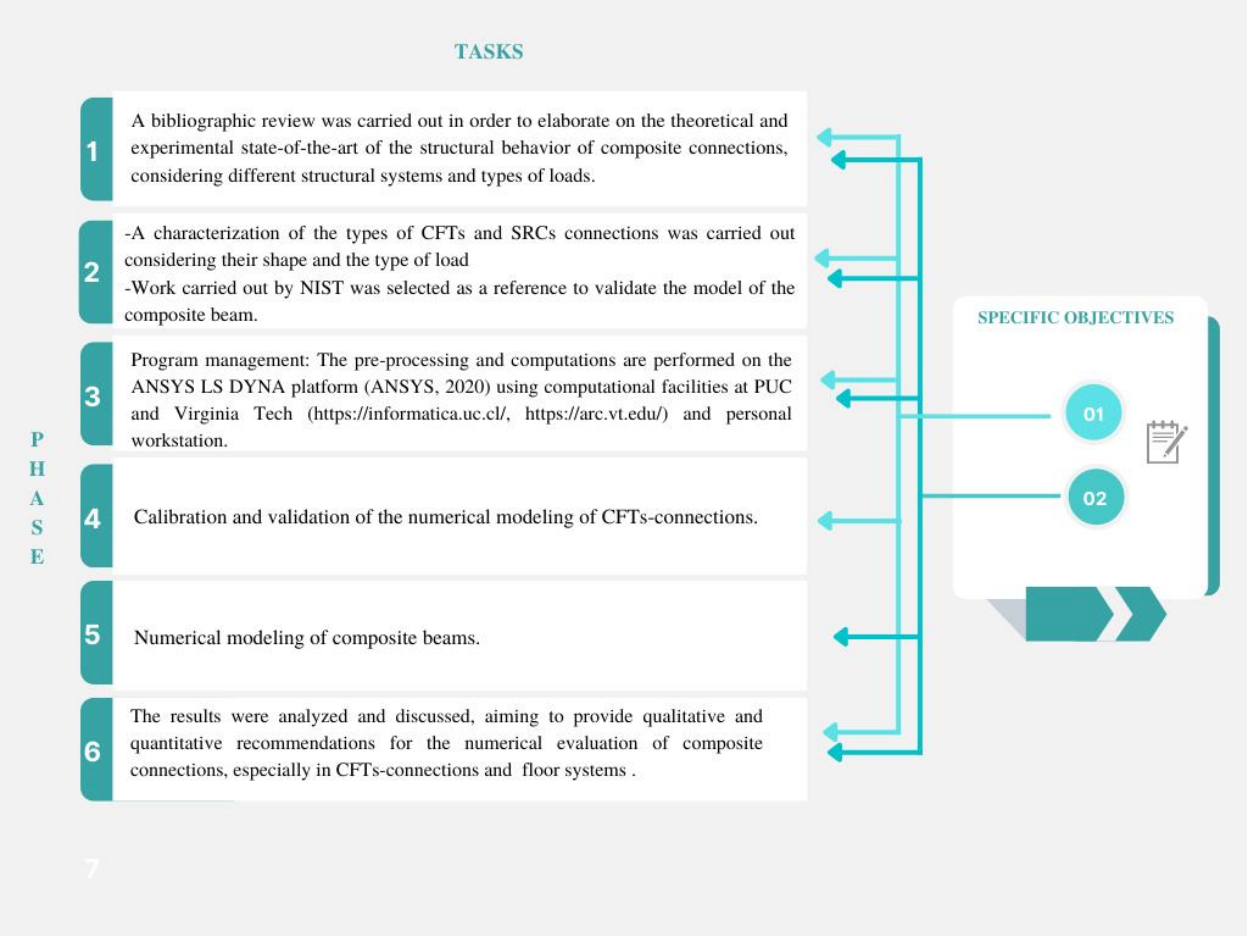

1.4. Dissertation outline

This dissertation is organized into four main chapters. The dissertation was originally conceived as two separate papers, but due to time constraints, it was not possible to keep it in that format. One of the papers (Chapter 2) has been submitted to a refereed journal, and the other (Chapter 3) is in progress. The papers were intended to reflect very different aspects of several composite construction topics, and thus each chapter is self-contained. The dissertation maintains the paper format, but the chapters, particularly in their literature reviews and description of modelling aspects, are longer than would be expected for a journal paper. In addition, each chapter has its own set of references.

The structure of the dissertation is as follows:

Chapter 2 presents a brief review of testing and analyses of concrete-filled connections, describes a database comprising 135 tests, and develops a numerical model capable of capturing most relevant behaviour modes up to the ultimate strength and deformation capacity of these connections. These behavioural modes include, among others, local buckling of the steel tubes and

friction/contact resistance between steel and concrete. This model is calibrated against a single test and its performance verified against three other very different tests available in the literature.

Chapter 3 develops three-dimensional finite elements models to study the influence of shear studs on the structural behaviour of composite beams with trapezoidal profiled sheets using the best available material models, element types and numerical schemes as described in the software documentation and analysis procedures available for ANSYS-LS DYNA (ANSYS, 2020). Various gravitational load scenarios are evaluated along the length of the steel beam to investigate their impact on the shear studs distribution. The experimental research carried out by the National Institute of Standards and Technology (Ramesh et al., 2019) will serve as a validation platform since it offers a unique opportunity to exercise the prediction capabilities of the proposed model approach in 3D finite elements and explore some configurations that could be difficult to investigate experimentally.

Chapter 4 gives the general conclusions and recommendations obtained in this dissertation.

Appendix A documents a database of composite connections, considering the connection type, section type, material properties, load type, failure mode, among others.

1.5. Original contributions

The present research project is distinctive in many ways. Some unique contributions of this dissertation are that it provides:

- a comprehensive database of composite connections, considering different aspect ratios, different types of loads (axial compression and tension, plane flexure, out-of-plane flexure) and different study parameters among which the stiffness of the connection, ultimate strength, stress concentration factors and fatigue performance are emphasized.

- qualitative and quantitative recommendations for the numerical evaluation of composite connections, especially in CFTs-connections, floor systems and columns.

- valuable information on the importance of shear studs distribution in composite beams.

In summary, this dissertation provides a unique set of data that can and have been used to verify advanced computational models and provide support for the development of simplified and advanced analysis techniques for the use of composite connections and their role in different structural systems.

Furthermore, this dissertation study is an effort to (1) develop new fundamental knowledge, (2) improve our understanding of the numerical evaluation of composite connections, (3) extend

design ranges, (4) provide calibration data, and (5) improve the prediction accuracy of the structural response of composite connections.

The author expects that, based on the results and conclusions obtained in this dissertation, the use of composite connections will have an immediate practical impact in the modelling, analysis, design and, consequently, in the construction of buildings, bridges, among other structures either for constructing new structures or retrofitting old structures.

References

AISC, 2010. *Specification for structural steel buildings. American Institution of Steel Construction (AISC) ANSI/AISC 360-10*. Chicago, Illinois.

Alsamsam, I., 1991. *SERVICEABILITY CRITERIA FOR COMPOSITE FLOOR SYSTEMS (PhD thesis)*. UNIVERSITY OF MINNESOTA.

American Petroleum Institute, 2010. Recommended Practice for Planning, Designing and Constructing Fixed Offshore Platforms—Working Stress Design. *Proceedings of the Annual Offshore Technology Conference*. N.W., Washington, D.C.: Institute American Petroleum. DOI: 10.2523/20837-ms

ANSYS, 2020. ANSYS Explicit Dynamics Analysis Guide. Canonsburg, PA 15317. Retrieved from http://www.ansys.com

Architectural Institute of Japan, 2012. *Guidebook on Design of Concrete Filled Steel Tubular Structures*. (AIJ, Ed.). Japan.

Batho, C., Lash, S. D., and Kirkham, R. H. H., 1939. The Properties of Composite Beams, Consisting of Steel Joists Encased in Concrete, Under Direct and Sustained Loading. *Journal of the Institution of Civil Engineers*, **12**(8), 382–386. DOI: 10.1680/ijoti.1939.14492

Buckner, C. D., and Viest, I. M., 1987. Composite Construction in Steel and Concrete. In American Society of Civil Engineers (Ed.), *Engineering Foundation Conference* (p. 830). Henniker, New Hampshire, United States.

Faschan, W., 1992. 1992 Faschan. *Composite Construction of Steel and Concrete. ASCE* (Vol. II, p. 576).

Griffis, L. G., 1994. Higgins Lecture : Composite Frame Construction. *American Institute of Steel Construction*, 1–72.

Han, L. H., Li, W., and Bjorhovde, R., 2014. Developments and advanced applications of concrete-filled steel tubular (CFST) structures: Members. *Journal of Constructional Steel Research*, **100**, 211–228. Elsevier Ltd. DOI: 10.1016/j.jcsr.2014.04.016

Hicks, S., and Uy, B., 2015. AS/NZS 2327 Composite Structures: A new Standard for Steel-Concrete Composite Buildings. *Steel Innovations Conference 2015*, (August 2016). DOI: 10.13140/RG.2.2.22769.68961

Johnson, R. P., 2008. Calibration of resistance of shear connectors in troughs of profiled sheeting. *Structures & Buildings*, (SB3), 117–126. DOI: 10.1680/stbu.2008.161.3.117

Kim, S. H., and Shinozuka, M., 2004. Development of fragility curves of bridges retrofitted by column jacketing. *Probabilistic Engineering Mechanics*, **19**(1), 105–112. DOI: 10.1016/j.probengmech.2003.11.009

M. Denavit, 2012. *Characterization of behavior of steel-concrete composite members and frames with applications for design*. University of Illinois at Urbana-Champaign.

Molenstra, N. J., 1990. *Ultimate Strength of Composite Beams (PhD thesis)*. University of Warwick.

Musa, I. A., and Mashiri, F. R., 2019. Stress concentration factor in concrete-filled steel tubular K-joints under balanced axial load. *Thin-Walled Structures*, **139**(February), 186–195. Elsevier Ltd. DOI: 10.1016/j.tws.2019.03.003

Oehlers, D. J., and Bradford, M. A., 1995. *COMPOSITE STEEL, AND CONCRETE STRUCTURAL MEMBERS. Fundamental Behaviour*. (PERGAMON, Ed.). Sidney.

Packer, J. A., and Henderson, J. E., 1997. *Hollow Structural Section Connections and Trusses – A*

Design Guide. (Canadian Institute of Steel Construction, Ed.) (2nd editio.). Toronto.

Perea, T., 2010. *Analytical and experimental study on slender concrete-filled steel tube columns and beam-columns*. Georgia Institute of Technology.

Ramesh, S., Choe, L., Seif, M., Hoehler, M., Grosshandler, W., Sauca, A., Bundy, M., et al., 2019. *Compartment Fire Experiments on Long-Span Composite-Beams with Simple Shear Connections Part 1 : Experimental Design and Beam Behavior at Ambient Temperature NIST Technical Note 2054 Compartment Fire Experiments on Long-Span Composite-Beams with Simple Sh*. DOI: 10.6028/NIST.TN.2054

Schäfer, M., 2019. European design code for composite structures in steel and concrete: Historical development and investigation in the second generation of Eurocode 4. *Steel Construction*, **12**(2), 70–81. DOI: 10.1002/stco.201800031

Voth, A. P., 2010. *Branch Plate-to-Circular Hollow Structural Section Connections, Doctoral Thesis*. University of Toronto.

Zhao, X.-L., Han, L.-H., and Lu, H., 2013. *Concrete-filled Tubular Members and Connections*. (Routledge, Ed.). London and New York: Taylor & Francis.

Chapter 2.

2. Numerical evaluation of CFTs-connection behavior

2.1. Introduction

In recent decades, the use of composite steel-concrete construction has increased throughout the world, particularly in high-rise buildings. Composite construction has been used since the late 1800s in the construction of bridges and buildings (Griffis, 1994). Its use increased substantially in the USA during the early 1900s as a result of the excellent performance of buildings with encased structural elements in the 1906 San Francisco Earthquake and Fire. The first formal research on composite members and their connections dates back to the late 1930s (Batho et al., 1939). Composite construction is used in buildings (Faschan, 1992), bridges (Roeder, Charles; Lehman, 2012), and industrial facilities (American Petroleum Institute, 2010), as well as for strengthening of existing structures (Kim and Shinozuka, 2004). It is important to mention that composite construction has also been widely used in seismic regions, especially for high-rise structures (Liu and Goel, 1988). The general term "composite construction" refers to concrete elements reinforced with steel as either concrete filled tube (CFTs) or steel encased (SRC) elements; some possible simple configurations of these members are shown in Figure 2.1.

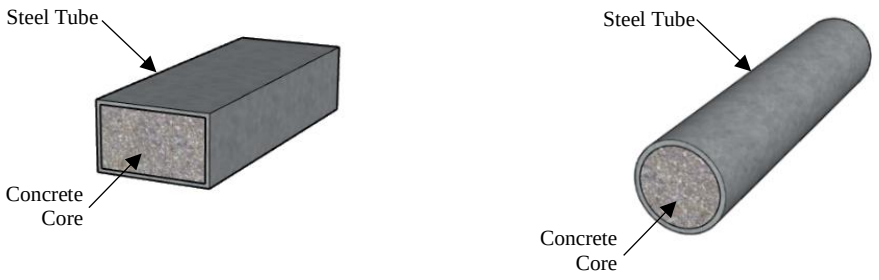

(a) Filled sections or concrete-filled rectangular or circular tubes (CFT)

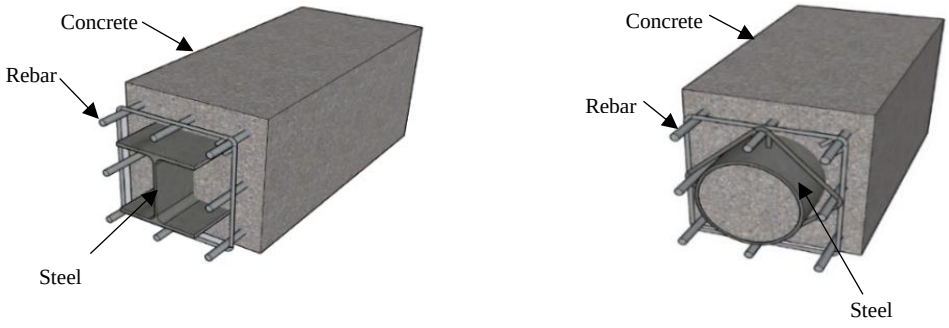

(b) Concrete encased composite sections (SRC)

Figure 2.1 Some possible configurations of a composite element.

The great advantage of composite construction is the synergetic action of both materials. Structural steel has high strength, ductility, lightness, and ease of construction. Concrete provides high rigidity, mass and fire resistance. Additionally, with CFT composite elements the costs and construction times are reduced because the tubes act as formwork (Han et al., 2014). These advantages have been widely studied and have led to the extensive use of hollow steel structures filled with concrete in civil engineering structures (Cheng et al., 2018; Gourley et al., 2008; Han et al., 2014; Liu et al., 2015; Viest et al., 1997; Zhang et al., 2004; Zhong and Zhang, 1999). While steel pipes filled with concrete are an inexpensive form of composite construction, their use has been limited due to both the complex nature of beam-to-column connections and the limited experience with these systems by many construction companies. There are many analytical (M. Denavit, 2012) and experimental (Perea, 2010) studies on the behavior of the beam-column CFTs under static and dynamic loads; however, relatively little work has been done on the beam-column connections with steel tubes filled with concrete in the USA, Europe, and Australia as compared to Japan and China. Connections of composite members to footings are a separate but important category that will be partially addressed in this chapter, where the experimental or analytical results are deemed to provide useful information.

Understanding how composite connections in tall buildings behave and should be modelled during the design process is the main long-term objective of the authors. As an example of where this knowledge will be applied is in modelling the transition zones in structures that go from an all-concrete set of bottom floors to an all-steel one in the top floors (Figure 2.2). This chapter presents the first two steps towards that goal.

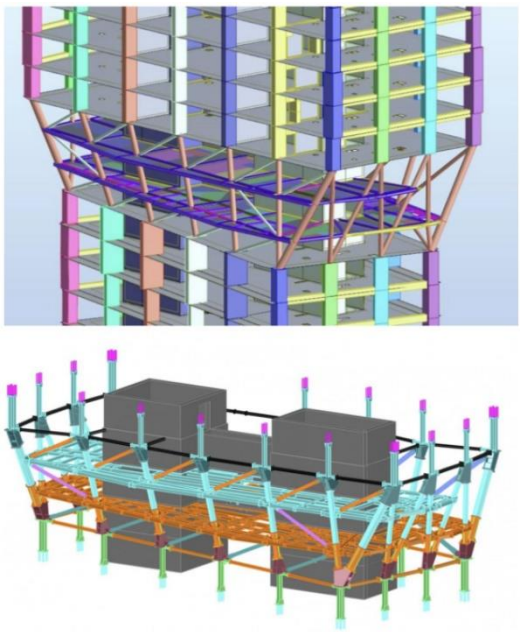

Figure 2.2 CFST hybrid structural systems for high-rise buildings. Mercury Tower in Malta (Hadid, 2021)

The first step is a brief, selected review of some important joint experimental/analytical and analytical research on composite connections. A data appendix containing important parameters on over one hundred thirty-five tests complements this brief review and provides the starting point

for a robust calibration and verification database for this and future similar analytical studies. The second step is the development of a new analytical model for composite connections subjected primarily to axial loads. The proposed model is calibrated and verified against three of the best-described tests in the literature. The results indicated that the model can reproduce the most important behavioral aspects observed in the tests as well as match experimental values obtained well into the inelastic range. The last two steps in the process, the consideration of connections with embedded steel shapes and connectors (and their associated complex states of stress) and the development of design guidelines, will be the subject of future research as those efforts are in their preliminary phase.

2.1.1 Joint Experimental/Analytical Research

Each of the investigations documented in the database described in this section defined the connection type according to its own criteria. For clarity, the author has consolidated those into a few types and used the nomenclature shown in Table 2.1 in the descriptions. In the table, they are organized in alphabetical order: DT-connections, K-connections, KT-connections, N-connections, T-connections, X-connection, and Y-connections.

Table 2.1 Labels (or tags) of the connections studied in this chapter.

DT	K	KT	N	T	X	Y
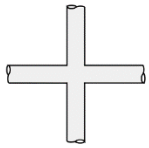	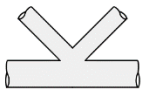	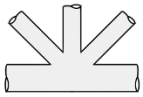	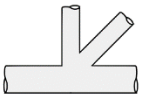	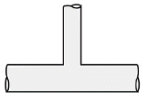	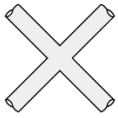	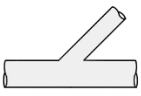

The behavior of CFTs-connections has been investigated through both analytical and experimental studies, initially focused on offshore structures for the North Sea and the Gulf of Mexico. Typical of these efforts is the work of Sayed (Javadi, 1979) consisting of an analytical study on composite tubular connections with T and K configurations for use in offshore structures. Tests showed that the T-connections filled with concrete had higher strength and lower hotspot stress values in the steel around the intersection lines when compared to unfilled T-connections. Moreover, the addition of concrete at the T-connections reduced the initiation and propagation of cracks in the connection surface when subjected to high loads and also produced an advantageous triaxial compression stress state in the connection. In K-connections, the presence of concrete significantly decreased the stress values in the steel. Smaller displacements were observed in the composite K-connections than in the welded K-connections. The research included the development and validation of a new solid finite element, labelled “Semi Loof,” that allows an efficient analysis of composite members fabricated from stainless steel shells and thick concrete infills. The results obtained allowed useful improvements in the analysis, design, manufacture, and installation of

composite connections in marine structures. For this and all other tests described here, additional details are given in the database in Appendix A.

Tebbett et al. (Tebbett et al., 1979) studied the ungrouted and grouted connections in piles at the bottom of the offshore platforms. They carried out an experimental program to verify the final strength of 10 T-connections (5 ungrouted and 5 grouted) subject to three different load conditions (tension, compression, and bending). For both ungrouted and grouted connections, one load test was carried out with axial tension, two tests with axial compression and two tests with in-plane flexure to obtain data for direct comparison with the existing API design specifications (American Petroleum Institute, 1976) (Figure 2.3). The tests showed that the strength of the ungrouted connections was at least 1.8 times the permissible workload determined from the RP2A API Code (American Petroleum Institute, 1976). For the grouted connections, a significant increase in axial tension, axial compression and in-plane bending load was observed. It was also shown that the stress concentration factors in the connection reduce appreciably with the presence of grout, which implies a corresponding important increase in the fatigue life of the connection.

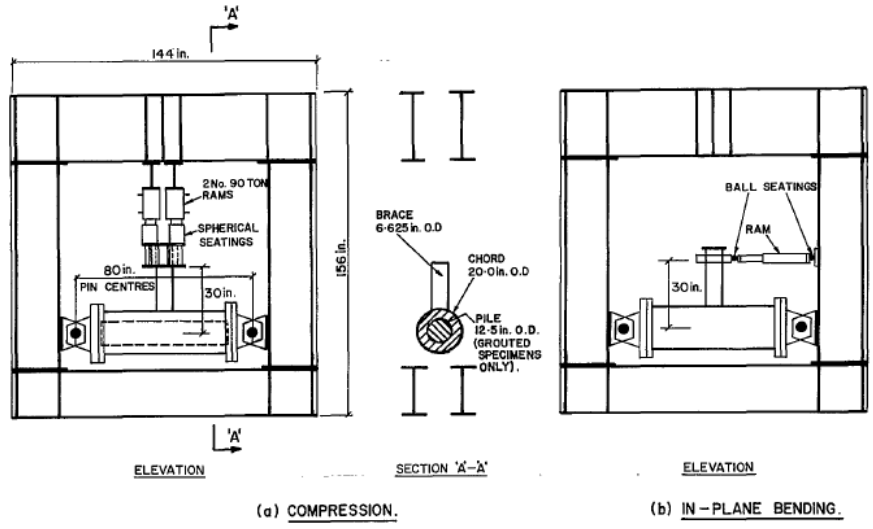

Figure 2.3 Details of test sample and test frame from Tebblet et al. (Tebbett et al., 1979)

Brown et al. (Brown et al., 1989) studied the distribution of tension around a welded tubular T-connections before and after the introduction of grout. Four samples were tested (T1 and T2 ungrouted and T1G and T2G grouted). All samples had a chord diameter of 914 mm and a nominal wall thickness of 32 mm. The tests were subjected to three load modes: axial load, in-plane flexure, and out-of-plane flexure. The results showed that the introduction of the grout in the chord member limited the deformation of the chord, reducing the bending stresses generated by the applied load. Under axial conditions, a reduction in the maximum stress concentration factor of 40 percent was noted in the hotspot area of the chord for the grouted specimens. For in-plane flexure, tension in the connection is generated by very local flexure of the chord member while, for out-of-plane flexure, the global deformation was the main parameter generating tension in the intersection of the union. With the reduction of the tension gradients due to the grout, the resistance to fatigue of the connection is increased, an important factor in welded offshore structures that are subject to large hydrodynamic forces. A number of these tests for offshore structures utilized grout as opposed to concrete as an infill; it is assumed herein that concrete will actually perform better givens its higher strength and stiffness.

Packer et al. (Packer, 1995) illustrated the structural behavior of T, X and K-connections of rectangular trusses when the chord member is filled with concrete (Figure 2.4). The behavior of the connections was examined by tests on 31 concrete-filled and unfilled connections: 6 T-connections were loaded in tension, 14 X-connections were loaded monotonically in transversal compression, and, finally, 11 K-connections were loaded with one diagonal in tension, the other diagonal in compression and the chord in tension. The tests confirmed that the T-connections have relatively large deformation capacity and, therefore, the LRFD loads must be based on the resistance of the connection. All concrete-filled T-connections showed a significant increase in stiffness relative to their unfilled counterparts, and none of the filled connections showed a decrease in connection yield or final strength by more than a few percent. On the other hand, the unfilled X-connections failed by web crippling the walls of the chords. For the completely filled connection, the concrete extended beyond both ends of the sample by several millimeters in the final load indicating significant slip between the steel and concrete. The final strength progressively increased as the length of the concrete increased, as did the rigidity in the direction of the load. Finally, the unfilled K-connections failed in the compression web member and the concrete-filled connections failed in the tensioned core member. For the concrete-filled T- and X-connections, it is recommended that the LRFD capacity be calculated from the existing design rules for unfilled hollow structural section connections, while for the concrete-filled K-connections it is recommended that the LRFD resistance is calculated from the factored resistance (N1*) for the compressed web element, and the factored resistance (N2*) for the stressed web member.

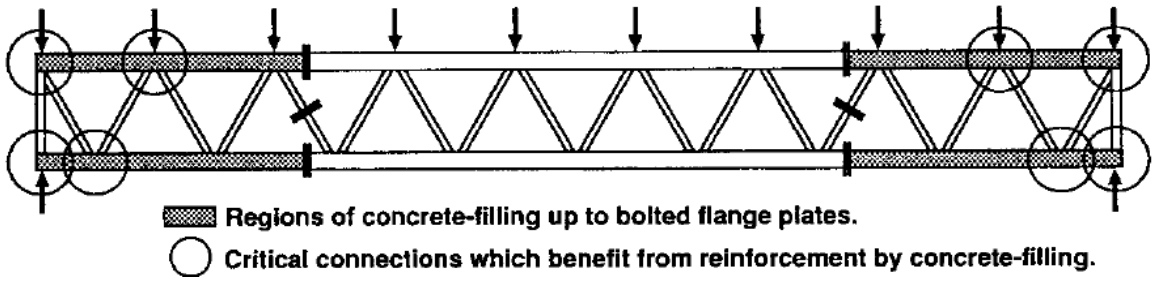

Figure 2.4 Partial Filling of HSS Chord Members in Critical Connection Regions from Packer et al. (Packer, 1995)

Silva et al. (Silva et al., 1998) tested a new grouted connection with a coupling pin for offshore platforms through finite element analysis and scale model testing (Figure 2.5). The main objective was the determination of the stress concentration factors in the connection. The testing program was comprised of four samples. Each test sample was a 1:4 scale model of the K-connection prototype. Although all the samples were of the K form, their geometrical configurations varied to study the effect of different construction tolerances. During the tests, the sample diagonals were subjected to a reversed axial load regime (tension and compression). The new grouted connection was able to develop the full resistance of the tubular section, transferring the load of the chord to the pin. There was no evidence of any unforeseen failure mode with this connection. The maximum stress concentration factors occur at the intersection of the middle surfaces of the diagonals and the chord. The magnitude of the stress concentration factors can be assessed by use of finite elements for the design of grouted connections.

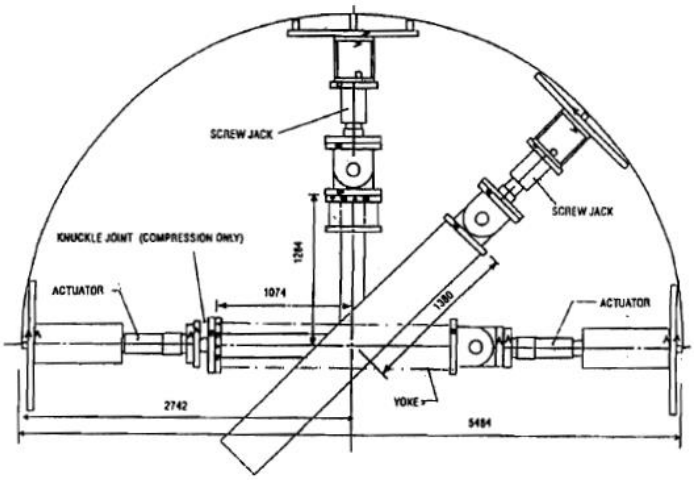

Figure 2.5 Test setup from Silva et al. (Silva et al., 1998)

Morahan and Lalani (Morahan and Lalani, 2002) developed experimental tests to evaluate fatigue and ultimate strength of tubular grouted connections. The samples tested were large-scale DT- and T-connections (Figure 2.6). Twelve grouted samples were subjected to tests under in-plane flexure, out-of-plane flexure, and axial compression on the cruciforms. Tests showed that the presence of grout reduced ovalization and reduced the stress concentration factor under axial loads. It is also observed that the stress concentration factors in grouted connections differ between compression and tension load due to the different load transfer mechanisms that exist for the two load cases. In compression, the chord is pushed against the grout plug while, under tension, the chord can be lifted from the plug. This variation depends on the configuration of the connection and the geometry. In general, stress concentration factors in grouted connections can be significantly reduced (60% in the chords and 45% in the diagonals) compared to welded connections without infilling. The results of this research generated a significant contribution to the creation of the detailed design manual for grouped connections (MSL, 1994).

Figure 2.6 Test arrangement from Morahan and Lalani (Morahan and Lalani, 2002).

Udomworarat et al. (Udomworarat, 2002) carried out an experimental study on the fatigue performance of composite tubular K-connections for truss bridges. Four types of tubular K-connections were considered (Figure 2.7). The samples had the same geometry; however, the interior details varied in order to provide better structural performance. A Type I connection represented the basic K-connections without any improvement of the connection details. A Type II connection was identical to Type I connection except that the chord was completely filled. A Type III connection was identical to a Type II connection, but 50 mm diameter holes were made on the intersection areas of the chord and the diagonals, and the diagonals were completely filled with concrete. Finally, a Type IV connection is identical to a Type III connection, except that two pieces of partial perfo-bond reinforcement were welded inside the chord with an inclined angle of 50 degrees. All the connections had a scale of approximately 1/3 of the actual structural size. The tests demonstrated that the concrete contributes to reducing the tension forces in the connections. By providing the filled concrete and additional reinforcing materials, the overall and local deformations of the chord wall can be considerably reduced, resulting in an increased fatigue life. The failure propagation patterns are different when the details of the structural connection are changed. From the point of view of the authors, the Type IV connection provides the best fatigue performance among these four types based on the increase in fatigue performance.

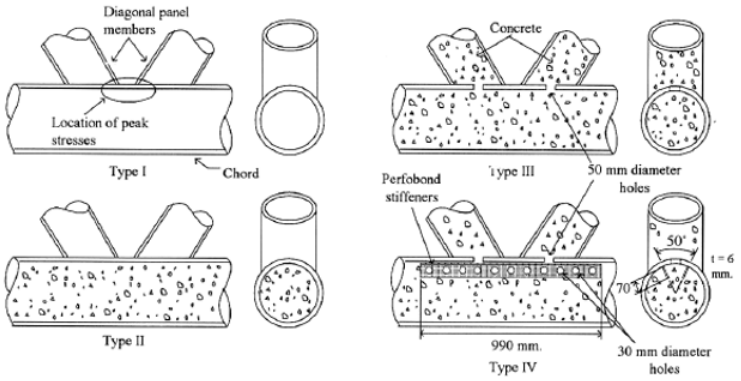

Figure 2.7 Composite tubular K-connection details from Udomworarat et al. (Udomworarat, 2002)

Sakai et al. (Sakai et al., 2004) conducted an experimental study to determine the maximum resistance and fatigue life in tubular K-connections filled with concrete. The study used 6 types of unfilled, concrete filled and reinforced specimens. Sample K1/2C is hollow (Figure 2.8.a). Sample K1/2D has a concrete filled chord while the diagonals are empty (Figure 2.8.b). Sample K1/2E is concrete filled in both the chord member and diagonal members (Figure 2.8.c). Sample K1/2F is composed of filled concrete, in both chord members and diagonal members, and reinforced by dowels, which are connected with holes in a chord member and diagonal members (Figure 2.8.d). Sample A-5 is composed of filled concrete, both in a member of the chord and in diagonal members and reinforced by dowels in a member of the chord (Figure 2.8.e). Finally, sample A-3 had a gusset plate, and is composed of filled concrete in both chord and diagonal members (Figure 2.8.f). Additionally, two fatigue samples were tested to improve manufacturing costs. In Sample A-1, the diagonal members overlap, and the chord is concrete filled (Figure 2.9.a). Sample A-2 is reinforced by an external reinforcement and the chord is concrete filled (Figure 2.9.b). Static and fatigue tests were carried out by loading the samples axially (tension and compression). The results showed that as reinforcement was increased, the final load gradually increased in the order K1/2C, K1/2D, K1/2E, A-5, A-3 and K1/2F. The ultimate strength of the tubular K-connection increased with the

filled concrete. The sample that showed greater resistance to fatigue was A-3, surpassing the 3.5 million cycles, followed by the sample A-1, with 3.0 million cycles, and finally the sample A-2 whose fissure in the welds began at 0.3 million cycles.

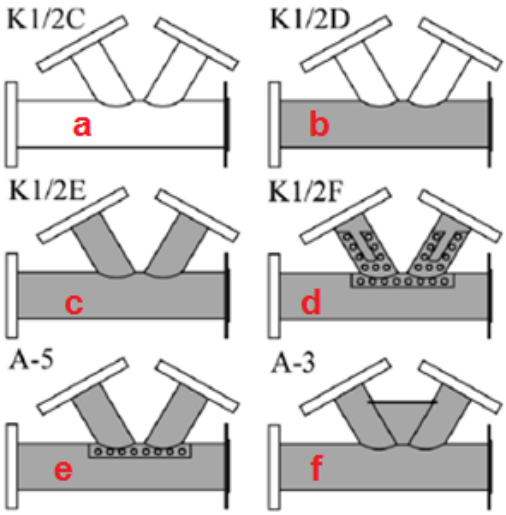

Figure 2.8 Types of connections tested by Sakai et al. (Sakai et al., 2004)

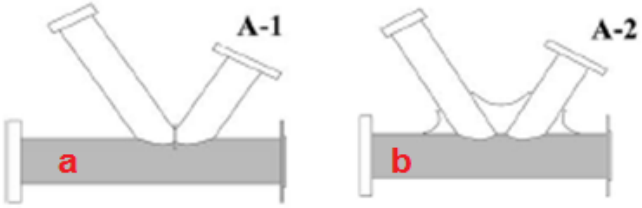

Figure 2.9 Fatigue specimens from Sakai et al. (Sakai et al., 2004)

Yin et al. (Yin et al., 2009) studied experimentally the hysteretic behavior of typical tubular N-connections (Figure 2.10). Four samples were built and tested under quasi-static cyclic axial loads. They included an unstiffened tubular N-connection, a doubler plate reinforced tubular N-connection, a tubular N-connection with a concrete filled chord member, and doubler plate reinforced tubular N-connection with concrete filled chord member. All the four samples are of the same configuration with the chord member being 245mm x 6mm (diameter and thickness), the diagonal member being 89mm x 6mm and the angle between the diagonal and the chord being 45^{o}. Hysteretic curves for the four samples showed no obvious degradation of stiffness with the increase in displacements. The authors concluded that the use of concrete-filled connections is the most effective way to improve the strength of tubular connections.

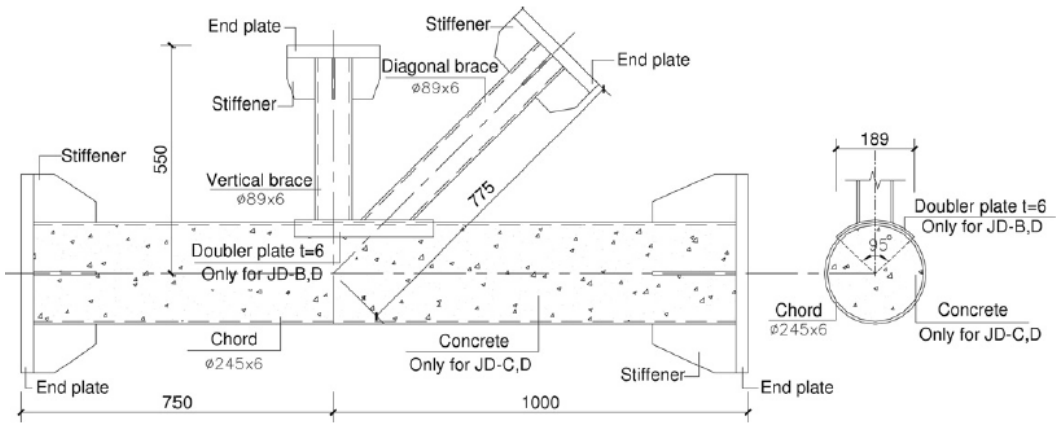

Figure 2.10 Test samples from Yin et al. (Yin et al., 2009)

Voth (Voth, 2010) examined, through experimental and numerical research, the behavior of rigid branch plate-to-CHS (circular hollow section) connections using through plates, as well as the behavior of non-orthogonal or skewed plate-to-CHS connections (Figure 2.11). Voth tested 12 small-scale unfilled plate-to-CHS (T-type and X-type) connections and 4 grouted T-type plate-to-CHS connections. The tests showed that unfilled specimens suffer large deformations under low load magnitudes. The presence of grout increases the capacity of the connections and can be used as an efficient retrofit method. The numerical models largely matched the experimental results.

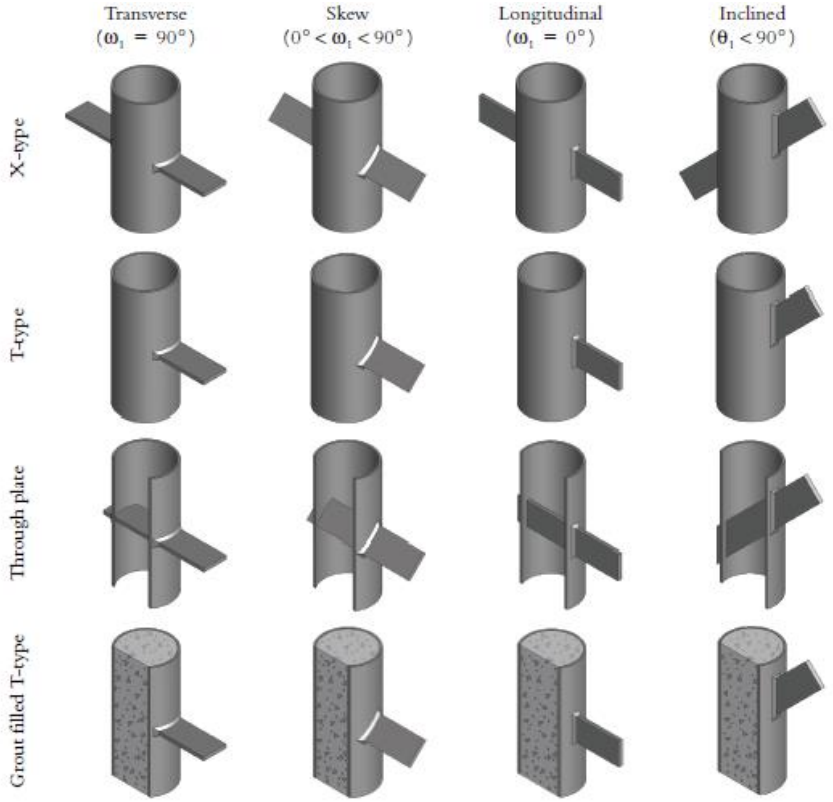

Figure 2.11 Types of connections from Voth (Voth, 2010)

Chen et al. (Chen et al., 2012) studied the ultimate strength of concrete filled tubular CHS T-connections under in-plane bending. They tested three samples with the same D/T ratio for the chords and different d/t ratios for the diagonal. The resistances obtained from the tests were compared with the design resistance given by the AISC standard (AISC, 2010) and the CIDECT standard (Wardenier et al., 2010). The results showed that the resistance values given by both design standards are very conservative. The authors proposed design equations for concrete-filled tubular steel T-connections, considering the width of the weld, the contribution of the concrete and the thickness of the chord.

Roeder and Lehman (Roeder, Charles; Lehman, 2012) investigated bridge foundation connections between steel piles filled with concrete and the foundation of bridge piers (Figure 2.12.a). The research included a detailed review of the results of previous research, including experimental programs and analytical studies of elements and connections CFT (concrete filled tube) and RCFT (concrete-filled tube with internal reinforcement). The experimental program did not include rectangular sections, nor tubes with diameters smaller than 4 inches. Ninety-one (19) tests were performed, distributed as follows: 28 CFT foundation connection tests, 26 beam-column tests, and 37 pure bending tests. The ratio D/t for the piles varied between 27 and 226; the diameter, D, varied between 4 and 20 inches. The embedded depth of the tube, the shear reinforcement in the foundations, the axial load ratio, and the properties of the steel tube were varied between the samples. Most tests evaluated the connection under axial compression and cyclic lateral load (Figure 2.12.b). Connections with very shallow embedment showed relatively poor performance with cone pullout failures. However, most of the samples had adequate embedment depth to provide excellent ductility and inelastic deformation capacity, without damaging the footing. The entire experimental program was validated by finite element analyses. Nonlinear continuous analysis models in ABAQUS (Hibbitt et al., 2011) provided an excellent correlation but at a great cost in time and complexity. The investigation resulted in improved models to predict the interactions of force, rigidity and axial load bending moment for CFT and RCFT components. Recommendations were given for the design of steel pile connections filled with concrete and the foundation.

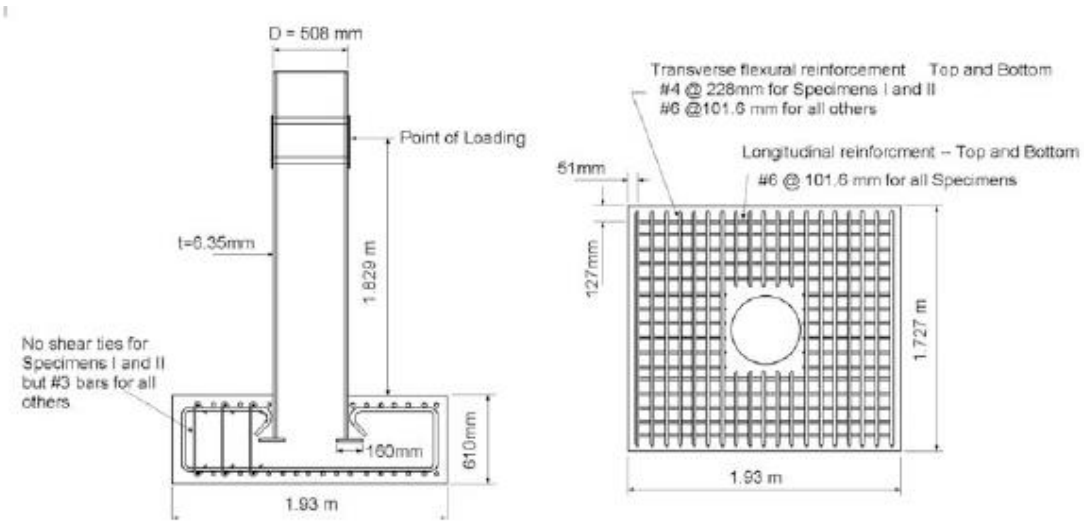

(a) Typical test sample from Roeder and Lehman.

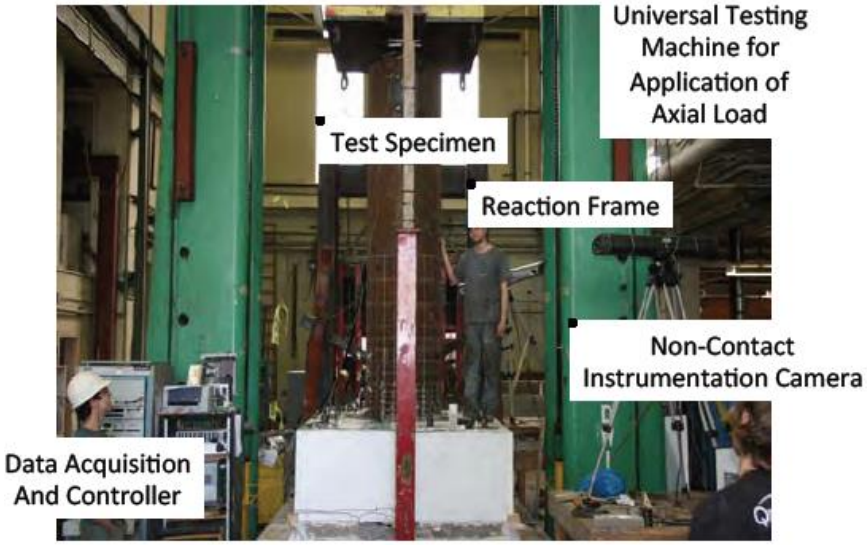

(b) Sample and test setup from Roeder and Lehman.

Figure 2.12 (Roeder, Charles; Lehman, 2012).

Xu et al. (Xu et al., 2015a) studied the behavior of concrete-filled tubular steel connections manufactured from circular hollow sections (CHS). They tested four types of connections: T, Y, K and KT (Figure 2.13), which covered two chord slenderness ratios (D/t = 60 and 75). An axial tensile force was applied in all the samples. The concrete filling in the tubular CHS connections greatly improved its performance under axial tensile load for both slenderness ratios. The authors recommended that the design strengths be calculated from the AISC design rules for the limit state of punching shear yielding for unfilled tubular CHS connections. In general, tubular CHS connections filled with concrete showed a significant increase in stiffness.

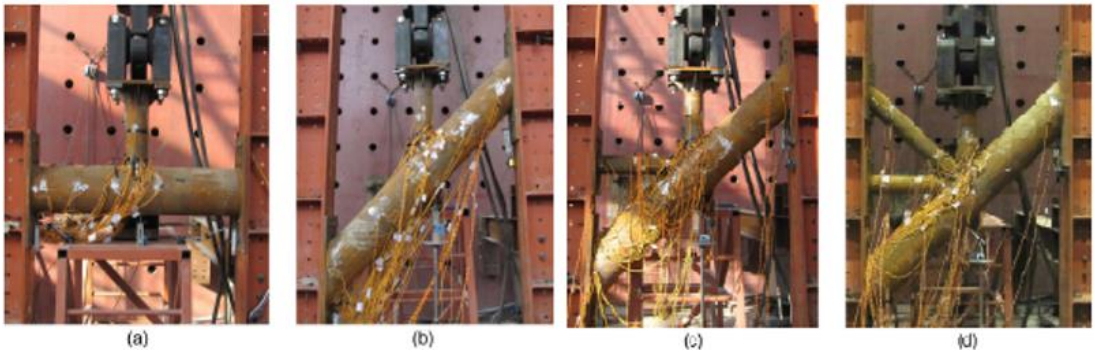

Figure 2.13 Test setup: (a) T-connection; (b) Y-connection; (c) K-connection; (d) KT-connection from Xu et al. (Xu et al., 2015a)

Chen et al. (Chen et al., 2015) carried out an experimental investigation to evaluate the resistance and behavior of unfilled and concrete-filled CHS T-connections with concave and straight chords under axial compression. Sixteen samples were tested (6 type A (concave, unfilled), 2 type B (concave, filled), 6 type C (straight, unfilled), and 2 type D (straight filled) as shown in Figure 2.14). In all the samples, the cross-section of the chord was the same, while the cross section of the diagonal changed. Two types of failure were observed in type A samples, namely, chord plastification and local buckling failure of diagonal. Only chord plastification was observed in samples of type B. In type C samples, local buckling failure of diagonal and material yielding failure of diagonal was observed, and type D samples showed local buckling failure of the diagonal. The final strengths of the CHS T-connections with concave chord are generally larger than those of traditional CHS T-connections with straight chord. The investigation demonstrated that the reinforcement of the chord member with concrete filling significantly improved the radial rigidity of the chord member. Finally, they showed that the design rules given in Eurocode 3 and the AWS standard are quite conservative for the traditional design of both unfilled and concrete-filled CHS T-connections with concave and straight cords, while the rules of design given in the API standard are generally more appropriate for the design of both types of connections.

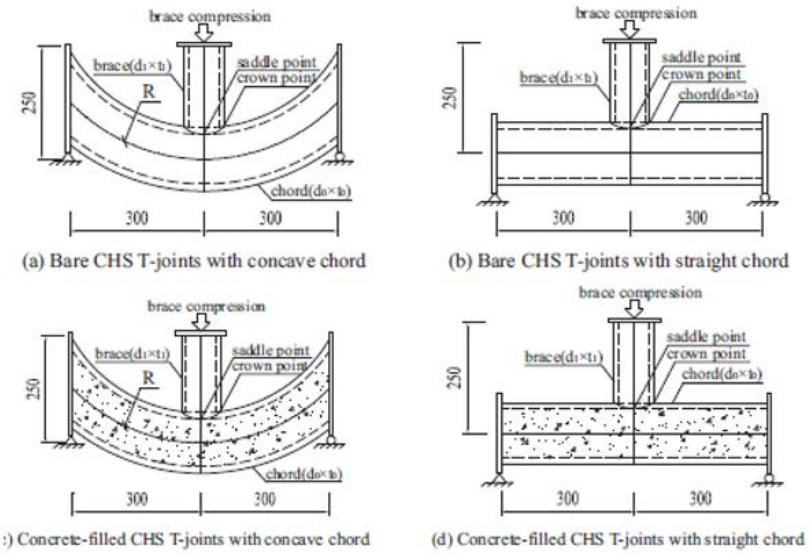

Figure 2.14 Schematic diagram of test samples from Chen et al. (Chen et al., 2015)

Huang et al. (Huang et al., 2015) investigated experimentally the resistance and failure modes of tubular concrete-filled connections. In addition, they compared the failure modes of the CFST K-connections and the CHS K-connections of the same size and investigated the effect of studs welded on the inner surface of the chord member. Figure 2.15 shows the configuration of the test. Eight samples were tested (2 without concrete filler, and 6 with concrete filler of which 3 had welded bolts inside the chord). The geometry of the sections of the chord and diagonals of the samples of the CFST K-connections was the same as that adopted in the CFST beams of certain arch bridges built in China (Chen and Radic, 2009). In the tests, a pattern of forces in tension and compression was applied to the diagonals. It was shown that the filling of the chord with concrete results in an increase in stiffness in the CFST-connections compared to the CHS-connections, as well as in a more uniform tension distribution in the connection for both the chord and the ends of the diagonal. The unfilled connections failed by chord face failure, while the concrete-filled connections failed due to punching shear and deformation in the diagonals. The failure mode of the concrete-filled connections with bolts welded to the interior of the chord was similar to that of the unfilled connections. However, the addition of studs welded in the connections produces an additional increase in the stiffness of the connection and increase the uniformity of the distribution of the tension in the connection.

Figure 2.15 View of a K-connection sample and of the test set-up from Huang et al. (Huang et al., 2015)

Xu et al. (Xu et al., 2017) developed design provisions for concrete-filled CHS connections subjected to in-plane bending through analytical and experimental studies (Figure 2.16.a). Four samples were tested under in-plane bending, varying the diameters and thicknesses of the chord and the diagonal (Figure 2.16.b). However, the length of the elements remained constant in all tests. To connect the chord and the diagonal, fillet welds were used. The finite element model was developed in ABAQUS (Hibbitt et al., 2011). The analytical models yielded results consistent with those of the experiments. Experimental results indicated that the only failure mode observed in the tests was the chord-wall punching shear failure at the crown (Figure 2.16.b). The chord deformations at the maximum load were below the specified deformation limit (3%) in the recommendations of CIDECT-1 (Wardenier et al., 2010). The study indicated that weld geometry should be considered when determining the strength of concrete-filled CHS connections. Finally, the authors proposed design equations for concrete-filled CHS connections, considering the actual shear stress distributions, the internal concrete and the effects of the curved failure faces.

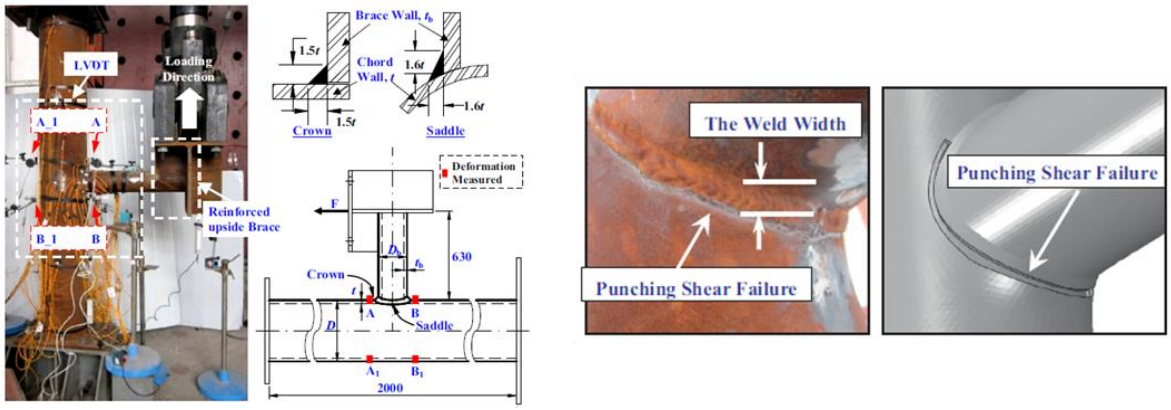

Figure 2.16 (a) Test set-up for samples, and (b) Failure mode of sample from Xu et al. (Xu et al., 2017)

Cheng et al. (Cheng et al., 2018) studied the structural behavior of partially infilled welded integral T-connections by using experimental and numerical methods (Figure 2.17.a). The static tests were performed by imposing a horizontal load and vertical axial compression at the end of the diagonal (Figure 2.17.b). Six integral T-shaped connections were tested, classified into two groups, with and without arc transition. In each group, three cases of chord concrete filling were considered: chord completely filled-concrete (i.e., concrete filling length of 1500 mm), chord partially filled-concrete (i.e., length of concrete filling 800 mm), and hollow chord (i.e., without concrete filling). The concrete-filled connections failed due to the deformation of the web plates in the connection core zone and the buckling of the web arc transitions. There were no differences in failure modes between partial and fully concrete-filled connections. The hollow connections failed due to buckling of the top flanges of chord near the core area of the connection. The tests showed that the partial filling of the chord reduces the sectional stresses almost as effectively as the complete filling of the chord. All of the data indicated that the critical length of the concrete-filled for the integral T-connections studied could be around 400 mm, that is, approximately twice the height of the section of the chord. The authors recommend a length of concrete-filled of three times the height of the section of the chord for the connections partially concrete-filled, so that the structural behavior is similar to that of the completely concrete-filled connections.

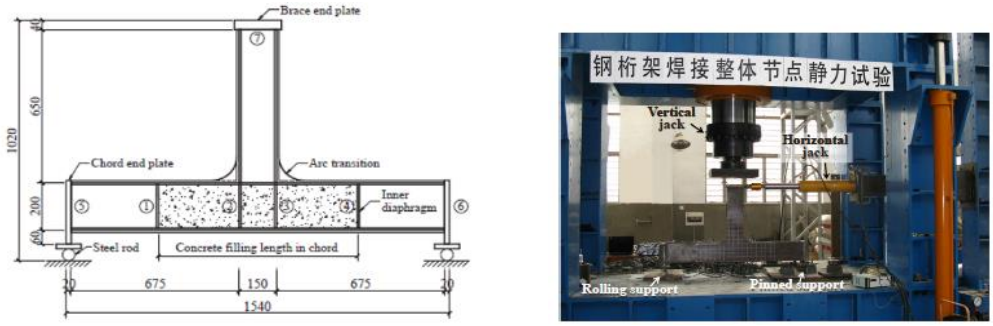

Figure 2.17 (a) Sample of welded integral T-connection, and (b) overall view from Cheng et al. (Cheng et al., 2018)

Musa et al. (Musa and Mashiri, 2019) studied the distribution of stress concentrations in seven K-type concrete filled connections subjected to axial loads. The results indicate that the stress concentrations factors (SCF) are largest between the diagonals and at the tip of the crown on the chord and diagonals. The maximum SCF occurs in the crown toe. SCFs are almost always higher in the chord than in the diagonals. The analytical models were consistent with the tests.

The investigations discussed above considered connection experimental/analytical efforts, i.e., a validation of the experimental models is carried out using analytical models, considering different aspect ratios, different types of loads (axial compression and tension, plane flexure, out-of-plane flexure) and different study parameters among which stand out the stiffness of the connection, ultimate strength, stress concentration factors and fatigue performance (see appendix A). However, it is necessary to carry out analytical investigations to expand the study parameters that for economic, infrastructure, or time reasons is not possible to study with experimental investigations. Another relevant aspect that is achieved with analytical investigations is the determination of the most relevant parameters that must be considered when modeling composite connections. Several researchers have proposed 3D finite element models to capture in a more real way the structural behavior of composite connections. Although a number of these focus on CFT members, a number of the conclusions are applicable to CFT connections and thus considered relevant to this review.

2.1.2 Analytical Research

This section summarizes some of the key modeling investigations, beginning with ones meant to establish both cross-sectional and short length member models, followed by descriptions of connection modelling. As noted earlier, there are numerous investigations on the topic, but the studies highlighted herein are only a few of those most relevant to the second part of the chapter. The data appendix A considered only studies for which most important details were found in the open literature; the intent is to make this an open resource and thus researchers are encouraged to contact the authors if they have additional data that should be included in this table.

2.1.2.1 Cross-Sectional and Short Length Models

Chen and Chen (Chen and H., 1973) conducted an analytical investigation to calculate the maximum load capacity of concrete-filled beam-columns. For this purpose, they constructed beam-column interaction curves, relating the slenderness, axial load and bending moment, considering the triaxial effects of the confined concrete. The Column Curvature Curve (CCC) method is adopted for the solution (Chen, 1969; Chen and Santathadaporn, 1969). The curves obtained showed that for a length-to-depth ratio (l/t) greater than 20 for square columns or 15 for circular columns, the effect of the triaxial state of tension in the concrete on the resistance of such columns is not important. To consider initial imperfections, the authors recommend an initial eccentricity of 0.002l for square sections and 0.001l for circular sections. Based on these values, the authors demonstrated that the maximum load capacity of axially loaded CFTs can be accurately predicted by comparing the results with data from the literature and assuming a certain eccentricity in the application of axial load.

Hajjar and Gourley (Hajjar and Gourley, 1996) developed a polynomial expression to represent the three-dimensional (3D) cross-sectional strength of square or rectangular CFTs, that is, the

combined axial and biaxial flexural capacity of a zero-length beam-column. The analysis was performed through a detailed analysis of non-linear fiber elements of zero-length CFTs. The fiber element method offers a high degree of precision as a numerical tool to analyze the moment-curvature-thrust behavior of the cross-sections of the CFT beam-column. The numerical results were validated against experimental results available in the literature (M. Tomii and K. Sakino, 1979a, 1979b). In this investigation the effects of creep and shrinkage are neglected as is the presence of shear connectors or internal reinforcing bars. Perfect bond between steel and concrete is assumed and the effects of residual stresses are incorporated directly into the stress-strain curve for steel, which then depends on the D/t ratio. It is important to note that the proposed formulation only applies to CFT sections with compressive strengths of concrete of up to 100 MPa, and ratios of tube width-to-thickness (D/t) of up to 50. The results obtained with the polynomial expression are consistent with the experimental results. The polynomial equation includes as variables the width-to-thickness of the steel tube and the relationship between the concrete compressive strength and the elastic limit of the steel tube.

Hajjar et al. (Hajjar et al., 1998) developed a three-dimensional distributed plasticity model for CCFTs and RCFTs considering both the geometric and material nonlinearities. The model uses the fiber element approach to model the distributed plasticity and tension between the steel tube and the concrete core in the connection region of the CFT beam-column. Figure 2.18 shows the discretization of the cross-sections of CFT. The steel constitutive model was calibrated for ASTM A500 and ASTM A36 steels, while the concrete constitutive model was calibrated for concrete strengths (f'c) of up to 50 MPa. The confinement of the concrete core of the CFT by the steel tube was incorporated into the concrete constitutive model. As in their previous work, residual stresses are incorporated into the steel constitutive model. In the model formulation, nonlinearity due to shear or torsion, reinforcement or shear connectors, local buckling, time-dependent effects on materials, shear deformations due to bending, and post-collapse behavior were not incorporated. The constitutive models for steel and concrete used in the development of this research are based on detailed studies by Molodan and Hajjar (Molodan and Hajjar, 1997), and Hajjar et al. (Hajjar et al., 1998). The validation of the model was performed by comparing the results of finite elements against individual CFT experiments. The model proved efficient for performing nonlinear static analysis, advanced design analysis, and cyclic behavior studies.

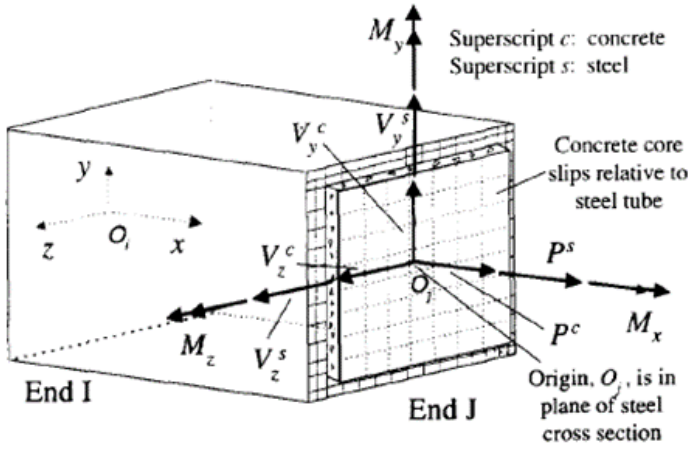

Figure 2.18 Distributed plasticity concrete-filled tube finite element model from Hajjar et al. (Hajjar et al., 1998)

Mamaghani and Packer (Mamaghani and Packer, 2002) developed a seismic design procedure for maximum strength and ductility evaluation of partially concrete-filled thin-walled steel bridge piers, with and without longitudinal stiffeners. The procedure is applicable for the design of new piers, reinforcement of piers of existing steel bridges and can be extrapolated to the seismic design of concrete-filled columns and steel connections. The main reason for working with piers, columns and/or partially concrete-filled connections is to increase ductility under seismic excitations, without considerably increasing the stiffness and/or resistance of the element. The columns were subjected to a constant axial load and cyclic lateral load. The results indicate that the steel controls the strength of columns without longitudinal stiffeners, while concrete governs for the cases with longitudinal stiffeners. Through the proposed design procedure, the maximum strength and ductility of the thin-walled steel bridge pillars are estimated.

Hu et al. (Hu et al., 2003) studied the non-linearity and the influence of the confinement pressure in CFTs subjected to axial compression loads. For this, they developed constitutive models for the concrete, steel tubes and steel reinforcing tie. These models were validated with experimental studies conducted by Scheidner and Huang et al. (Huang et al., 2002; Schneider, 1998). Circular (CU), square (SU), and square sections with steel reinforcement diagonals (SS) were considered in the study. The authors made finite element models (Figure 2.19), which included the sliding and friction (coefficient of friction = 0.25) between concrete and steel through interface elements. They assumed that the ratio of Poisson concrete as $\upsilon = 0.2$ and that the stress-strain curve of the steel was elastic-perfectly plastic. For the CU sections, the lateral confinement pressure (f_l) decreases with the increase in the width-to-thickness ratio (D/t), but for a D/t ratio <40 the steel tubes provide a good confinement. For the SU sections, the lateral confinement pressure is inversely proportional to the width-to-thickness ratio (b/t). Because the lateral confinement pressure in the square columns is not uniform, the circular columns have higher confinement pressure and therefore the material exhibits less degradation. Finally, the SS sections have the same behavior as the SU sections; however, the use of reinforcing diagonals improves the lateral confinement pressure and prevents local buckling of the steel tube. It is important to indicate that these results can be extrapolated to concrete-filled connections subjected to axial loads.

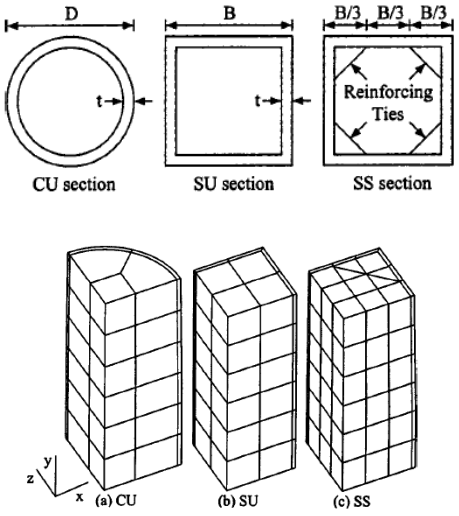

Figure 2.19 Finite Element model of CTF from Hu et al. (Hu et al., 2003)

Liang et al. (Liang et al., 2007) studied the local and post-local buckling behavior of steel plates under non-uniform compression and in-plane bending in concrete-filled thin-walled steel tubular beam-columns. The study was carried out using finite nonlinear models, which incorporate residual stresses, initial geometric imperfections, strain hardening, and in-plane bending. For research purposes, the authors took the compression residual stress as 25% of the yield strength of the steel plate. It is important to mention that residual stresses were incorporated into the model by prestressing. The stress-strain curve for steel plates with residual stresses is modeled as established by Ramberg and Osgood (Ramberg and Osgood, 1943). The results show that before local buckling is reached, there is a minimal increase in the lateral deflections of the plate with increasing applied load. After local buckling, there is a significant reduction in the rigidity of the steel plates; however, the steel plates can still carry high loads without failure. The numerical results indicate that lateral stiffness, local buckling, tension capacity and ultimate strength are reduced by increasing the width-thickness ratio of a steel plate under a stress gradient. Finally, design formulas are proposed for the calculation of the ultimate resistance of steel plates under non-uniform compression and bending. The results of this investigation are useful in understanding compression and bending behavior of steel connections filled with concrete because they incorporate parameters of geometric and material nonlinearities.

Choi and Xiao (Choi and Xiao, 2010) developed a numerical program for CFT columns under axial load, taking as reference the stress-strain model developed by Xiao et al. (Xiao, 1989; Xiao et al., 1991). The numerical results were compared with several experimental programs available in the literature (Huang et al., 2002; Sato, 1995; Tomii et al., 1977; Xiao, 1989). The numerical program can be implemented for other types of elements, such as concrete-filled connections. The investigation assumes that as long as there is no external load, there will be no deformation or initial separation between the concrete infill and the steel tube, i.e., neither of them has initial stress. It is also assumed that the axial deformations of the concrete and the steel tube are identical. The numerical program involves eleven unknowns (five concrete and steel stresses, five concrete and steel deformation values, and the applied axial load). The incremental analysis method was adopted for the resolution of the problem. The authors demonstrated that the results of the numerical program accurately represent the limit and stress-strain relationship of the CFT columns. However, in some cases when comparing experimental results with the analytical model, the latter was not able to predict the hardening behavior due to deformation or resistance degradation due to local buckling.

2.1.2.2 Connection Models

Shen and Choo (Shen and Choo, 2012) conducted a numerical study of the fracture mechanics in tubular T-connections with grout-filled chords. For this, they studied two configurations, welded T-connection and T-connection with grout-filled cord (Figure 2.20). The results were compared with experimental studies in the literature (Bowness and Lee, 1995, 1998; Mashiri et al., 2002). The stress intensity factors (SIFs) for welded and grout connections are calculated using a numerical method and subsequently compared to those in design codes (British Standards., 1993; Standards, 2013). The study was carried out using 3D finite models, using the Abaqus finite element software (Hibbitt et al., 2011). The results show that the contact analysis between the steel and the grout is highly non-linear. Both SIF and stress concentration factors (SCF) are not sensitive to the load on the diagonal. The stress distribution is more uniform in the grouted connections than

in welded connections. Finally, the numerical model indicates that the fatigue life of the tubular connection with a completely grouted chord will improve significantly compared to the original welded connection.

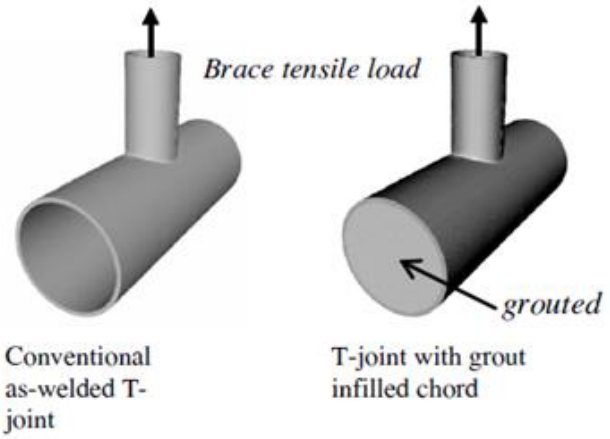

Figure 2.20 Types of connections from Shen and Choo (Shen and Choo, 2012)

Raj and Joy (Raj and Joy, 2016) carried out an analytical evaluation and comparison of the fatigue resistance behavior of the composite circular K- and KT-connections (Figure 2.21). Six models were developed for the analysis of the K-connection and another 6 models for the analysis of the KT-connection. Models of both unfilled and concrete-filled connections were analyzed. The results indicate that when only the chords of the K- and KT-connections are filled, the maximum resistance increases 2.1 and 2.0 times respectively. However, when the entire K-connection is filled, the resistance increases 5.9 times and 6.0 times for the KT-connection. The above shows that the maximum strength increases as the amount of concrete infill increases. The use of a concrete infill provides a mechanism for redistribution of the stresses. Finally, when comparing the K- and KT-connections, the latter shows greater resistance, so it is advisable to use them in tubular structures.

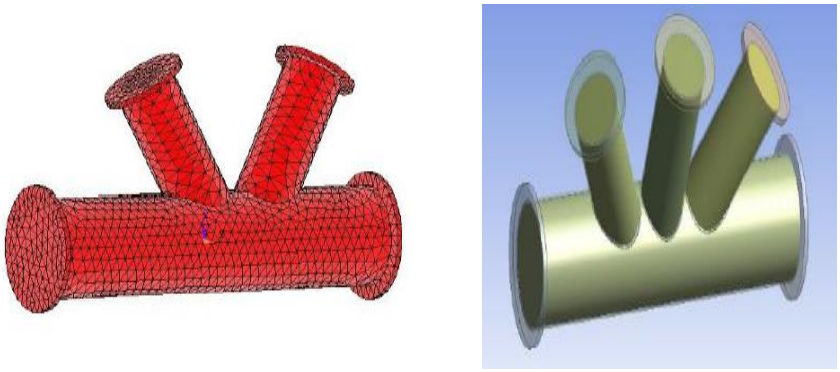

Figure 2.21 Models FEA K and K-T Schematic view from Raj and Joy (Raj and Joy, 2016)

Hou and Han (Hou and Han, 2017) studied the analytical behavior of concrete-filled double skin steel tubular (CFDST) K-connections and of hollow circular section (CHS) (Figure 2.22.a). In addition, they studied the mechanism of load transfer and possible failure modes of these connections. Finite element models were made in ABAQUS (Hibbitt et al., 2011) of the CFDST and CHS circular connections subject to static loading (Fig. 2.22b). The contact between the concrete and the steel tube was modeled in such a way that it allowed independent deformation of each material, but restricted the penetration between the two materials. A friction factor equal to 0.5 was assumed as reported by Hou et al. (Hou et al., 2015). The analytical results also were validated with the experimental program carried out by Hou et al. (Hou and Han, 2017). The studies showed that the main modes of failure for the CHS K-connections are chord plastification and chord punching shear. CFDST K-connections with interleaved concrete and double-skin steel pipes have greater resistance against local buckling. However, they may have different failure modes, depending on the hollow ratio of the CFDST chord (χ). The failure modes include local buckling of the compression diagonal, fracture of the tension diagonal, chord plastification, chord punching shear, and local bearing failure of the chord. Finally, considering the different failure mechanisms, the authors propose simplified formulas for the design of CFDST K-connections.

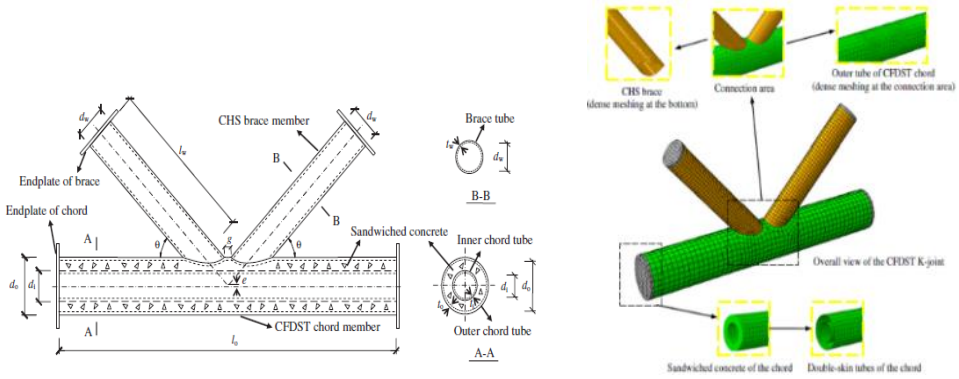

Figure 2.22 (a) Scheme of a typical CFDST K-connection. (b) Models FE from Hou and Han (Hou and Han, 2017)

Zheng et al. (Zheng et al., 2018) developed three-dimensional finite element models to assess stress concentration factors (SCF) in steel tubular concrete-filled T-connections (Figure 2.23). The results obtained were compared with existing experimental results in the literature (Chan et al., 2010; Xu et al., 2015b) to validate the analytical models. This comparison is given in four locations: chord saddle (CS), chord crown (CC), diagonal saddle (DS) and diagonal crown (DC). The parameters that were considered for the determination of the SCF were the thickness ratio ($\tau = t/T$), diameter ratio ($\beta = d/D$), diameter to thickness ratio of chord ($2\gamma = D/T$), and relative chord length ($\alpha = 2L/D$). The numerical results showed that as τ increases under either tensile or compressive loads the SCF also increases. As β increases under tensile forces, SCF decreases, except for the stress on the chord crown. For compressive forces, the SCF increases as β increases. The 2γ ratio as well as the SCFS increases under tensile forces, except the tensions in the diagonal crown, which decrease under both tension and compression forces. However, as 2γ increases under compression, the SCF decreases. The influence of α on SCF is negligible under tensile and compressive force, except for stresses located in the chord crown, where, as α increases under tensile and compressive forces, SCFs increases. SCFS in the chord caused by axial tensile force is

much larger than those under compression. Finally, the authors developed parametric formulas to determine the SCFs for CFST T-connections under axial force in the diagonal.

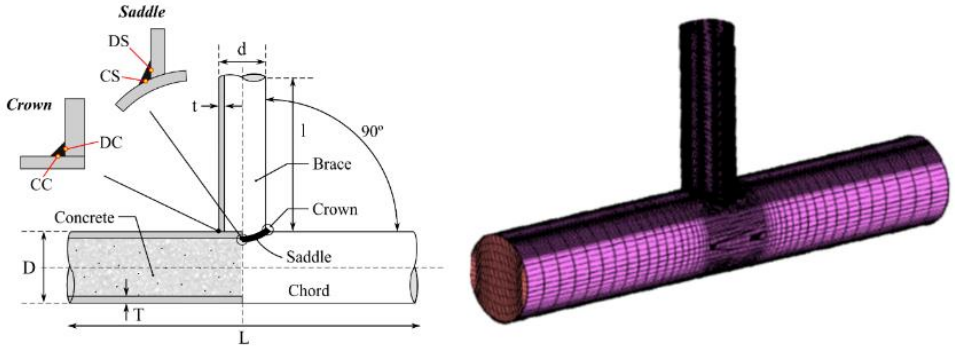

Figure 2.23 Geometric parameters of CFST T-connections and FE model from Zheng et al. (Zheng et al., 2018)

This section presented a brief summary of the analytical investigations of CFTs-connections, which in recent decades have increased due to the increases in computational horsepower, leading to the study of many parameters that are very difficult to evaluate with experimental investigations. Some important parameters are the contact between steel and concrete and the stress concentrations in the weld. It is also important to note that the aspect ratios and residual stresses have a significant influence on the structural modeling of composite connections subjected to axial loads. Analytical modeling for CFTs-connections is presented in the next section, results are verified against three of the best-described tests in the literature.

2.2 Finite element modeling

As described in the previous section, numerous combined experimental/analytical investigations have been carried out to ascertain the structural behavior of CFTs-connections. Although experimental programs have provided some insight into the effect of varying geometric properties, materials, and load types on the behavior of CFTs-connections, the number of variables that have been and can be tested in the future is limited. Thus, numerical finite element modeling or some similar robust numerical modeling methodology is required to expand the range of study variables. To complement the development of a database and the state-of-the-art report summarized in the previous sections, this research developed a new analytical model for CFT connections, with the final goal of doing extensive parametric studies to suggest improvements to current design provisions. This chapter limits itself to the description of this new model, which was calibrated to one test by Voth (Voth, 2010) and further verified by comparatives studies with the result from tests by Sakai et al. (Sakai et al., 2004), Chen et al. (Chen et al., 2015), and Huang et al. (Huang et al., 2015) (see Figure 2.24). The selection of these specimens was based on the fact that they represent common types of tubular concrete-filled connections (Han et al., 2014) and represent four of the best-described tests in the literature.

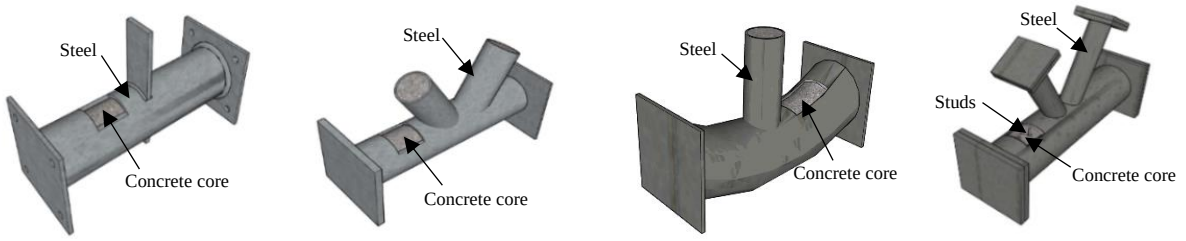

Voth (Voth, 2010) | Sakai et al. (Sakai et al., 2004) | Chen et al. (Chen et al., 2015) | Huang et al. (Huang et al., 2015)

Figure 2.24 Schematic views of connections used in the analytical studies.

2.2.1 Software/Solver interface

The pre-processing and computations are performed on the ANSYS LS DYNA platform (ANSYS, 2020) using computational facilities at PUC and Virginia Tech (https://informatica.uc.cl/, https://arc.vt.edu/). Due to the high degree of non-linearities that accompany the inelastic behavior of CFTs-connections, the study was carried out using an explicit integration scheme with the double-precision LS DYNA (Hallquist, 2006) smp solver. Under the explicit scheme, the iterative process associated with an implicit nonlinear problem is avoided, and because the mass matrix is diagonal, the equations of motion can be decoupled. Therefore, the inversion of the lumped mass matrix is trivial, which results in low memory requirements. However, one aspect to consider with the explicit solver is that the integration method is only stable if the time step size is smaller than a critical time step size (conditionally stable time interval) according to the stability criteria of Courant et al. (Courant et al., 1967) defined by Eq. 2.1:

$$\Delta t \leq \frac{L}{c} \qquad (2.1)$$

where L is the characteristic element length (shortest edge or height), c is the speed of sound, and Δt is the time step. The critical time step size correlates to the highest natural frequency in the system and is calculated for linear systems without viscous damping. Due to nonlinearities, critical time step size may change with each cycle. Thus, the choice of an implicit scheme does not necessarily lead to computation time savings.

2.2.2 3D Models

Three-dimensional models were constructed to reproduce all the geometric properties and materials of the experimental test specimens, including details related both to weld type and geometry and the application of the loads. Symmetry was considered in one plane, and therefore the models of Voth (Voth, 2010), Sakai et al. (Sakai et al., 2004), Chen et al. (Chen et al., 2015) and Huang et al. (Huang et al., 2015) included half of the original geometry (Figure 2.25.a-d). Note that one model included shear studs, which considerably increased the number of degrees of freedom in the model (Figure 2.25.d).

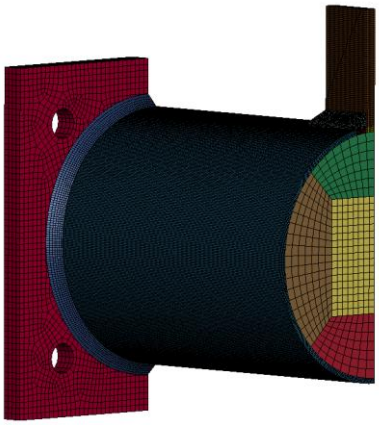

a. Voth (Voth, 2010)

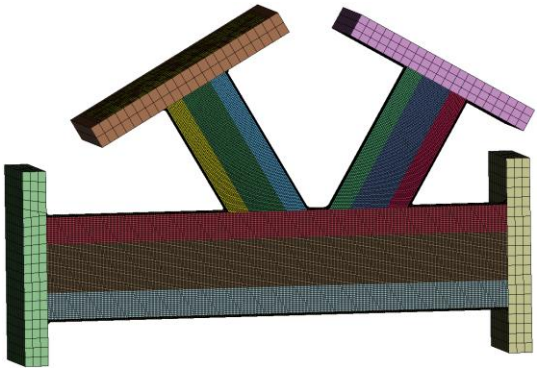

b. Sakai et al. (Sakai et al., 2004)

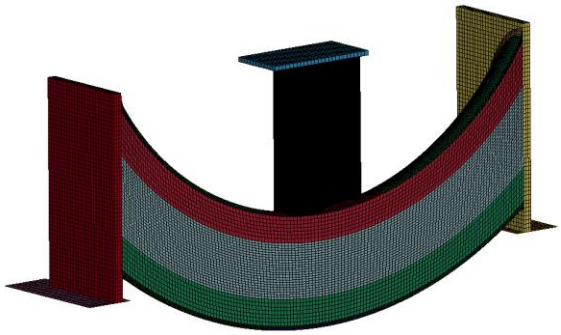

(c) Chen et al. (Chen et al., 2015)

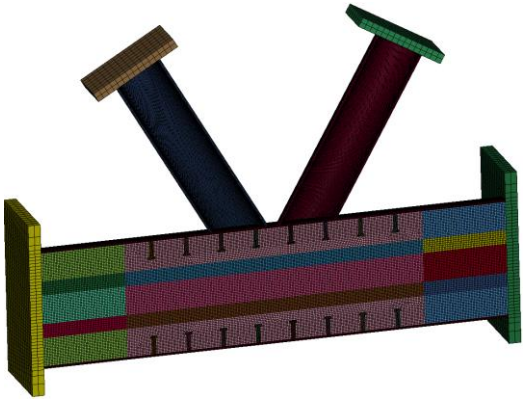

(d) Huang et al. (Huang et al., 2015)

Figure 2.25 Finite element meshes for the CFTs connections studied.

2.2.3 Meshing

The geometric discretization of the different components of the CFTs-connections is carried out using block structural meshes with reduced integration hexahedral elements. These elements offer the advantage that they can be used in elements with a high aspect ratio without sacrificing precision. Because hexahedron meshes are difficult to join, numerous discretization schemes were attempted in order to obtain the highest reliability in the results. In the region of the weld bead, it is not possible to use hexahedral meshing, so tetrahedral meshing is used. Mesh size was established in all models using numerical convergence tests that indicated that models with upwards of $3x10^5$ nodes were needed for the model of Voth (Voth, 2010), while $1x10^6$ nodes were needed for the model of Huang et al. (Huang et al., 2015). A close-up view of the Voth specimen near the plate, including the weld, is shown in Figure 2.26 and a close-up view of the Huang specimen near the diagonals, including the presence of shear studs, is shown in Figure 2.27 to give an idea of the discretization levels. The properties of each model are presented in Table 2.2.

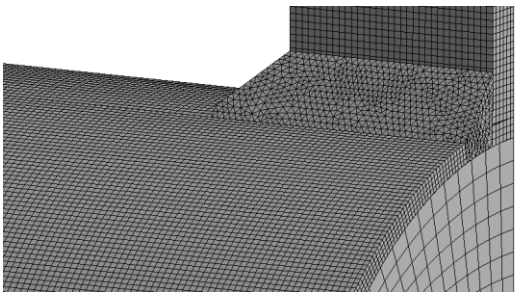

Figure 2.26 Mesh near plate for the Voth test.

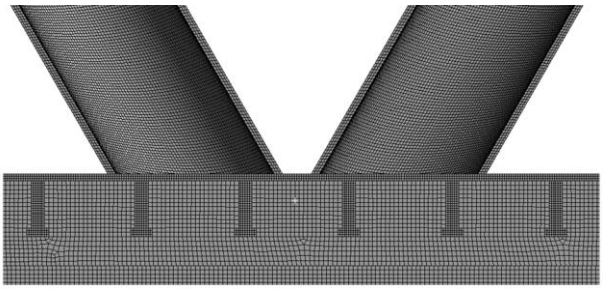

Figure 2.27 Mesh near diagonals for the Huang test.

Table 2.2 Model properties.

Source	Type	Geometric (Diameter - Ø or Plate - PL, mm)		Number of elements	Number of nodes	Degrees of freedom	Load time (sec).	Mesh size (mm)	
		Chord	Diag.					Concrete	Steel
Voth (Voth, 2010)	T-type branch plate	Ø 219.17	PL 100X19	293238	335403	1006209	0.1	6	1.5
Sakai et al. (Sakai et al., 2004)	K-type	Ø 328.5	Ø 216.3	2705547	3121608	9364824	0.1		
Chen et al. (Chen et al., 2015)	CHS T-types with concave chord	Ø 140	Ø 114	485417	594922	1784766	0.3		
Huang et al. (Huang et al., 2015)	K-type	Ø 100	Ø 60	1612473	1958565	5875695	0.2	4	1.5

To avoid the development of spurious hourglassing deformation modes resulting from the excitation of zero energy degrees of freedom, the Belytschko-Bindeman (Belytschko and Bindeman, 1993) hourglassing control mechanism is used in all models. An hourglass coefficient (QM) of 0.10 is used, as previously proposed by Bruhl (Bruhl, 2015) for the behavior and design of steel-plate composite walls for blast loads. To further reduce computation costs, reduced integration linear elements are used in areas where yielding was not expected.

2.2.4 Material Models

Inelastic finite element models of CFT connections must incorporate the material nonlinearities of both structural steel and concrete. The material model used for concrete is the MAT_72REL3 model developed by Malvar et al. (Malvar et al., 1997) This model is a three-invariant model which uses three shear failure surfaces and includes damage and strain rate effects (Figure 2.28). The advantage of the MAT_72REL3 concrete material model is that the complex behavior of concrete can be modeled by specifying only the density and unconfined compressive strength when detailed stress-strain data for the concrete materials are not available. As this is the case for most of the tests reported in the data appendix, the use of a more sophisticated material model, which would require many more material parameters, appears unjustified.

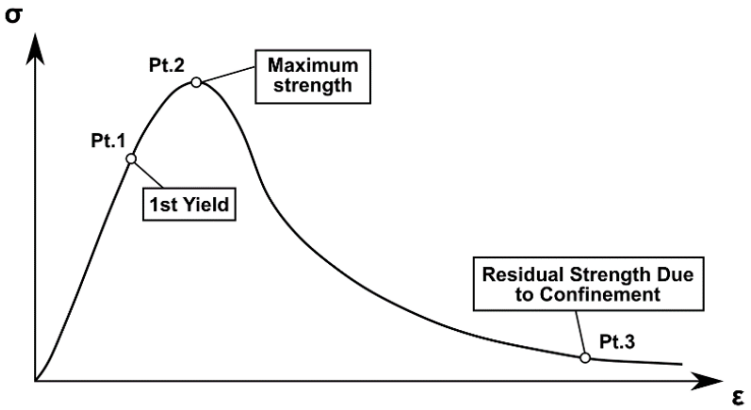

Figure 2.28 Three failure surfaces in the Concrete Damage Model. (Modified from (Malvar et al., 1997)

For the structural steel, the material models utilized plasticity data extracted from the experimental investigations. For Voth (Voth, 2010) and Chen et al. (Chen et al., 2015), a multilinear isotropic hardening material model was used since all required material parameters for the steels were available (Figures. 2.29.a-b).

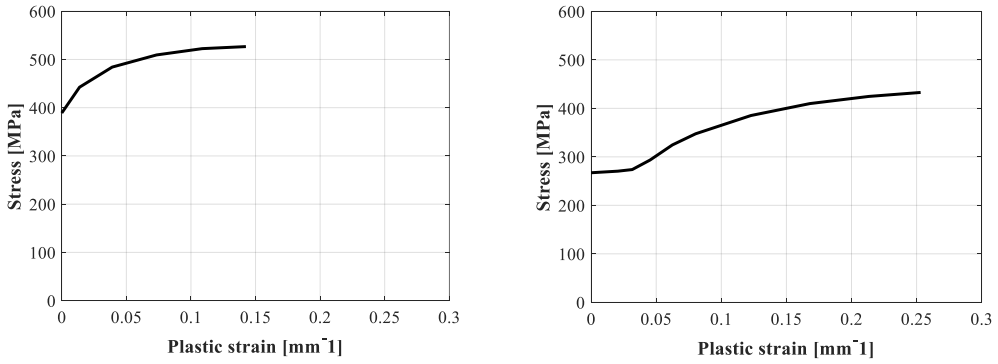

(a) (b)

Figure 2.29 Steel stress-strain curve. Multilinear isotropic hardening material model: (a) Voth (Voth, 2010) and (b) Chen et al. (Chen et al., 2015)

For the Sakai et al. (Sakai et al., 2004) and Huang et al. (Huang et al., 2015) models, a bilinear isotropic hardening model was used since only the yield and ultimate strength of steel were available. For the latter, Equations 2.2 and 2.3 were used to obtain the real stresses and strains of the steel (Figure 2.30). It is important to note that these models have been widely adopted in nonlinear FEA (Gordan et al. 2014, Mullins and Gunnars 2009, Nakashima et al. 1995).

$$\varepsilon_{true} = \ln\ (1 + \varepsilon_{ing}\ ) \qquad (2.2)$$

$$\sigma_{true} = \sigma_{ing}\ (1 + \varepsilon_{ing}\ ) \qquad (2.3)$$

Where ε_{true} is the true strain, ε_{ing} is the engineering strain, σ_{true} is the true stress, σ_{ing} is the engineering stress.

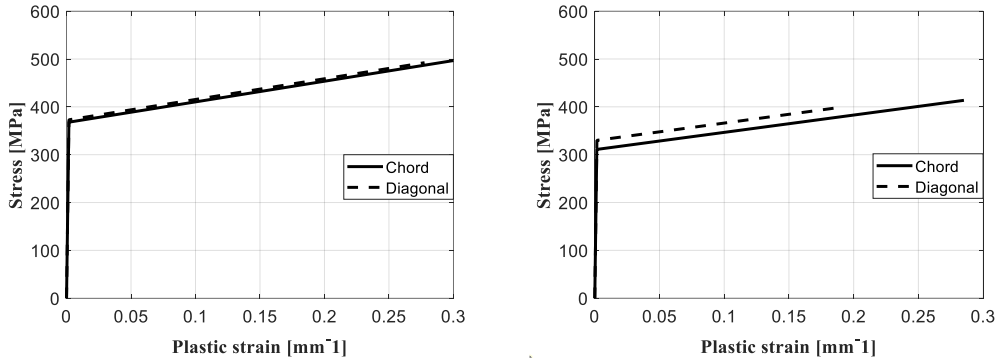

(a) (b)

Figure 2.30 Steel stress-strain curve. Bilinear isotropic hardening material model: (a) Sakai et al. (Sakai et al., 2004) and (b) Huang et al. (Huang et al., 2015)

2.2.5 Concrete – structural steel contact

A complex phenomenon in modeling CFTs-connections is the contact between structural steel and concrete. For this purpose, two types of contacts were considered, with the first being the *CONTACT_TIED_SURFACE_TO_SURFACE_FAILURE (CTSSF). This contact allows modeling the failure of the contact element for a stress condition described by Eq. (2.4):

$$\left[\frac{\max(0.0, \sigma_{normal})}{FS}\right]^2 + \left[\frac{\sigma_{shear}}{FD}\right]^2 > 1 \qquad (2.4)$$

where σ_{normal} is the normal stress, σ_{shear} is the shear stress, FS is the static coefficient of friction and FD is the dynamic coefficient of friction. A good estimate for the value of the contact resistance is to initially use the tensile strength of the concrete. In this investigation, a sensitivity analysis was performed to obtain the optimum contact value between steel and concrete.

It is important to note that theoretically, the concrete subjected to traction resists between 5% and 10% of the compressive strength (f'_c). Based on this assumption, it could be argued that the tensile contact resistance between the concrete and the steel could not be higher than the concrete tensile strength. To verify the influence of this variable, different contact resistances were analyzed for the same model. Figure 2.31 shows the behavior of the Voth model for different contact resistances. At first glance (Figure 2.31.a) it can be seen that the bonded contact (CTSSF contact without failure) reaches the maximum strength of the concrete ($f_{'c}$ = 38.5 MPa), that is, there is no contact failure between the steel and the concrete. However, when we assign a CTSSF contact with a resistance of 10%f'c or less we notice the same behavior (path) of the curve; the same happens when we use resistance of 9MPa (Figure 2.31.b). To review the failure condition of the contact, and this is where we must make a quantitative evaluation, one must analyze the curve for a very small deformation (Figure 2.31.b). We can observe that for contact resistances of 2 MPa and 3.8 MPa the failure is less sudden than for 9 MPa and the Bonded type of contact. Although the numerical model can be assigned any value of contact resistance between steel and concrete, physically this value will not exceed 10%. Another important aspect observed in Figure 2.31.b is the correlation between the dynamic effects and the value of the contact resistance between the two materials. As we use a lower contact resistance, the curves tend to have fewer bumps (zigzags) which are extremely important for model stability. Therefore, Figure 2.31.a indicates that using a contact resistance equal to or less than 10% of the compressive strength of the concrete is an acceptable value since it produces more stability in the model and the curve trace is closer to the experimental plot.

The second type considered was *CONTACT_AUTOMATIC_SINGLE_SURFACE (CASS). This contact allows modeling the friction between the steel and the concrete, using a frictional type of body interaction and assigning a friction coefficient. In this investigation, a friction coefficient equal to 0.3 was used. The properties of the materials and the parameters of each model are presented in Table 2.3.

Table 2.3 Material properties.

Source	f'_c (MPa)	Steel (C = chord; D = diagonal)							Contact type	Contact resistance (MPa)
		E (GPa)	f_y (MPa)		f_u (MPa)		ε (%)			
			C	D	C	D	C	D		
Voth (Voth, 2010)	38.5	211.5	389	326	527	505	30	37.7	CTSSF	3.8
Sakai et al. (Sakai et al., 2004)	31	200	368	373	459	432	35	32	CASS	3
Chen et al. (Chen et al., 2015)	30	205	298	310	350	365	22.63	28.26	CTSSF	3.00
Huang et al. (Huang et al., 2015)	45	200	311	330	425	485	33	21	CTSSF	4

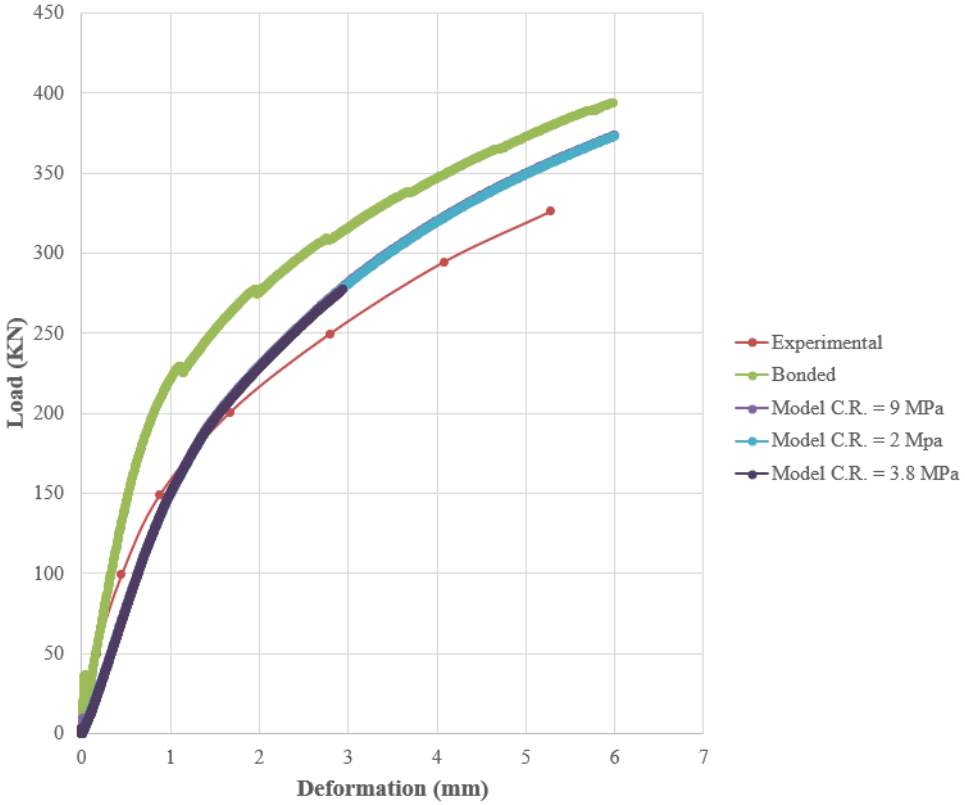

(a) Load vs Deformation curves for different contact resistances

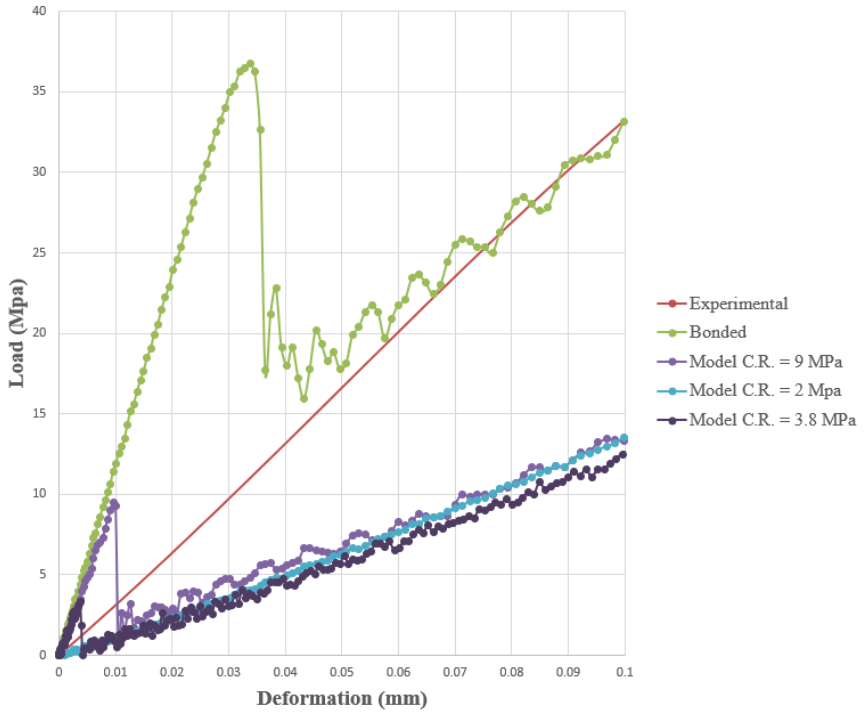

(b) Curves for a deformation of 0.1 mm

Figure 2.31 Model Voth (Voth, 2010)

2.2.6 Load Application

The load application regime followed those described in the experimental investigations studied, including careful modeling of boundary conditions. The loads were applied in the shortest possible time to optimize the computational cost, but at the same time avoid dynamic effects. Because the loading rate in the experiments was known to be quasi-static, a load application time was assumed, and a load application speed was back-calculated.

2.3. Results, discussion and future research

In general, the numerical models are able to trace well the reported behavior of the selected specimens, including the transition points in the load-deformation curves, ultimate strength and maximum deformation. Figure 2.32 shows the comparisons of the load-deformation curves for the unfilled and filled connections modeled, while Figure 2.33 shows the load-deformation curves for the filled connections with and without studs.

Figures 2.32 and 2.33 plots indicate very good agreement considering that the shape of the curves for the four specimens varied substantially. Reiterating, the analytical model is only calibrated to the Voth (Voth, 2010) specimen and the responses of the Sakai et al. (Sakai et al., 2004), Chen et al. (Chen et al., 2015) and Huang et al. (Huang et al., 2015) specimens are basically blind tests of the model's capabilities. The initial stiffness and the entire curve for the analytical models show larger stiffness and slightly larger strengths than the experiments. These differences can be attributed to the over-stiffness common in most FE models, but also to (a) the non-linear behavior of the concrete-structural steel interface, (b) the presence of residual stresses, and (c) initial imperfections in the specimen geometry, boundary conditions and loading configurations. As no data are available for these conditions in the tests, they are not considered in the numerical model.

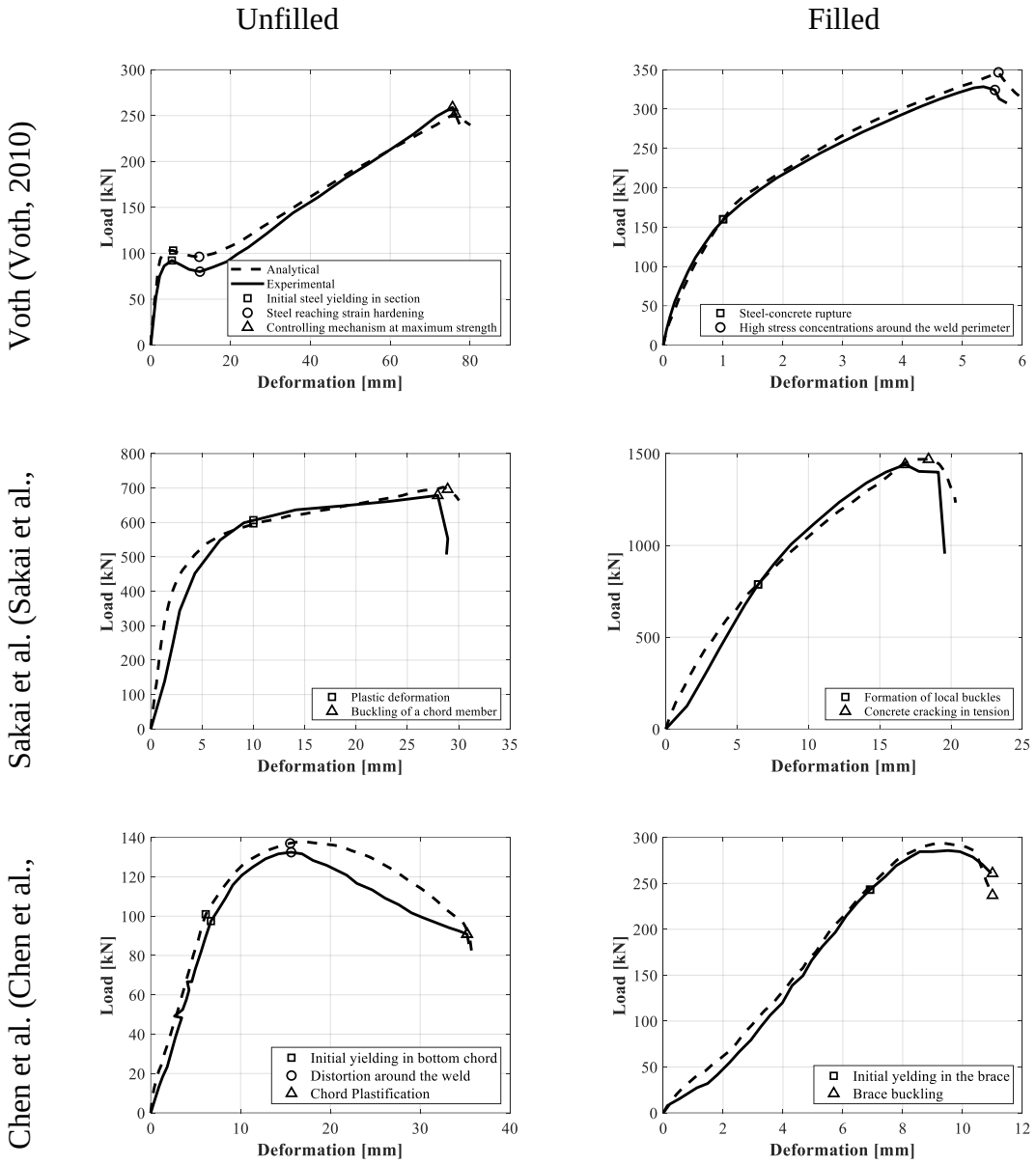

Figure 2.32 Comparison of load vs. strain curves.

Another relevant aspect observation from Figure 2.32, when comparing the unfilled versus the filled connections, is that the filled connections seem to show a better match. This can be attributed to the fact that the concrete, by preventing or delaying the buckling of the steel, reduces the uncertainty of the non-linear behavior of the steel. Figure 2.32 also shows that filling the connections with concrete is a good alternative to significantly improve the strength of the connections; however, in some cases (Sakai et al., 2004), this comes with a tradeoff between strength and ductility.

Figure 2.33 shows the effect of shear studs on the structural behavior of the tests carried out by Huang et al. (Huang et al., 2015). The addition of the shear studs increased the resistance and final deformation of the connections. Moreover, the stiffness of the connection increases significantly. The model is capable of tracking these changes well.

Figures 2.32 and 2.33 also illustrate important behavioral milestones for each specimen. These include initial steel yielding in section, high stress concentrations around the weld perimeter, strain in strain concentration areas reaching 10 and 20 times yield strain, steel-concrete rupture, concrete cracking in tension, steel reaching strain hardening, formation of local buckles, steel crack formation and controlling mechanism at maximum strength. Again, there is a very good match, both in terms of strength and deformation, as seen when these milestones are reached.

A very detailed discussion of the behavior of all specimens is not possible given space limitations. However, two examples will be discussed to demonstrate the model's capabilities. The first example is shown in Figure 2.34, which illustrates the variation of the stresses and strains for the unfilled and filled Voth specimens (note the large difference in the horizontal scale for the two tests). For the unfilled specimen, the plot at 1mm (Figure 2.34.a, Point 1) shows that most of the specimen was in the elastic range, but substantial stress concentrations are already present. The filled specimen at the same deformation (Fig. 2.34.b, Point 3) shows that rupture has begun at the steel-concrete interface in the weld between the plate and round section. For the unfilled specimen, yielding starts close to 100 kN (Point 2, Figure 2.34.a), while for the filled specimen it is in the elastic range (Point 2, Figure 2.34.b). An increase due to strain hardening occurs in the unfilled specimen (Point 3, Figure 2.34.a), while for the filled specimen a contact failure between the concrete and the steel is observed, which leads to a loss in the stiffness of the system (Point 3, Figure 2.34.b). At points 4 and 5 of the unfilled specimen, significant stresses begin to be seen in the perimeter part of the weld, as well as large deformations of the specimen (Points 4 and 5, Figure 2.34.a). Finally, the unfilled specimen fails under a load of 250 kN and at a deformation close to 68 mm (Point 6, Figure 2.34.a). On the other hand, for the filled specimen, an increasingly evident failure between the steel-concrete contact is noted, especially below the surface where the tensile load is being applied (Points 4, 5 and 6 Figure 2.34.b). The filled specimen reaches its maximum strength of 340 kN (Point 5, Figure 2.34.b) and subsequently fails at a strain close to 6 mm (Point 6, Figure 2.34.b).

The second example is shown in Figure 2.35, which illustrates the sequence of the variation of the stresses and strains for the unfilled Sakai specimen at 1, 2, 8, 18, 27 and 30 mm of deflection (Figure 2.35.a). Like the Voth specimen at 1 mm, most of the specimen is shown to be in the elastic range; however, at 8 mm, buckling at the diagonal joint of the chord begins. On the other hand, in the filled specimen (Fig. 2.35.b), it is observed that throughout the deformation sequence the concrete does not suffer any damage, and this agrees with what was observed in the experimental tests (Sakai et al., 2004). Only after point 1 does the concrete begin to crack in the diagonal-chord interface; at this point the steel has already undergone large deformations to the point that it has already detached from the concrete. At point 2, the detachment of the steel and the concrete can be clearly seen.

It is important to note that the design philosophy of composite connections is that they reach the ultimate strength specified in the codes, regardless of the type of failure or the behavior that occurs

in the concrete-steel interface while reaching the ultimate strength. This means that both the steel and concrete reach very large strains such that slip does not prevent the achievement of almost the full plastic capacity of the sections. Taking the above into account, Tables 2.4 and 2.5 show the comparisons of the ultimate strengths for the specimens examined. The finite element models were able to adequately predict the ultimate strengths of the connections unfilled and filled with concrete.

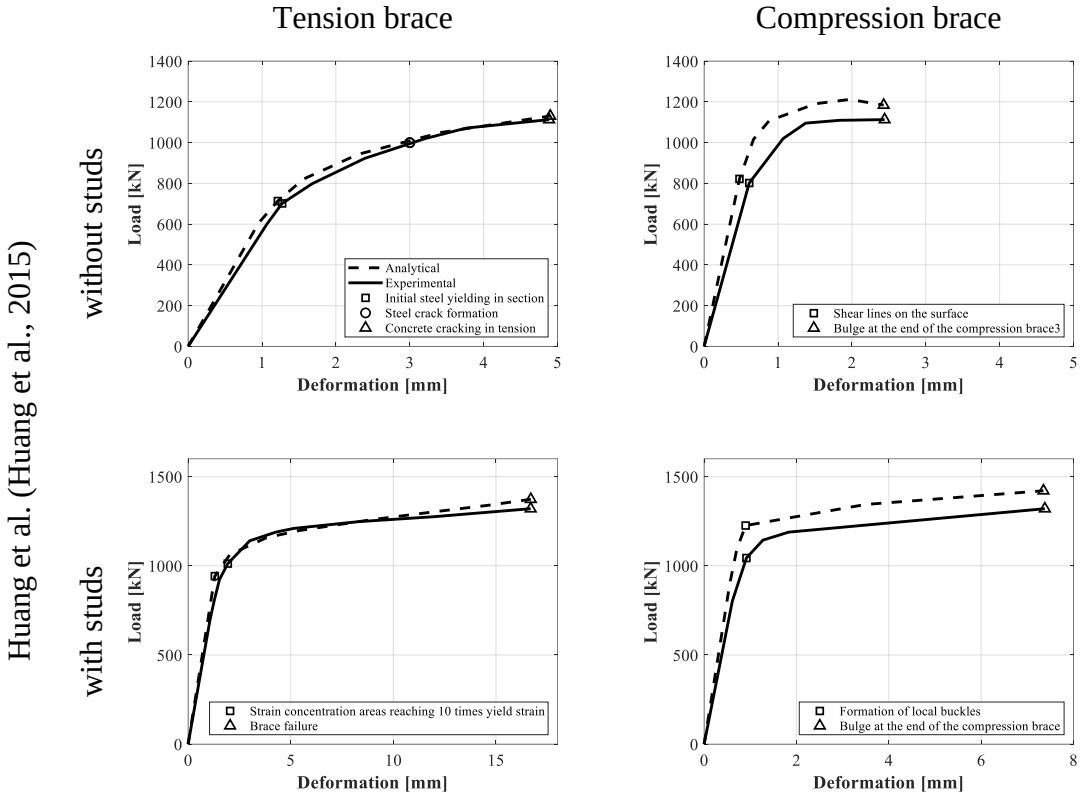

Figure 2.33 Comparison of load vs. strain curves.

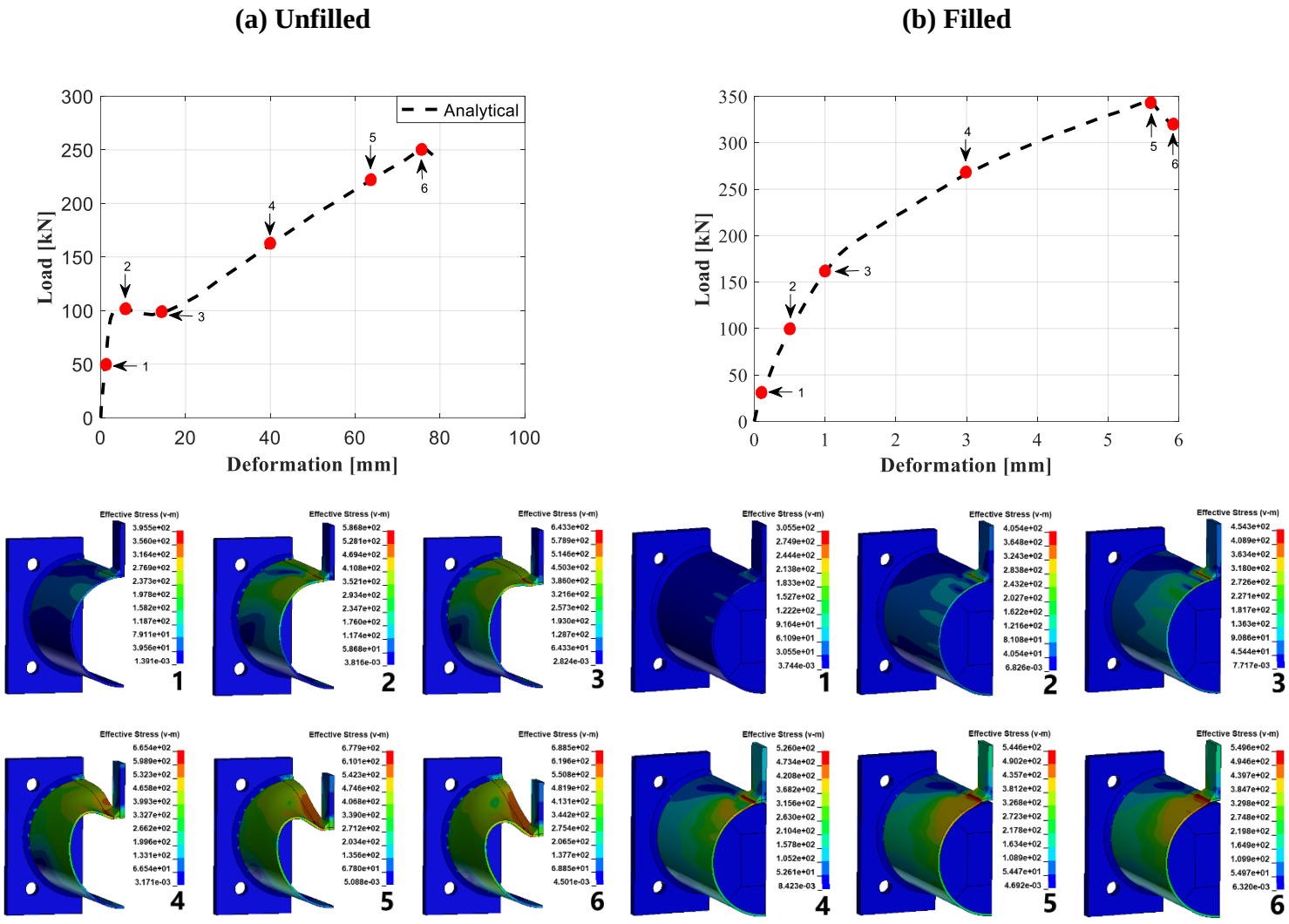

Figure 2.34 Sequence of stresses and strains of the Voth specimen.

(a) Unfilled

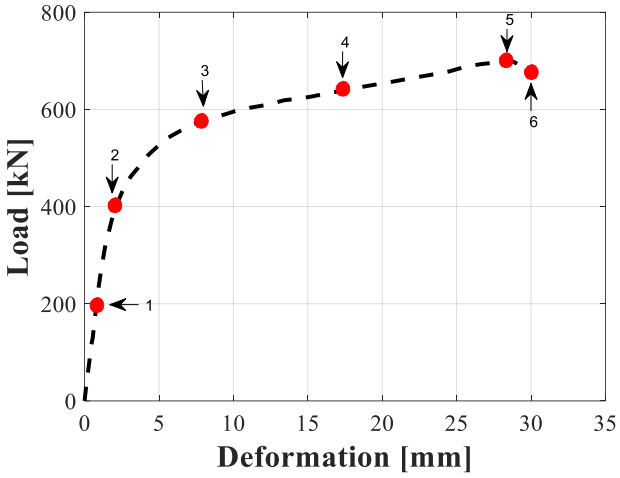

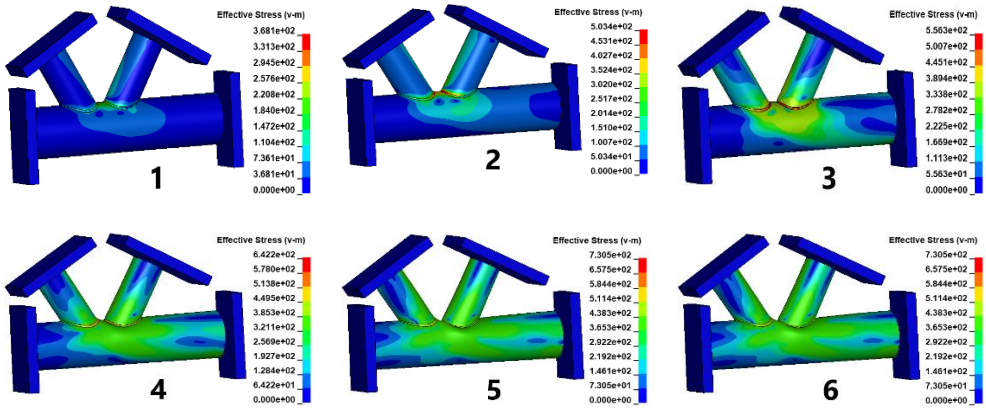

2.35 Continued

(b) Filled

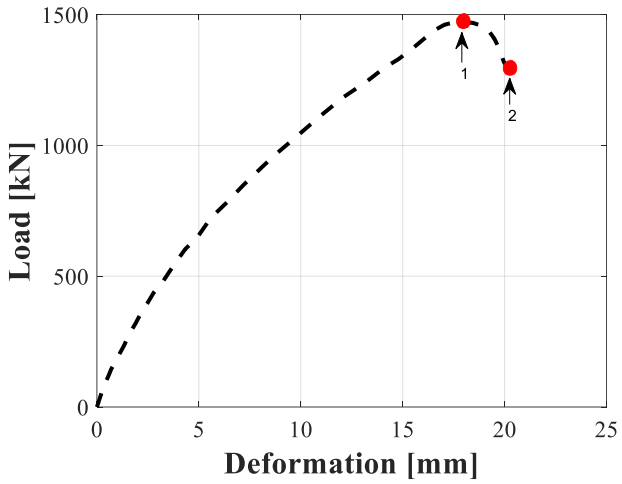

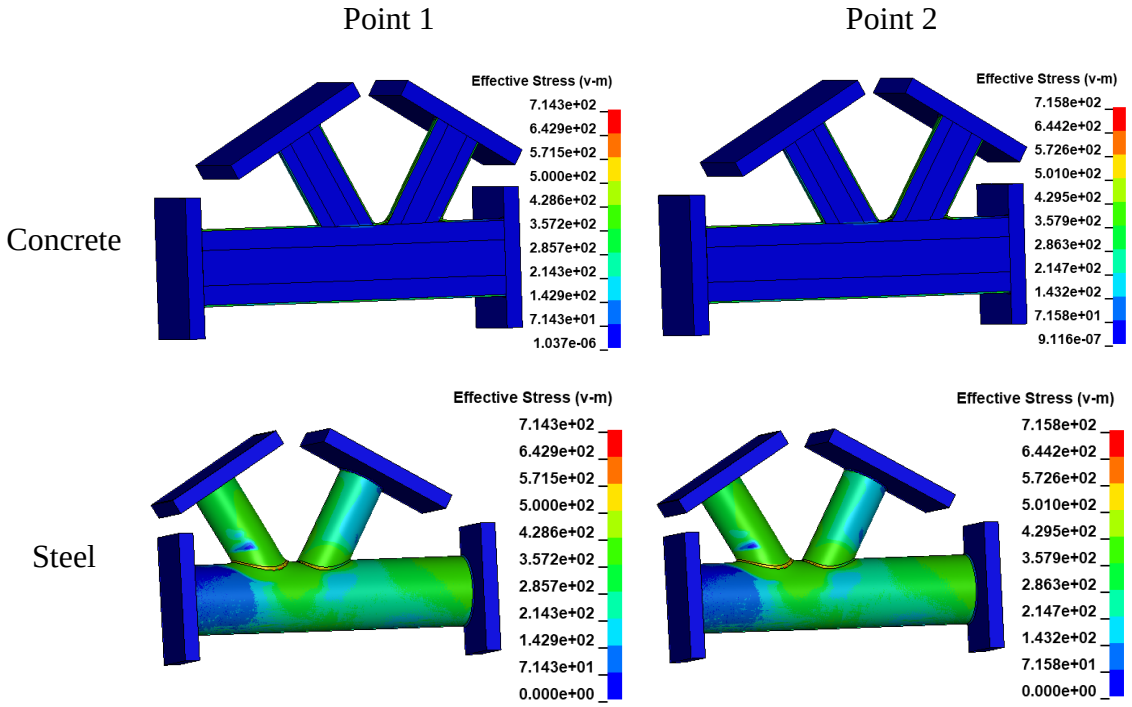

Figure 2.35 Sequence of stresses and strains of the Sakai specimen.

Table 2.4 Comparison of ultimate strength obtained from test results with FEA results.

Researcher	Ultimate strength CTFs-Connections (kN)					
	Unfilled			Filled		
	Exp.	Num.	Num./Exp.	Exp.	Num.	Num./Exp.
Voth (Voth, 2010)	258.9	252.1	0.97	328.4	348.2	1.06
Sakai et al. (Sakai et al., 2004)	678.5	714.4	1.05	1440.8	1442.8	1.001
Chen et al. (Chen et al., 2015)	132.5	140.3	1.06	285.8	294.0	1.03

Table 2.5 Comparison of ultimate strength obtained from test results with FEA results (studs).

Researcher	Ultimate strength CTFs-Connections (kN)						
	Connection	Tension brace			Compression brace		
		Exp.	Num.	Num. /Exp.	Exp.	Num.	Num./ Exp.
Huang et al. (2015)	Without studs	1112.9	1130.8	1.02	1112.9	1184.1	1.06
	With studs	1320.3	1373.1	1.04	1320.3	1420.9	1.08

Figures 2.36 through 2.39 show excellent visual correlation when comparing the deformation responses. The Voth model with the connection without concrete (Figures 2.36.a,b) shows that the deformation of the specimen could be reproduced analytically to very large deformations and agrees with the results of Voth and Parker (Voth and Packer, 2012). The contours of the von Mises stress plots (Figures 2.36.c-d) indicate that the greatest stresses occur in the upper part of the specimen. Figure 2.36.e shows that the cross-section is deformed into a heart shape by the way the load is applied and the boundary conditions imposed. In the Voth model with the concrete-filled chord (Figures 2.36.f-g), the experimental tests do not explicitly show the detachment of the steel tube from the concrete; however, this can be inferred by the way the specimen is deformed (Figures 2.36.f,h). In this model, the stresses are concentrated in the perimeter part of the weld (Figures 2.36.h-i), while the concrete does not suffer damage. Figure 2.36.j shows that the concrete does not undergo any kind of large deformation, while the steel tube is detached from the concrete just below the load plate and the weld.

In the model of Sakai et al., for the connection without concrete fill, one diagonal member is in compression and the other diagonal member is in tension, resulting in plastic deformation near the weld joint in the diagonal member being compressed (Figs. 2.37.a-b). Figures 2.37.c-d show the von Mises stresses, with maximum values at the vertex of the diagonals and the weld as expected. Figure 2.37.e shows that the cross-section is only moderately damaged. In the model of Sakai et al., the concrete is not damaged in the concrete-filled chord and diagonals (Figures 2.37.f-g). However, it is observed that the steel detaches from the concrete at the vertex of the compression

member (Figures 2.37.h-i). The cross-section of the concrete at the ends of the chord does not suffer deformations (Figure 2.37.j). In this type of connection, the compression member is the most vulnerable element.

In the model of Chen et al. for the connection without concrete fill, a plasticization of the chord occurs around the vertical member (Figures 2.38.a-b). The von Mises stresses are about equal along the chord and the vertical member, and they are almost zero at the ends (Figures 2.38.c-d). The cross-section does not suffer any significant distortion (Figure 2.38.e). For the specimen with the concrete-filled chord, the analytical model does not accurately show the yielding failure that occurs in the vertical member. This is probably due to the lack of modeling of residual stresses and initial imperfections in the test (Figures 2.38.f-g). Figures 2.38.h-i show that the concrete does not suffer damage, as well as deformations of the cross-section of the chord (Figure 2.38.j).

Finally, in the model of Huang et al. for the connection without studs, bulges were observed at the end of the compression brace (Figs. 2.39.a-b). Figures 2.39.c-d show the von Mises stresses, with maximum values at the end on the compression brace and the weld as expected. Figure 2.39.e shows that the chord cross-section that did not suffer any distortion. For the connection with studs on the interior surface, the model shows a similar failure mode as that without concrete (Figures 2.39.f-g). However, it is observed that the steel detaches from the concrete at the vertex of the tension brace member (Figures 2.39.h-i). The cross-section of the concrete at the ends of the chord does not suffer deformations (Figure 2.39.j).

Unfilled

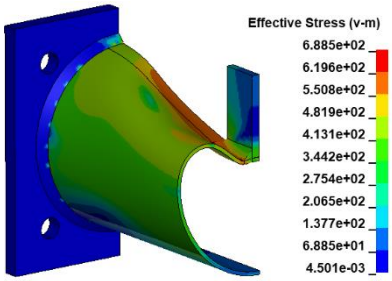

(a) Experimental test

(b) Numerical model general view.

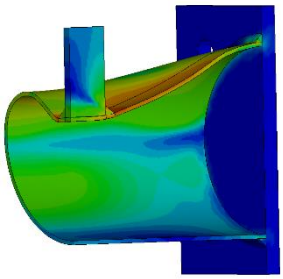

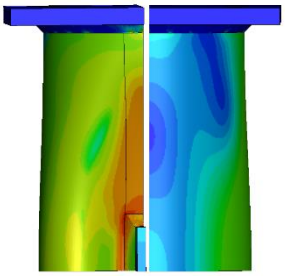

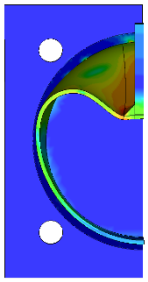

(c) Numerical model internal view

(d) Numerical model plan view

(e) Numerical model front view

Filled

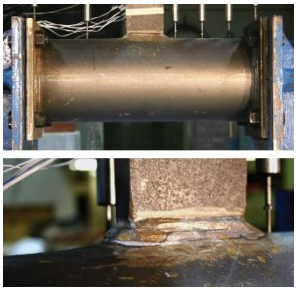

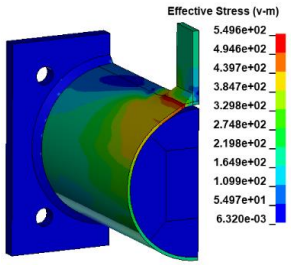

(f) Experimental test

(g) Numerical model general view

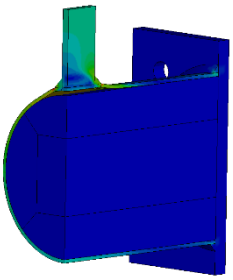

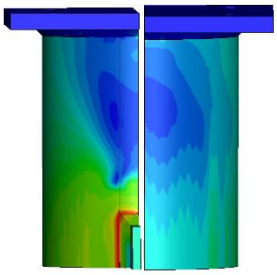

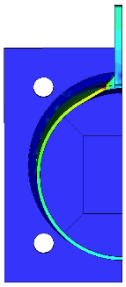

(h) Numerical model internal view

(i) Numerical model plan view

(j) Numerical model front view

Figure 2.36 Model Voth. (Vot, 2010)

Unfilled

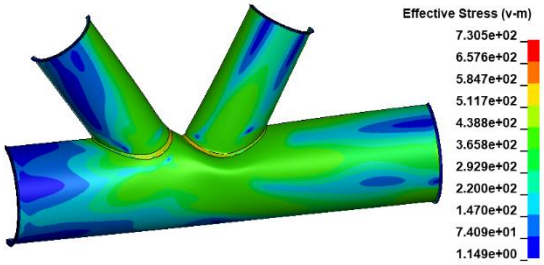

(a) Experimental test

(b) Numerical model general view

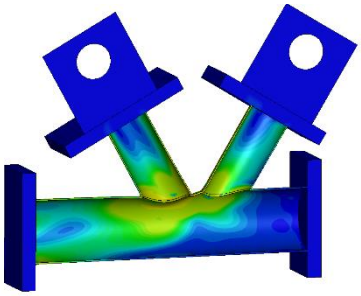

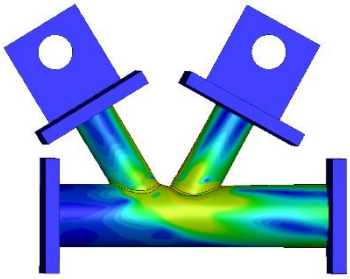

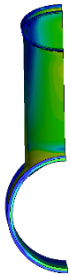

(c) Numerical model internal view

(d) Numerical model plan view

(e) Numerical model front view

Filled

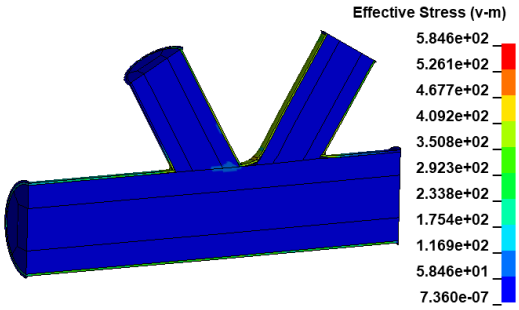

(f) Experimental test

(g) Numerical model general view

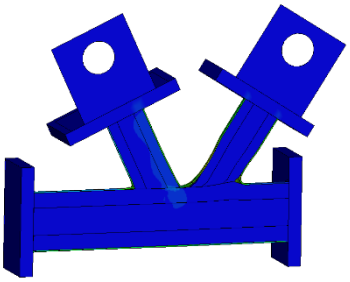

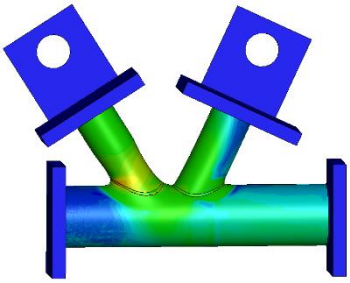

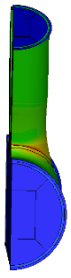

(h) Numerical model internal view

(i) Numerical model plan view

(j) Numerical model front view

Figure 2.37 Model Sakai et al. (Sakai et al., 2004)

Unfilled

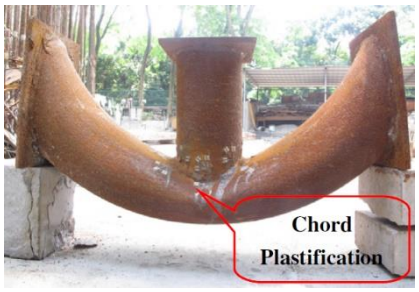

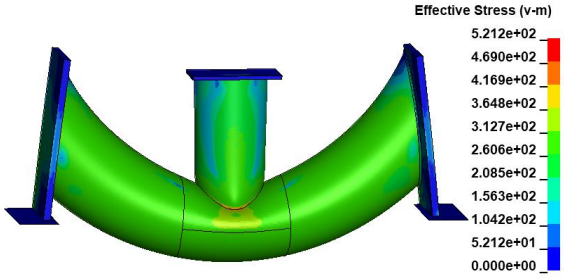

(a) Experimental test

(b) Numerical model general view

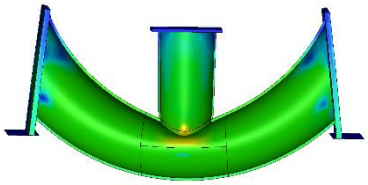

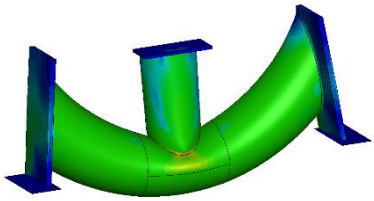

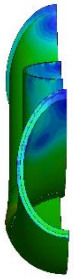

(c) Numerical model internal view

(d) Numerical model plan view

(e) Numerical model front view

Filled

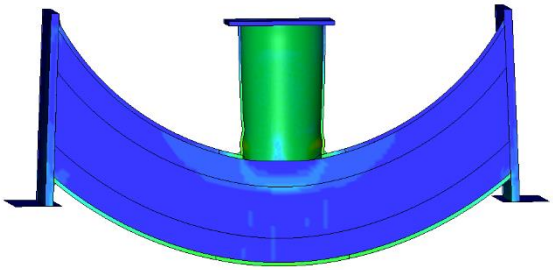

(f) Experimental test

(g) Numerical model general view

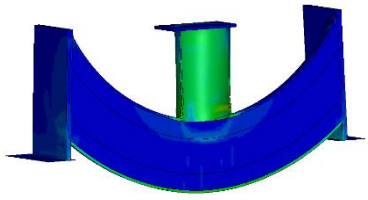

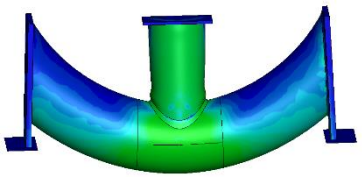

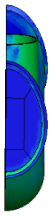

(h) Numerical model internal view

(i) Numerical model plan view

(j) Numerical model front view

Figure 2.38 Model Chen et al. (Chen et al., 2015)

Without studs

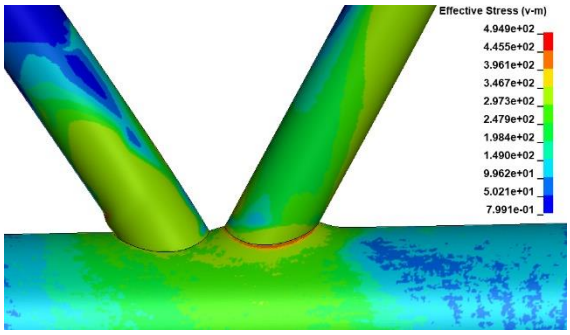

(a) Experimental test

(b) Numerical model general view

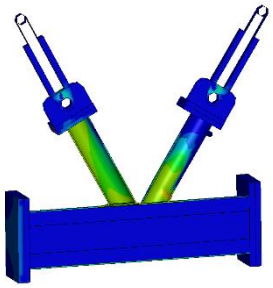

(c) Numerical model internal view

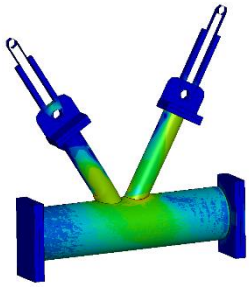

(d) Numerical model plan view

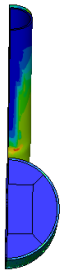

(e) Numerical model front view

With studs

(f) Experimental test

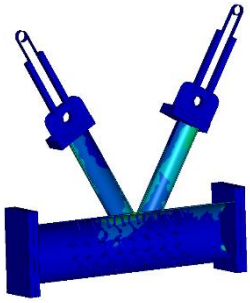

(g) Numerical model general view

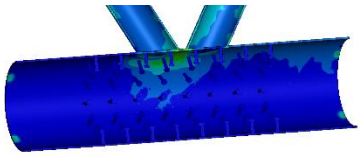

(h) Numerical model internal view

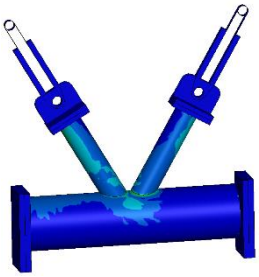

(i) Numerical model plan view

(j) Numerical model front view

Figure 2.39 Model Huang et al. (Huang et al., 2015)

Since the concrete was not seriously damaged in the specimens tested, the authors considered it convenient to demonstrate that the models were able to capture the failure in the concrete. Therefore, the model of Sakai et al. (Sakai et al., 2004) was subjected to twice the original displacement of the experimental test, that is, 60 mm. Figure 2.40 shows the damage suffered by the model through the plot of the plastic volumetric strain, which is contained within the output data of the concrete material MAT_072REL3 (historical variable 5). Figure 2.40 indicates that the concrete in both diagonals (tension and compression) as well as that in the central part of the chord suffered extensive damage.

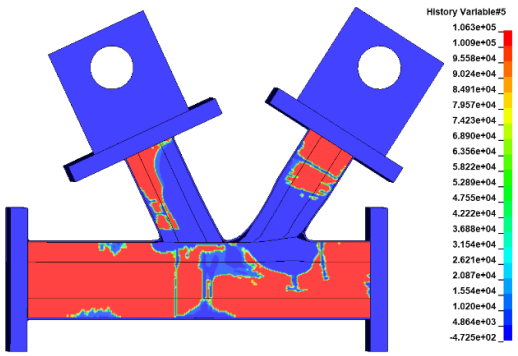

Figure 2.40 Damage in concrete for the Sakai et al. (Sakai et al., 2004) model subjected to twice the test deformation.

2.4. Conclusions

A state-of-the-art report on experimental and analytical models for composite connections is presented in the chapter. The initial overview reveals that the previous studies mainly focused on the influence of concrete filling on the structural behavior of composite connections, as well as the numerical simulation of composite connections. An important contribution from the data appendix is what the authors believe is the first comprehensive database on experimental tests for this kind of connection. The authors intend to keep developing this database by adding more tests as they become available as well as contacting the researchers who have conducted the tests described therein in order to obtain more information relevant to numerical modeling (primarily more detailed material stress-strain information).

The initial results from the proposed numerical model indicate that it can reproduce the most important behavioral aspects observed in the tests, such as the buckling of the thin unfilled specimens, the effect of partial infilling, and the evolution of deformation and strength. The ability of the models to trace the transition points in load-deformation curves will also lead to the inference that the model can track well the steel-concrete interaction. The results also highlight the great advantages that infilling the connection provides in terms of both delaying buckling and more fully utilizing the strength and stiffness of the steel.

It should be noted that the nature and extent of the damage suffered may vary due to the geometric characteristics and load application in each particular connection. Thus, it is difficult to generalize

the response and the damage evolution from a particular connection to those of all the specimens shown in the database. Detailed numerical or experimental studies are needed to realistically simulate the response and damage of any given connection.

Currently, the authors are using the model in numerical simulations using optimization processes to determine the most important parameters that influence structural behavior of the CFTs-connections. The intent is to identify the governing structural parameters and find experimental data that will highlight their importance. In particular, current efforts are focused on determining the best numerical ranges for the parameters that affect significantly the contact between the steel and the concrete; those values appear to be in a range of 5-10% of the value of the resistance to compression of the concrete.

In the future, the models can be used:

- to realistically model the performance of composite connections under static and cyclic loads,
- to evaluate parametrically variables that are difficult or costly to determine experimentally,
- to assess behavior under multi-states of stress,
- to assess damage evolution between the contact surface between the steel and concrete,
- to determine the effect of embedded steel sections and mechanical shear connector, and,
- to understand the role of stress concentration factors and residual stresses from welding.

References

AISC, 2010. *Specification for structural steel buildings. American Institution of Steel Construction (AISC) ANSI/AISC 360-10*. Chicago, Illinois.

American Petroleum Institute, 1976. *Recommended practice for planning, designing and constructing fixed offshore platforms.* (7th Editio.). Texas.

American Petroleum Institute, 2010. Recommended Practice for Planning, Designing and Constructing Fixed Offshore Platforms—Working Stress Design. *Proceedings of the Annual Offshore Technology Conference*. N.W., Washington, D.C.: Institute American Petroleum. DOI: 10.2523/20837-ms

ANSYS, 2020. ANSYS Explicit Dynamics Analysis Guide. Canonsburg, PA 15317. Retrieved from http://www.ansys.com

Batho, C., Lash, S. D., and Kirkham, R. H. H., 1939. The Properties of Composite Beams, Consisting of Steel Joists Encased in Concrete, Under Direct and Sustained Loading. *Journal of the Institution of Civil Engineers*, **12**(8), 382–386. DOI: 10.1680/ijoti.1939.14492

Belytschko, T., and Bindeman, L. P., 1993. Assumed strain stabilization of the eight node hexahedral element. *Computer Methods in Applied Mechanics and Engineering*, **105**(2), 225–260. DOI: 10.1016/0045-7825(93)90124-G

Bowness, D., and Lee, M. M. K., 1995. The development of an accurate model for the fatigue assessment of doubly curved cracks in tubular joints. *International Journal of Fracture*, **73**(2), 129–147. DOI: 10.1007/BF00055725

Bowness, D., and Lee, M. M. K., 1998. Fatigue crack curvature under the weld toe in an offshore tubular joint. *International Journal of Fatigue*, **20**(6), 481–490. DOI: 10.1016/S0142-1123(98)00017-6

British Standards., 1993. *BS 7608:1993 Code of practice for fatigue design and assessment of steel structures*. *British Standards Institution*.

Brown, G. M., Holmes, R., and McCann, D. L., 1989. Improving structural integrity by injection of grout into fatigue-critical nodes in offshore structures. *Proceedings of the Annual Offshore Technology Conference*, **1989-May**, 253–258. DOI: 10.4043/5984-ms

Bruhl, J. C., 2015. *Behavior and Design of Steel-Plate Composite (SC) Walls for Blast Loads*.

Chan, J., Chen, J., and Jin, W. L., 2010. Experiment investigation of stress concentration factor of concrete-filled tubular T joints. *Journal of Constructional Steel Research*, **66**(12), 1510–1515. Elsevier Ltd. DOI: 10.1016/j.jcsr.2010.06.004

Chen, B., and Radic, J., 2009. Construction of arch bridges. *Proc. of the 2nd Chinese–Croatian Joint Colloquium. Fuzhou; October 5-9, 2009.*

Chen, J., Jin, W. L., Ye, Y., and Sheng, X. H., 2012. Design of concrete filled tubular CHS T-joints under in-plane bending. *Tubular Structures XIV - Proceedings of the 14th International Symposium on Tubular Structures, ISTS 2012*, (mm), 89–94. DOI: 10.1201/b13139-15

Chen, W. F., 1969. *General solution of an inelastic beam-column problem* (Vol. 1969). Bethlehem, Pennsylvania, USA.

Chen, W. F., and H., C. C., 1973. Analysis of Concrete-Filled Steel Tubular Beam- Columns. *Memoires, IABSE*, **33**(2), 37–52.

Chen, W. F., and Santathadaporn, S., 1969. Curvature and the solution of eccentrically loaded columns. *Journal of the Engineering Mechanics Division, ASCE*, **95**(February), 21–39.

Chen, Y., Feng, R., and Wang, C., 2015. Tests of bare and concrete-filled CHS T-joints with concave chord under axial compression. *Construction and Building Materials*, **93**, 144–156.

Elsevier Ltd. DOI: 10.1016/j.conbuildmat.2015.04.056
Cheng, B., Xiang, S., Zuo, W., and Teng, N., 2018. Behaviors of partially concrete-filled welded integral T-joints in steel truss bridges. *Engineering Structures*, **166**(July 2017), 16–30. Elsevier. DOI: 10.1016/j.engstruct.2018.03.061
Choi, K. K., and Xiao, Y., 2010. Analytical studies of concrete-filled circular steel tubes under axial compression. *Journal of Structural Engineering*, **136**(5), 565–573. DOI: 10.1061/(ASCE)ST.1943-541X.0000156
Courant, R., Friedrichs, K., and Lewy, H., 1967. On the Partial Difference Equations of Mathematical Physics. *IBM Journal*, **11**, 215–234.
Faschan, W., 1992. 1992 Faschan. *Composite Construction of Steel and Concrete. ASCE* (Vol. II, p. 576).
Gourley, B. C., Cenk, T., Denavit, M. D., Schiller, P. H., and Hajjar, J. F., 2008. A Synopsis of Studies of the Monotonic and Cyclic Behavior of Concrete-Filled Steel Tube Members, Connections, and Frames. *Report No. NSEL-008*, (April).
Griffis, L. G., 1994. Higgins Lecture : Composite Frame Construction. *American Institute of Steel Construction*, 1–72.
Hajjar, J. F., and Gourley, B. C., 1996. Representation of concrete-filled steel tube cross-section strength. *Journal of Structural Engineering*, **122**(11), 1327–1335. DOI: 10.1061/(ASCE)0733-9445(1996)122:11(1327)
Hajjar, J. F., Schiller, P. H., and Molodan, A., 1998. A distributed plasticity model for concrete-filled steel tube beam-columns with interlayer slip. *Engineering Structures*, **20**(8), 663–676. DOI: 10.1016/S0141-0296(97)00107-7
Hallquist, J., 2006. LS-DYNA. California. DOI: 10.1002/ima.22028
Han, L. H., Li, W., and Bjorhovde, R., 2014. Developments and advanced applications of concrete-filled steel tubular (CFST) structures: Members. *Journal of Constructional Steel Research*, **100**, 211–228. Elsevier Ltd. DOI: 10.1016/j.jcsr.2014.04.016
Hibbitt, H., Karlsson, B., and Sorensen, P., 2011. ABAQUS, Standard User's manual, Version 6.11. USA.
Hou, C., and Han, L. H., 2017. Analytical behaviour of CFDST chord to CHS brace composite K-joints. *Journal of Constructional Steel Research*, **128**, 618–632. Elsevier Ltd. DOI: 10.1016/j.jcsr.2016.09.027
Hou, C., Han, L. H., and Zhao, X. L., 2015. Behaviour of circular concrete filled double skin tubes subjected to local bearing force. *Thin-Walled Structures*, **93**, 36–53. Elsevier. DOI: 10.1016/j.tws.2015.03.004
Hu, H. T., Huang, C. S., Wu, M. H., and Wu, Y. M., 2003. Nonlinear analysis of axially loaded concrete-filled tube columns with confinement effect. *Journal of Structural Engineering*, **129**(10), 1322–1329. DOI: 10.1061/(ASCE)0733-9445(2003)129:10(1322)
Huang, C. S., Yeh, Y. K., Liu, G. Y., Hu, H. T., Tsai, K. C., Weng, Y. T., Wang, S. H., et al., 2002. Axial load behavior of stiffened concrete-filled steel columns. *Journal of Structural Engineering*, **128**(9), 1222–1230. DOI: 10.1061/(ASCE)0733-9445(2002)128:9(1222)
Huang, W., Fenu, L., Chen, B., and Briseghella, B., 2015. Experimental study on K-joints of concrete-filled steel tubular truss structures. *Journal of Constructional Steel Research*, **107**, 182–193. Elsevier Ltd. DOI: 10.1016/j.jcsr.2015.01.023
Javadi, F. H. S., 1979. *Joints of composite construction in marine structures*. Imperial College of Science and Technology.
Kim, S. H., and Shinozuka, M., 2004. Development of fragility curves of bridges retrofitted by

column jacketing. *Probabilistic Engineering Mechanics*, **19**(1), 105–112. DOI: 10.1016/j.probengmech.2003.11.009

Liang, Q. Q., Uy, B., and Richard Liew, J. Y., 2007. Local buckling of steel plates in concrete-filled thin-walled steel tubular beam-columns. *Journal of Constructional Steel Research*, **63**(3), 396–405. DOI: 10.1016/j.jcsr.2006.05.004

Liu, Y., Xiong, Z., Luo, Y., Cheng, G., Liu, G., and Yang, J., 2015. Double-composite rectangular truss bridge and its joint analysis. *Journal of Traffic and Transportation Engineering (English Edition)*, **2**(4), 249–257. Elsevier Ltd. DOI: 10.1016/j.jtte.2015.05.005

Liu, Z., and Goel, S. C., 1988. Abstract: introduction. *Journal Structural Engineering*, **114**(7), 1488–1506.

M. Denavit, 2012. *Characterization of behavior of steel-concrete composite members and frames with applications for design*. University of Illinois at Urbana-Champaign.

M. Tomii and K. Sakino, 1979a. Experimental studies on the ultimate moment of concrete filled square steel tubular Beam-Columns. *Architectural Institute of Japan*, (275), 55–63.

M. Tomii and K. Sakino, 1979b. Elasto-plastic behavior of concrete filled square steel tubular Beam-Columns. *Architectural Institute of Japan*, (280), 11–1120.

Malvar, L. J., Crawford, J. E., Wesevich, J. W., and Simons, D., 1997. A plasticity concrete material model for DYNA3D. *International Journal of Impact Engineering*, **19**(9–10), 847–873. DOI: 10.1016/s0734-743x(97)00023-7

Mamaghani, I. H. P., and Packer, U. A., 2002. Inelastic behaviour of partially concrete-filled steel hollow sections. *Proceedings, Annual Conference - Canadian Society for Civil Engineering*, **2002**(July), 1781–1790.

Mashiri, F. R., Zhao, X. L., and Grundy, P., 2002. Fatigue tests and design of welded T connections in thin cold-formed square hollow sections under in-plane bending. *Journal of Structural Engineering*, **128**(11), 1413–1422. DOI: 10.1061/(ASCE)0733-9445(2002)128:11(1413)

Molodan, A., and Hajjar, J. F., 1997. *A cyclic distributed plasticity model for three-dimensional concrete- filled steel tube beam-columns and composite frames, Rep. No. ST-96-6*. Minneapolis, USA.

Morahan, D. J., and Lalani, M., 2002. Fatigue and ultimate limit state of grouted tubular joints. *Proceedings of the International Conference on Offshore Mechanics and Arctic Engineering - OMAE*, **3**, 621–626. DOI: 10.1115/OMAE2002-28633

MSL, E. L., 1994. *JOINT INDUSTRY PRQTECT MSL Engineering Limited*.

Musa, I. A., and Mashiri, F. R., 2019. Stress concentration factor in concrete-filled steel tubular K-joints under balanced axial load. *Thin-Walled Structures*, **139**(February), 186–195. Elsevier Ltd. DOI: 10.1016/j.tws.2019.03.003

Packer, B. J. A., 1995. Concrete-filled HSS connections. *Journal of Structural Engineering*, **121**(3), 458–467.

Perea, T., 2010. *Analytical and experimental study on slender concrete-filled steel tube columns and beam-columns*. Georgia Institute of Technology.

Raj, A. V, and Joy, A., 2016. Comparative Study on Fatigue Behavior of K and K-T Steel Truss Joints. *International Journal of Science and Research (IJSR)*, **5**(6), 1842–1846. DOI: 10.21275/v5i6.18061603

Ramberg, W., and Osgood, W., 1943. *Description of stress–strain curves by three parameter*. *NACA technical note*. Washington DC, USA.

Roeder, Charles; Lehman, D., 2012. *Initial investigation of reinforced concrete filled tubes for use in bridge foundations*.

Sakai, Y., Hosaka, T., Isoe, A., Ichikawa, A., and Mitsuki, K., 2004. Experiments on concrete filled and reinforced tubular K-joints of truss girder. *Journal of Constructional Steel Research*, **60**(3–5), 683–699. DOI: 10.1016/S0143-974X(03)00136-6

Sato, T., 1995. *Study on interaction between steel tube and co ncrete of circular concrete- filled steel tubular structure system. Thesis*. Osaka Univ., Osaka, Japan.

Schneider, S. P., 1998. Axially loaded concrete-filled steel tubes. *Journal Structural Engineering*, **124(10)**, 1125–1138.

Shen, W., and Choo, Y. S., 2012. Stress intensity factor for a tubular T-joint with grouted chord. *Engineering Structures*, **35**, 37–47. Elsevier Ltd. DOI: 10.1016/j.engstruct.2011.10.014

Silva, L., Carroll, B., Olsen, T., and Caldwell, D., 1998. Testing of a new grouted joint for offshore platforms. *Proceedings of the Annual Offshore Technology Conference*, **2**, 389–400. DOI: 10.4043/8829-ms

Standards, B., 2013. *BS 7910: Guide to methods for assessing the acceptability of flaws in metallic structures*. *BSI Standards Publication* (Vol. 3). DOI: 10.1007/s13398-014-0173-7.2

Tebbett, I. E., Beckett, C. D., and Billington, C. J., 1979. The punching shear strength of tubular joints reinforced with a grouted pile. *Proceedings of the Annual Offshore Technology Conference*, **1979-May**, 915–926.

Tomii, M., Yoshimura, K., and Morishita, Y., 1977. Experimental studies on concrete filled steel tubular stud columns under concentric loading. *Proc., Int. Colloquium on Stability of Structures under Static and Dynamic Loads, SSRC/ASCE, Washington, D.C*, 718–741.

Udomworarat, Pison; Miki, Chitoshi; Ichikawa, Atsushi; Komechi, Masanori; Mitsuki, Kaoru; Hosaka, T., 2002. Fatigue performance of composite tubular K-joints for truss type bridge. *Structural Eng./Earthquake Eng.*, **19**(2), 65s-79s.

Viest, I. M., Colaco, J. P., Furlong, R. W., Griffs, L. G., Leon, R. T., and Wyllie, L. A., 1997. *Composite Construction Design for Buildings* (McGraw-Hil.). New York.

Voth, A. P., 2010. *Branch Plate-to-Circular Hollow Structural Section Connections, Doctoral Thesis*. University of Toronto.

Voth, A. P., and Packer, J. A., 2012. Branch Plate-to-Circular Hollow Structural SectionConnections. I: Experimental Investigation and Finite-Element Modeling. *Journal of Structural Engineering*, **138**(8), 995–1006. DOI: 10.1061/(asce)st.1943-541x.0000505

Wardenier, J., Kurobane, Y., Packer, J. A., van der Vegte, A., and Zhao, X.-L., 2010. *Design guide for circular hollow section (CHS) joints under predominantly static loading*. (CIDECT, Ed.) (2nd Ed.). Geneva, Switzerland. Retrieved from https://www.scopus.com/inward/record.uri?eid=2-s2.0-34247616873&partnerID=40&md5=177a766f0dd6e9d9ba52c0fdc2472d4b

Xiao, Y., 1989. *Experimental study and analytical modeling of triaxial compressive behavior of confined concrete. Ph.D. thesis*. Kyushu Univ., Fukuoka, Japan.

Xiao, Y., Tomii, M., and Sakino, K., 1991. Triaxial compressive behavior of confined concrete. *Journal of Concrete Research and Technology, Japan Concrete Institute*, **2(1)**, 1–14.

Xu, F., Chen, J., and Chan, T. M., 2017. Mechanical behaviour of concrete-filled CHS connections subjected to in-plane bending. *Engineering Structures*, **148**, 101–112. Elsevier Ltd. DOI: 10.1016/j.engstruct.2017.06.033

Xu, F., Chen, J., and Jin, W. L., 2015a. Experimental investigation and design of concrete-filled steel tubular CHS connections. *Journal of Structural Engineering (United States)*, **141**(2), 1–7. DOI: 10.1061/(ASCE)ST.1943-541X.0001050

Xu, F., Chen, J., and Jin, W. L., 2015b. Experimental investigation of SCF distribution for thin-

walled concrete-filled CHS joints under axial tension loading. *Thin-Walled Structures*, **93**, 149–157. Elsevier. DOI: 10.1016/j.tws.2015.03.019

Yin, Y., Han, Q. H., Bai, L. J., Yang, H. D., and Wang, S. P., 2009. Experimental Study on hysteretic behaviour of tubular N-joints. *Journal of Constructional Steel Research*, **65**(2), 326–334. Elsevier Ltd. DOI: 10.1016/j.jcsr.2008.07.006

Zhang, Z., Pan, S. S., and Huang, C. L., 2004. Design and construction of Tongwamen Bridge, China. *Proceedings of the Institution of Civil Engineers: Bridge Engineering*, **157**(1), 1–7. DOI: 10.1680/bren.2004.157.1.1

Zheng, J., Nakamura, S., Ge, Y., Chen, K., and Wu, Q., 2018. Formulation of stress concentration factors for concrete-filled steel tubular (CFST) T-joints under axial force in the brace. *Engineering Structures*, **170**(April), 103–117. Elsevier. DOI: 10.1016/j.engstruct.2018.05.066

Zhong, S. tong, and Zhang, S., 1999. Application and development of concrete-filled steel tubes (CFST) in high rise buildings. *Advances in Structural Engineering*, **2**(2), 149–159. DOI: 10.1177/136943329900200207

Chapter 3.

3. Advanced Modeling of Shear Studs in Steel-Concrete Composite Beams

3.1. Introduction

The use of composite construction in steel and concrete has been incorporated into many structural systems since the late 19th century (Fisher, 1970; Oudheusden, 1971; Thurlimann, 1985). Beginning in the 1960s, composite floor systems have gained widespread acceptance in the design and construction of modern building and bridge structures. This adoption is primarily due to the development of simple design rules developed by AISC based on exhaustive experimental investigations (Johnson., 1970; Oehlers and Bradford, 1995; Roeder, 1984; S. Balakrishnan., 1962; Viest, 1960; Viest et al., 1997).

As discussed in the next section (3.2 Background), current design provisions for composite beams are predicated on older tests that do not represent the type of construction used today insofar as connector capacity, span lengths, amount of partial interaction and distribution of connectors is concerned. The governing specification (AISC 360, 2016) began to address the connector capacity issues in its 2005 edition by clearly addressing the issue of the strong and weak position of the connectors (Easterling et al., 1993; Rambo-Roddenberry et al., 2002). On the other hand, issues related to connection ductility demand and its determination (Mujagic et al., 2015; Mujagic, 2004) have not received similar attention until very recently. The need for a reexamination of the AISC design provisions with respect to connector ductility has been brought to the fore by the unexpected failure, at about 80% of the predicted capacity, of the longest composite beam with partial interaction that has been tested (NIST, 2019). This unexpected brittle failure for a beam that meets all current criteria requires that advanced models capable of tracking shear connection failures be developed, so that parametric studies can be run to develop more realistic design provisions. This chapter presents the development and calibration studies for such a model.

3.2. Background

In most composite floor systems designed today, the strength, ductility, and stiffness depend on the behavior of the shear connection. In this system, the steel deck initially acts as a permanent formwork during the casting of fresh concrete. Once the concrete hardens, composite action is obtained through the use of mechanical anchors, such as shear studs, which are welded through the steel deck to the upper flange of the beams (Figure 3.1). For the typical configuration of a composite beam, Figure 3.1 shows that the steel deck has stiffeners (ribs) in the center of its troughs; these ribs serve to stiffen the deck during concrete casting but become an obstacle to the welding of the shear studs during the construction process. The presence of this rib results in the studs being placed off-center (Figure 3.2.a), in either a strong or weak position depending on the amount of concrete that interacts with the front of the stud. These different positions result in vastly different connector strength (Figure 3.2.b). The typical composite floor configuration is complemented by slab steel reinforcement (welded wire fabric, in general) that minimizes cracking

due to shrinkage and temperature stresses. Floors of these types are the most common in multi-story steel office buildings in the USA; this is the system addressed in this chapter.

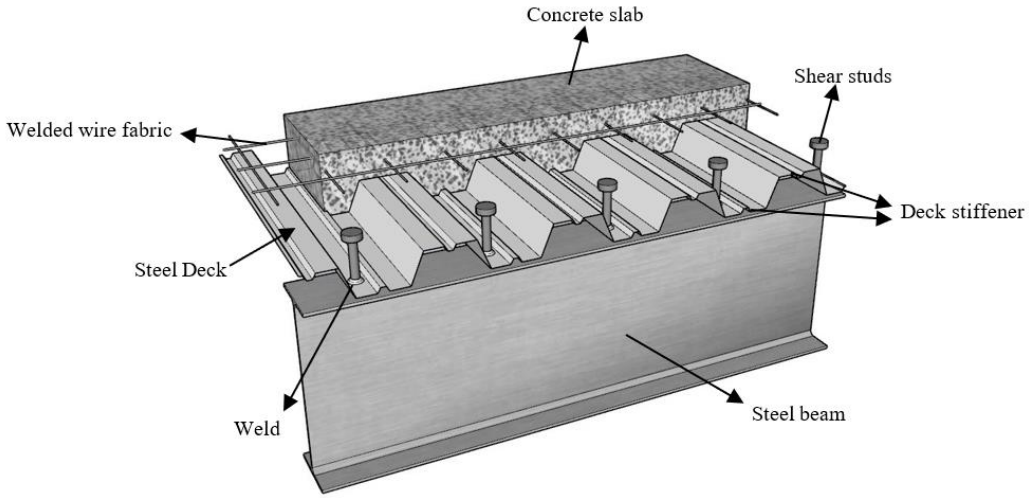

Figure 3.1 Typical composite steel beam configuration.

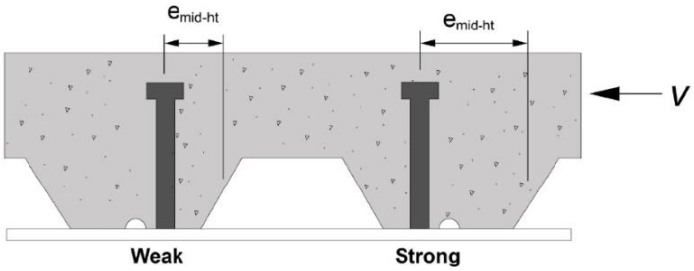

(a) Weak and strong stud positions (Easterling et al., 1993)

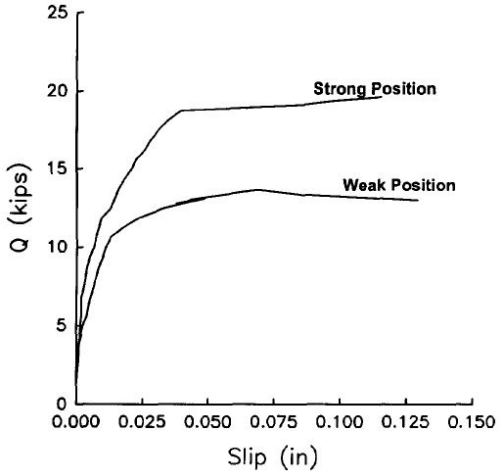

(b) Load vs. slip for strong and weak position shear studs for push-out tests (Easterling et al., 1993)

Figure 3.2 position and strength of shear studs in push-out tests.

The main function of the shear studs is to resist shear forces at the steel-concrete interface, to transfer those forces to the slab primarily through concrete bearing and to prevent vertical separation between the steel deck and the steel beams. These functions provide superior composite action for the system as a whole.

3.2.1 Connector Strength and the Pushout Test

The most common shear connector is the headed shear stud or anchor (Figure 3.1), for which the installation process (stud gun) was patented shortly after the end of WWII by Ted Nelson (Nelson, 1946). The welding process results in a full-strength weld that allows the stud to transfer the forces by mechanical bearing against the concrete to the steel beam below. In addition, the presence of normal forces means that (1) friction and adhesion between the deck and concrete, and (2) mechanical bearing to the ribs also contribute to the shear capacity of the system. The value of Q_n, which is obtained from pushout tests, is a combination of all these mechanisms, with the majority of the strength being assumed to come from the bearing component.

The most important characteristics that are considered for the design of composite beams are the load-displacement relationships and shear capacity. However, to determine these characteristics as accurately as possible, large-scale tests of composite beams are required. This is often costly and time-consuming, so a simplified methodology, based on push-out tests, has been widely adopted. Several types of push-out tests (Figure 3.3.a) have been proposed in order to identify the damage mechanisms and the factors that have a significant influence on the structural behavior of composite beams. In most cases the experimental tests have been validated by numerical models, which, in turn, have been used to carry out parametric studies (Alsamsam, 1991; Davies, 1969; Easterling et al., 1993; Johnson, 1971; Lam and El-Lobody, 2005; Oehlers, 1989; Slutter and Driscoll, 1965). This approach is used not only for Nelson shear studs but also for innovative shear connectors. For example, Oguejiofort and Hosain (Oguejiofor and Hosain, 1997) conducted a numerical investigation of push-out tests using the ANSYS program (Figure 3.3.b-c).

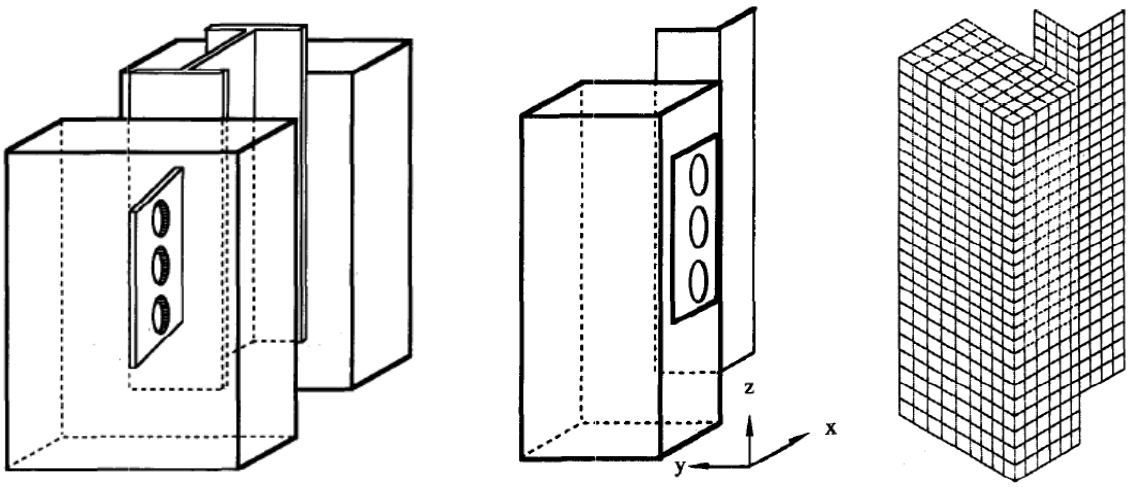

(a) Typical push-out specimen (b) One-quarter section of specimen modeled (c) FE discretization.

Figure 3.3 Configurations for analyses of push-out tests for perfobond connector (Oguejiofor and Hosain, 1997)

They derived the following two mathematical expressions to predict the shear studs capacity for the perfobond rib connector as a function of connector geometry and material properties (Eqs. 3.1.a-b):

$$q_u = 4.47htf'_c + (3.30nd^2 + 0.01A_{cc})\sqrt{f'_c} + 0.90A_{tr}f_{yr} \qquad (3.1.a)$$

$$q_u = 4.50htf'_c + 3.31nd^2\sqrt{f'_c} + 0.91A_{tr}f_{yr} \qquad (3.1.b)$$

Where: h = height of connector (mm), t = thickness of connector (mm), f'$_c$= compressive strength of concrete (MPa), Acc = shear area of concrete per connector (mm^2) = longitudinal area of slab minus connector area, A_{tr} = total area of transverse reinforcement (mm^2), f_{yr} = yield strength of reinforcement (MPa).

Considering the computational costs and the time required to develop 3D FEM models, Guezouli and Lachal (Guezouli and Lachal, 2012) proposed a 2D nonlinear model (Fig. 3.4a) to capture the structural behavior of the push-out tests, and the results of the proposed model were compared with an experimental investigation (Figure 3.4.b-c). They showed that the contact interface between steel and concrete significantly influences strength, stiffness, and forces in shear studs (Figure 3.5).

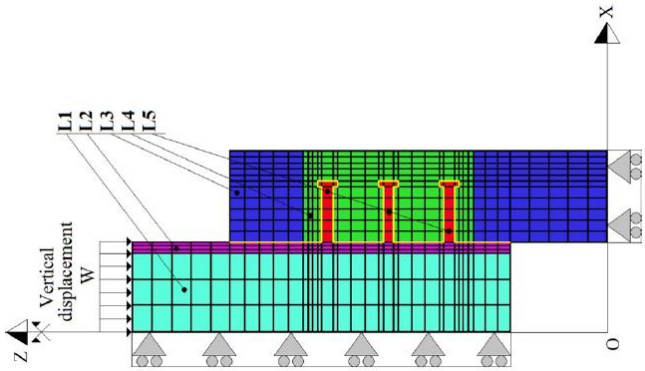

(a) 2D FE model.

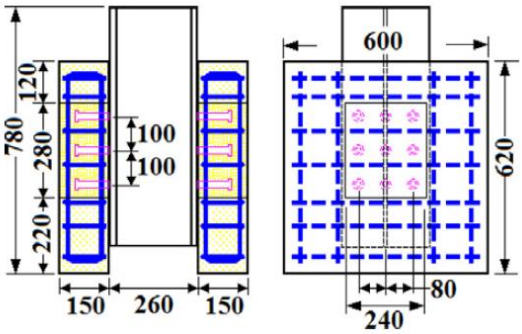

(b) Geometry of the specimen (mm). (c) Test setup.

Figure 3.4 Structural configuration and numerical model (Guezouli and Lachal, 2012)

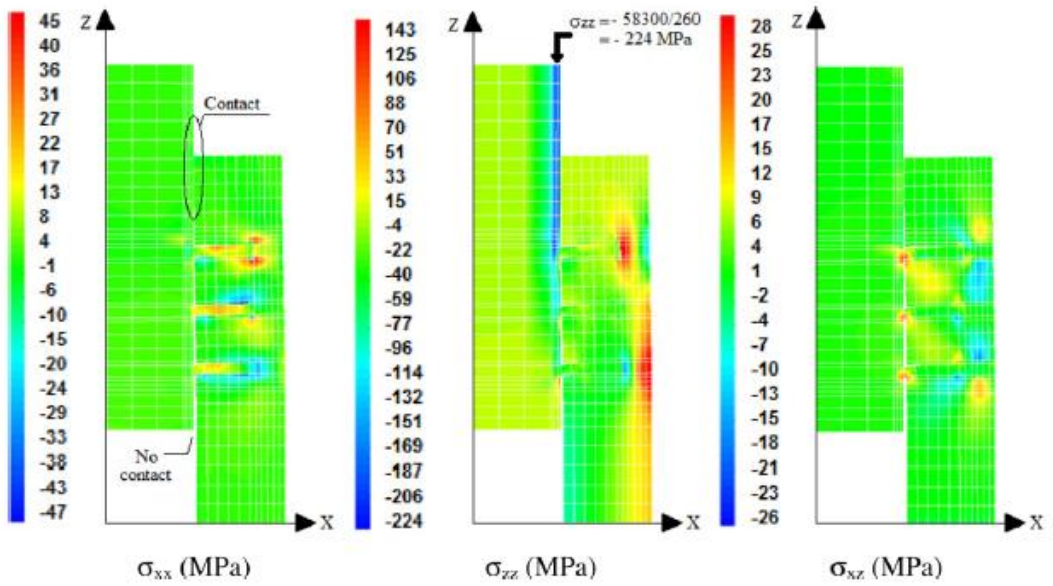

(a) Stress isovalors plotted for the whole specimen for a Z-vertical displacement W= 3 mm and friction coefficients: $\mu_1 = 0.2$, $\mu_2 = 0.3$.

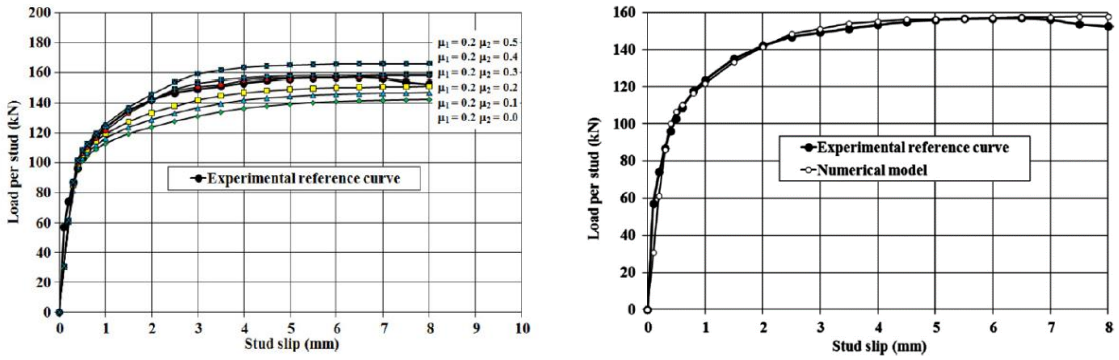

(b) Friction coefficient l2 influence (with $\mu_1 = 0.2$). (c) 2D model validation

Figure 3.5 Results of the 2D nonlinear model (Guezouli and Lachal, 2012)

Yanez et al. (Yanez et al., 2018) performed numerical simulations using 3D finite element models considering the nonlinearity of steel and concrete, as well as the nonlinear behavior of contacts, the models were built and analyzed in ANSYS (Figure 3.6.a). The model was compared with 24 push-out tests that were used to predict the structural behavior of the system (Figure 3.7.a). They studied two different shear stud diameters and two stud positions (Figure 3.6). The numerical model demonstrated its efficiency and accuracy in predicting the characteristics of the plastic trend of the load-slip relationship (Figure 3.7). However, the initial stiffness appears to be higher in the experimental results. This condition appears to be related to physical interactions (e.g. friction) that were not included in the numerical approach.

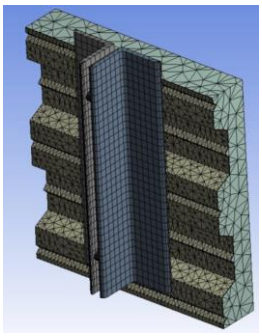

(a) Finite element push-out test model.

(b) Experimental model for a push-out test.

Figure 3.6 Test setup and numerical model (Yanez et al., 2018)

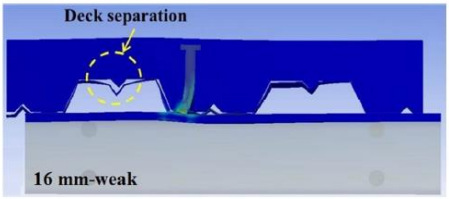

(a) Graphical visualization of the push-out test for 16 mm stud diameter placed in the weak position.

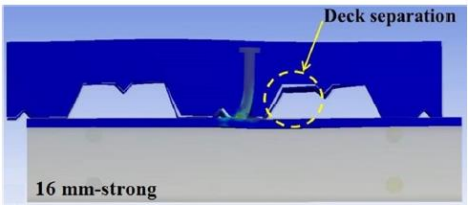

(b) Graphical visualization of the push-out test for 16 mm stud diameter placed in the strong position.

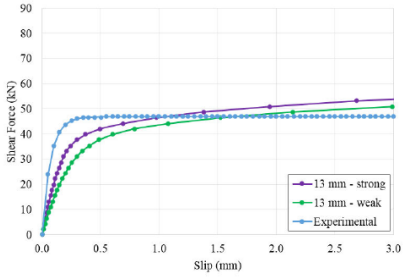

(c) Numerical solution for 13mm - strong and 13mm - weak solution.

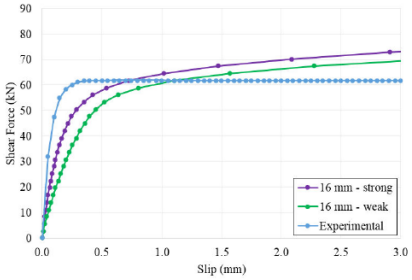

(d) Numerical solution for 16mm - strong and 16mm - weak solution.

Figure 3.7 Results of the 3D nonlinear model (Yanez et al., 2018)

Recently, Katwal et al. (Katwal et al., 2020), built three-dimensional finite element models to study the load transfer mechanism between shear studs and profiled steel sheeting in push tests (Figure 3.8). The models were developed in ABAQUS and considered the nonlinearity of the materials and the nonlinearity of the contact surfaces between the different elements. Parametric studies indicate that the load carried by shear studs and steel sheeting are strongly correlated with the number of shear studs, bolt diameter, concrete strength, sheeting orientation, rib height, presence of transverse load, etc. (Figure 3.9)

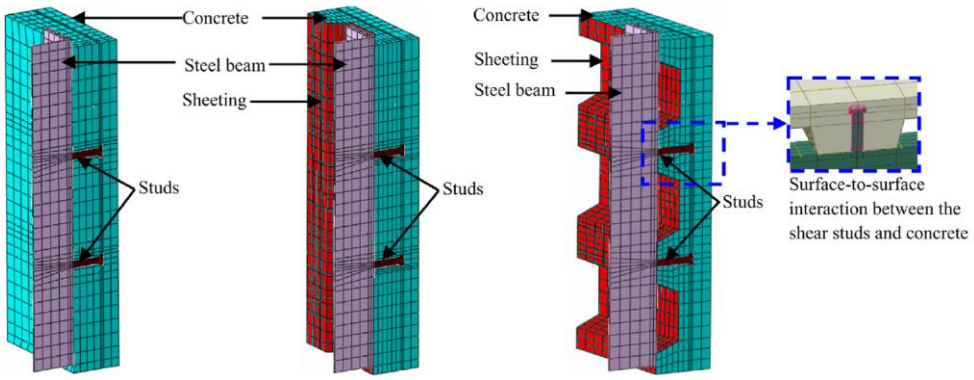

Figure 3.8 Typical FE models for simulating push test specimens.

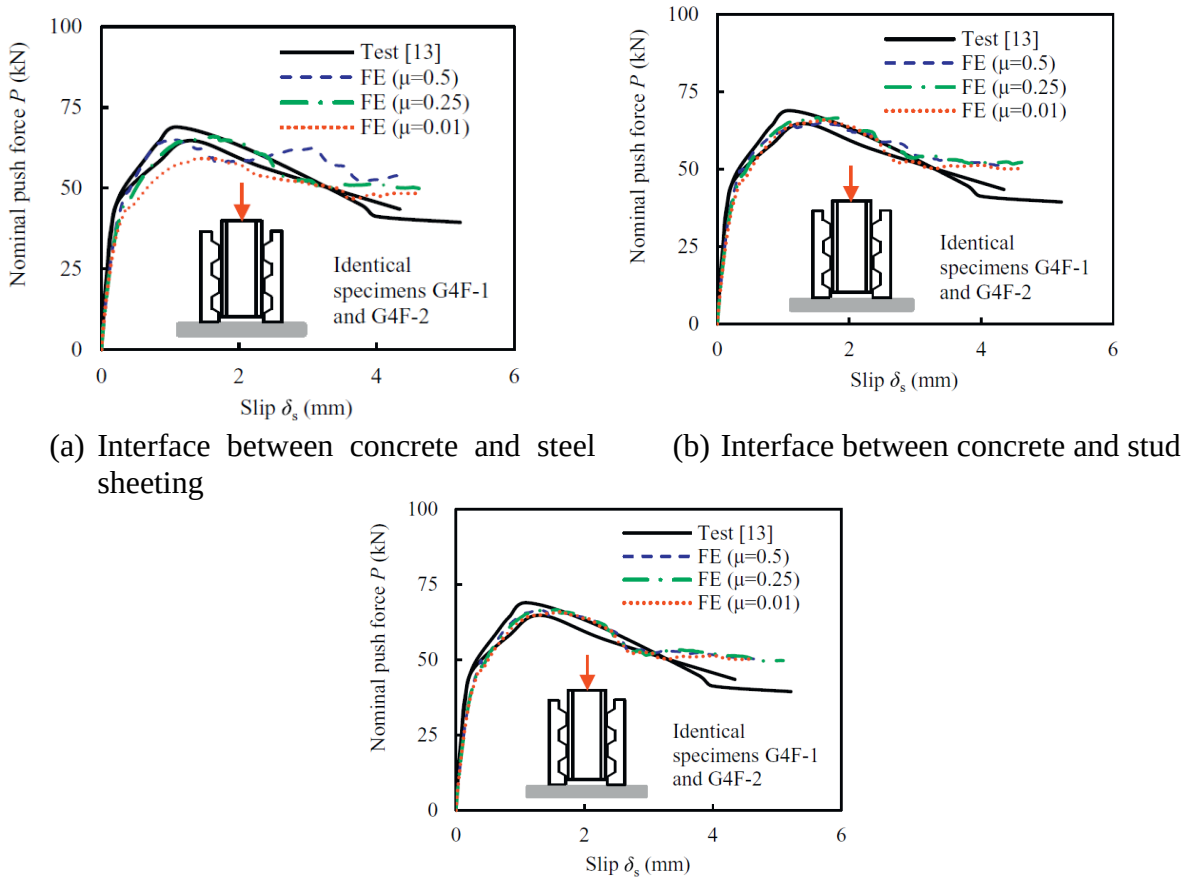

(a) Interface between concrete and steel sheeting

(b) Interface between concrete and stud

(c) Interface between the slab and beam

Figure 3.9 Typical FE models for simulating push test specimens (Katwal et al., 2020)

The most modern pushout test configuration is shown in Figure 3.10 (AISI S923, 2020). In this configuration, a steel beam connected with studs is pushed against two symmetrically placed slabs and the total load and the slip at the bottom of the steel beam are measured. The total force divided by the number of connectors is graphed against the slip to provide an average load-deformation curve. The maximum load is taken as Q_n. A minimum deformation to failure of about 5mm (1/4 in.) is deemed to show adequate ductility for the system. The test configuration shown in Figure 3.10 has an additional set of exterior steel beams meant to provide some normal (or clamping) force to prevent early separation of the slab. These normal forces have not traditionally been part of the test.

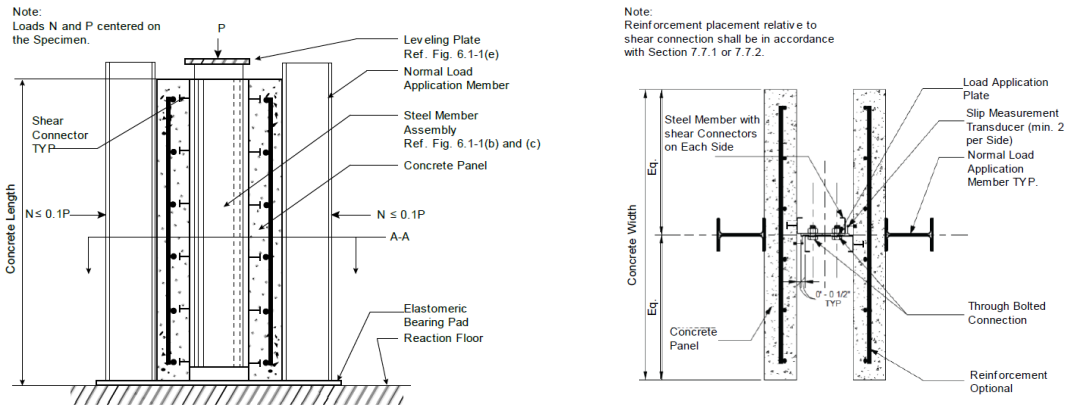

Figure 3.10 Modern pushout test configurations (AISI S923, 2020)

The scatter of pushout test results is generally large, with coefficients of variation greater than 15% (Rambo-Roddenberry, 2002), primarily because the results are driven by the failure of the weaker stud or the concrete surrounding it, which results immediately in an asymmetric loading configuration and a rapid progression of failure. Because the design by AISC-LRFD (AISC-LRFD, 2001) utilizes a single resistance factor in member design, a resistance factor of 0.9 is used in the flexural design of the beam; no resistance factor is associated with the connector itself, which is probably the more variable of the three components (steel beam, concrete slab, connectors). The use of a partial safety factor for the connector, as done in the Eurocode (EN 1994, 2004), typically results in significantly more shear studs being required. The USA approach to this discrepancy has been to point out that not one properly designed composite floor has ever failed in the field once it was completed. While this is correct, the reasons behind the lack of failures is that it is almost impossible to load a composite floor to its design capacity and that the one-dimensional design idealization ignores important two-dimensional force redistribution capabilities.

It has long been understood that there are important differences between the stresses set up in a pushout test and those around a shear stud in a typical composite floor. However, because the use of load-deformation curves from pushout tests is still the industry standard, the research reported herein begins with the modeling of the pushout test to better understand its correlation (or lack thereof) to the stud behavior in an actual beam.

3.2.2 Partial Interaction

Typically, two cases of composite action are considered: (1) full interaction, where the strength of the shear connection ($\sum Q_n = NQ_n$) is greater than the strength of either the steel (A_sF_y) or concrete ($0.85f'_cA_c$) portions of the section, or (2) partial interaction, where the capacity of the shear connection is below that of both the steel and concrete portions. Here, N = number of shear studs in shear span, Q_n is the shear strength of an individual stud, A_s is the area of the steel section, F_y is the yield stress of the steel, f'_c is the concrete cylinder compressive strength, and A_c is the solid area of the slab.

Most office floor systems today are of the partial interaction type because:

(1) the steel beam size is controlled by the need to cast the floor system without shores, and thus only a relatively small portion of the full composite action is needed to meet ultimate strength demands;
(2) the reductions in live loads that have accrued in office floors due to changes in partition materials, transition to a digital environment, and design live load reductions due to the larger bays in use today mean that the total gravity loads are considerably lower than in the past; and,
(3) the use of plastic design principles in the design of floor beams results in large strength gains at lower levels of interaction. A typical beam (W18x35, such as the one described later in the chapter as part of the NIST tests) will achieve 82% of its full composite strength with only 50% interaction. The most economical floor systems require low amounts of interaction (for American construction, in the range of 20% to 50%).

Plastic design, as used in the design of studs, makes the assumption that a connector has rigid-plastic behavior with infinite deformability. As noted earlier, it is assumed that a minimum of about ¼ in. (5 mm) obtained from pushout tests will be sufficient for a beam with even low levels of interaction (25% or more) to reach its design capacity. In addition, the assumptions imply that for many practical situations, the anchors can be distributed uniformly over the shear span. These assumptions have been at the foundation of composite beam design since their introduction into the design codes (Viest et al., 1958). Those assumptions were verified with extensive proprietary tests at Lehigh University in the 1960s and 1970s with beams up to 32 ft. (9754 mm) long.

3.2.3 Connector Ductility

Recently, the increase in floor spans, with bays in the 45 ft. (13716 mm) to 60 ft. (18288 mm) range, means that larger slips are imposed on the connectors near the ends of the beams, and that designers potentially could be entering an area where conventional assumptions do not apply (Mujagic, 2004). Thus, there have been discussions within AISC as to the need to impose some ductility limits on the connectors. That effort culminated in the introduction of a seemly harmless sentence at the end of Section I3.2d in the 2016 AISC Specification (AISC, 2016). That sentence states:

The effect of ductility (slip capacity) of the shear connection at the interface of the concrete slab and the steel beam shall be considered.

Unfortunately, the Specification and its Commentary do not provide any specific guidelines on how to prove this requirement. They do say:

Based on the available studies (Mujagic et al., 2015; Selden et al., 2015)*, beams are not susceptible to connector failure due to insufficient deformation capacity, and thus, need not be checked for this limit state if they meet one or more of the following conditions:*

(1) Beams with span not exceeding 30 ft (9.1 m);
(2) Beams with a degree of composite action of at least 50%; or
(3) Beams with an average nominal shear connector capacity of at least 16 kips per ft (233 kN per m) along their shear span, corresponding to a 3/4-in. (19 mm) steel headed stud anchor placed at 12-in. (300 mm) spacing on average.

Thus, much work needs to be done to extend these limits, as they do not necessarily cover the majority of the cases. In addition, while the current Commentary states that only one of these conditions needs to be fulfilled, that may not be sufficient in cases with large point loads near the ends of the beams, where the traditional uniform distribution of shear studs may also not apply. These two limitations, connector ductility, and shear effects are the primary topics addressed in this chapter.

3.3. Literature Review

There are many shapes or types of anchors that are used to ensure shear transfer in composite beams. These include shear studs (Qureshi, 2010; Rambo-Roddenberry, 2002), angles (Balasubramanian and Rajaram, 2016; Maleki and Bagheri, 2008), slotted plates with or without transverse bars, and bent-up tab shear transfer plate (Irwan et al., 2011; M.Irwan et al., 2009) among others. The deformability of these elements largely determines the structural behavior of composite beams, influencing their bending strength and stiffness, as noted in the original development of the theoretical composite beam behavior (Newmark et al., 1951). The complete solution for the behavior of a steel beam connected to a concrete slab by elastic springs, including vertical separation, was given by Robinson and Narieane (Robinson and Narieane, 1988). Additional load cases and further refinements were provided by (Alsamsam, 1991) and Cosenza and Mazzolani (Cosenza and Mazzolani, 1993).

Initially, in composite beam studies, a complete interaction between steel and concrete was considered (Heins and Kuo, 1975; Kostem, 1988) and shear connectors were modeled as rigid springs (Moffatt and Lim, 1976), elastic springs (Arizumi et al., 1981) or as smeared over the entire interface (Hirst and Yeo, 1980). In other cases, three-dimensional bars were proposed to model the non-linear behavior of shear connectors (Razaqpur and Nofal, 1989). However, this formulation did not consider rotational degrees of freedom and ignored bending deformations. Although in

some cases these models presented reasonable correlations to experimental results, they were not efficient enough to be implemented in 3D nonlinear finite element analysis. A review of early numerical models based on stiffness formulations and finite elements implementations is given by Leon and Viest (Leon and Viest, 1997); as that review is mainly of historical interest, details of those efforts are not given here. In addition, reviews of early experimental investigations on composite beams and pushout tests (up to about 2010) will not be given here as the number of tests is large and excellent summaries and databases area available elsewhere (Mujagic, 2004; Rambo-Roddenberry et al., 2002; Zhao and Leon, 2013) (Mujagic, 2004; Rambo-Roddenberry, 2002) .

The implementation of 3D nonlinear finite element methods (FEM) to predict the structural behavior of composite beams began to appear in the late 1999s (Thevendran et al., 1999) and early 2000s (Baskar et al., 2002; El-Lobody and Lam, 2003). These FEM investigations presented challenging problems in terms of the modelling of the inelasticity in the materials, the steel-concrete contact, and the types of elements needed to eliminate numerical problems. Efficient nonlinear three-dimensional finite element models were also implemented to characterize the behavior of shear connectors (Ellobody and Young, 2006; Lam and El-Lobody, 2005). Qureshi (Qureshi, 2010) studied the behavior of head studded shear studs in composite steel-concrete beams with profiled sheeting by constructing a three-dimensional finite element model. The 3D FEM model accurately predicted slip, shear connector strength, and maximum failure force, and captured the separation of the steel deck from the concrete slab. However, once the model went beyond the maximum load, it overestimated the ductility of the connector. The results of the 3D FEM model were validated by experimental push tests (Figure 3.11).

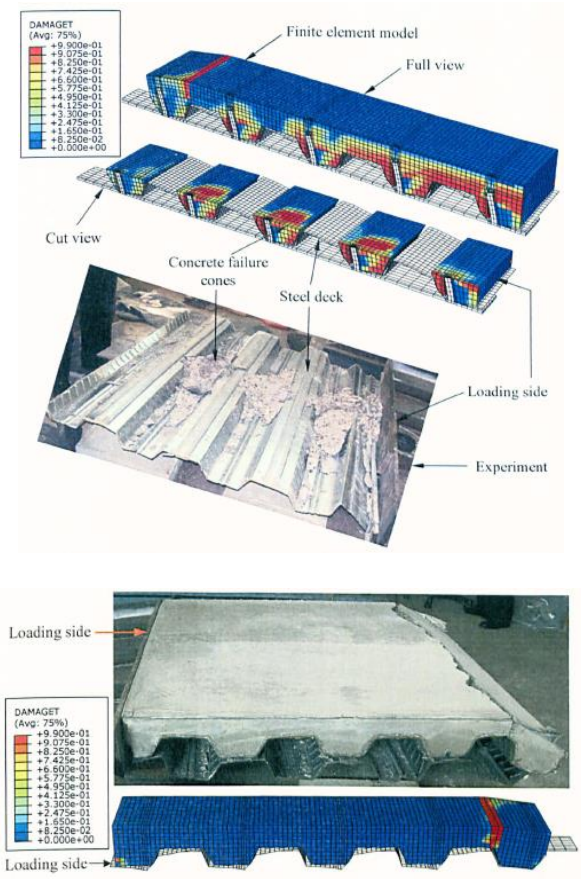

Figure 3.11 Experimental and numerical comparison of the failure mechanisms of the specimen (Qureshi, 2010)

Chung and Chan (Chung and Chan, 2011) used advanced two-dimensional (2D) and three-dimensional (3D) finite element modeling with high-strength materials and deformable shear studs to evaluate the structural behavior of composite beams (Figures 3.12). They showed that the Eurocode (overestimates the moment capacities for composite beams made with high-strength steel, but underestimates the moment capabilities with composite beams using heavily reinforced slabs.

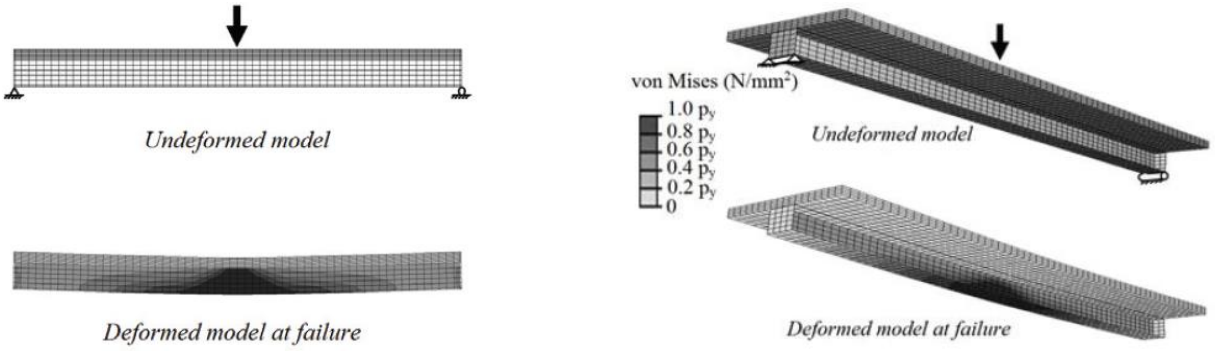

(a) 2D model (b) 3D model

Figure 3.12 Finite Element Modelling (Chung and Chan, 2011)

Tahmasebinia et al. (Tahmasebinia et al., 2013) carried out a probabilistic study on the influence of the uncertainties of the materials and the connection to shear on the nonlinear behavior of continuous and simply supported composite beams using three-dimensional FEA models. In addition, Tahmasebinia et al. (Tahmasebinia et al., 2013) represented the behavior of shear studs without the need to use load-slip curves obtained experimentally. The results show good agreement between the statistical representations and the nonlinear structural behavior of the composite beams (Figure 3.13).

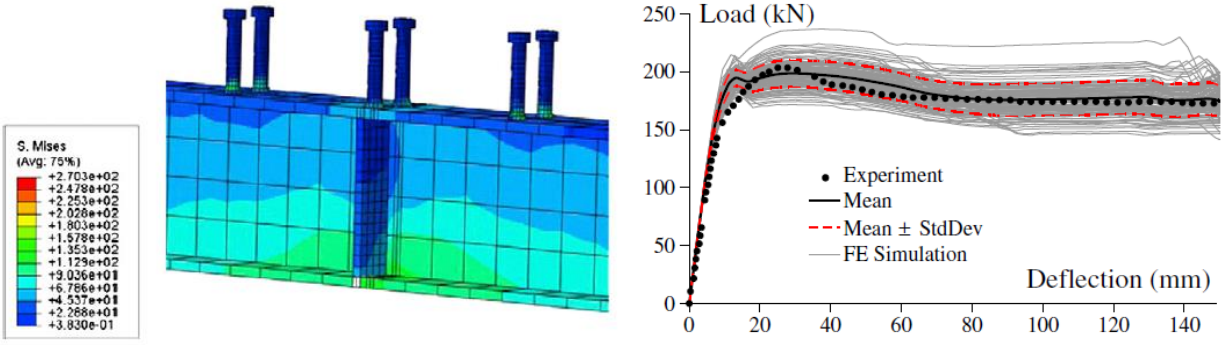

(a) Stress distributions calculated for the shear connectors at the end support and at mid-span of sample

(b) Comparisons between the numerical and experimental results for the sample

Figure 3.13 Numerical and experimental results of the sample (Tahmasebinia et al., 2013)

Liu et al. (Liu et al., 2016) used the FEM to investigate the behavior of composite beams simply supported with HSFGB (High-strength friction-grip bolts) anchors considering the spacing and pretension of the bolts, as well as the configuration of the longitudinal reinforcement. The reduction in bolt spacing increases the ultimate strength of the composite beam and the use of HSFGB shear connectors increases shear strength and ductility (Figure 3.14).

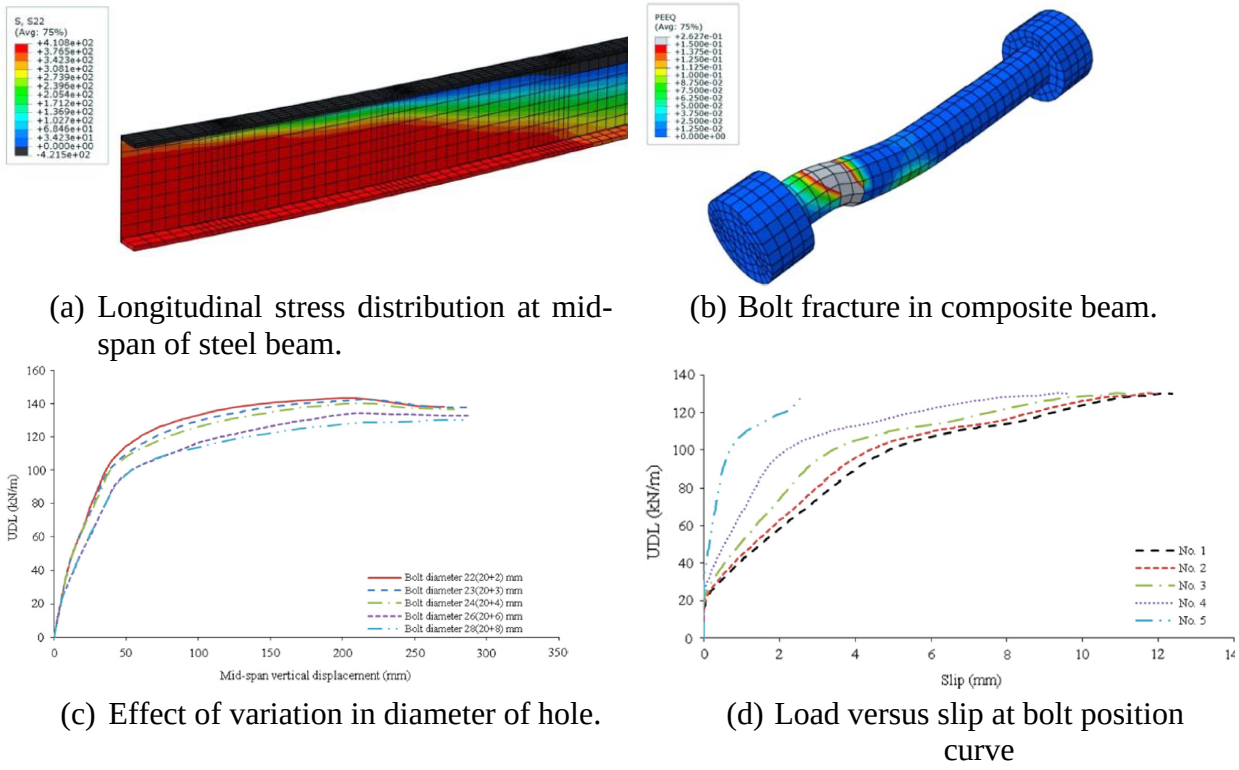

(a) Longitudinal stress distribution at mid-span of steel beam.

(b) Bolt fracture in composite beam.

(c) Effect of variation in diameter of hole.

(d) Load versus slip at bolt position curve

Figure 3.14 Numerical results of the developed model (Liu et al., 2016)

By increasing the intensity of the load, the composite beams present a sliding problem at the steel-concrete interface, this effect increases the curvature and deformation, but reduces the stiffness (Hicks and Smith, 2014; Zeng et al., 2019). However, under dynamic conditions, sliding can be a great advantage since it increases damping (Di Sarno and Elnashai, 2005). Therefore, to determine the real behavior of composite beams using numerical models, the contact between the shear connector and the concrete must be accurately modeled. A very recent work described high-definition FEM simulation techniques that were able to accurately capture the stiffness, ultimate strength, and failure mechanisms of composite beams (Adhikari et al., 2021) (Figure 3.15).

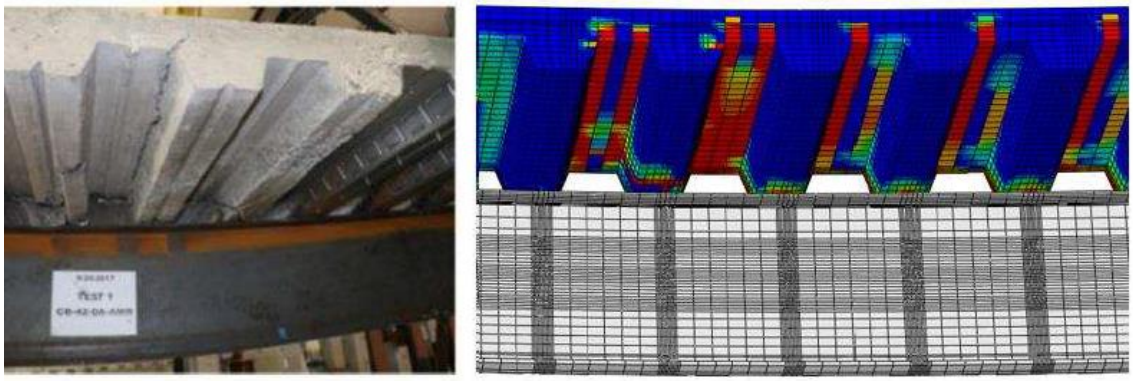

Figure 3.15 Comparison of experimental and numerical load patterns (Adhikari et al., 2021)

As can be seen, rigorous investigations have been carried out on the nonlinear structural behavior of composite beam systems, considering shear connectors as the main variable. These investigations have helped determine and improve design parameters, which are very difficult or cannot be determined through experimental investigations. However, there are some uncertainties that remain in the numerical modeling of nonlinear finite elements of composite beams including how to model (1) the contact resistance between steel-concrete, (2) the effects of residual stresses in the steel, (3) the many parameters required to define the concrete material models, (4) the influence of local buckling once the steel-concrete contact resistance has been overcome, (5) the influence of the location and spacing of the shear connectors, and (6) the incorporation of the stiffeners in the flanges of the steel deck. This research aims to address items (1) and (5) in the list above.

3.4. Problem Statement and Solution Approach

Experimental investigations carried out on the structural behavior of shear studs according to design (A. AISC 360-16, 2016) and construction (ICC, 2018) criteria indicate that there are failure mechanisms that have not been fully understood (Green et al., 2004; Tan and Uy, 2009) and that "actual" the transfer force to break shear studs can be significantly less than the design value (El-Lobody and Lam, 2003; NIST Technical Note 254-2019). In fact, when point loads are present close to the supports, the resistance of the composite section will depend primarily on the distribution of shear studs along the steel beam. From the mechanics standpoint, the lengths with the lowest shear spans (M/V) should have the most studs. However, traditionally studs are distributed uniformly in girders even when the loads are mostly from point loads (filler beams). Additionally, other experimental investigations have shown that if the shear studs are grouped near the edge of the slab this would produce sudden failures, that is, brittle behavior (Hawkins and Mitchell, 1984). These failures are the result of high shear stresses in the stud and can cause significant reductions in strength and ductility. In recent work, Gautam et al. (Gautam et al., 2019) tested different group arrangements of shear studs in simply supported and continuous box-type beams. They showed that the degree of shear connection is inversely proportional to the displacement of the test beam and that the maximum value of displacement decreases with the degree of shear connection. The complexity of the problem is illustrated by the extensive provisions in Chapter 17, Anchoring to Concrete in ACI 318-19 (ACI 318-19, 2019).

In view of the given background, the goal objective of this research is to develop three-dimensional finite elements to study the influence of shear stud strength, ductility, and distribution on the structural behavior of composite beams with trapezoidal profiled sheets. The intent is to use extremely refined meshes, the best material models, and the most robust solution algorithms available in ANSYS-LS DYNA (ANSYS, 2020) to:

- Determine the significance of the pushout test in assessing the required strength and ductility of composite beams.
- Model the failure of the NIST beam (NIST Technical Note 254-2019)
- Assess the effect of adding a few additional studs to the end of the beam as a requirement for long beams (longer than 30 ft.) to be exempt from the current AISC requirement of checking connection ductility.

Thereby, for a better understanding of the structural performance of shear studs in composite beam systems, more experimental programs are required. However, it is known that these programs have a high cost in terms of time, fabrication, and experimentation, so the obvious recourse is to consider numerical simulations to perform parametric analyses. These analyses can investigate a range of configurations that can be anticipated when considering the variation material properties, shear connector strength and stiffness, location and spacing of the anchors, and failure mechanisms.

3.5. Numerical modeling

The numerical studies conducted within this research fall into two broad categories: (a) pushout tests and (b) beam tests. As noted earlier, it is recognized that the stress state in the pushout test does not correspond to that in a real composite beam. For the purposes of this study, it was deemed important to model the pushout test so that comparisons could be made between the two conditions. The modelling assumption for both the pushout and composite beam tests are very similar, so a general modeling description for both will be given first, and differences between them will be discussed in the individual modeling sections.

3.5.1 General

Reliable FEM modeling requires that material models, meshing density, element types and solution schemes be thoroughly understood. Consequently, it is necessary to work with specialized structural modeling programs that are sufficiently documented and validated in the area of composite structures. In this research, the pre- and post-processing of three-dimensional models in finite elements was executed with ANSYS-LS DYNA (ANSYS, 2020) and LS-PrePost (Hallquist, 2006) using the computational facilities of the Pontificia Universidad Católica de Chile, Virginia Tech and a specially designed and assembled workstation.

Due to the robustness of the models and the fact that the inelastic structural behavior of composite beams is accompanied by geometric and material nonlinearities, it is necessary to have large computer resources to conduct reliable simulations. At the same time, there is a need to maintain reasonable computation times and pre- and post-processing times. Because the initial intent was

to model the severe unloading that takes place as shear studs fail, the numerical modeling is carried out using an explicit integration scheme with the LS DYNA mmp (massively parallel processing) solver (Lapoujade et al., 2014). The explicit scheme avoids the iterative process required for an implicit scheme but requires a small-time step for numerical stability (Courant et al., 1967). The size of the critical time step is correlated to the highest natural frequency of the system and is calculated for linear systems without viscous damping.

3.5.2 Test specimens considered in the investigation

The National Institute of Standards and Technology (NIST Technical Note 254-2019) carried out an experimental investigation on the behavior of composite steel and concrete beams under combined gravity and fire loads, considering the design (AISC, 2010) and construction requirements (ICC, 2018) in the United States. To calibrate and validate the numerical models for this fire resistance investigation, Specimen 1 was subjected to vertical loads only.
Figure 3.16 shows the details of Specimen 1 and its associated boundary conditions. The specimen is 12.8m long and consists of a A992 Grade 50 W18 x 35 beam, a 20-gauge 76mm deep galvanized steel deck with 83 mm of lightweight concrete above the deck and a 6x6 W1.4xW1.4 welded wire fabric. The design was driven by the need to provide a 2-hour fire rating for the composite floor slab.

The design forces were a moment of 548 kN-m and a shear of 171 kN. The loads were to be applied by three hydraulic actuators, each applying two loads at five equal spacings. This six-point load was deemed sufficient to simulate a uniformly distributed load. Figure 3.17 shows the forces in Specimen 1 at failure for the idealized simply-supported model used in design. While the moment diagram is quite similar for the uniformly and six-point load cases, the same is not true for the shears. Significant concentrated shears at the end of the beam are present, and probably contributed to the early failure.

Because the test program was geared to determine fire resistance and subassemblages with two or more bays were to be tested, it was important to incorporate typical shear connections to a column at the ends of the beam. Therefore, the specimen incorporated double-angle connections (A36 L5×3×3/8 angles) with 8mm fillet welds to the column and three A325 76mm bolts in standard holes to the beam. While theoretically these connections were close to a pin for design purposes, the test data indicates that Specimen 1 behaved like a partially restrained (PR) beam, which significantly increased the shears at the ends.

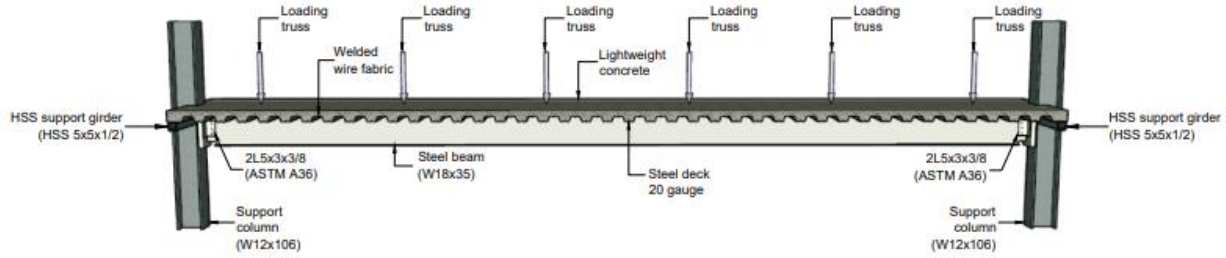

(a) 3D elevetation

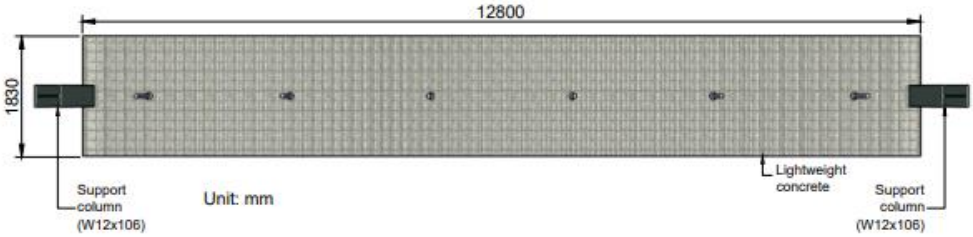

(b) Plant view

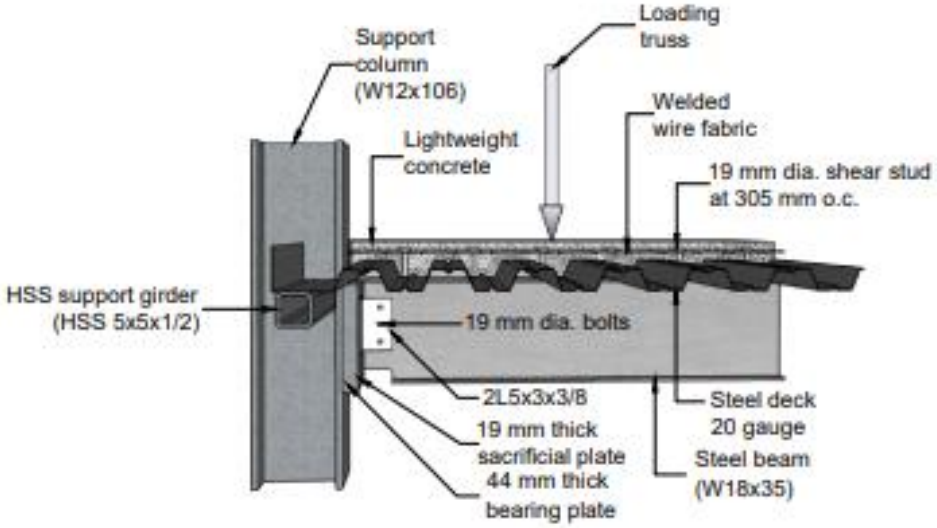

(c) Connection detail

Figure 3.16 General configuration of Specimen 1 (NIST Technical Note 254-2019)

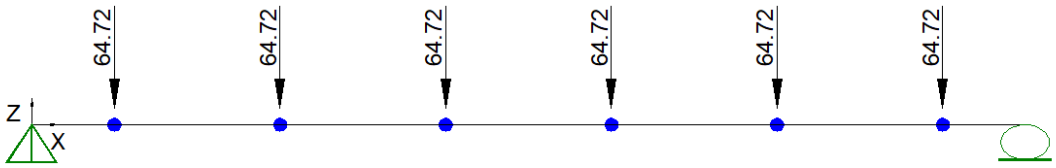

(a) Point loads system

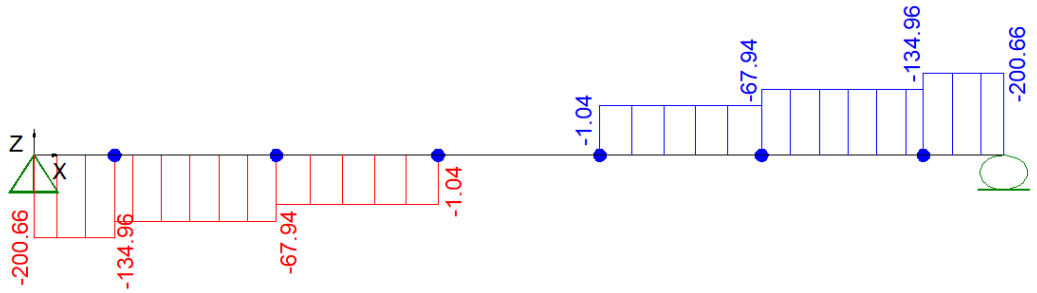

(b) Shear diagram

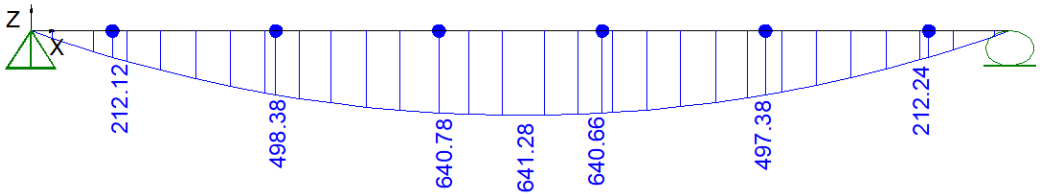

(c) Moment diagram

Figures 3.17. Moment and shear diagrams (Units: Kn-m)

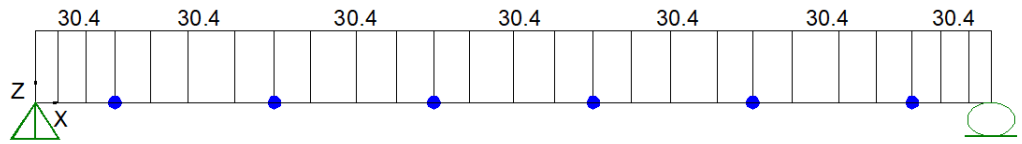

(d) Distributed load system

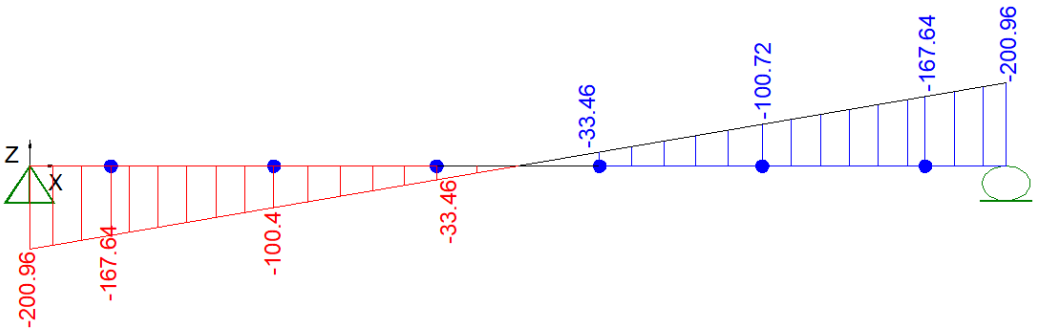

(e) Shear diagram

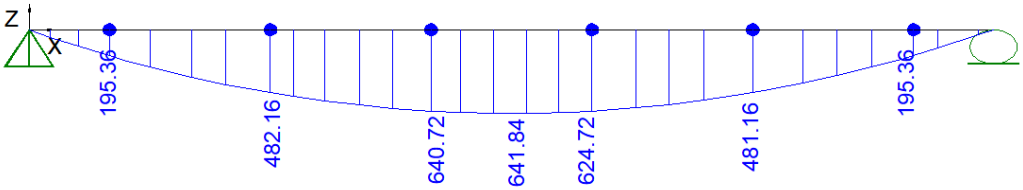

(f) Moment diagram

Figure 3.17 Moment and shear diagrams (Units: Kn-m) Continued.

3.5.3 Modeling approach

In order to setup a suitable model to simulate the structural behavior of composite beams and pushout tests, the geometric models, meshing, boundary conditions, load application, material models and contact types described below are used.

3.5.3.1 Finite element models and meshing

Figure 3.18 shows the complete finite element model of the composite beam. The model for the pushout test was an extract from this bigger model in order to make comparisons as valid as possible. Considering the symmetry of the model in terms of both geometry and loading, a quarter of the original geometry of the beam was considered (Figure 3.18). This was done primarily to reduce computational costs. As will be seen in a later discussion, this simplification had no impact on the results.

Finite element model T (FEM T) was developed (Figure 3.19), which represents the original geometry of the composite beam (Specimen 1), including the real trapezoidal geometry of the profiled steel sheet with stiffeners and with all shear studs centered with the axis of the steel beam. Figure 3.20 illustrates in greater detail the distribution of the shear studs and the beam-column connection.

Figure 3.21.a illustrates the model adopted for the study, considering beam elements to represent the rebars, shell elements to represent the steel beam, the steel deck and connections, and three-dimensional solid elements to represent the concrete and the shear connectors of the composite beams. Figure 3.21.b shows a detail of the joint view of the steel beam, steel deck, and concrete slab. Figures 3.21.c and 3.9.d show the details of the mesh around the bolt and the mesh of the shear stud, respectively

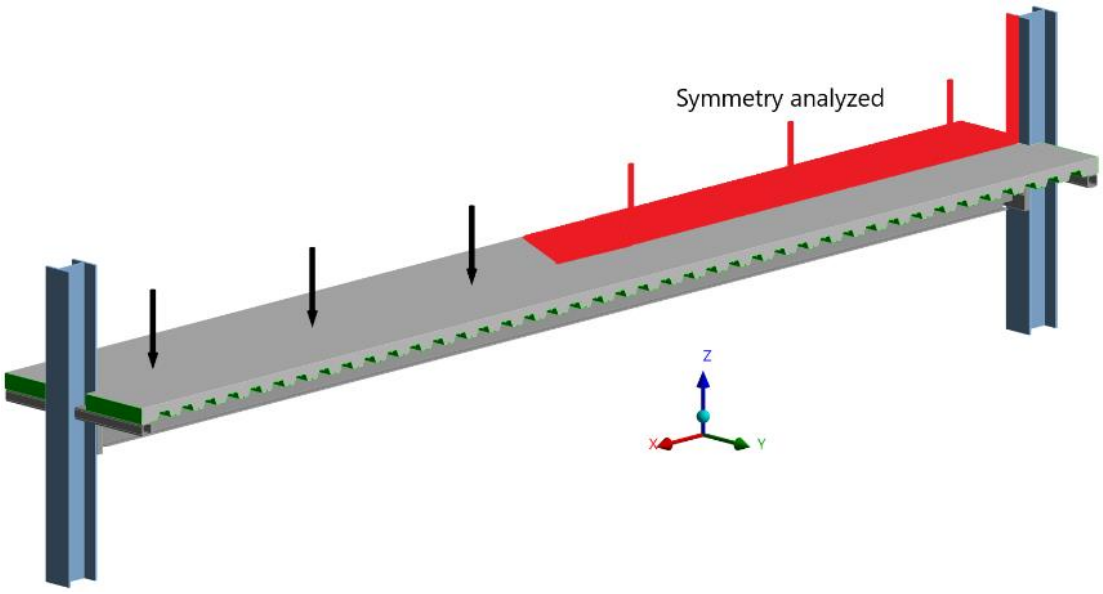

Figure 3.18 Finite element model.

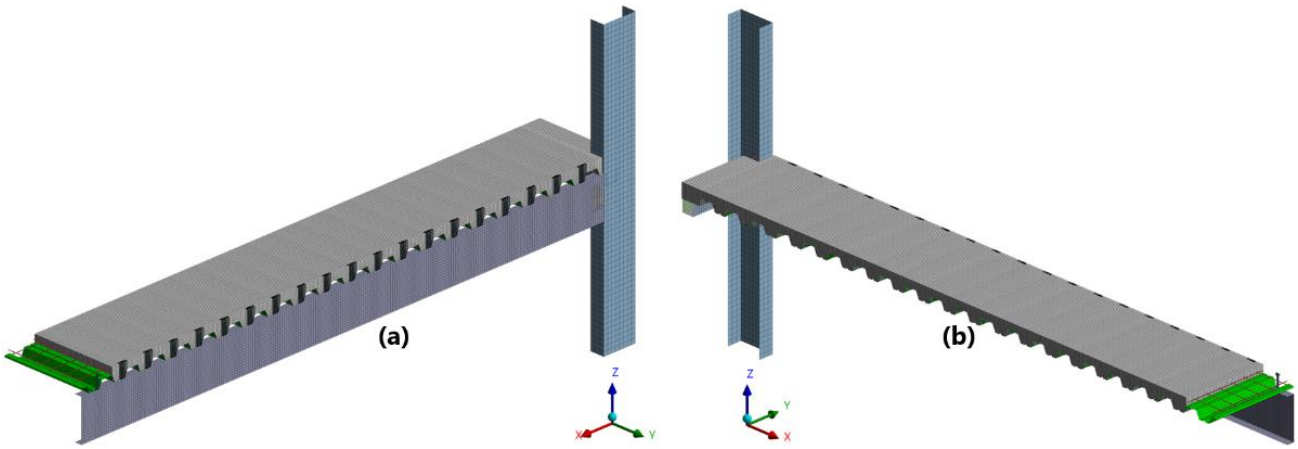

Figure 3.19 Overview of the FEM I: (a) Front view and (b) Front-back view.

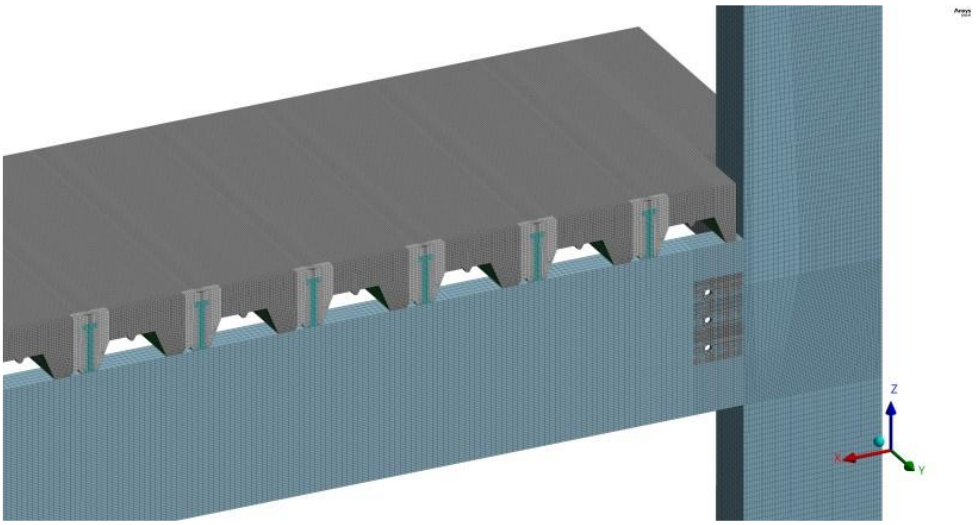

Figure 3.20 Shear studs distribution in numerical model.

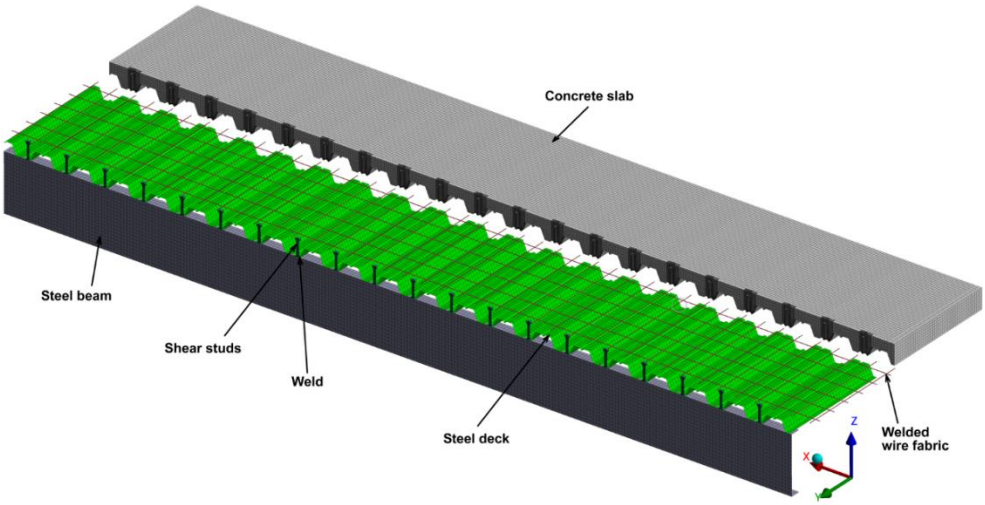

(a) Model adopted for parametric study

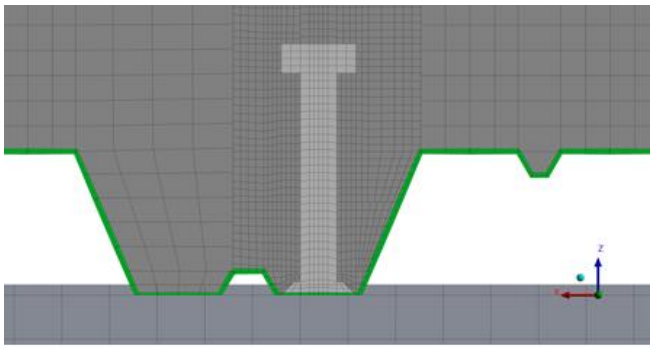

(b) Joint view of steel beam, steel deck, shear stud and concrete slab.

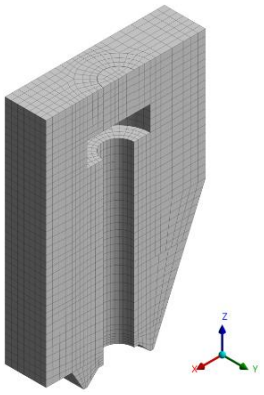

(c) Concrete around the shear stud

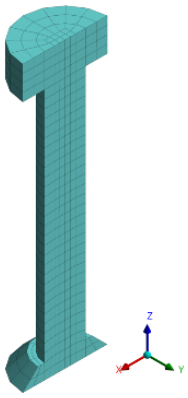

(d) Shear stud

Figure 3.21 Finite element type and mesh.

Figure 3.22 shows the models that were extracted to carry out the pushout tests. The one-stud model was constructed for the purpose of comparison with the experimental investigation of Lam and El-Lobody (Lam and El-Lobody, 2005) (Figure 3.22.a). The two-stud models were built in order to predict the capacity of the FEM model, understand the behavior of the studs according to their position (weak or strong), the importance of the coefficient of friction between steel and concrete, and the influence of the ribs on the geometry of the steel deck.

The TS-I model (Figure 3.22.b) represents the push-out model with the studs located in the internal channels of the steel deck. in the TS-II model the right stud moves towards the external channel of the steel deck (Figure 3.22.c); when loaded from the left (see arrow in Figure 3.22.g) the studs are in the strong position; when loaded from the right, they are in the weak position. In the TS-III model (Figure 3.22.d) shear studs are located in the external channels of the steel deck. All these models incorporate the ribs in the steel deck. Finally, the TS-IV model does not consider the ribs on the steel deck (Figure 3.22.d).

On the other hand, it is important to note that push-out tests are generally confined by a framework of elements to simulate a confining force or normal load on the shear studs (Easterling et al., 1993;

Leskela, 2017; Rambo-Roddenberry et al., 2002; Yanez et al., 2018) (Figure 3.22.f). This normal load (N) is defined by AISI as 10% of the load applied to the main beam (P) (Figure 3.22.g).

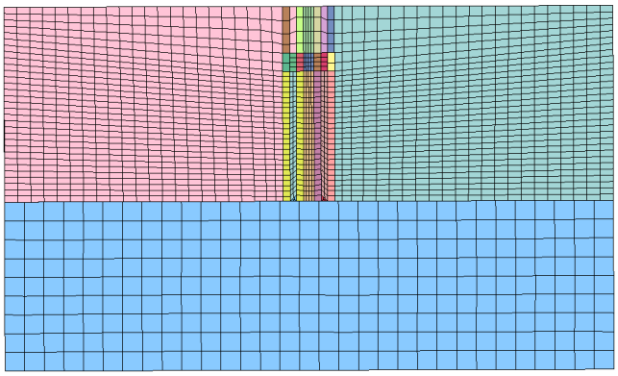

(a) One-stud

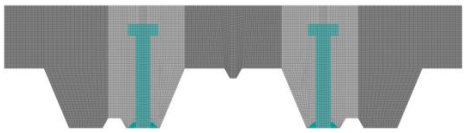

(b) Two-stud-I (TS-I)

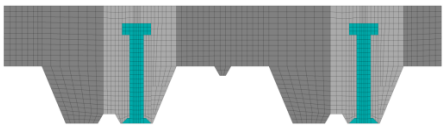

(c) Two-stud-II (TS-II)

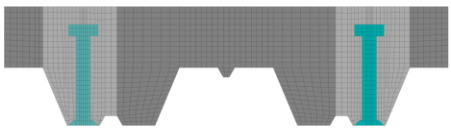

(d) Two-stud-III (TS-III)

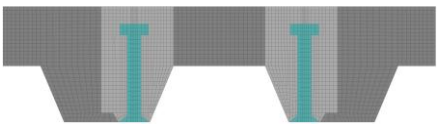

(e) Two-stud-IV (TS-IV)

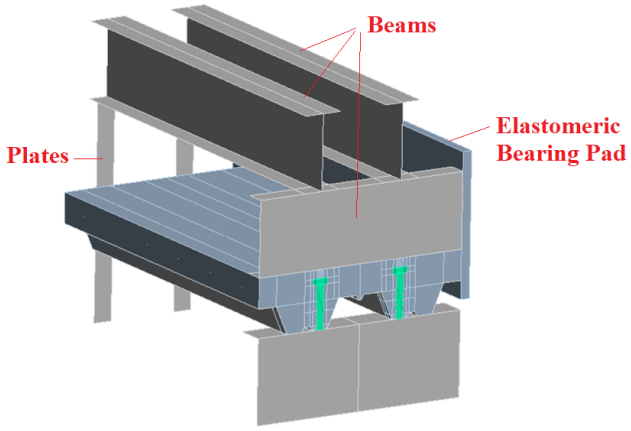

(f) Confinement elements

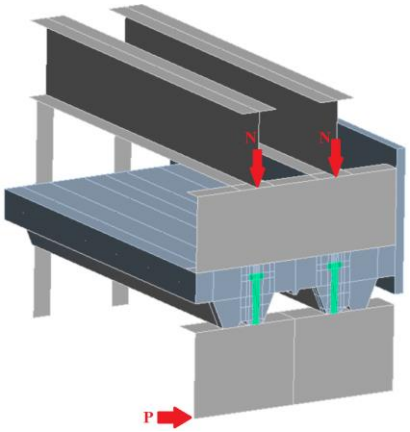

(g) Confining or normal loads on shear studs.

Figure 3.22 Finite element model of pushout test.

Beam elements (Figure 3.23) are capable of representing axial, bending and shear stress. They are used to model slender components in which length is at least one order of magnitude longer that the dimensions of the cross section. They include six degrees of freedom (three translations and three rotations) at each node. They represent a very efficient numerical modeling technique for slender components.

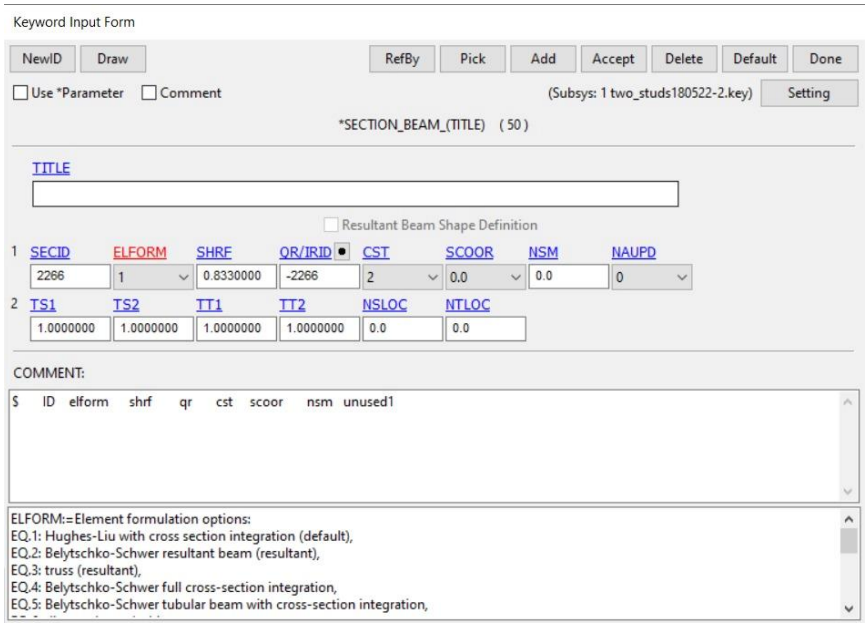

Figure 3.23 Beam element definition.

The shell element model is a three or four node formulation (Figure 3.24). At each node, 6 degrees of freedom are active (three translations and three rotations). In addition, said model is independently stable under perpendicular loads and in the plane of the element. This model is simple and computationally cheap.

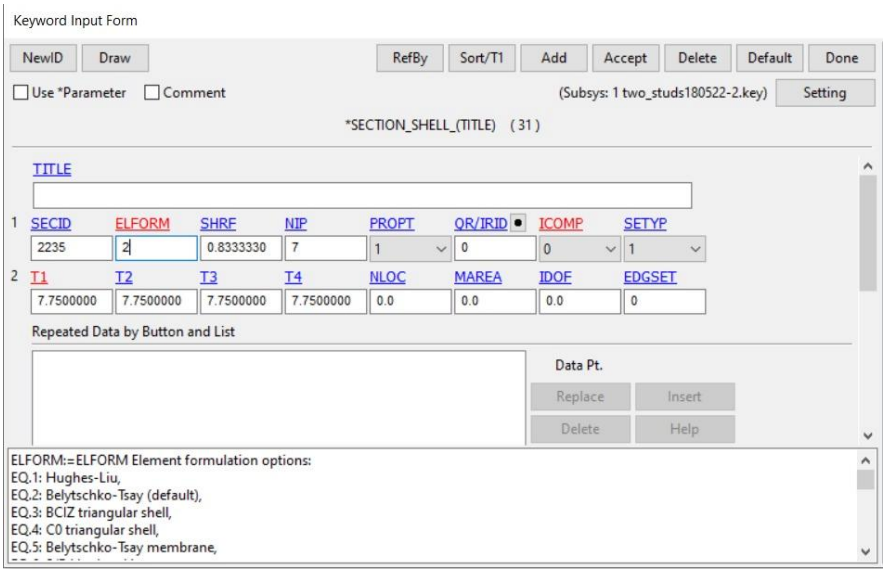

Figure 3.24 Shell element definition.

Three-dimensional eight-node solid hexahedral elements with reduced integration offer (Figure 3.25) the advantage that they can be used in structures or components that have a high aspect ratio and guarantee good precision, in addition to the direct obtaining of residual stresses. At each node there are three degrees of freedom, corresponding to the three translations of a three-dimensional problem.

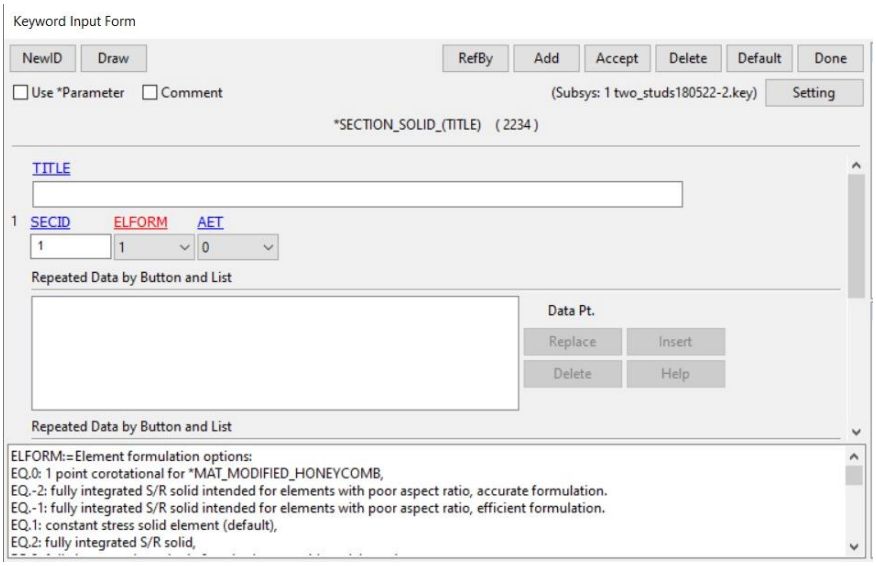

Figure 3.25 Solid element definition.

Regarding the mesh size (Figure 3.21.b), note that the concrete mesh was refined in the vicinity of the shear stud with elements down to 5 mm, while the rest of the concrete slab mesh used a spacing of 18 mm.

In order to mesh the non-regular geometry of the concrete and the shear studs with hexahedral elements, the geometries of these components were cut into different volumes. For those areas with similar mesh size, the interface between the volumes of a same material includes share nodes between them. For those cases where different mesh sizes were used or where use of a continuum hexahedral mesh was not feasible, contacts with a constraints type formulation were used. This contact formulation adds constraint equations to “tie” the displacements between contacting surfaces (ANSYS, 2020).

To validate the use of a non-continuum mesh to model a continuum material, a test on a simply-supported concrete beam with a concentrated load was performed (Figure 3.26). For this purpose, two beams were compared, one completely homogeneous and another one with an embedded denser mesh at the top connected with *contacts with constraint* type formulation. The results and the nonlinear models are shown in Figure 3.26. It can be seen that no important differences in the stress contour appear in the different models at the global level, but there are, of course, differences at the local level.

Model A - Continuous mesh

Model B - Non-continuous mesh

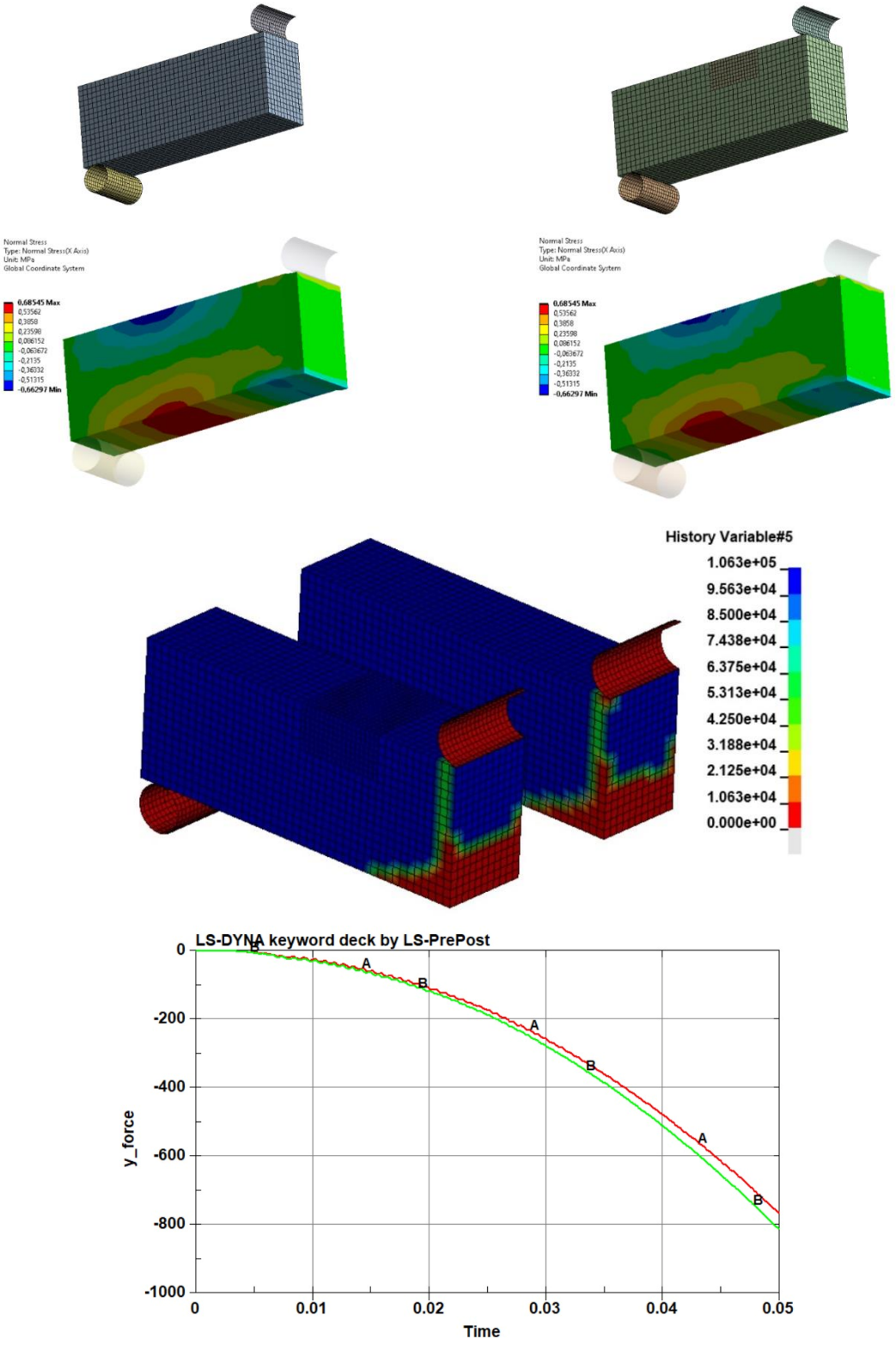

Figure 3.26 Validation of the use of mesh.

3.5.3.2 Contacts between elements

Different contact types were used depending on their location and desired behavior. Details of each of them follows:

Bonded Contact with Failure:

For the connection between the concrete with steel parts (studs or steel deck), bonded contacts with failure are used. For these contacts, the contact elements stay bonded until a stress condition, defined by the following expression, is reached:

$$\left[\frac{\max\left(0.0, \sigma_{\text{normal}}\right)}{\text{FS}}\right]^2 + \left[\frac{\sigma_{\text{shear}}}{\text{FD}}\right]^2 > 1 \qquad (3.2)$$

where σ_{normal} is the normal stress, σ_{shear} is the shear stress, FD is the normal tensile stress at failure and FD is the shear stress at failure. For FD and FS a stress magnitude of MPa was used.

Additionally, a bonded contact with failure was used for the connection between the stud and the steel deck to model the brittle failure mode of the first stud that was detected in the experimental analysis. Figure 3.27 shows some areas where the bonded contact with failure (red surfaces) was used:

Frictional Contacts:

A frictional interaction was defined between all parts of the model, even for self-contact of different surfaces of a component. This behavior will only work when there is no bonded contact on an active condition, that is for those regions were no bonded contact was defined or where the bonded contact has failed.

Bonded Contact with a Constraint Type Formulation

In order to be able to mesh the non-regular geometry of the concrete and the shear studs with hexahedral elements, the geometries of these components were cut into different volumes. For those areas with similar mesh size, the interface between the volumes of a same material includes share nodes between them. For those cases where different mesh size was used or where a continuum hexahedral mesh was not feasibly, contacts with a constraint type formulation were used. This contact formulation adds constraint equations to "tie" the displacements between contacting surfaces (ANSYS, 2020).

Figure 3.28 shows an example of a region where the bonded contact with constraint type (blue surface) formulation was used.

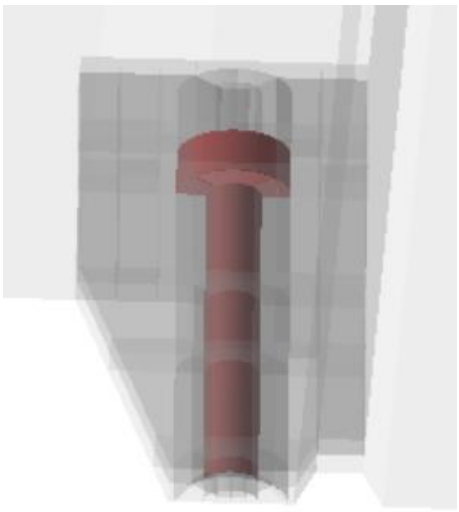

(a) Shear stud and concrete

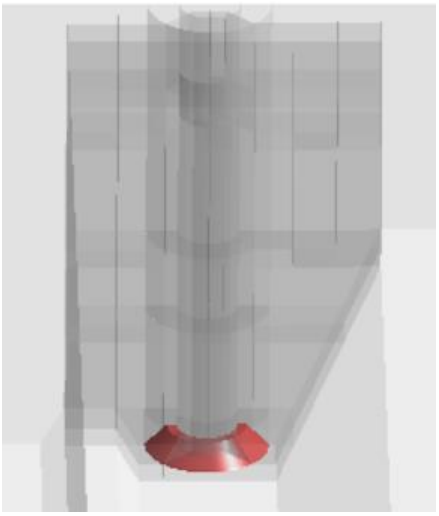

(b) Weld and concrete

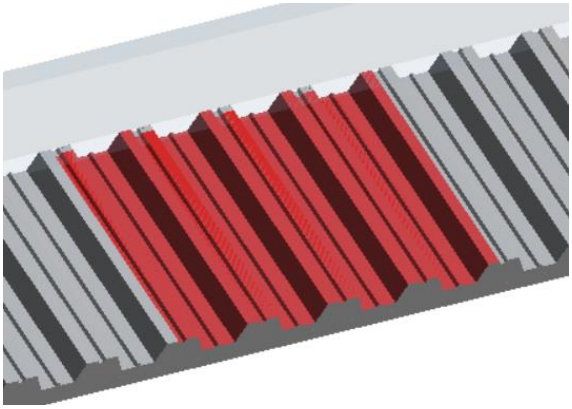

(c) © Steel deck and concrete

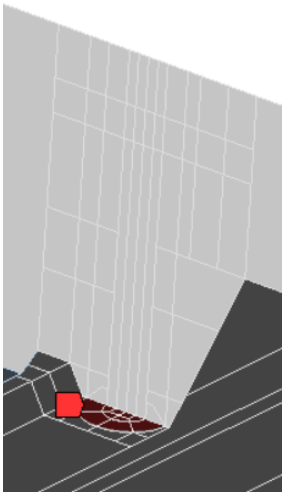

(d) Steel deck and shear stud

Figure 3.27 Examples of regions with bonded contacts with failure (red shape in (d) indicates symmetry region)

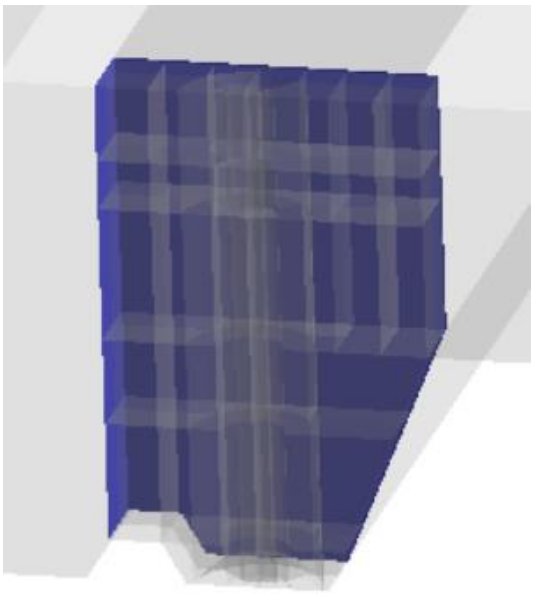

Figure 3.28 Contact bonded.

The behavior of the different connection types, for a variety of load and boundary conditions, are shown in Figure 3.29. In these studies, a top plate 25mmx25mmx5mm is used to introduce a load into a lower plate of 50mmx25mmx5mm. In Figure 3.29a, the shear stress of 6MPa is applied to the side of the top plate for a bonded with failure condition over a 0.1sec interval. Failure occurs at a force of about 72 kN at about or average shear stress of about 5.5 MPa, which appears reasonable given the lack of a normal force and the given concrete strength of 70MPa. In Figure 3.29b, the frictional component with a normal force of 2MPa and a longitudinal force of 12MPa is shown. Note that for the general case of a bonded with friction surface contact, the total force will be the addition of the two components shown in Figure 3.29. The bonded component will work first until its capacity is exceeded; afterward, the frictional component takes over, with an initial value similar to that of the bonded case. Figure 3.30 shows the overall behavior.

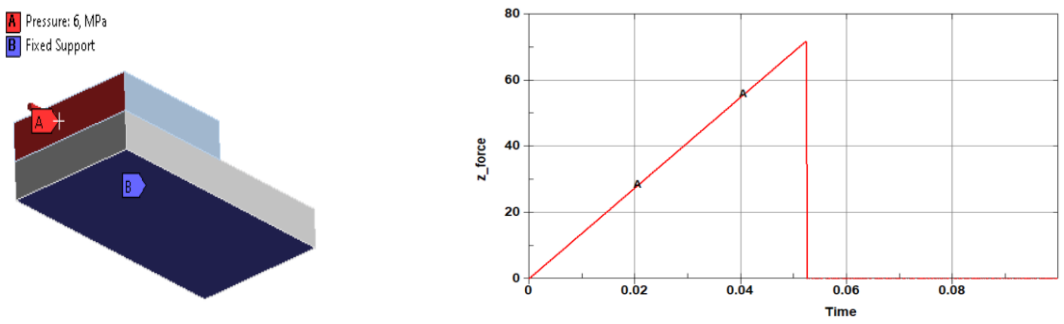

(a) Shear force on a bonded with failure specimen without friction

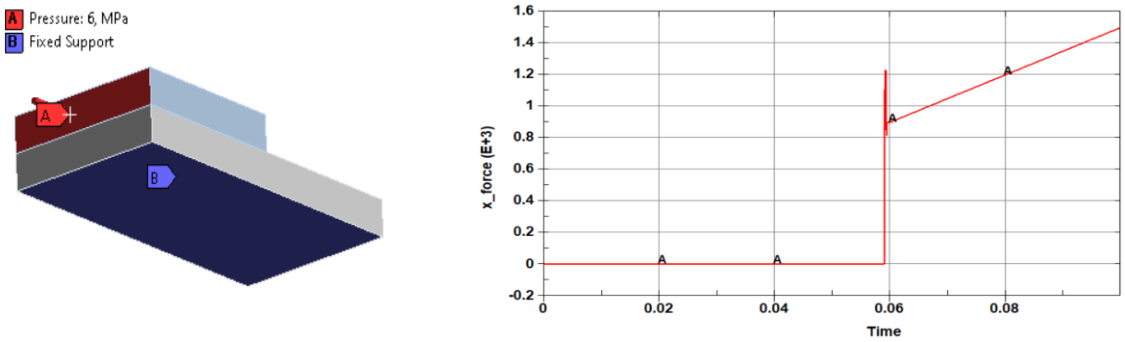

(b) Frictional component

Figure 3.29 Behavior of different types of contacts.

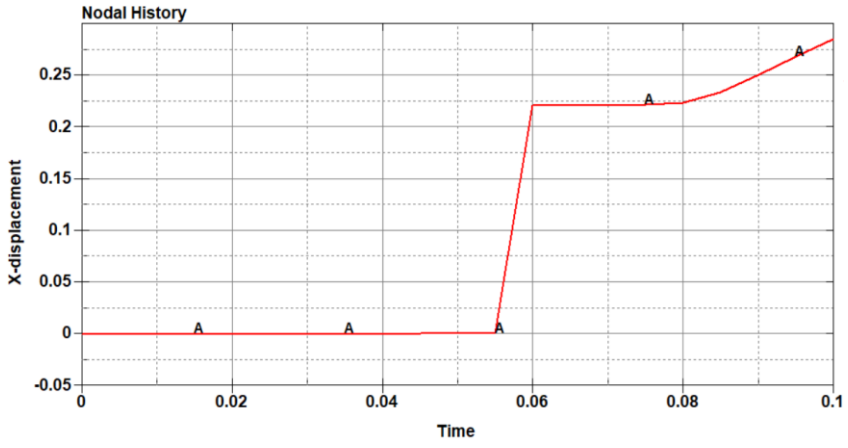

Figure 3.30 Overall behavior of bonded with friction.

Boundary conditions

The extremes of the vertical column were fixed, as shown in Figure 3.31.

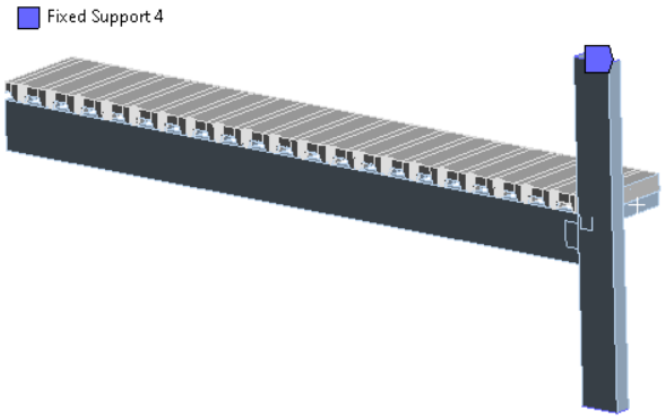

Figure 3.31 Boundary conditions.

Symmetry conditions were defined in the planes shown in Figures 3.32 and 3.33.

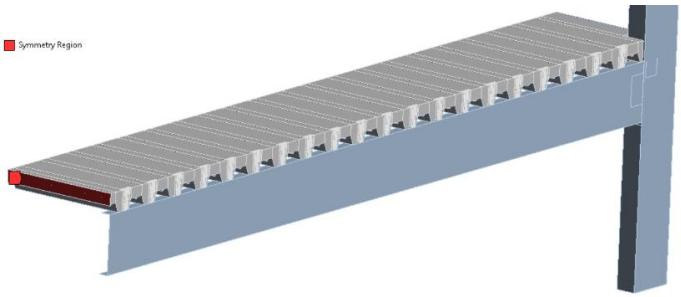

Figure 3.32 Transverse symmetry condition.

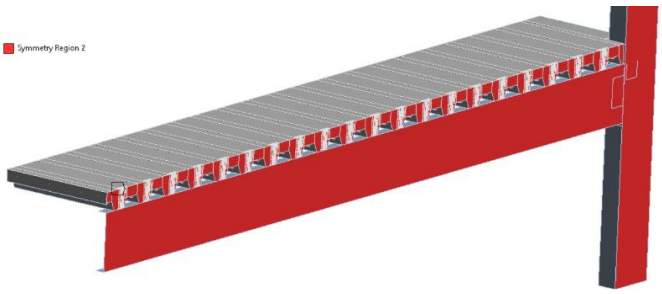

Figure 3.33 Longitudinal symmetry condition.

The boundary conditions that were used in the pushout tests models are shown in Figure 3.34. For the one-stud model (Figure 3.34(a)), in order to compare with the results of El-Lobody and Lam (2003), the top of the slab is fixed, the load is applied at the bottom of the beam (x-direction), and

the load and deformation are measured. This is an unusual set of boundary conditions, and this needs to be kept in mind when assessing the results. The stud was placed in the middle and the deck rib was ignored. In addition to this one-to-one comparison, the stud was also placed in the strong position and the deck rib was modeled explicitly; the El-Lobody and Lam model had the stud at the middle of the through and a flat deck configuration.

For the two-stud configuration (Figure 3.34.b), one stud is in a strong position and one in a weak position, and all deck ribs are modeled. In this case, the bottom of the beam is fixed and the load is applied as a uniform load on the concrete surface.

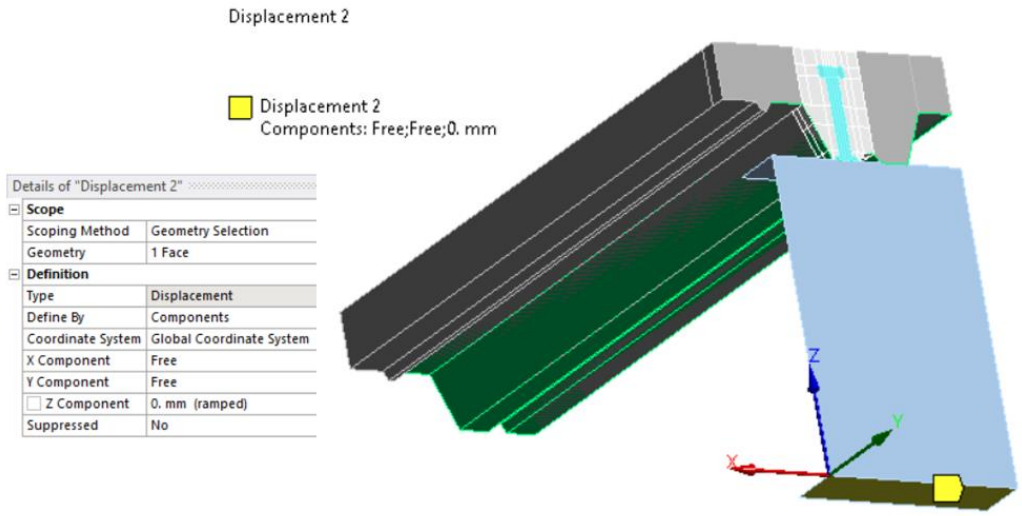

(a) One-stud

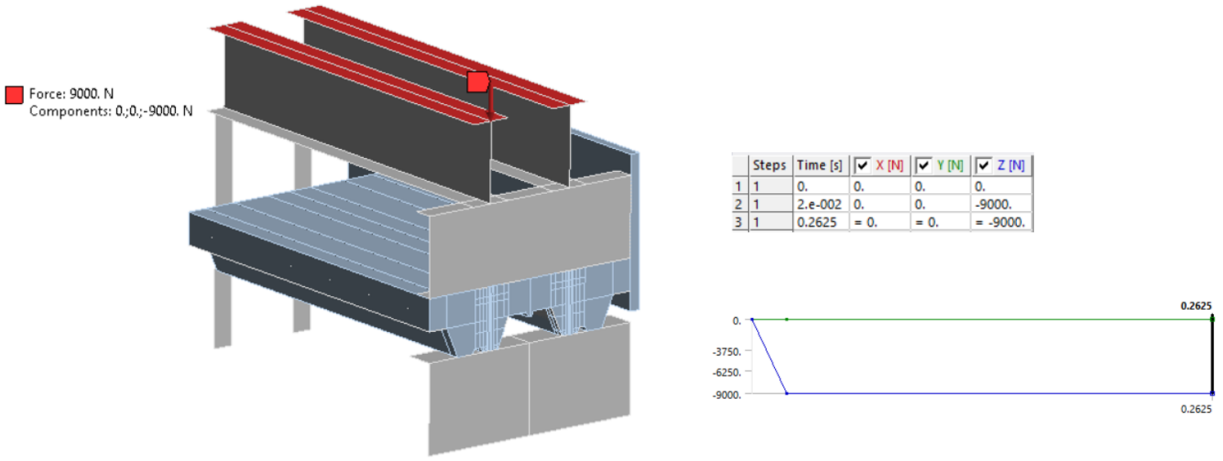

(b) Two-studs

Figure 3.34 Longitudinal symmetry condition.

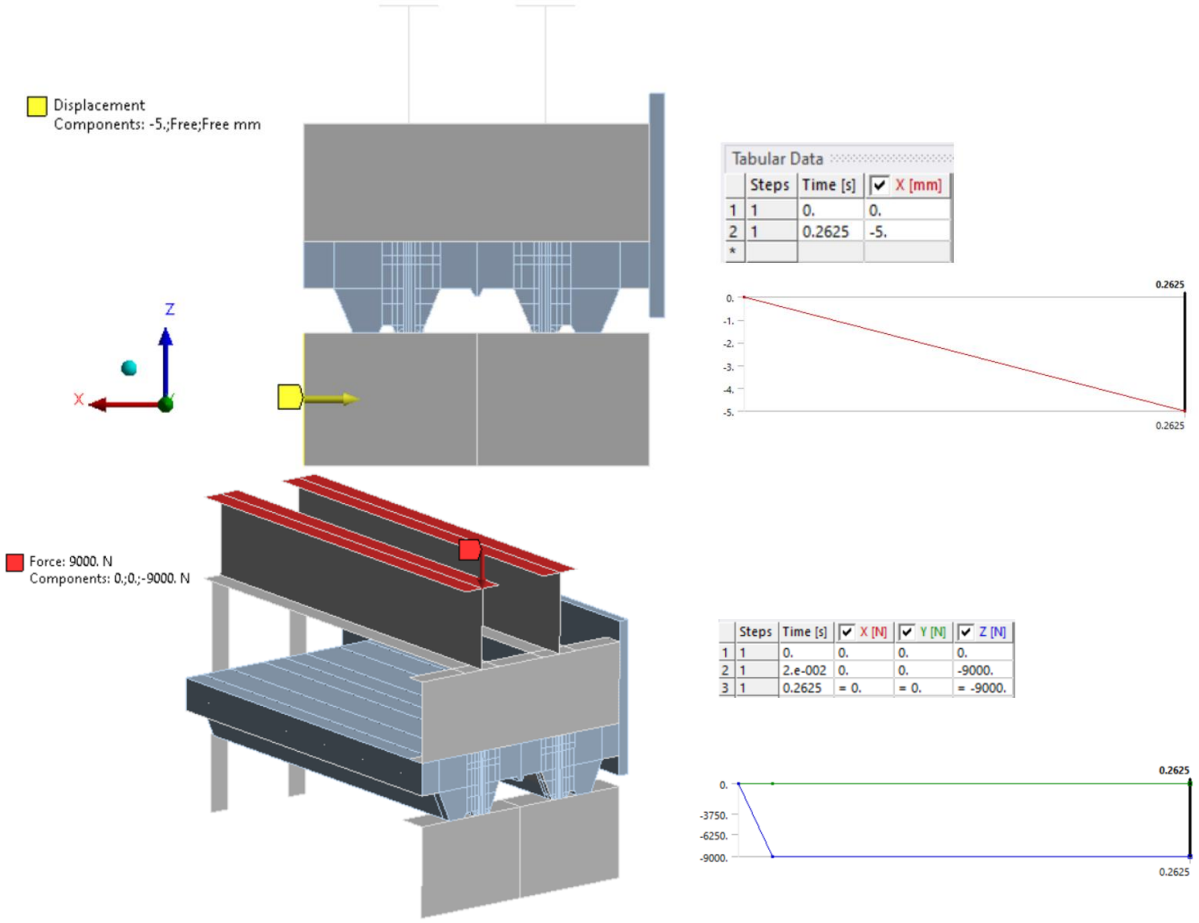

(b) Two-studs

Figure 3.34 Continued.

3.5.3.3 Loading scenario

Six-point loads of equal magnitude were applied along the longitudinal axis of the model to model a uniformly distributed load (Fig. 3.35). In our case, as we are taking advantage of the symmetry of the model, only 3 are used as shown in the Figure 3.36. Note that NIST researchers conducted a series of pre-test load runs to determine the influence of the change in inclination of the loading system (Figure 3.35) as the beam deflected. During the test, they monitored the loads through a set of strain gages (blue rectangles in Figure 3.35) and determined the actual loads applied through equilibrium equations. The loads were applied by sets of two actuators at each of the top of the triangular trusses; one actuator was in load control and the other in deflection control to eliminate any out-of-plane rotation.

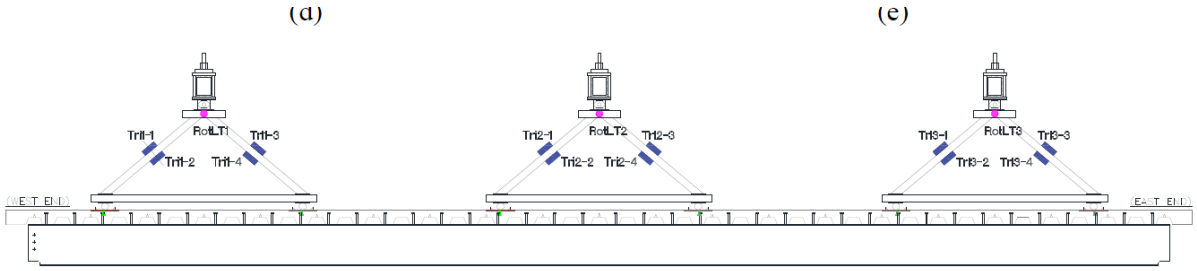

Figure 3.35 NIST loading system.

Figure 3.36 shows the applied loads for the pushout test models. The application of the load in the model of one-stud (Figure 3.37.a) at the bottom of the beam was made to represent the same behavior of the experimental evaluation carried out by Lam and El-Lobody (Lam and El-Lobody, 2005). For its part, the application of the load in the two-stud model (Figure 3.37.b) was made in order to observe the influence of the position of the studs subjected to a pure shear force. Note that a very thin rubber pad is present at the support of the concrete slab (left on upper left portion of Figure 3.37) o minimize stress concentration effects.

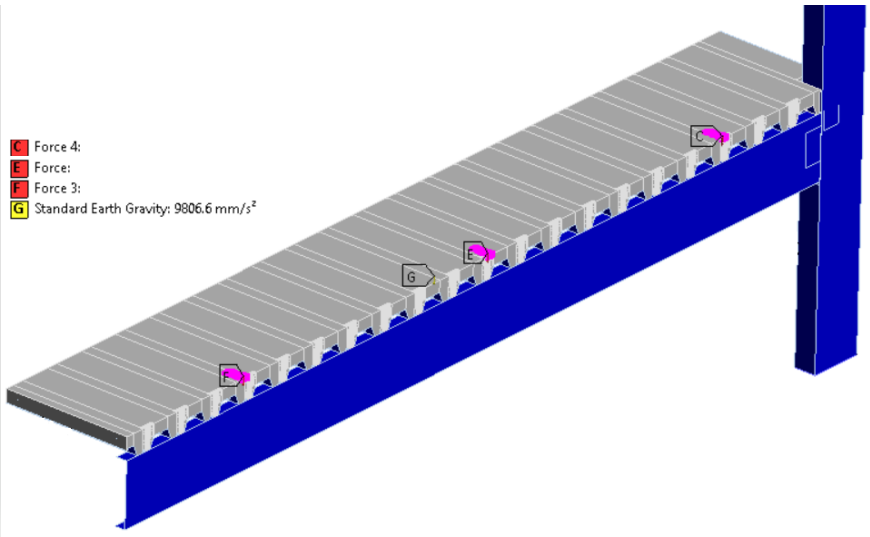

Figure 3.36 Loads applied to the model

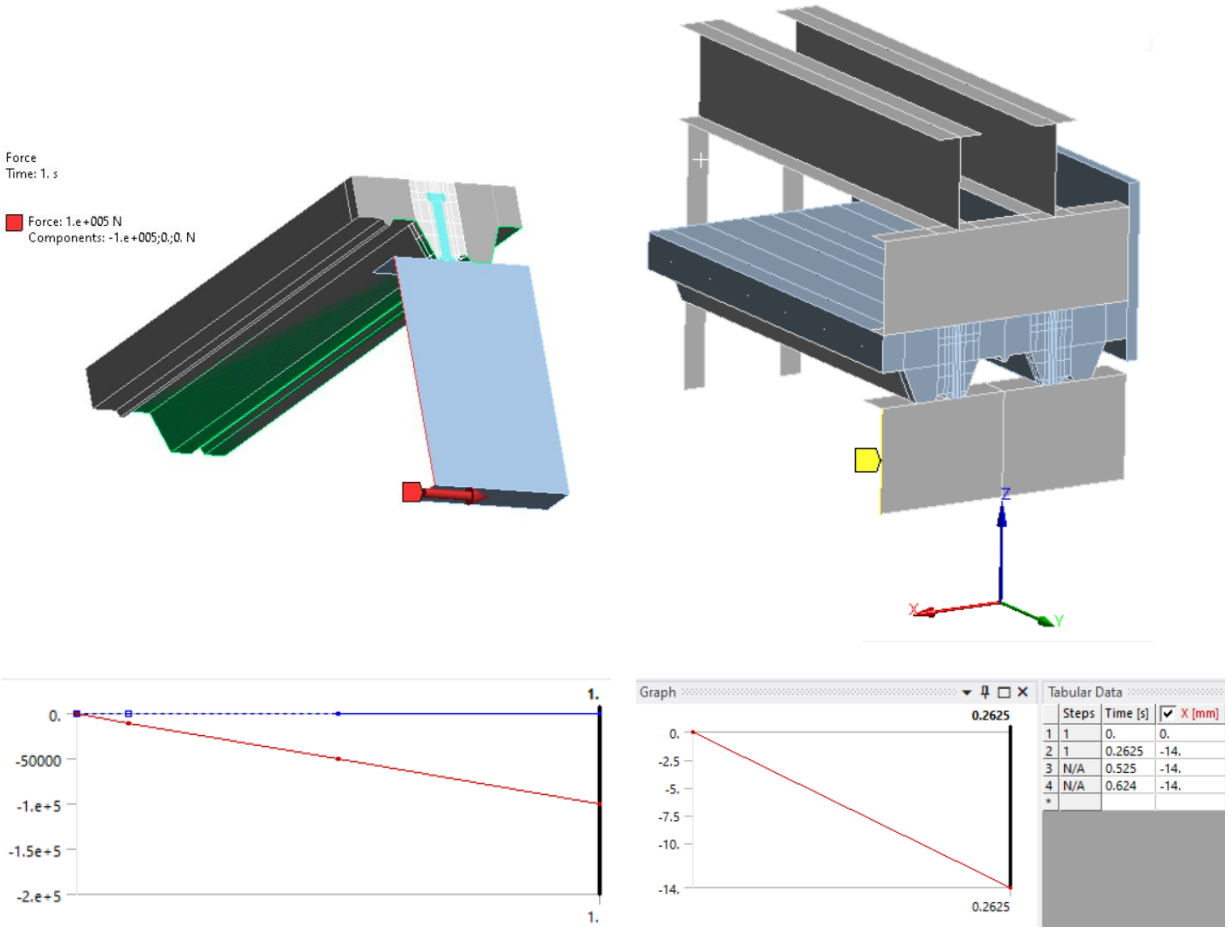

(a) One-stud (b) Two-studs

Figure 3.37 Loads applied to the pushout model.

3.5.4 Material models

3.5.4.1 Concrete

Concrete is a very complex material to model, even assuming that it is an isotropic material before cracking. In order to adequately represent the nonlinear behavior of the concrete slab, the material model MAT_72R3 (Malvar et al., 1997) is used. This model appropriately incorporates material behavior along multiple radial paths in space such as uniaxial, biaxial, and triaxial tension and compression (Figure 3.38). The model uses three shear failure surfaces and includes damage rate and strain rate effects. The advantage of the MAT_72R3 concrete material model is that the complex behavior of concrete can be modeled by specifying only the uniaxial unconfined compressive strength when detailed stress-strain data is not available for concrete materials. The unconfined compressive strength parameter describes not only the elastic response, but also the

inelastic (plastic) response that includes shear failure envelope, compressibility (compaction), and tensile failure. Obviously, a single parameter cannot accurately characterize all aspects of all concretes. However, it is practical to have a concrete material model available to the analyst that requires minimal input but provides a robust representation of the many response characteristics of this complex material, including damage and failure.

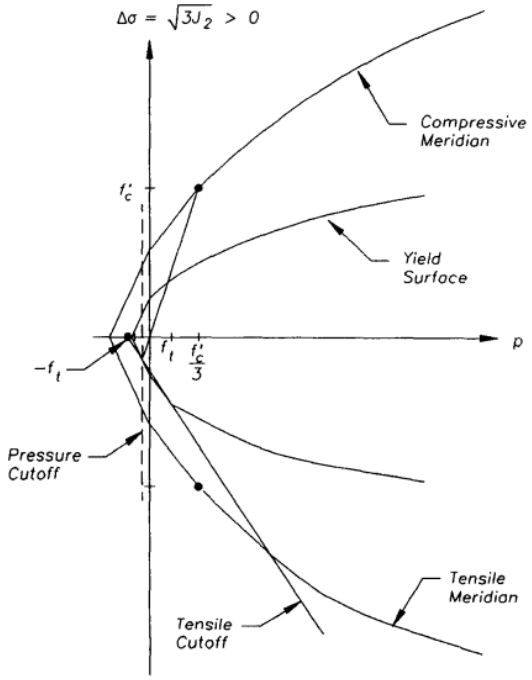

Figure 3.38 Failure surfaces in the Malvar model (Malvar et al., 1997)

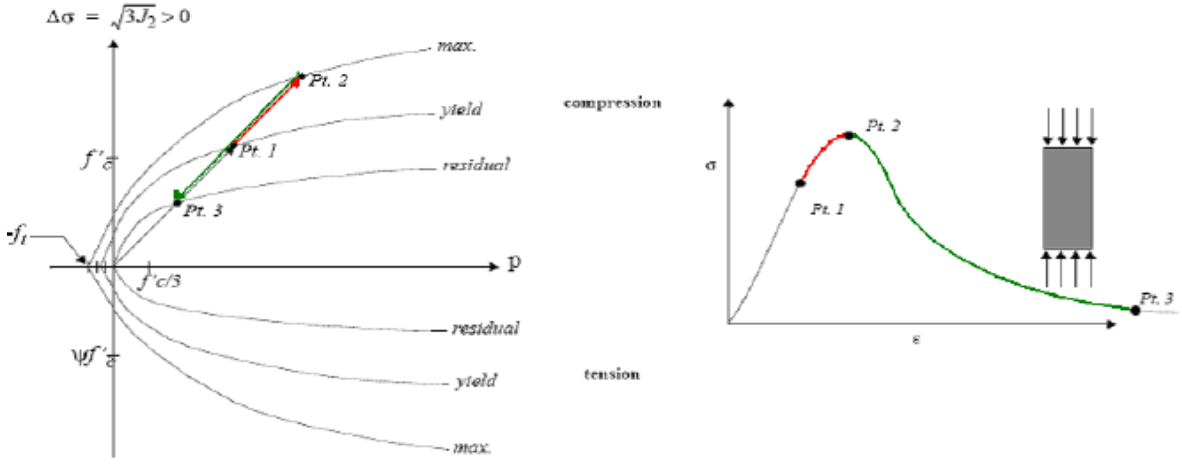

(a) Failure surfaces in concrete damage material model; (b) Concrete constitutive behavior

Figure 3.39 Failure surfaces in concrete damage material model. (Markovich et al., 2009)

For purposes of evaluating concrete damage in this chapter, we will proceed as described by Markovich et al. (Markovich et al., 2009) and shown in Figure 3.39:

- The material response is considered linear up to point 1 (Pt.1), the first yield, the path shown in grey in Figure 1 (b). After yielding, a hardening plasticity response occurs until point 2 (Pt.2), the maximum strength, is reached (red). After reaching the maximum strength, softening occurs until a residual strength (Pt.3), which depends on the amount of confinement, is obtained, (green). The higher the amount of confinement pressure applied on a specimen, the higher the maximum and residual strengths become.

- After the stress reaches the initial yield surface and before reaching the maximum failure surface, the stress is calculated as a linear interpolation between the two see Figure 3.38.b (a):

$$\Delta\sigma = n\left(\Delta\sigma_{\mathrm{m}} - \Delta\sigma_{\mathrm{y}}\right) + \Delta\sigma_{\mathrm{y}} \qquad (3.3)$$

- After reaching the maximum failure surface, the current failure is similarly interpolated between the maximum and the residual stresses:

$$\Delta\sigma = n(\Delta\sigma_{\mathrm{m}} - \Delta\sigma_{\mathrm{r}}) + \Delta\sigma_{\mathrm{r}} \qquad (3.4)$$

where η, parameter indicating the relative location of the current failure surface, varies between 0 and 1, and depends on the accumulated effective plastic strain parameter λ. The value η equals 0 when λ= 0; this is the initial value of η before any plasticity has occurred Then, when η = 1 at some value λ=λm the meaning is that the maximum failure surface has been reached. Finally, when reduces to η = 0 at some larger value of η the residual failure surface is reached. This would permit Δσ sequentially to take on the values Δσy, Δσm and Δσy. These ranges of the parameters η and λ are summarized in the following table, where λend is some large value of λ.

Table 3.1 Damage Evaluation (Markovich et al., 2009)

η	λ	Current position
$0 \le \eta < 1$	$0 \le \lambda < \lambda_m$	Between yield failure surface to maximum failure surface
η=1	$\lambda = \lambda_m$	On maximum failure surface
$0 < \eta \le 1$	$\lambda_m < \lambda \le \lambda_{end}$	Between maximum failure surface to residual failure surface

Figure 3.40 shows the variable η as a function of λ/λm., It can be seen that the slope of the curve can be used to determine the state of the material. A negative slope indicates that the material is suffering damage. Values of the slope close to zero are reached close to the maximum stress of the material or once the residual stress has been reached. The η vs λ slope, is registered in the LS-

Dyna results as history variable 5. Figure 3.41 shows the values used in the analysis by LS-Dyna for this material.

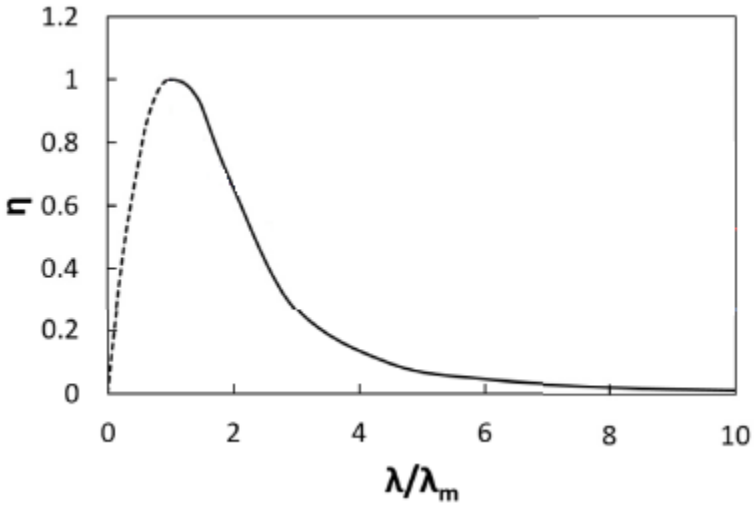

Figure 3.40 (Modified from Lee et al. (Lee et al., 2021))

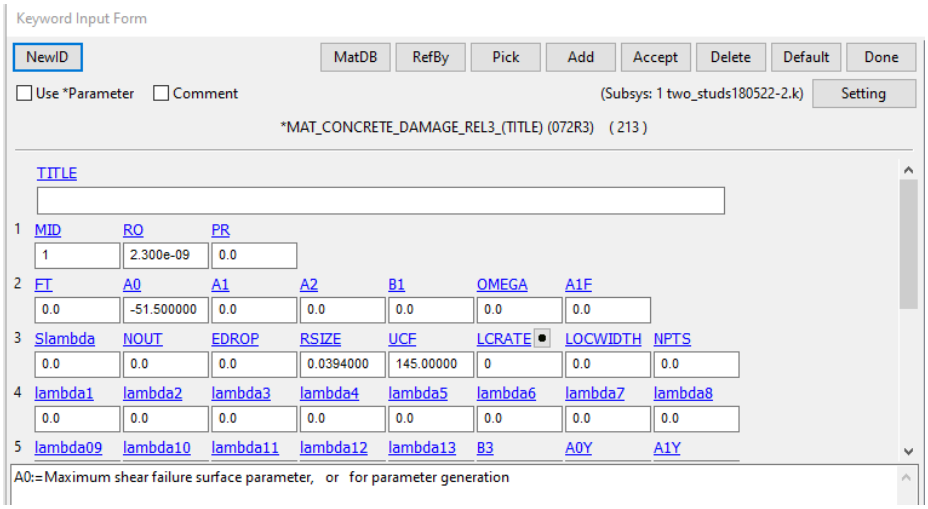

Figure 3.41 Definition of the material model MAT_72R3.

Figure 3.42 shows the behavior of the model with different confinement conditions (0 MPa, 15 MPa and 30MPa lateral pressures). For these cases a uniform pressure was applied first and then one direction only was increased.

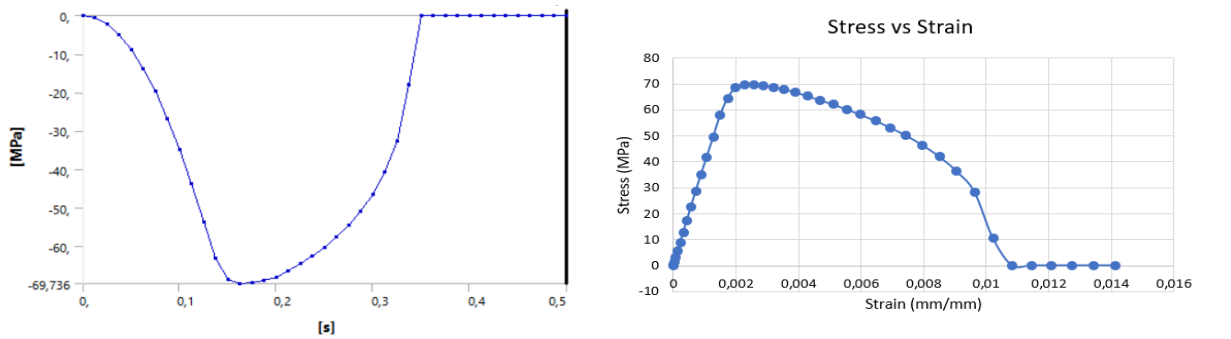

(a) Lateral Pressure = 0 MPa

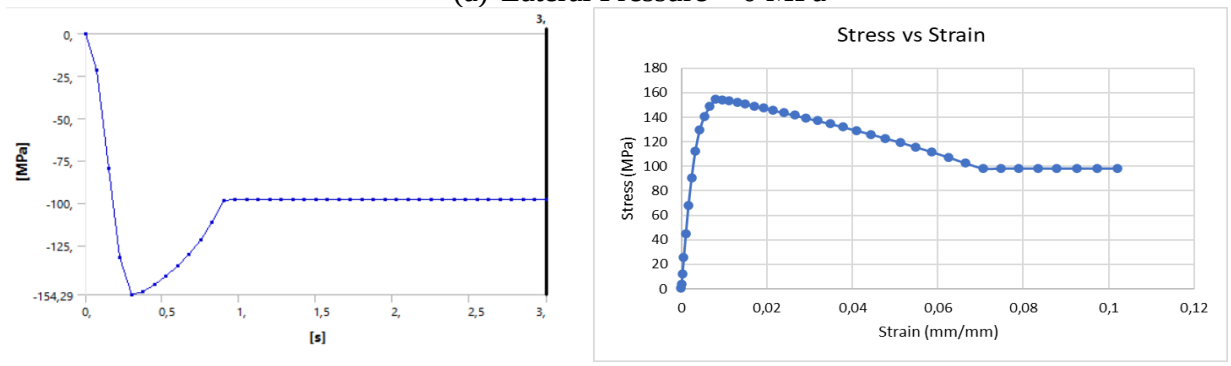

(b) Lateral Pressure = 15 MPa

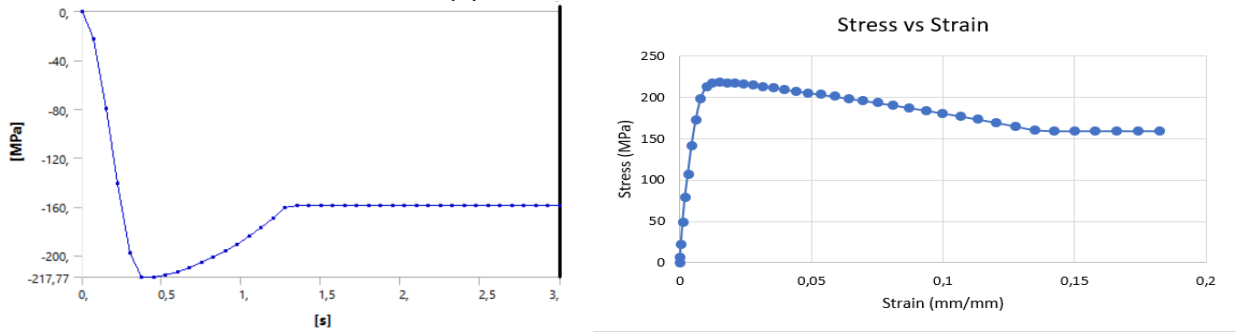

(c) Lateral Pressure = 30 MPa

Figure 3.42 Effect of confining pressure on Malvar concrete model.

Figure 3.43.a shows a plot of the stress difference vs. mean stress for this material model in LS-Dyna. Figure 3.33a shows the values for this research with a concrete of 70MPa, while Figure 3.43.b shows the results for Malvar for a concrete of 45MPa. There is very good agreement between the results of the Malvar model and the experimental ones.

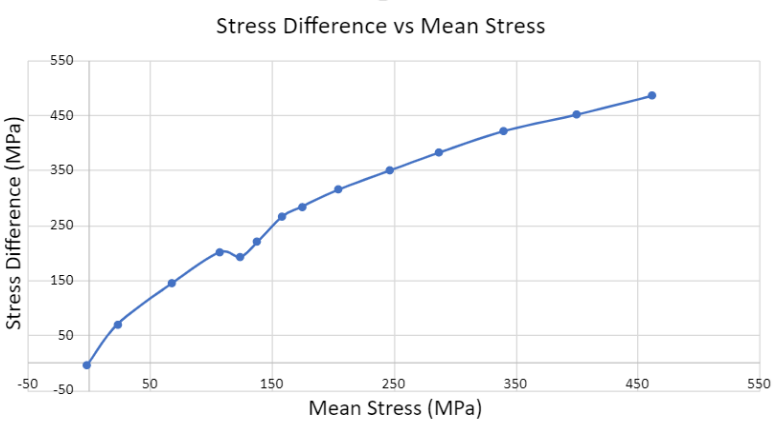

(a) This research

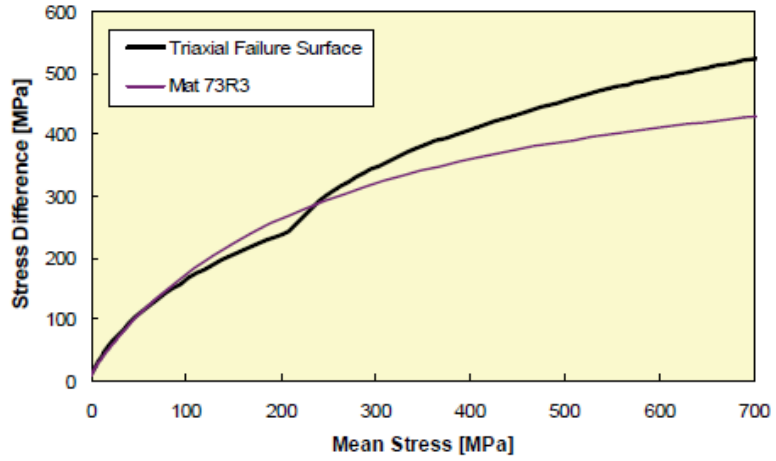

Figure 4 Comparison of laboratory and default Mat 72R3 triaxial compression failure surface of for a 45.6 MPa concrete.

(b) Schwer and Malvar (2005)

Figure 3.43 Stress difference vs. mean stress for different mean stresses.

3.5.4.2 Structural Steel

The multilinear isotropic hardening material model is used as all the material parameters required for the steel deck, beam, shear stud and welded wire fabric were available. The input data for the multilinear isotropic hardening model are the real stress vs. plastic strain; for this reason, the maximum elastic strains must be subtracted from all post-yield strains, resulting in Figure 3.44.

It is important to note that the material of the shear stud is of great importance in the modeling of the shear interface between the steel beam and the concrete slab, since the region around the shear stud is a region of severe and complex stresses. Shear forces are transferred across the steel beam-concrete slab interface by the mechanical action of shear studs.

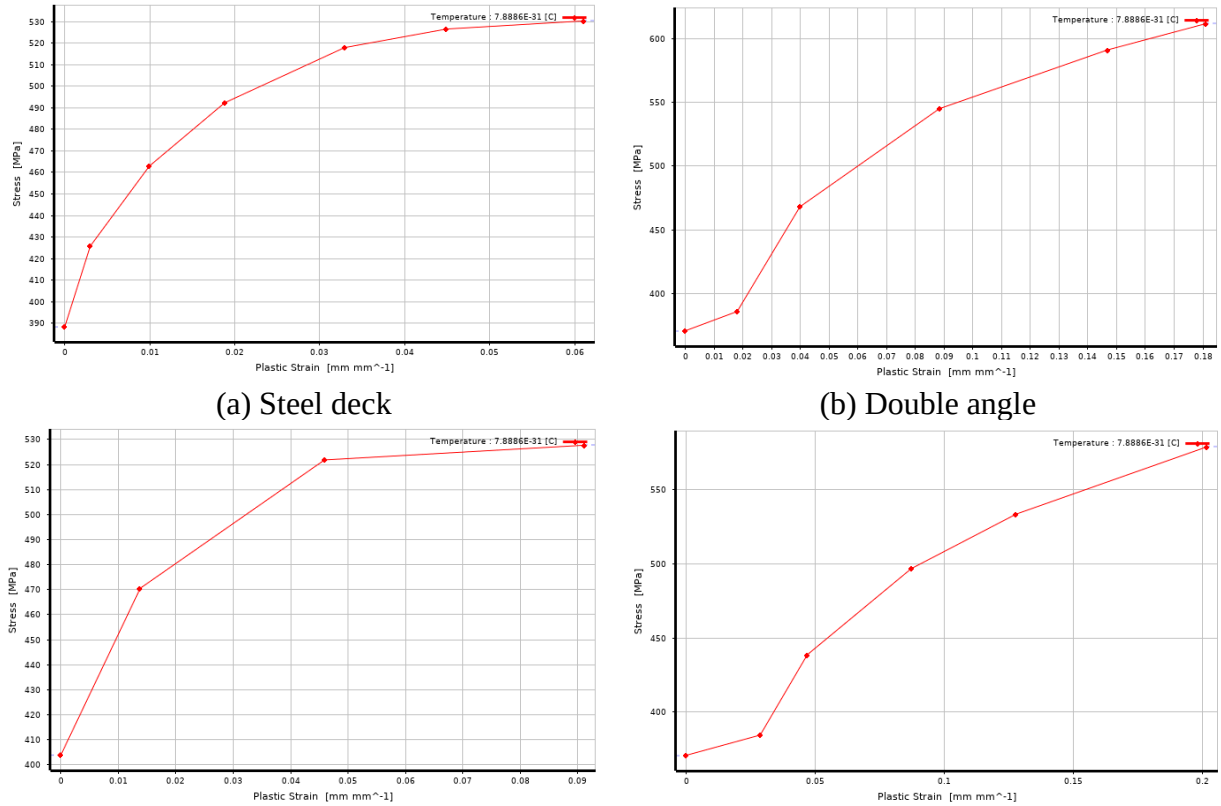

(a) Steel deck (b) Double angle

(c) Shear stud (d) Beam

Figure 3.44 Steel stress-strain curves - multilinear isotropic hardening material model.

3.6. Results

3.6.1 Pushout test

The pushout analyses consisted of:

(1) verification runs to compare the results of the one-stud model with those of El-Lobody and Lam (El-Lobody and Lam, 2003), including standalone comparisons and ones with the stud in the weak and strong position (Figure 3.33), and

(2) a series of runs of the two-stud model with the studs in different strong-weak positions to assess the influence of the position (see Figure 3.34).

Figure 3.45 shows the contours of the history variable 5 for concrete(see Section 3.5.4.1), showing regions with values less than or close to one that indicate the presence of damage to the material. As shown in Figure 3.45(a) for the case of the stud embedded in solid concrete (standalone case), the non-linear behavior of the system begins at a load of about 110 kN, with a damaged cone appearing in the concrete around the shear stud. Figure 3.45(b) shows the post-yielding behavior, with the system near its ultimate strength. The damage has spread, in a narrow strip, throughout all the concrete in front of the stud.

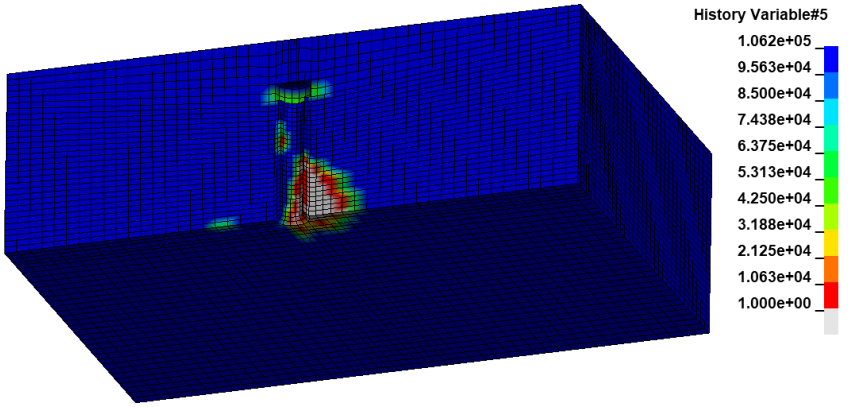

(a) P = 110 kN

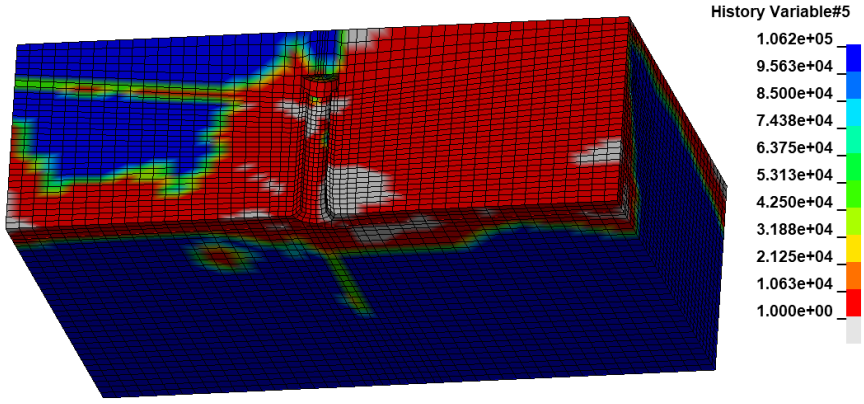

(b) P = 125 kN

Figure 3.45 Stress contours for stud embedded in a solid slab.

Figure 4.46.a shows the Von Misses stress contour and their respective strains in the steel. It can be seen that for a 125 kN force, large stresses are observed in the shaft of the stud as well as steel-concrete contact failures. Figure 4.46.b shows the effective plastic strain when the maximum values is close to 5%, indicating a plastic hinge at the top of the weld, with a strong shear deformation pattern.

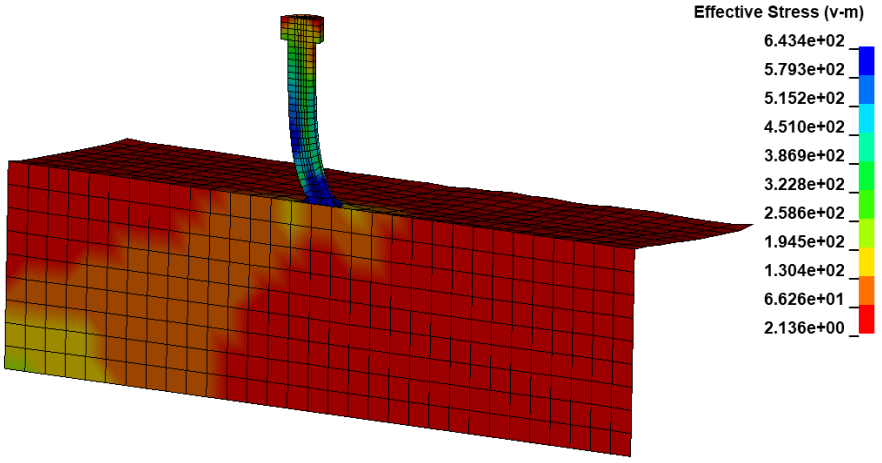

(a) Von Misses stress contour

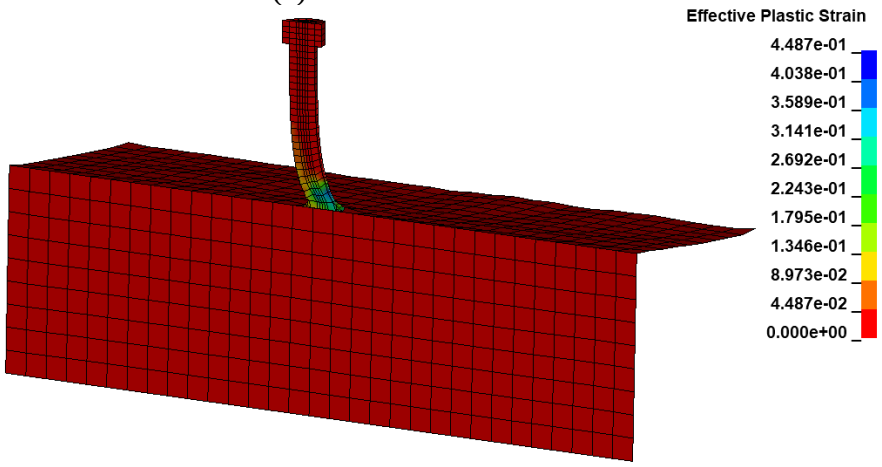

Effective plastic deformation

Figure 3.46 Stress contours and deformed shapes

Figure 3.47 shows the comparison of the one-stud model with the experimental results obtained by Lam and El-Lobody (Lam and El-Lobody, 2005). It is clearly observed that the ultimate stiffness and strength of the stud model considering the NIST (NIST Technical Note 254-2019) geometric configuration is consistent with the experimental results of Lam and El-Lobody (Lam and El-Lobody, 2005). However, a small difference is observed between the loads of both models (about 5%). This may be due to many factors such as the type of welding, definition of the contact resistance in the stud, beam, steel deck, residual stresses, and others.

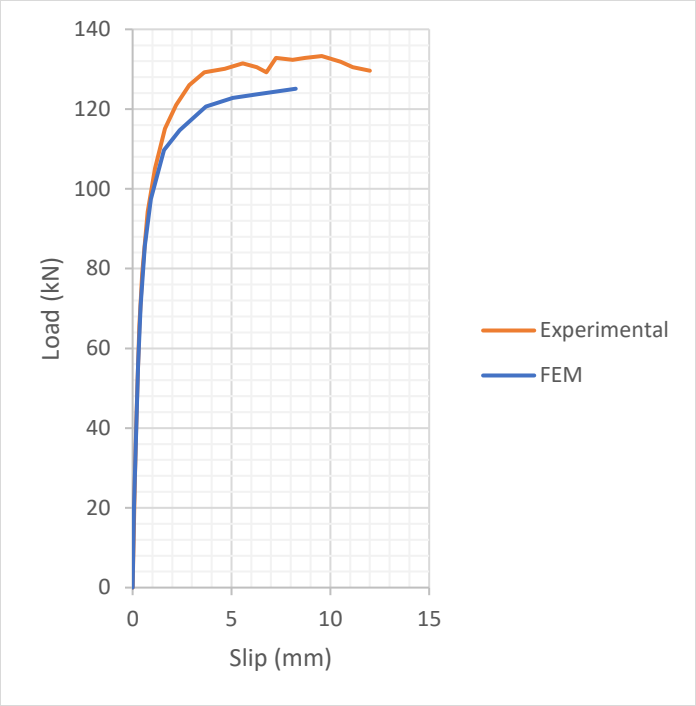

Figure 3.47 Comparison between pushout model and experimental results

Figure 3.48 shows the force-slip behavior of each of the models studied in this chapter. It can be seen that the curves vary substantially depending on the position of the shear studs, which shows the importance of the position of the studs in the global behavior of these structural systems.

The TS-I model (Figure 3.48.a) indicates that the maximum resistance is 105 kN and, from a 1mm slip the system, the stud presents a non-linear behavior. The TS-II.a model (Figure 3.48.b, weak position)) reaches a maximum resistance of 70 kN and its non-linear behavior begins at a displacement of 2mm. For models TS-II.b (strong), TS-III and TS-IV (Figure 3.48.c-e) the maximum resistances are 127 kN, 87kN and 97kN, while the non-linear behavior of each of them starts at 1.3 mm , 1.9 mm and 1.20, respectively.

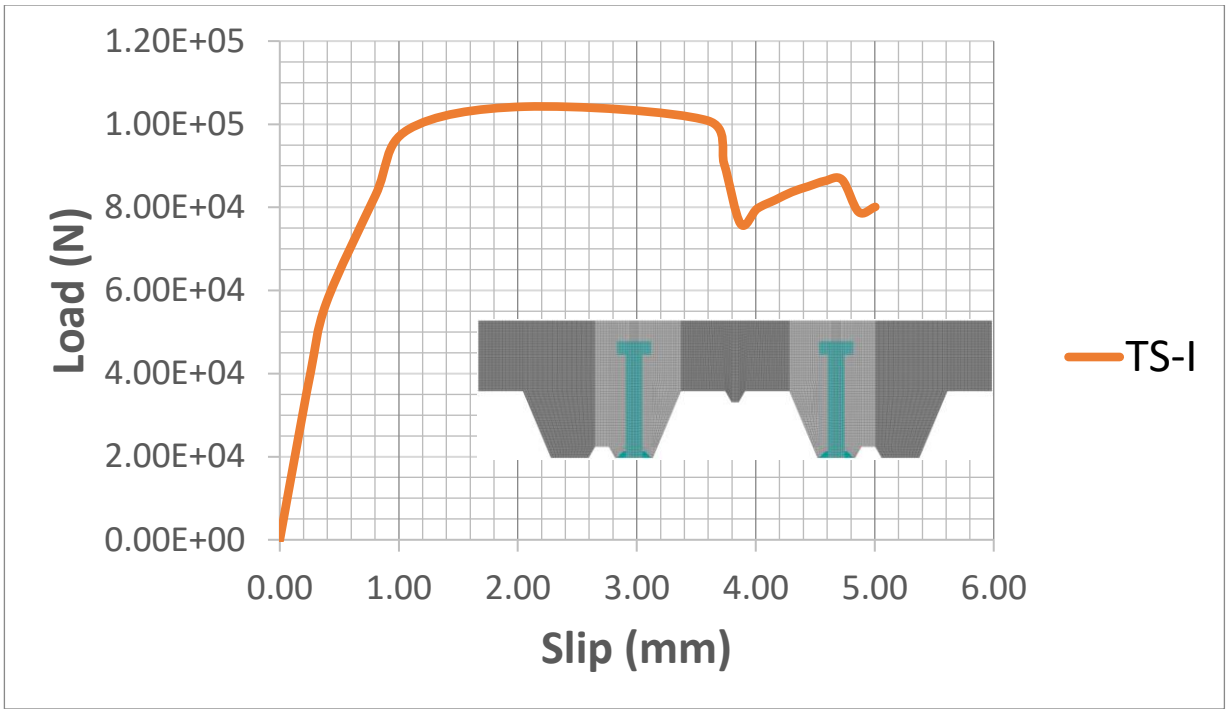

(a) Model TS-I

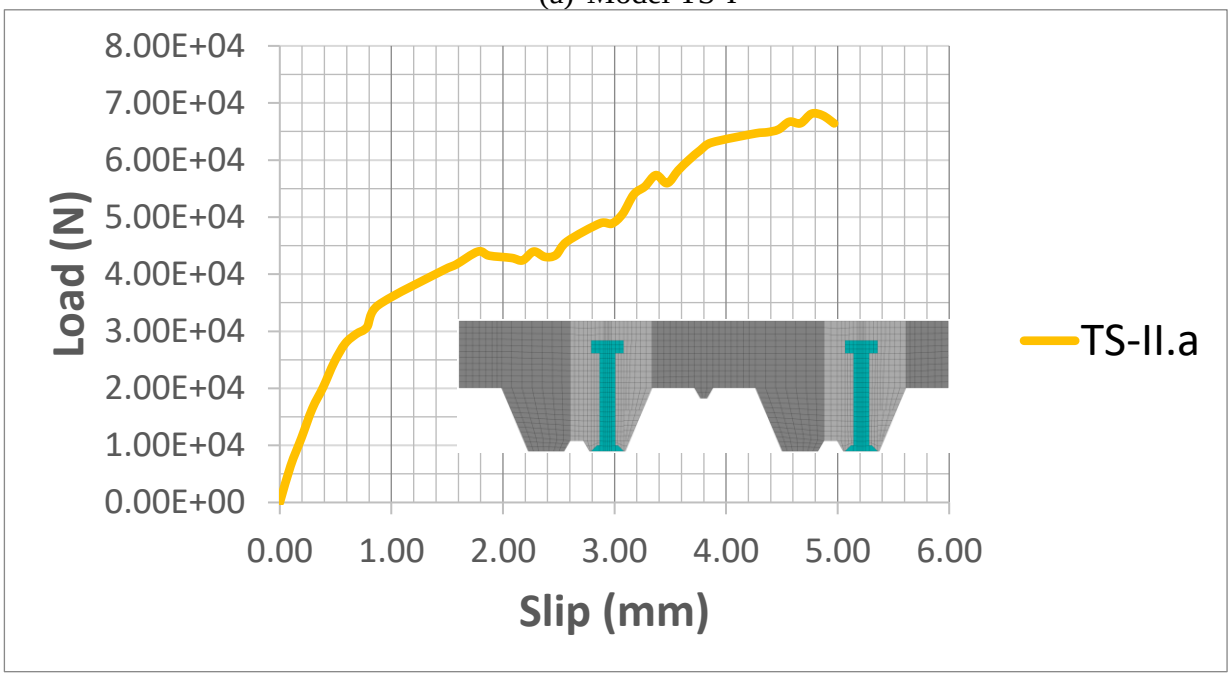

(b) Model TS-II.a

Figure 3.48 Force vs Slip Curves.

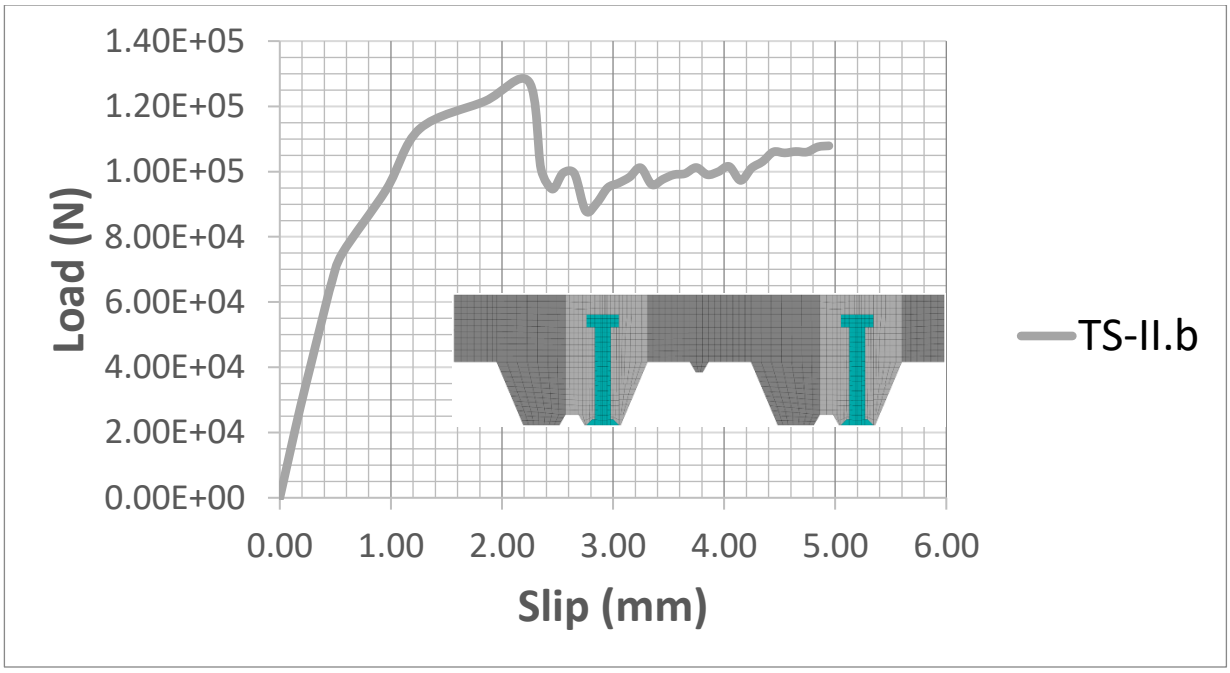

(c) Model TS-II.b

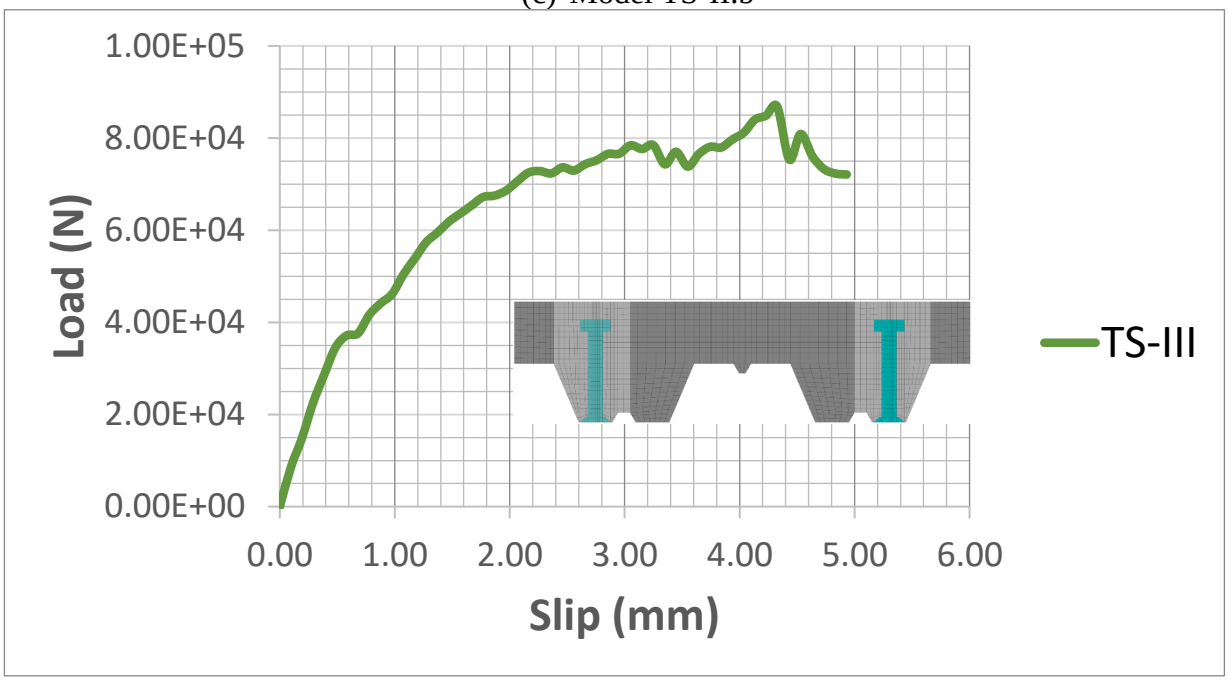

(d) Model TS-III

Figure 3.48 Force vs Slip Curves (continued).

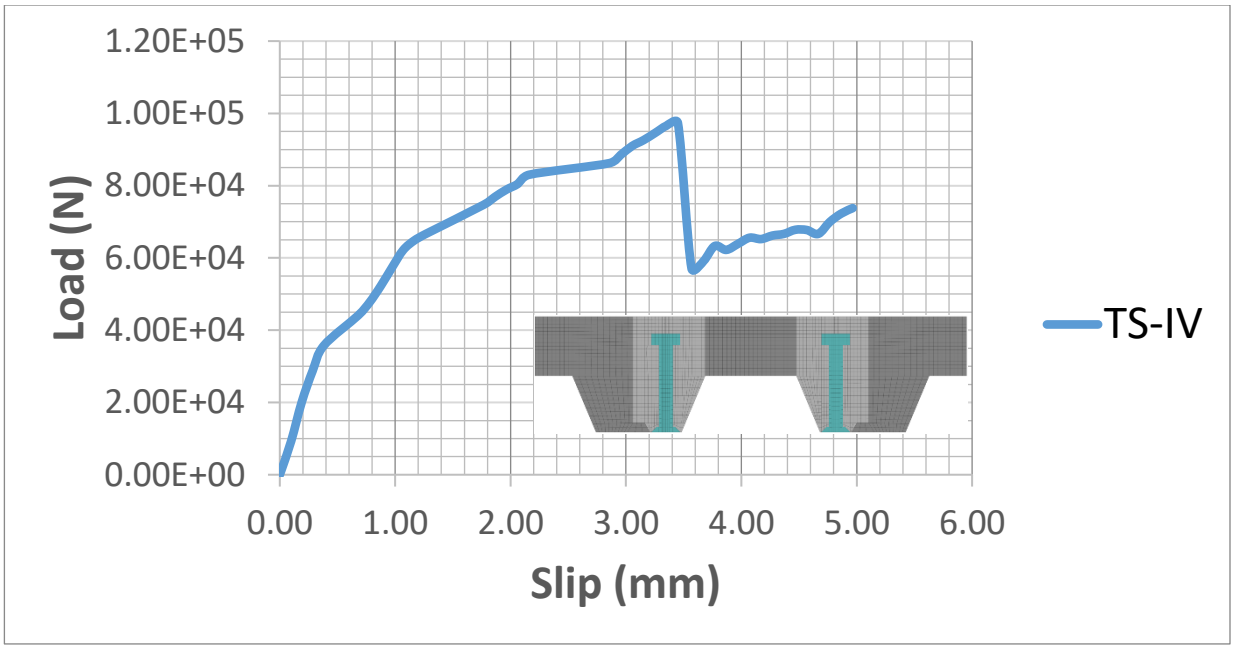

(e) Model TS-III

Figure 3.48 Force vs Slip Curves (continued).

Next, we will proceed to show the results of each of the pushout tests. For a better illustration and understanding of the results, an isometric view of each analyzed model will be shown first and then the results will be shown for the conditions of 25%, 50%, 75% and 100% of the imposed displacement, which has a value maximum of 5 mm. The LS and RS nomenclature is used to refer to the left shear stud and the right shear stud, respectively.

We start with the TS-I model (Figure 3.49). Figure 3.49.a illustrates the behavior for a displacement of UX = 1.25, for this displacement condition the shear stud does not suffer plastic deformation (Figure 3.49.a-1), however cone-shaped damage to the concrete begins to be observed, mainly on the right stud (Figure 3.49.a-2). The damage in the upper part of the slab is minor (Figure 3.49.a-3); however, damage is observed in the lower part of the slab, especially in the contact area between the slab and the rubber support (Figure 3.49.a-4).

For a displacement UX = 2.50 mm, very small plastic strains begin to be observed (0.002326 mm/mm) (Figure 3.49.b-1) in both shear studs, and the damage areas in the concrete increase. The entire area surrounding the right shear stud has sustained damage, while the left shear stud has cone-shaped damage (Figure 3.49.b-2). Damage is beginning to be observed in the upper part of the concrete slab (Figure 3.49.b-3) while the lower part has suffered significant damage, especially in the contact area between the slab and the rubber pad (Figure 3.49.b -4).

When the system is subjected to 75% of the imposed displacement (3.75 mm) the very low plastic strains continue, of the order of 0.006 mm/mm (Figure 3.49.c-1), affecting the cross-section of the concrete slab, as well as the upper and lower zones (Figures 3.49.c-2-4).

Finally, when the total displacement imposed (5 mm) is reached, the plastic strain of the shear studs is 0.012 mm/mm (Figure 3.49.d-1), which indicates that for this type of pushout configuration, the shear studs are not subjected to large deformation. Therefore the maximum capacity offered by these elements to the system, in general, are not being used. The concrete suffers significant damage throughout the area affected by the studs (Figure 3.49.d-2-4). Figure 3.50 illustrates the plastic deformation history of the shear stud. The deformation mode and plastic strain contours of the stud, seems to correspond to a bending condition; however, no important geometric changes appear even for a slip magnitude of 5 mm.

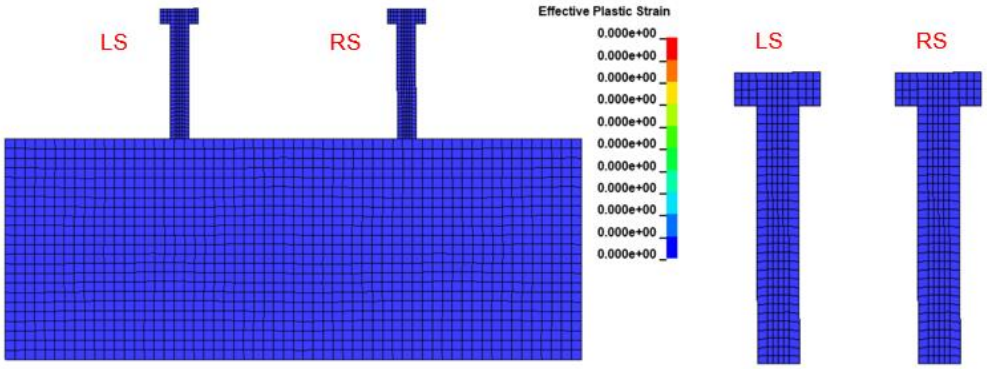

(a-1) Plastic deformation of the shear stud

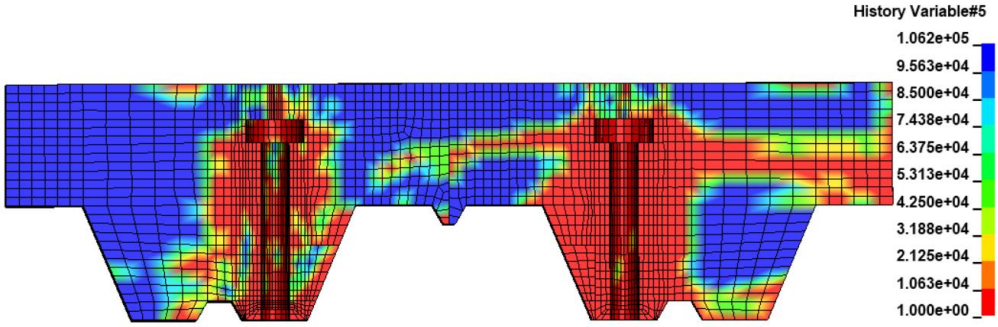

(a-2) Cross-section of the concrete slab

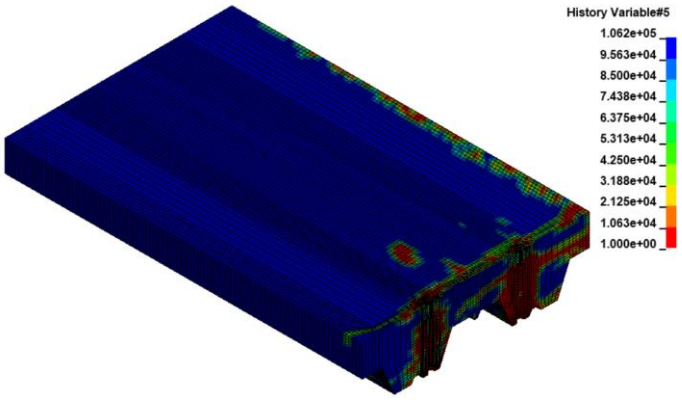

(a-3) Concrete slab top

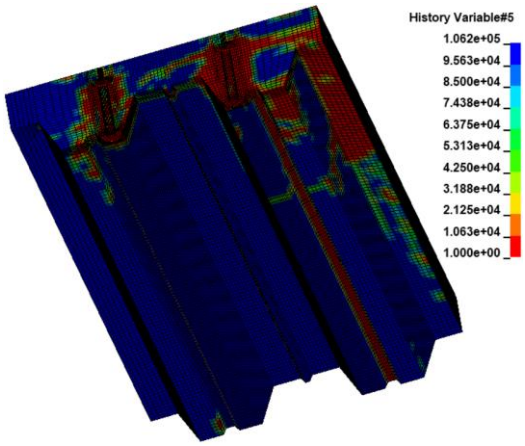

(a-4) Concrete slab bottom

(a) percentage of applied force of 25% (UX = 1.25 mm)

Figure 3.49 Stress contours and deformed shapes.

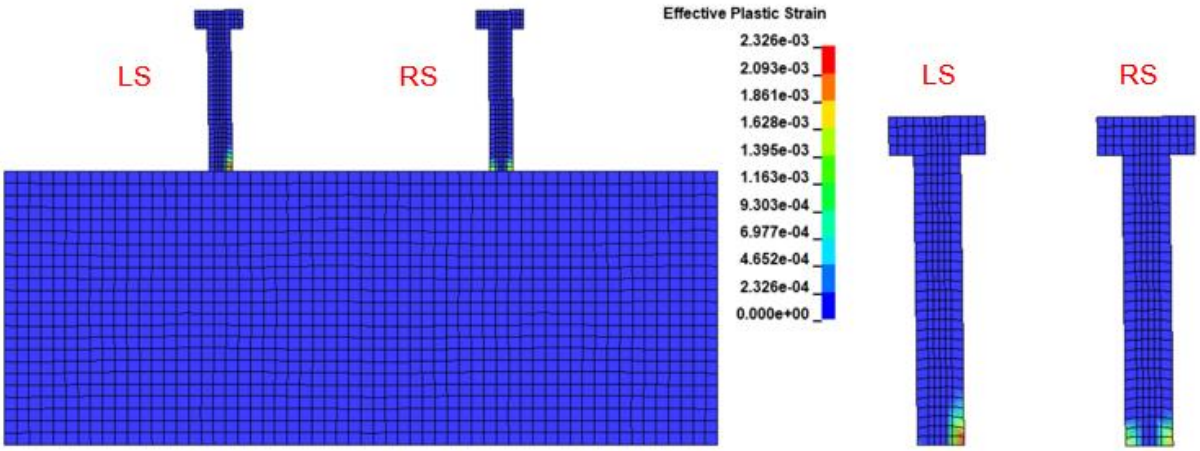

(b-1) Plastic deformation of the shear stud

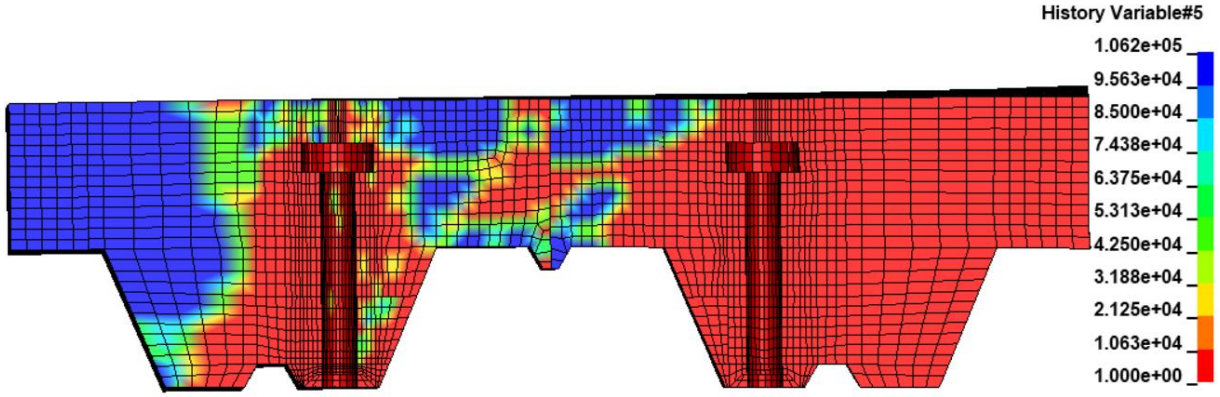

(b-2) Cross-section of the concrete slab

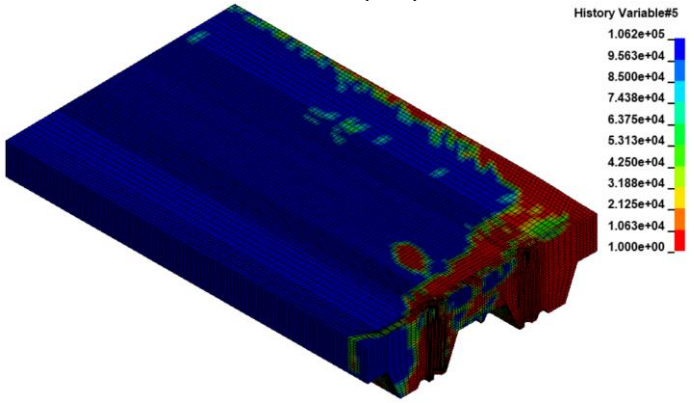

(b-3) Concrete slab top

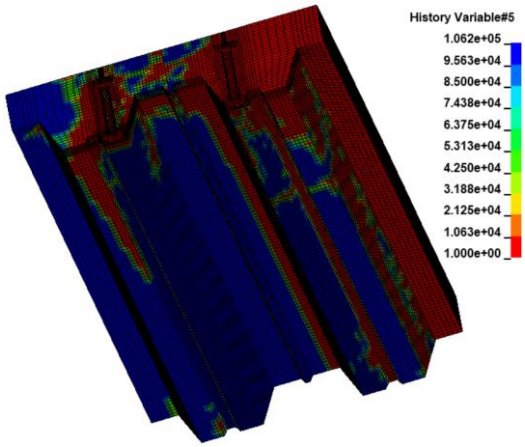

(b-4) Concrete slab bottom

(b) Percentage of applied force of 50% (UX = 2.5 mm)

Figure 3.49 Continued.

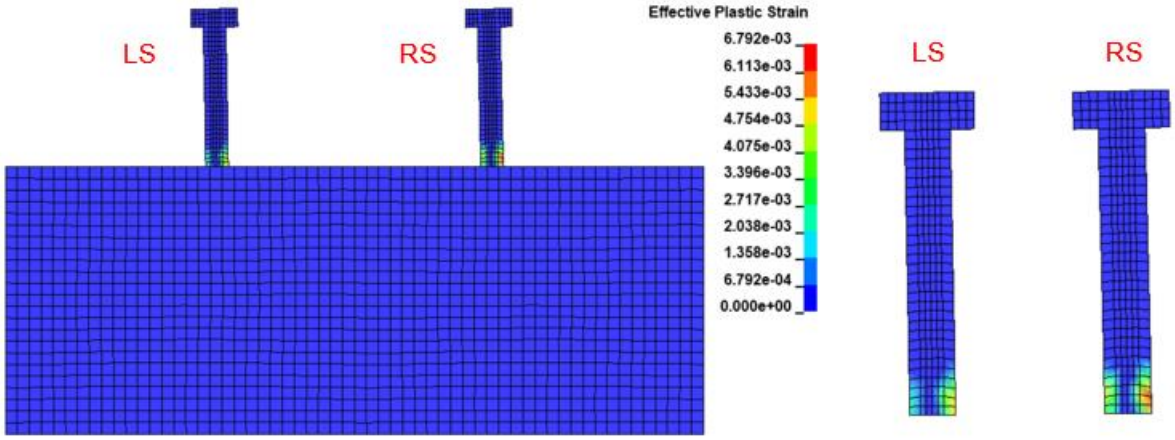

(c-1) Plastic deformation of the shear stud

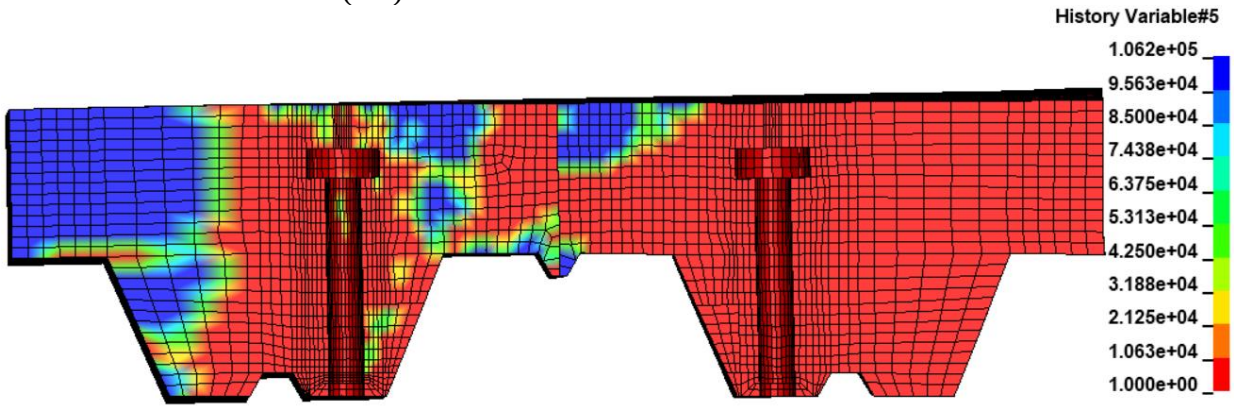

(c-2) Cross-section of the concrete slab

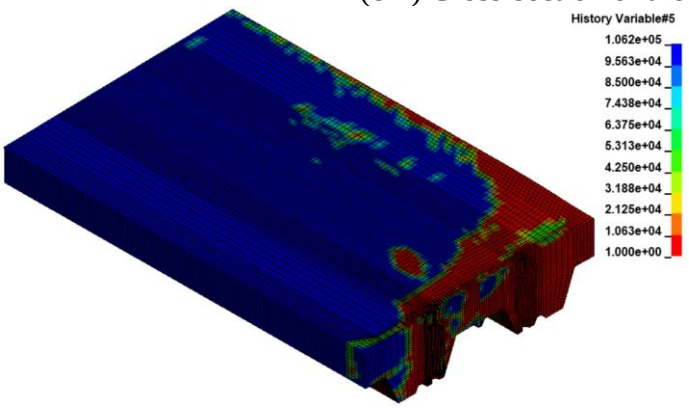

(c-3) Concrete slab top

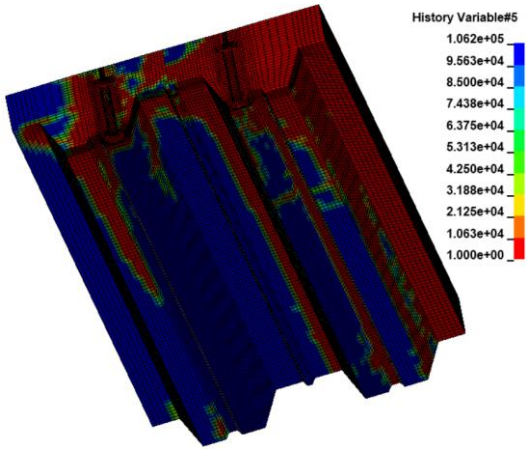

(c-4) Concrete slab bottom

(c) Percentage of applied force of 75% (UX = 3.75 mm)

Figure 3.49 Continued.

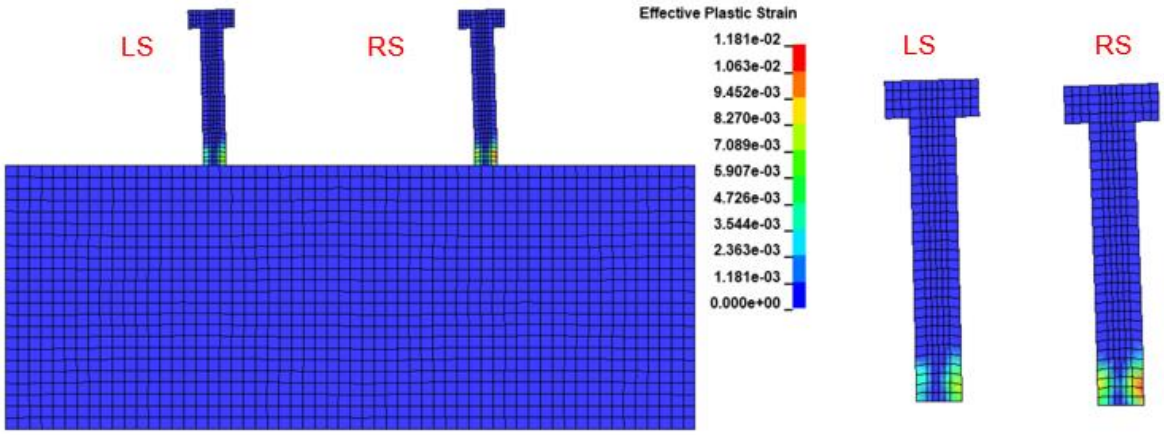

(d-1) Plastic deformation of the shear stud

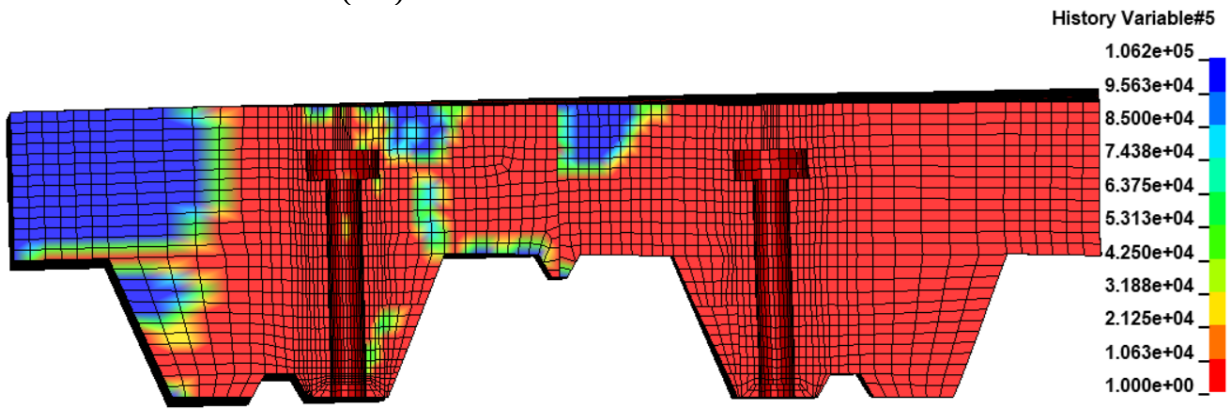

(d-2) Cross-section of the concrete slab

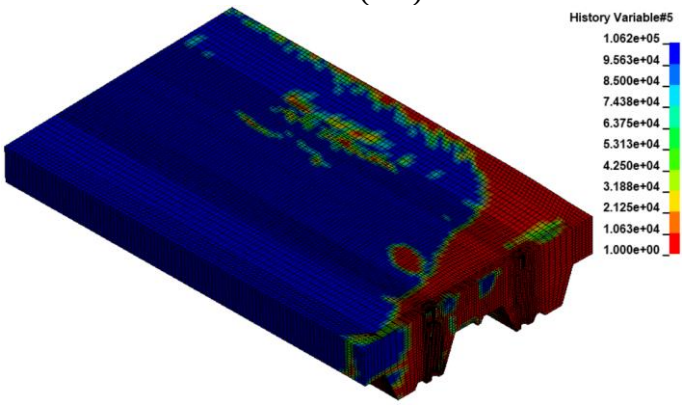

(d-3) Concrete slab top

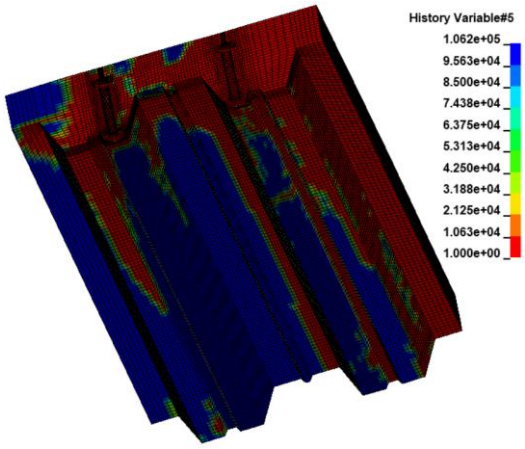

(d-4) Concrete slab bottom

(d) Percentage of applied force of 100% (UX = 5 mm)

Figure 3.49 Continued.

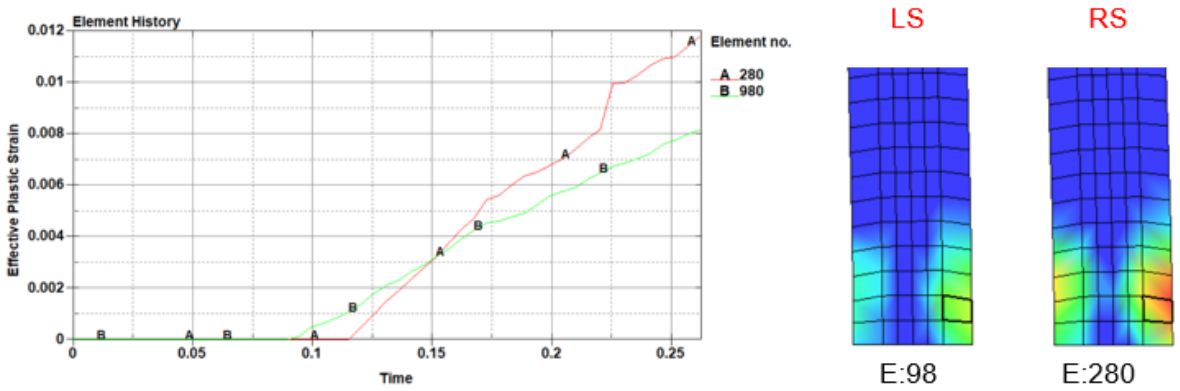

Figure 3.50 History of plastic deformation of the shear stud.

Figure 3.51 shows the plastic strains in the shear studs and stress contours in the concrete for the TS-II.a model, with the studs in the weak position. Figure 3.51.a illustrates the behavior for a displacement of UX = 1.25, where the shear studs begin to show plastic deformations (Figure 3.51.a-1), as well as damage to the concrete around the studs, mainly on the right upright (Figure 3.51.a-2). There is no damage in the upper part of the slab (Figure 3.51.a-3). However, damage is observed in the lower part of the slab, especially in the contact area between the steel deck and the shear studs (Figure 3.51.a-4).

For a displacement UX = 2.50 mm, the plastic strains reach important values (0.05 mm/mm) (Figure 3.51.b-1). The entire area surrounding the right shear stud has been damaged, while the left shear stud shows cone-shaped damage (Figure 3.51.b-2). Damage is beginning to be observed in the upper part of the concrete slab (Figure 3.51.b-3) while the lower part has suffered significant damage, especially in the contact area between the slab and the rubber (Figure 3.51.b- 4).

When the system is subjected to 75% of the imposed displacement (3.75 mm) the plastic strain continue to increase to the order of 0.012 mm/mm (Figure 3.51.c-1); however, these values remain small, but large damage is observed in the entire surrounding area of the shear studs (Figures 3.51.c-2-4).

Finally, when the total imposed displacement (5 mm) is reached, the plastic strain of the shear studs is close to 0.12 mm/mm (Figure 3.51.d-1), which indicates that for this type of pushout configuration, the shear studs reach large plastic deformations, so the capabilities that these elements offer to the system are used to the maximum. The concrete suffers significant damage throughout the area affected by the studs (Figure 3.51.d-2.4). To illustrate the plastic deformation history of the shear stud, Figure 3.52 is shown. The deformation mode and the plastic deformation contours of the stud studs seem to correspond to a shear condition; however, no important geometric changes appear even for a slip magnitude of 5 mm.

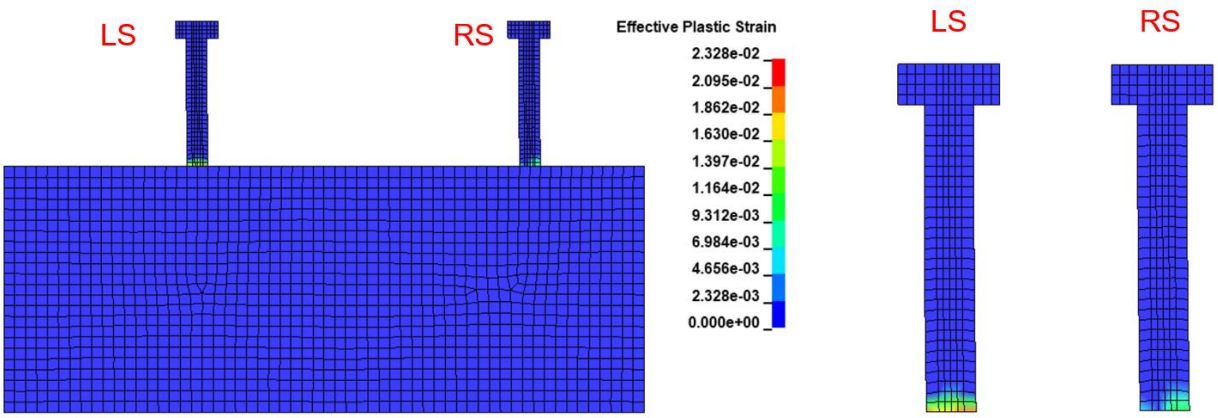

(a-1) Plastic deformation of the shear stud

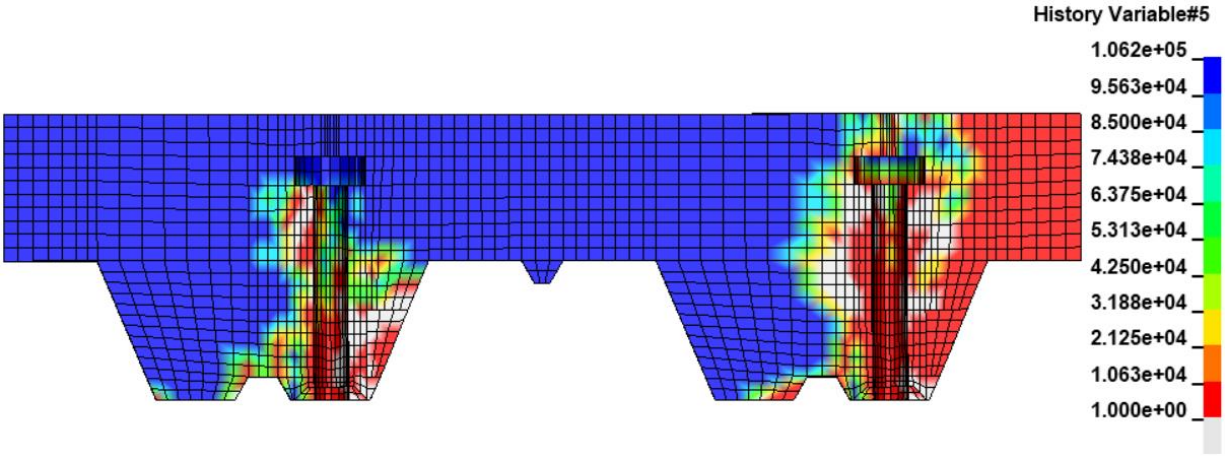

(a-2) Cross-section of the concrete slab

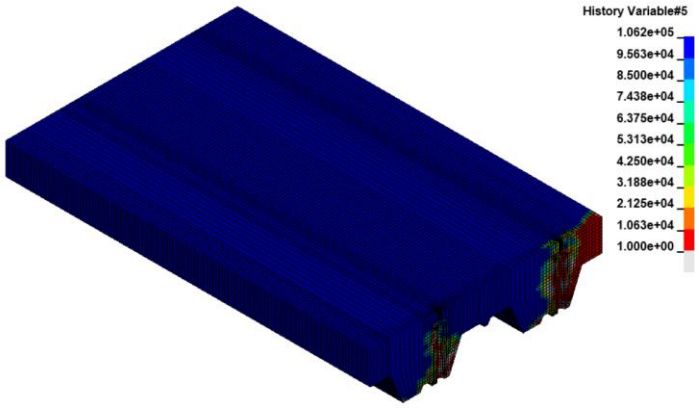

(a-3) Concrete slab top

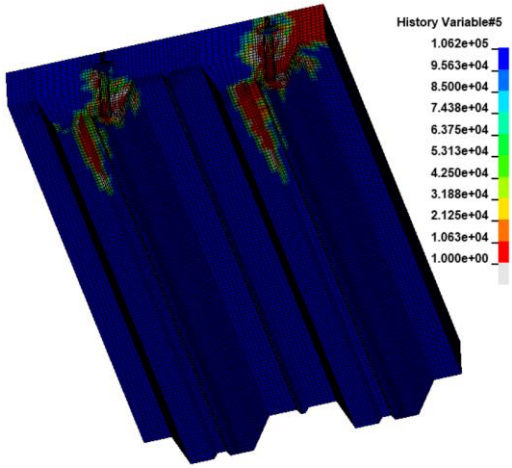

(a-4) Concrete slab bottom

(a) Percentage of applied force of 25% (UX = 1.25 mm)

Figure 3.51 Stress contours and deformed shapes.

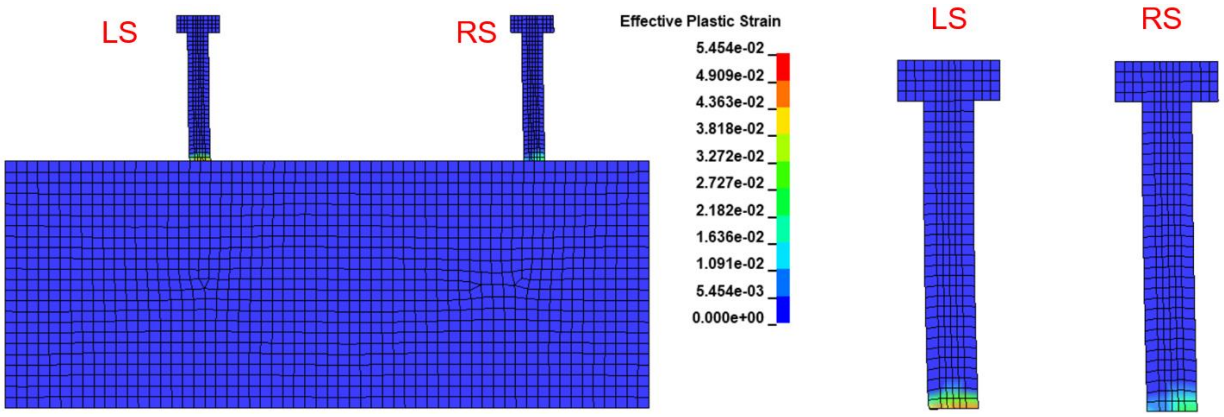

(b-1) Plastic deformation of the shear stud

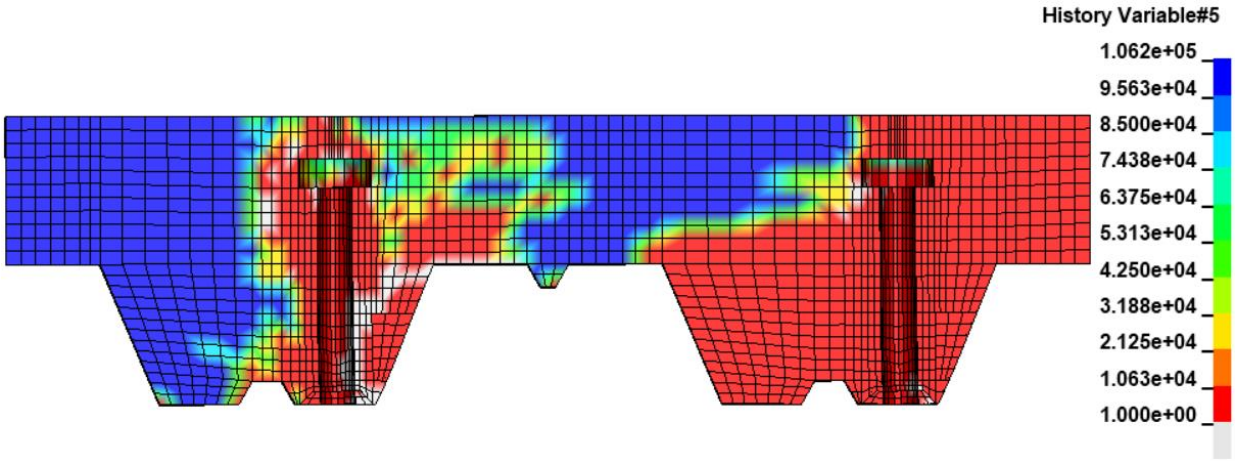

(b-2) Cross-section of the concrete slab

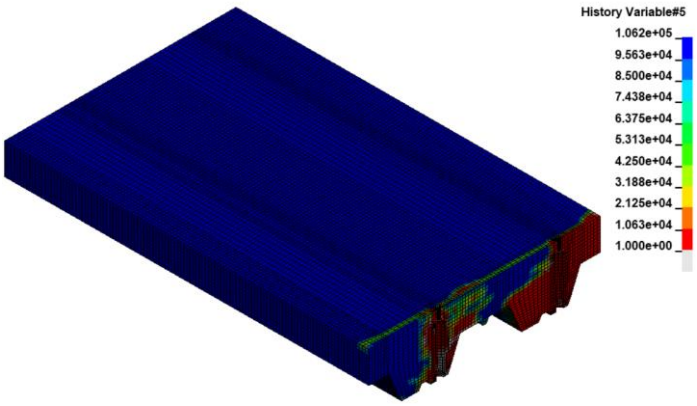

(b-3) Concrete slab top

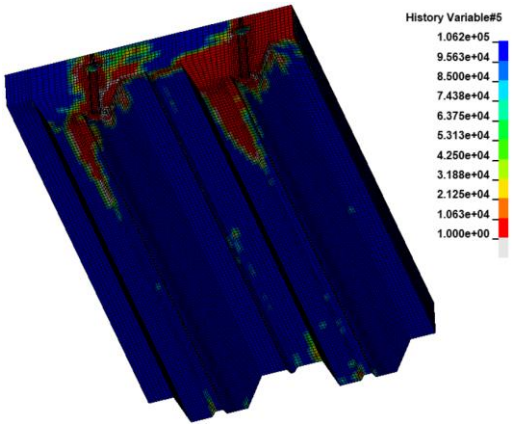

(b-4) Concrete slab bottom

(b) Percentage of applied force of 50% (UX = 2.5 mm)

Figure 3.51 Continued.

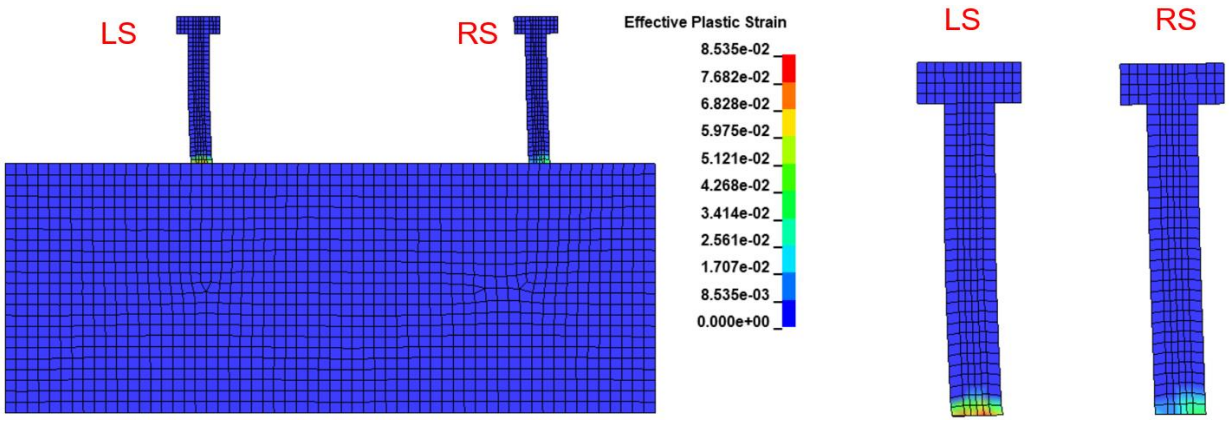

(c-1) Plastic deformation of the shear stud

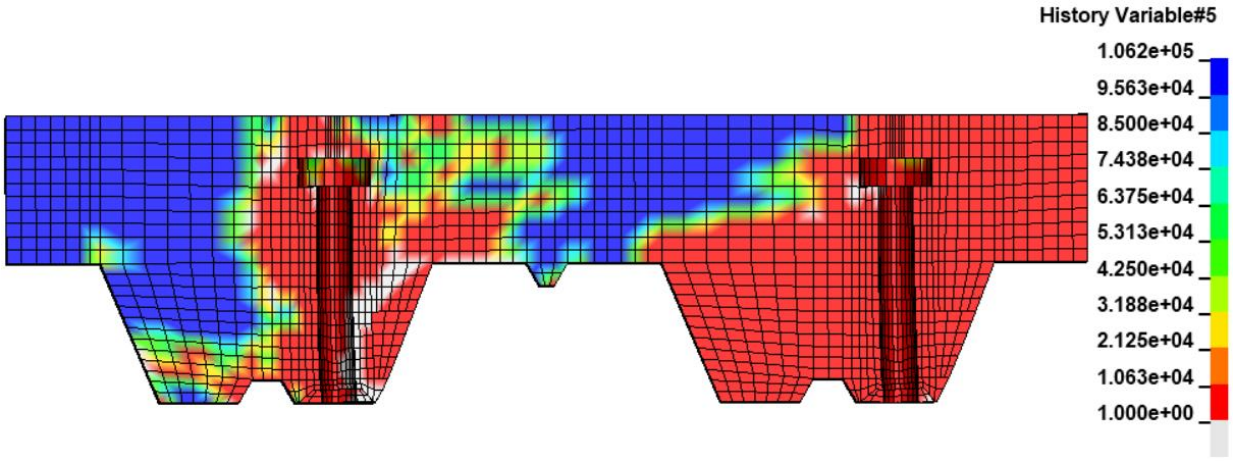

(c-2) Cross-section of the concrete slab

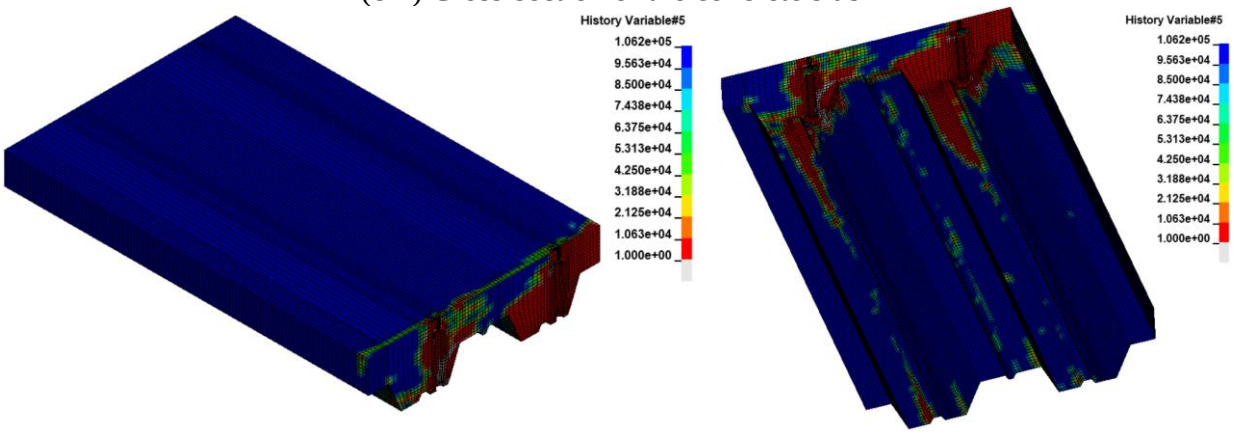

(c-3) Concrete slab top (c-4) Concrete slab bottom

(c) Percentage of applied force of 75% (UX = 2.75 mm)

Figure 3.51 Continued.

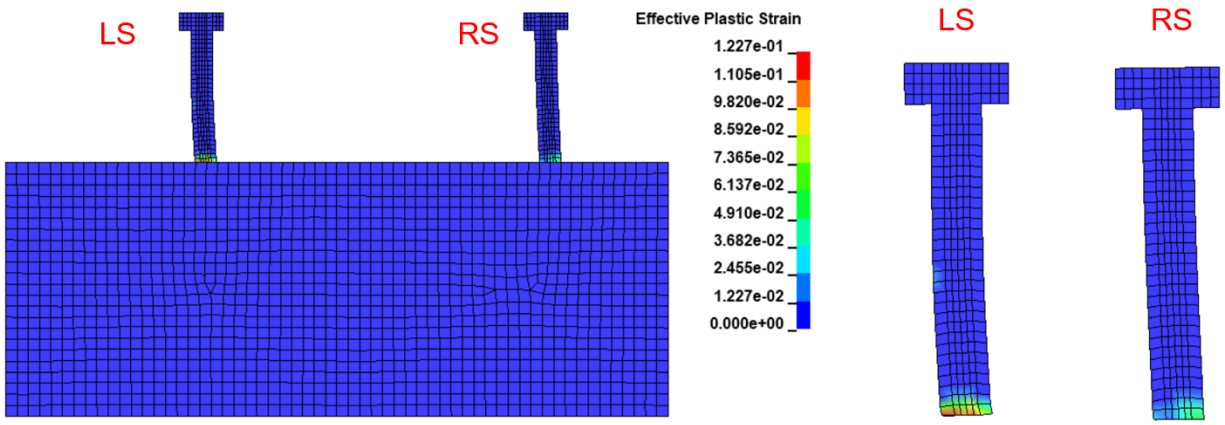

(d-1) Plastic deformation of the shear stud

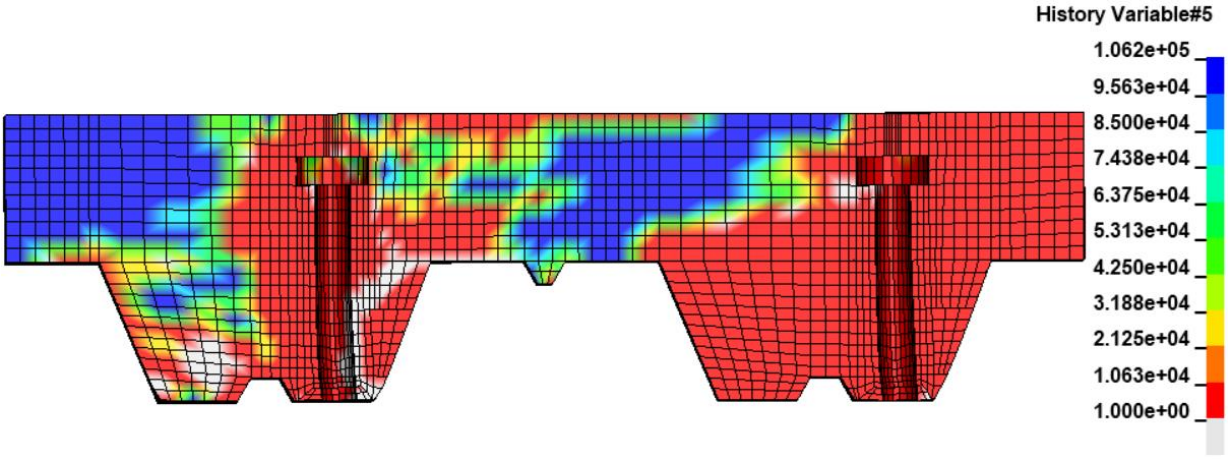

(d-2) Cross-section of the concrete slab

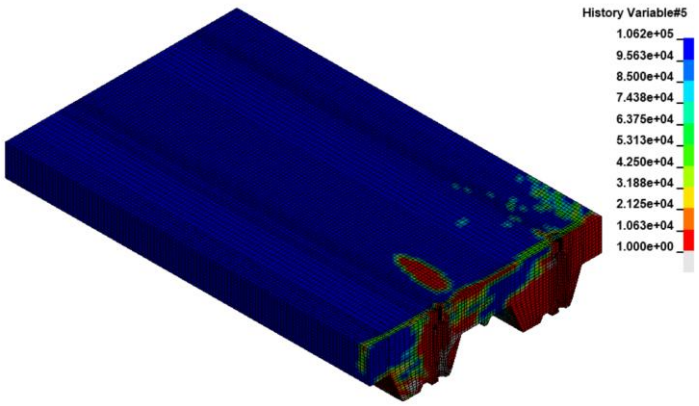

(d-3) Concrete slab top

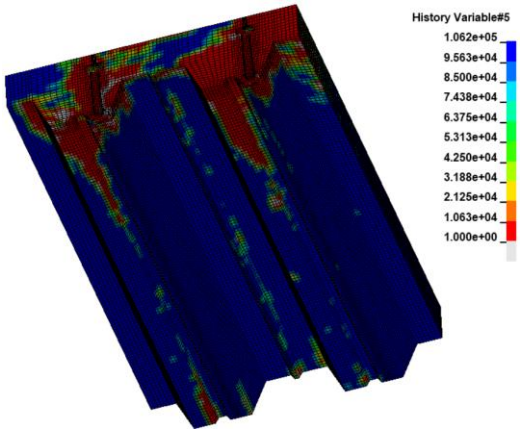

(d-4) Concrete slab bottom

(d) Percentage of applied force of 100% (UX = 5 mm)

Figure 3.51 Continued.

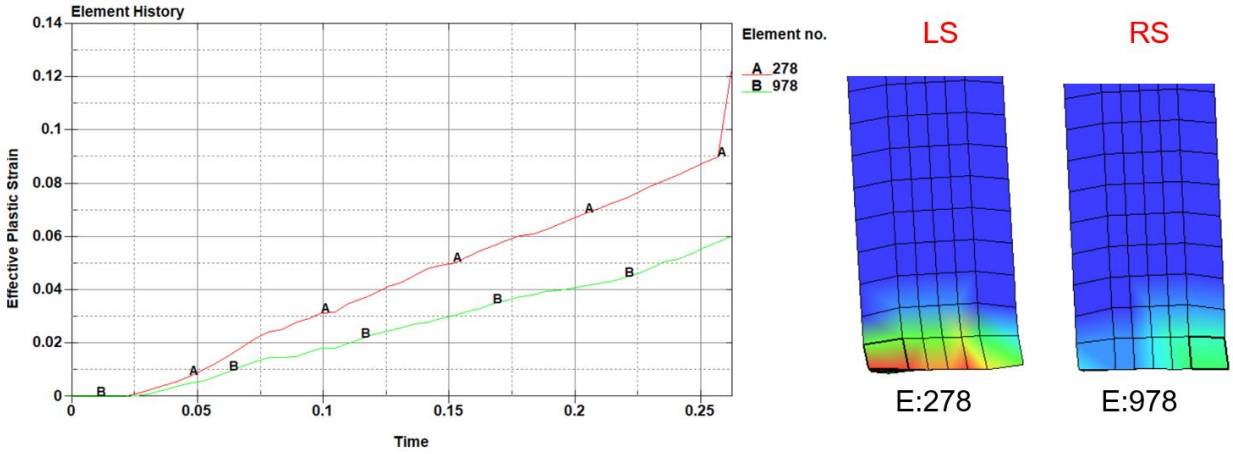

Figure 3.52 History of plastic deformation of the shear stud.

Figure 3.53 shows the plastic deformations in the shear studs and the stress contours in the concrete for the TS-II.b model. Figure 3.53.a illustrates the behavior for a displacement of UX = 1.25 mm. For this displacement condition, the right stud begins to show plastic deformations (Figure 3.53.a-1), as well as cone-shaped concrete damage around the left shear stud around it (Figure 3.53.a-2). Minor damage appears in the upper part of the slab (Figure 3.53.a-3). However, significant damage is observed in the lower part of the slab, especially in the contact area between the steel deck and the shear bolts. (Figure 3.53.a-4).

For a displacement UX = 2.50 mm, the plastic strains still remain at small values (0.00675 mm/mm) (Figure 3.53.b-1). The entire cross-sectional area of the section is damaged (Figure 3.53.b-2). Damage is observed at the top and bottom of the concrete slab (Figure 3.53.b-3-4).

When the system is subjected to 75% of the imposed displacement (3.75 mm) the plastic strains increase to the order of 0.016 mm/mm (Figure 3.53.c-1) but these values remain relatively small. Damage is observed in the entire surrounding area of the shear studs as well as in the support area between the rubber and the concrete slab (Figures 3.53.c-2-4).

Finally, when the total imposed displacement (5 mm) is reached, the plastic deformation of the safety pins is close to 0.021 mm/mm (Figure 3.53.d-1), which indicates that for this type of pushout configuration, the shear studs do not reach large plastic deformations. The concrete suffers significant damage throughout the area affected by the studs (Figure 3.53.d-2.4). To illustrate the plastic deformation history of the shear stud, Figure 3.54 is shown. The deformation mode and the plastic deformation contours of the stud seem to correspond to a bending condition. However, no important geometric changes appear even for a slip magnitude of 5 mm.

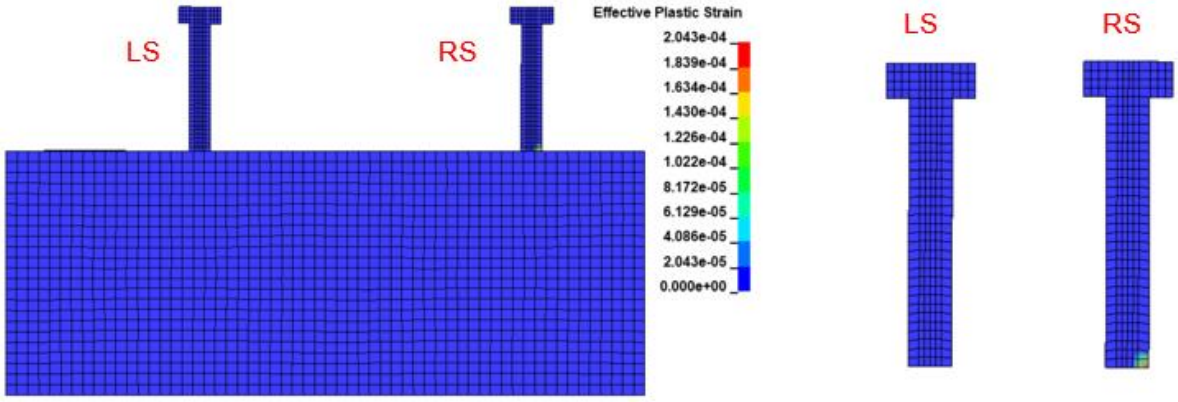

(a-1) Plastic deformation of the shear stud

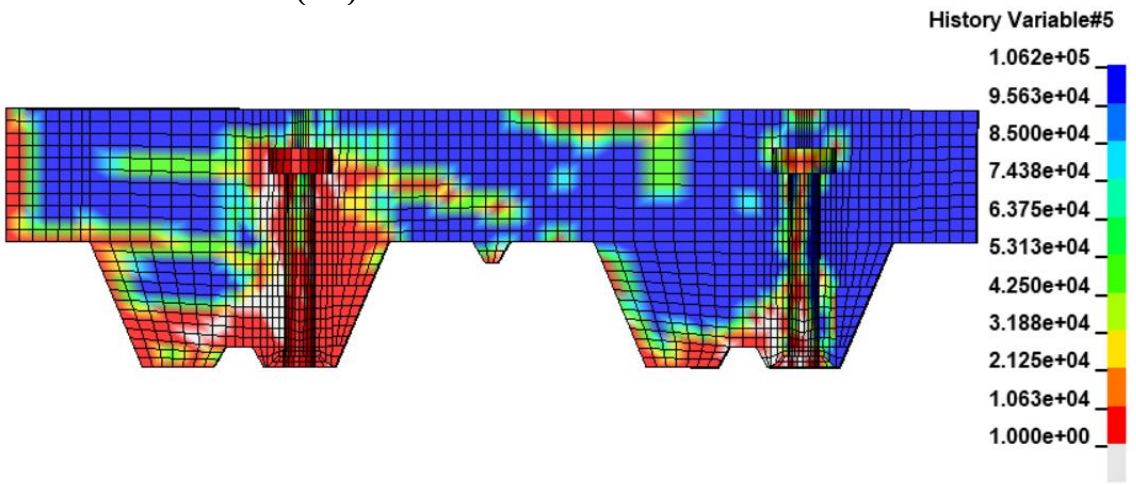

(a-2) Cross-section of the concrete slab

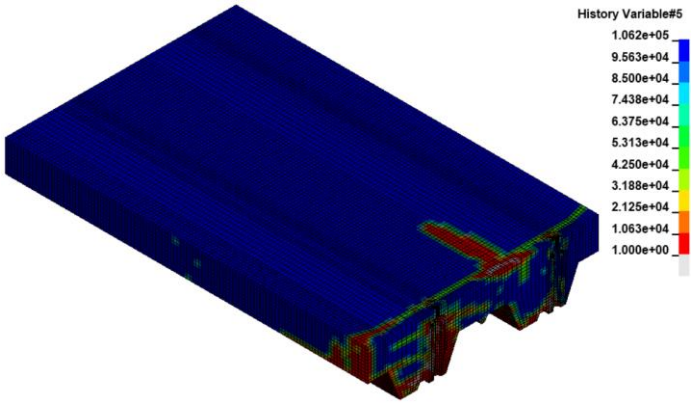

(a-3) Concrete slab top

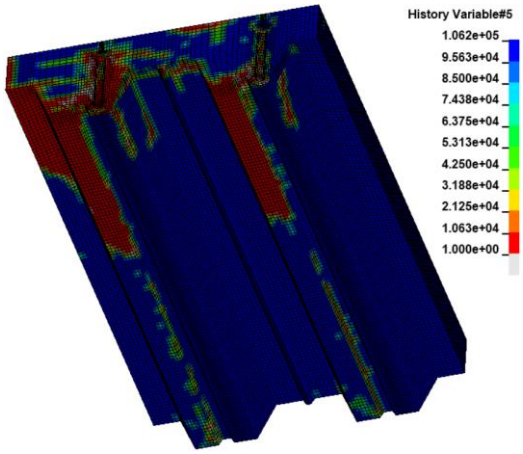

(a-4) Concrete slab bottom

(a) Percentage of applied force of 25% (UX = 1.25 mm)

Figure 3.53 Stress contours and deformed shapes.

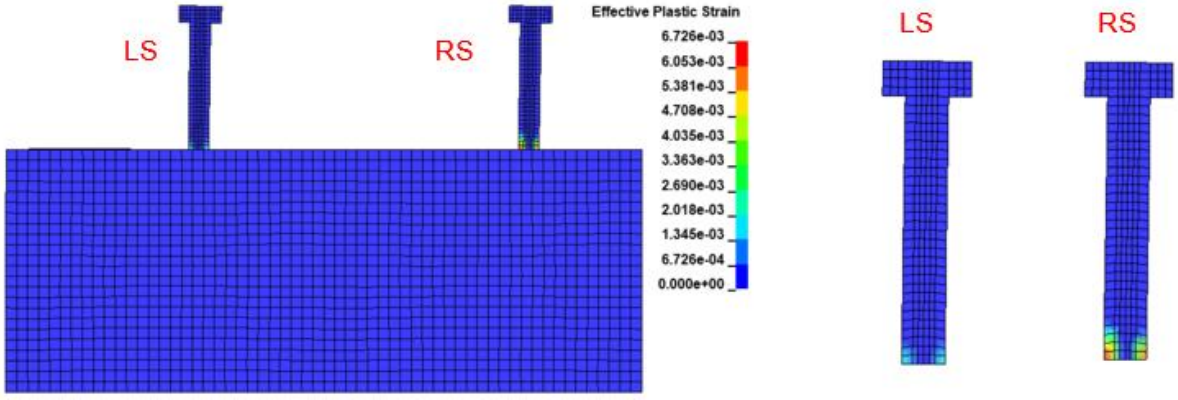

(b-1) Plastic deformation of the shear stud

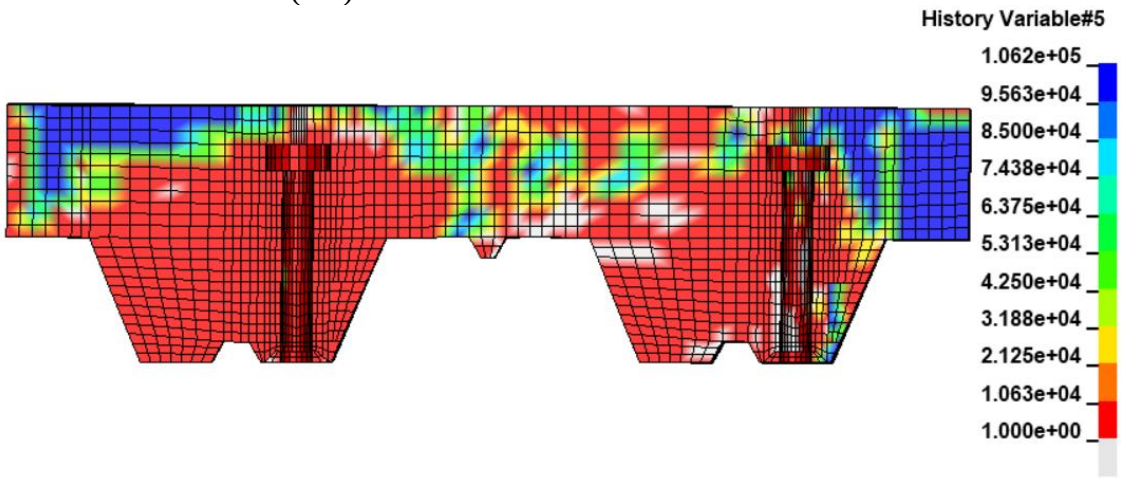

(b-2) Cross-section of the concrete slab

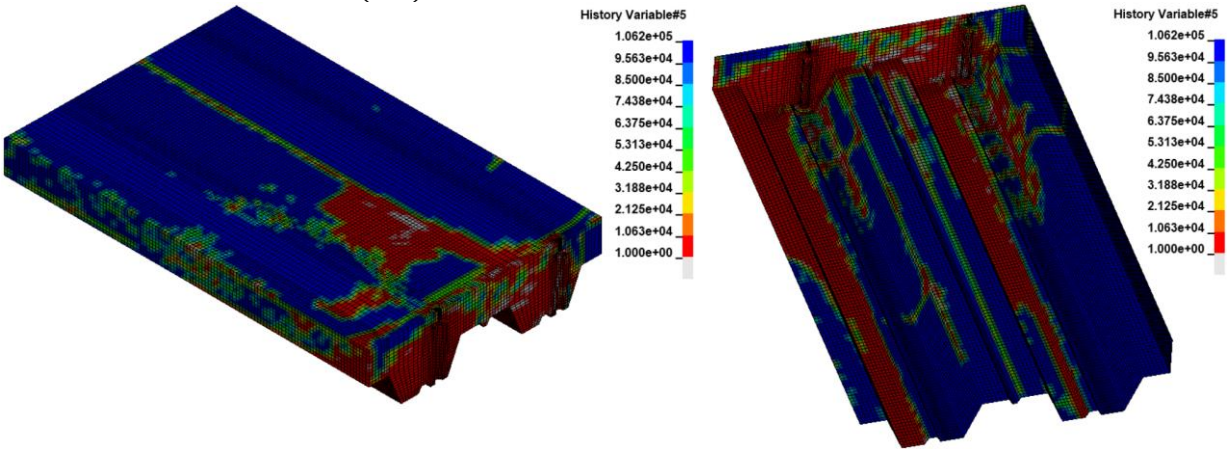

(b-3) Concrete slab top (b-4) Concrete slab bottom

(b) Percentage of applied force of 50% (UX = 2.5 mm)

Figure 3.53 Continued.

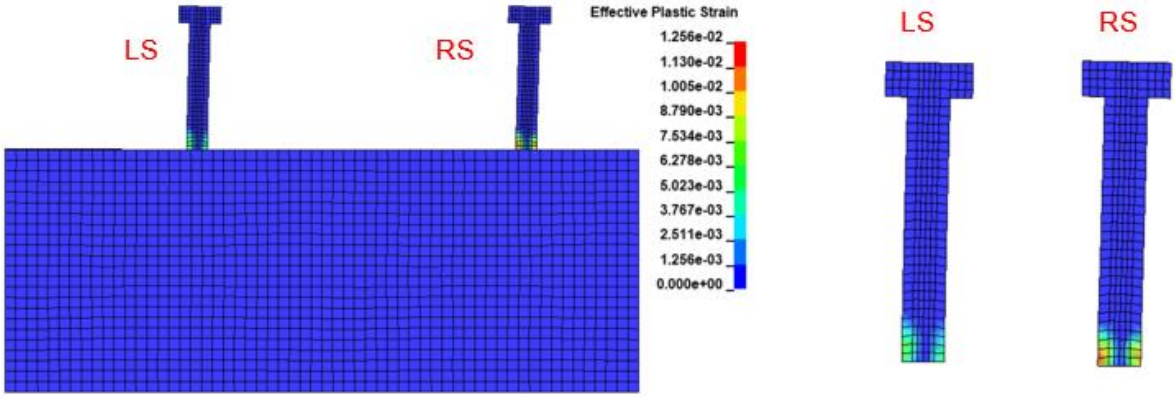

(c-1) Plastic deformation of the shear stud

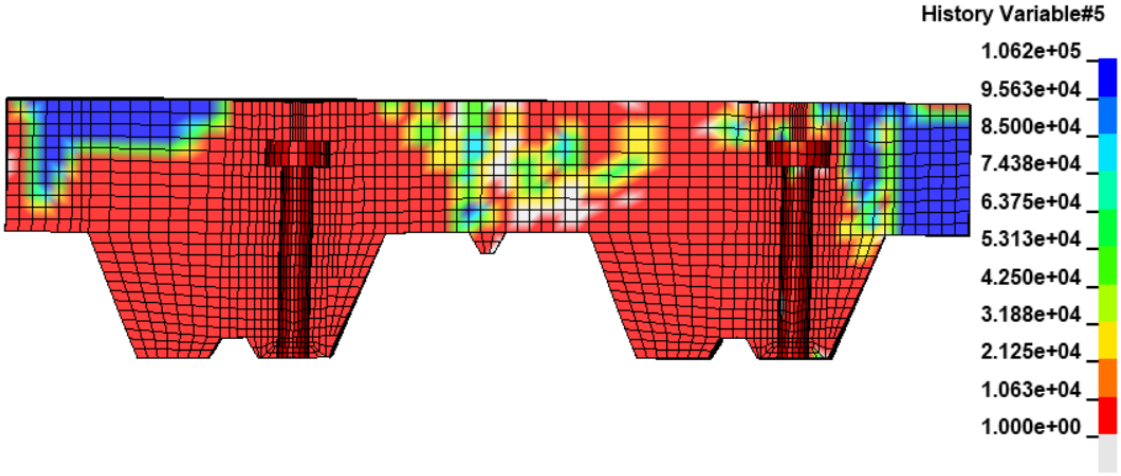

(c-2) Cross-section of the concrete slab

Figure 3.53 Continued.

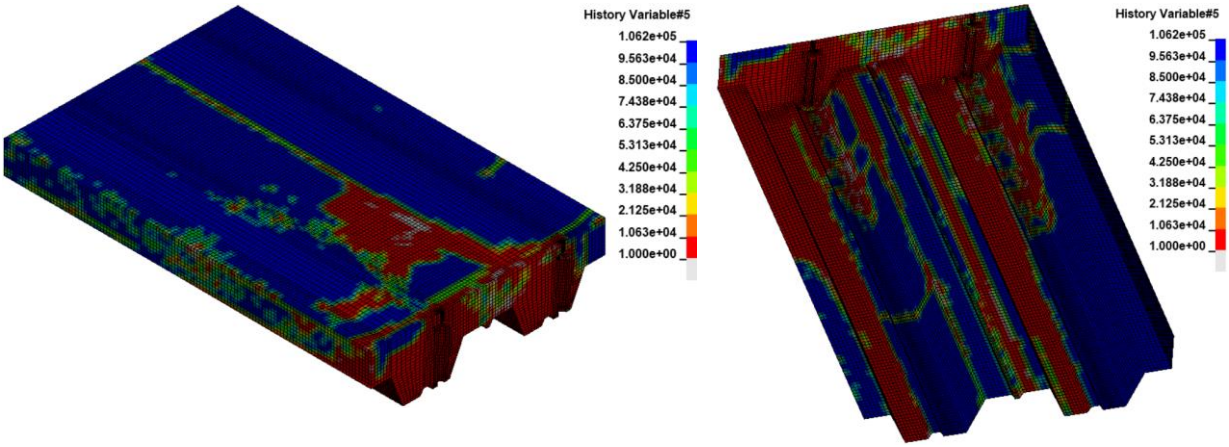

(c-3) Concrete slab top (c-4) Concrete slab bottom

(c) Percentage of applied force of 75% (UX = 2.75 mm)

Figure 3.53 Continued.

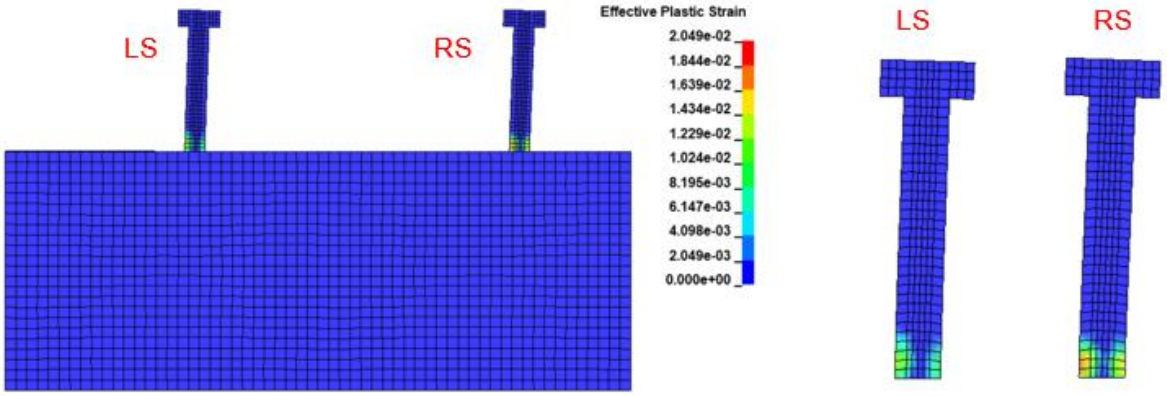

(d-1) Plastic deformation of the shear stud

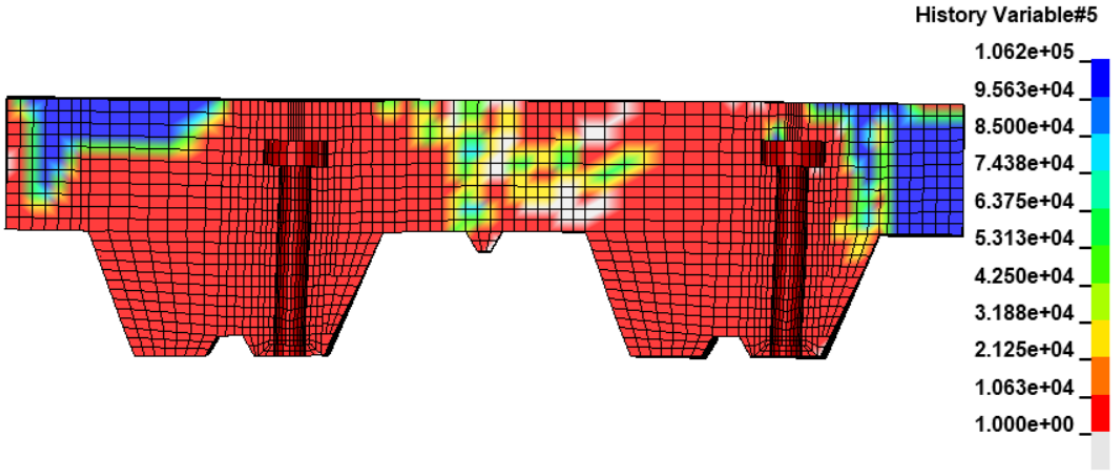

(d-2) Cross-section of the concrete slab

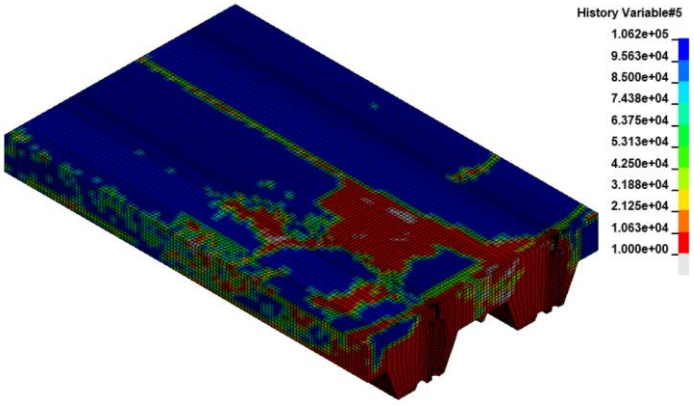

(d-3) Concrete slab top

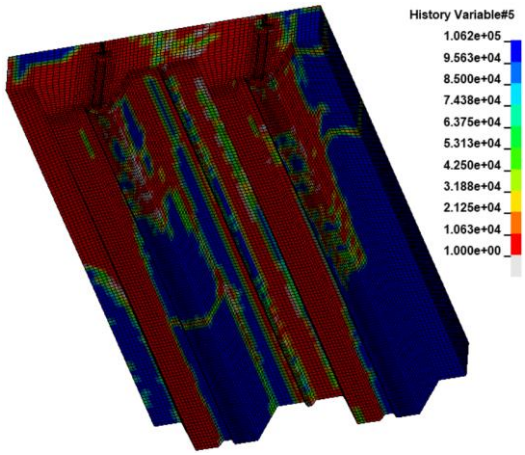

(d-4) Concrete slab bottom

(d) Percentage of applied force of 100% (UX = 5 mm)

Figure 3.53 Continued.

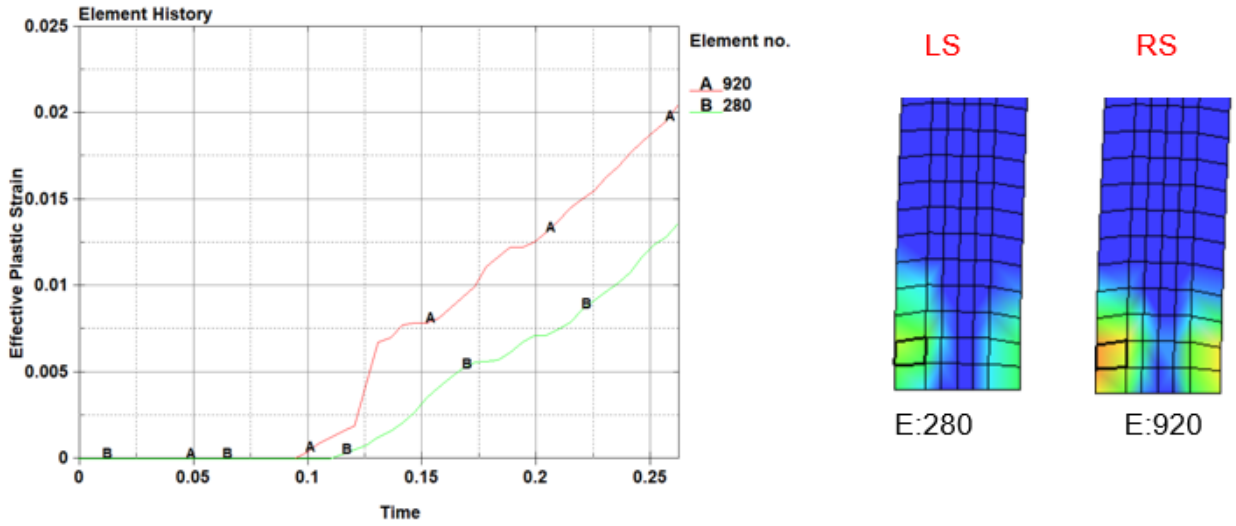

Figure 3.54 History of plastic deformation of the shear stud.

Figure 3.55 shows the plastic deformations in the shear studs and the stress contours in the concrete for the TS-III model. Figure 3.55.a illustrates the behavior for a displacement of UX = 1.25 mm. For this displacement condition the left shear stud begins to present plastic strains of the order of 0.017 mm/mm (Figure 3.55.a-1), as well as damage in the concrete on the periphery of the shear studs, mainly the right shear stud (Figure 3.55.a-2). No damage is observed in the upper part of the slab (Figure 3.55.a-3). H owever, significant damage is observed in the lower part of the slab (Figure 3.55.a-4).

For a displacement UX = 2.50 mm, the plastic strains increase significantly (0.083 mm/mm), especially the left shear stud (Figure 3.55.b-1). There is damage around the entire right stud and part of the left shear stud (Figure 3.55.b-2). Minor damage is observed in the upper part of the slab and significant damage is observed in the lower part of the concrete slab (Figure 3.55.b-3-4).

When the system is subjected to 75% of the imposed displacement (3.75 mm), the plastic strains increase to the order of 0.19 mm/mm (Figure 3.55.c-1). Damage is observed in the entire area surrounding the shear studs as well as in the support area between the rubber and the concrete slab (Figures 3.55.c-2-4).

Finally, when the total imposed displacement (5 mm) is reached, the plastic strain of the shear stud is close to 0.23 mm/mm (Figure 3.55.d-1), which indicates that for this type of configuration of pushout tests, the shear studs will reach very large plastic deformations. The concrete suffers significant damage throughout the area affected by the studs (Figure 3.55.d-2.4). To illustrate the plastic deformation history of the shear stud, Figure 3.56 is shown. The deformation mode and the plastic deformation contours of the stud seem to correspond to a bending condition, however, no important geometric changes appear even for a slip magnitude of 5 mm.

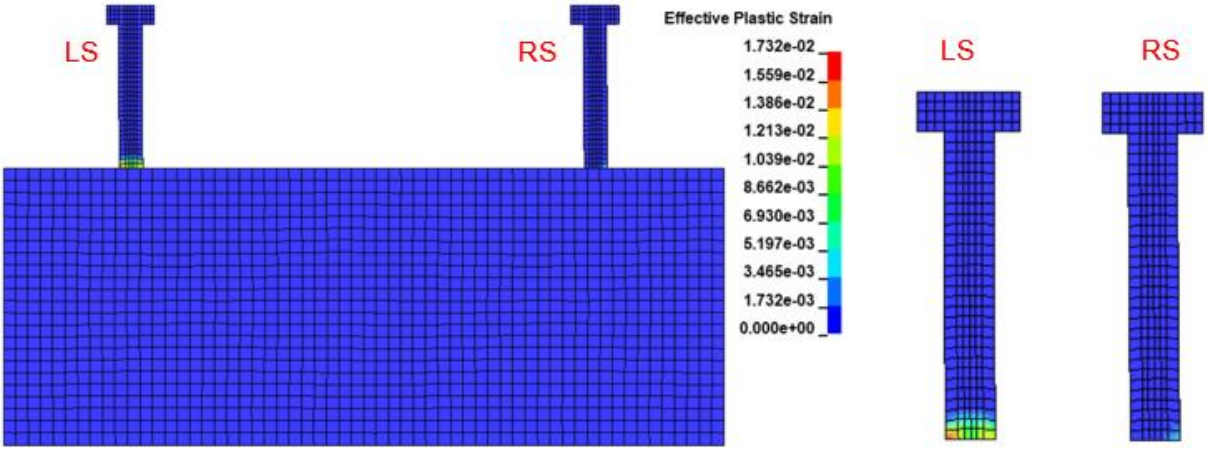

(a-1) Plastic deformation of the shear stud

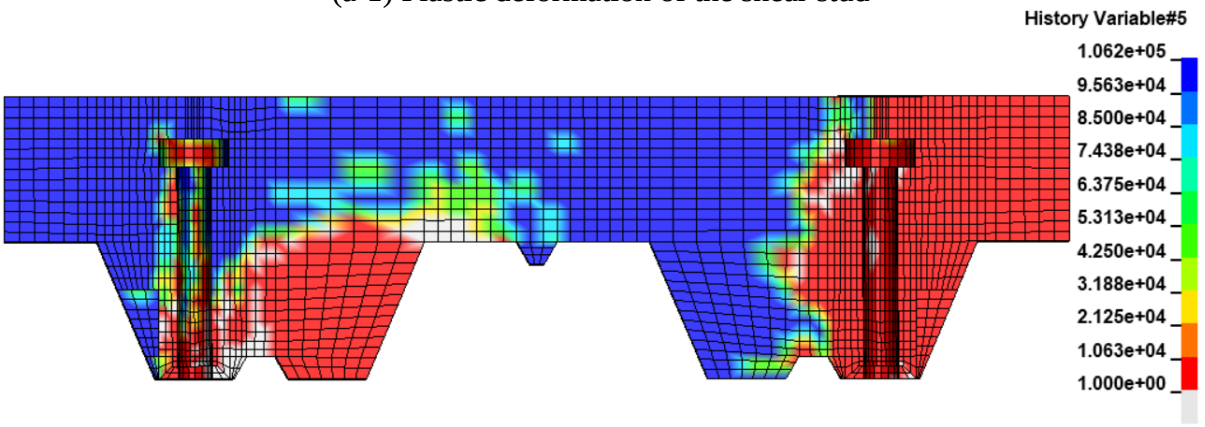

(a-2) Cross-section of the concrete slab

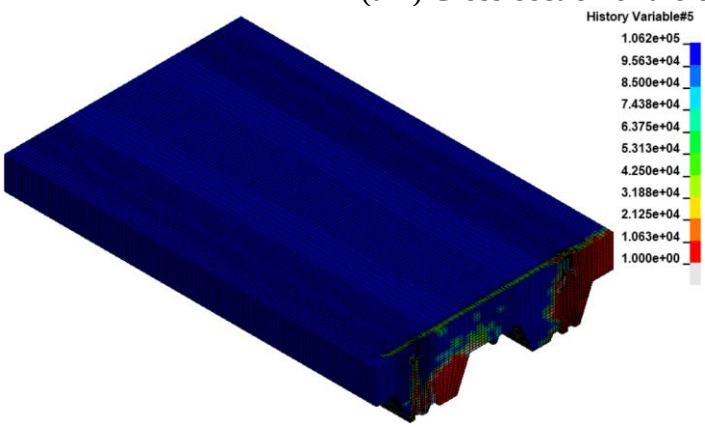

(a-3) Concrete slab top

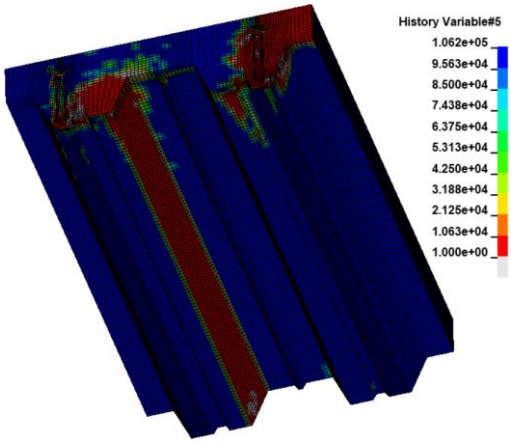

(a-4) Concrete slab bottom

(a) Percentage of applied force of 25% (UX = 1.25 mm)

Figure 3.55 Stress contours and deformed shapes.

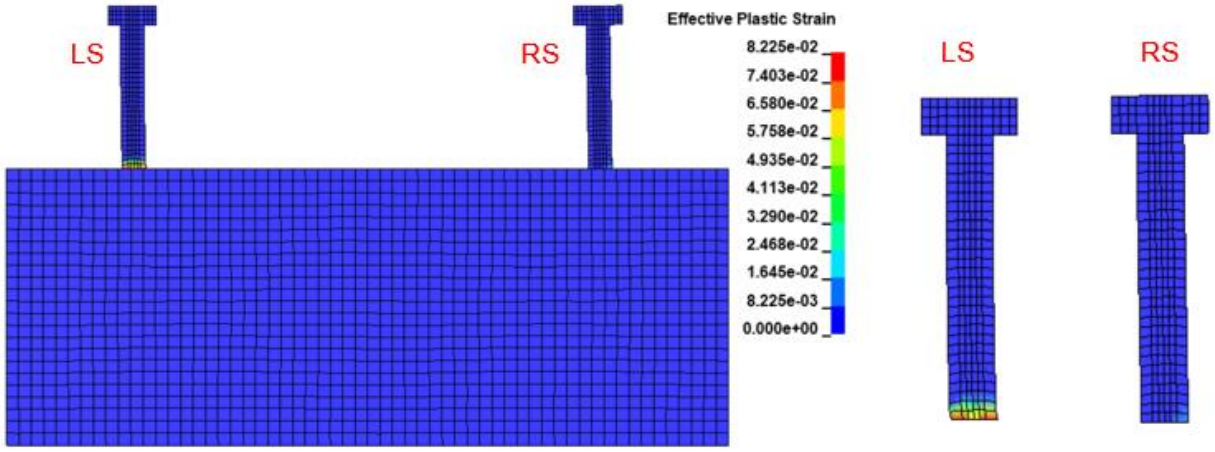

(b-1) Plastic deformation of the shear stud

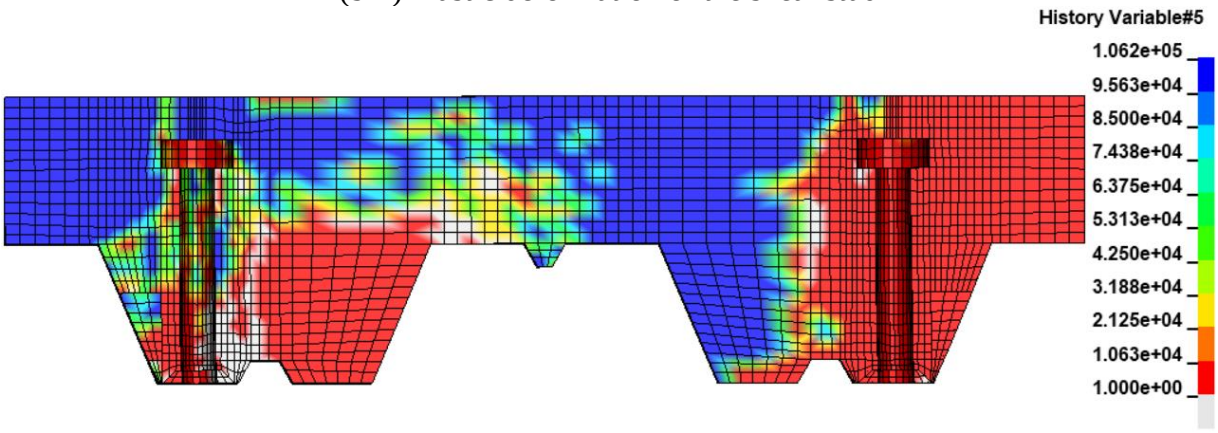

(b-2) Cross-section of the concrete slab

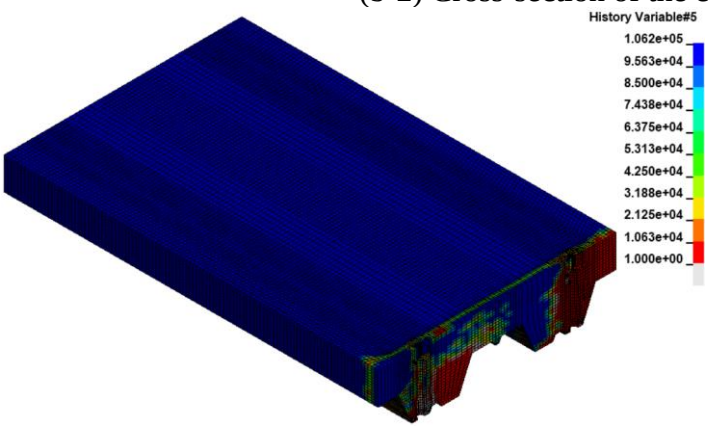

(b-3) Concrete slab top

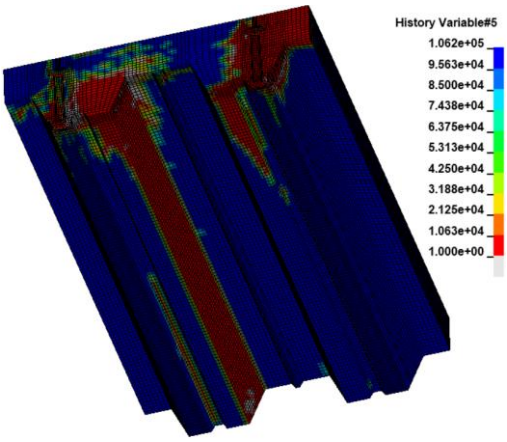

(b-4) Concrete slab bottom

(b) Percentage of applied force of 50% (UX = 2.5 mm)

Figure 3.55 Continued.

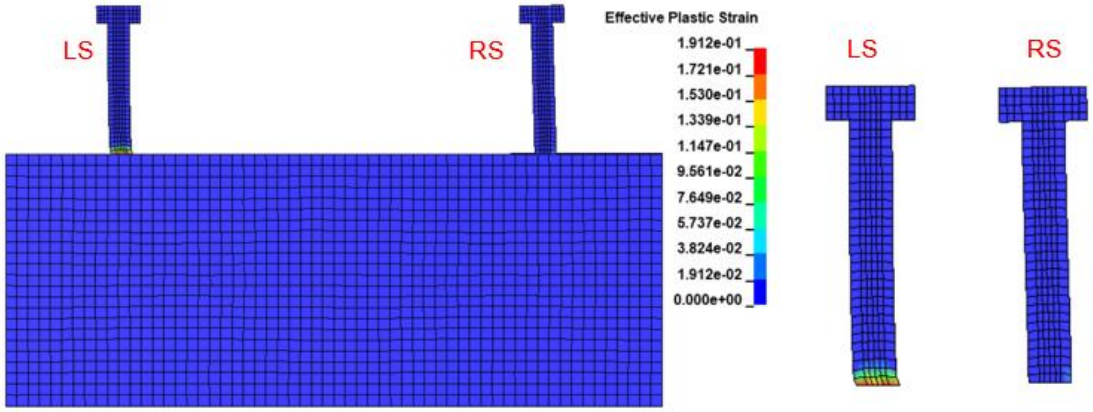

(c-1) Plastic deformation of the shear stud

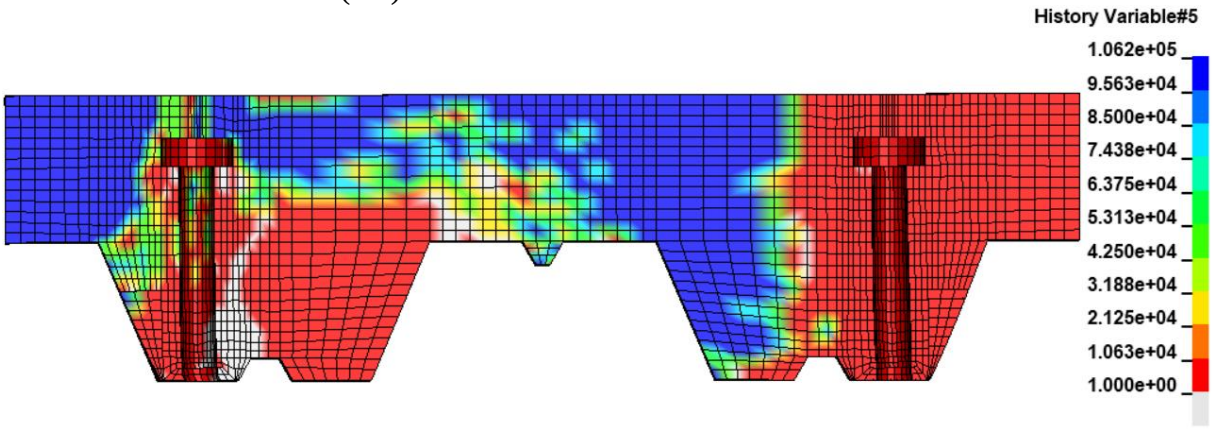

(c-2) Cross-section of the concrete slab

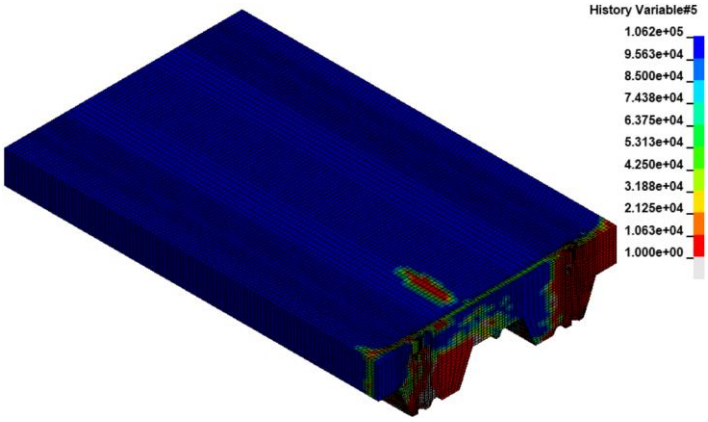

(c-3) Concrete slab top

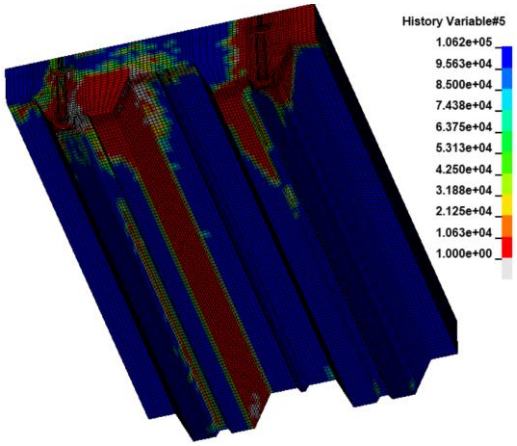

(c-4) Concrete slab bottom

(c) Percentage of applied force of 75% (UX = 2.75 mm)

Figure 3.55 Continued.

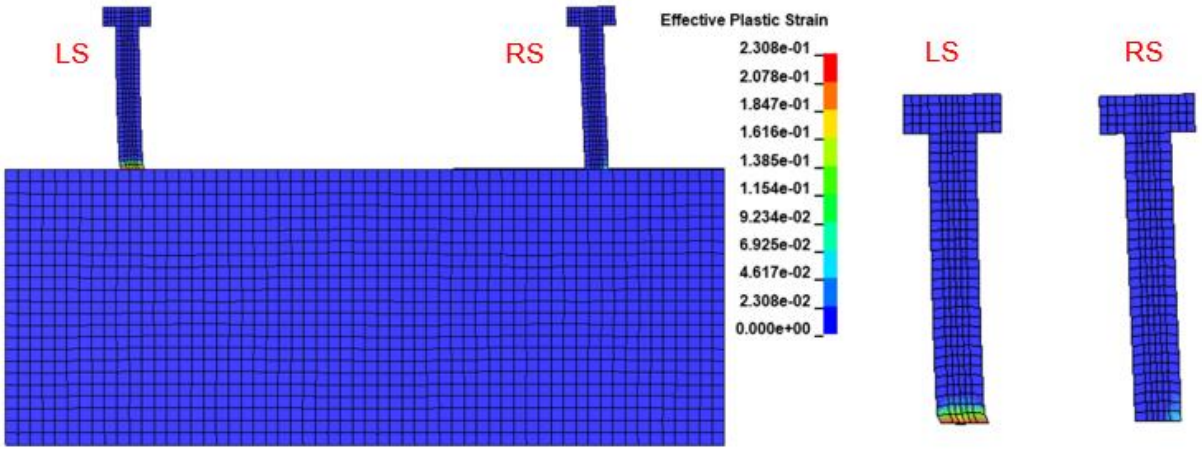

(d-1) Plastic deformation of the shear stud

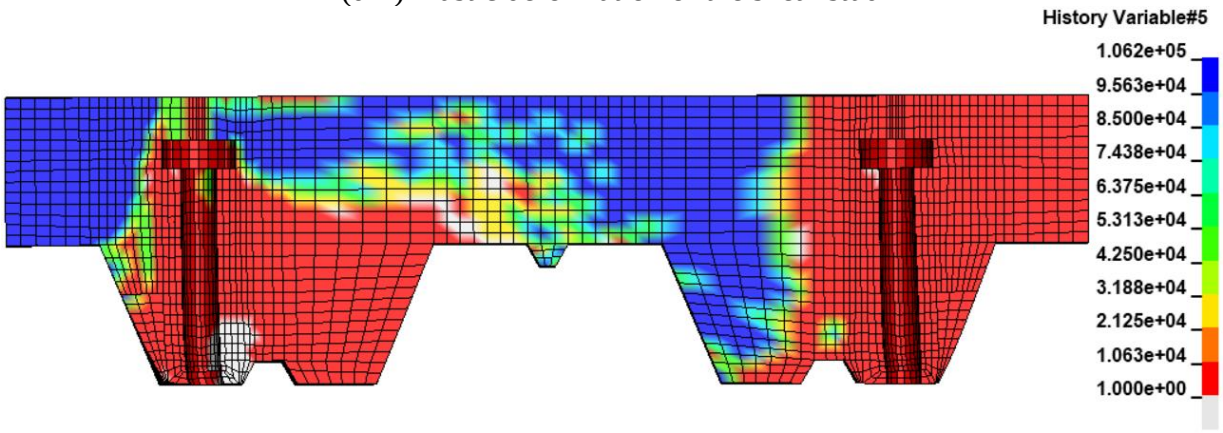

(d-2) Cross-section of the concrete slab

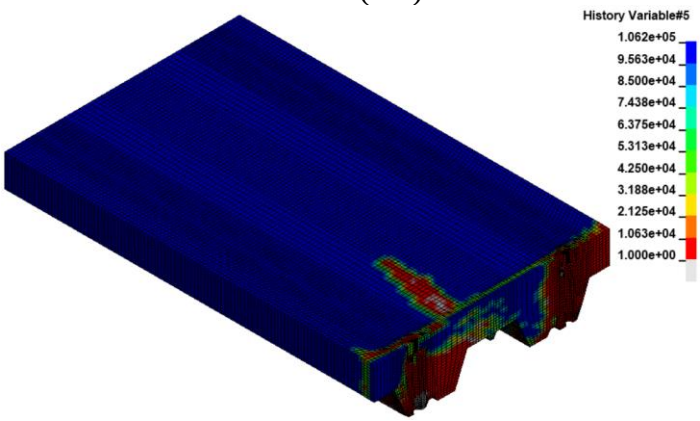

(d-3) Concrete slab top

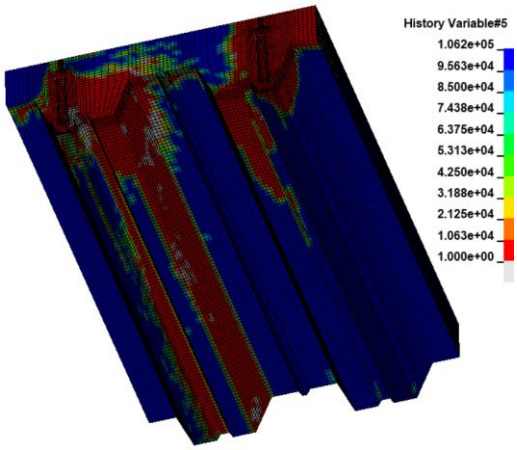

(d-4) Concrete slab bottom

(d) Percentage of applied force of 100% (UX = 5 mm)

Figure 3.55 Continued.

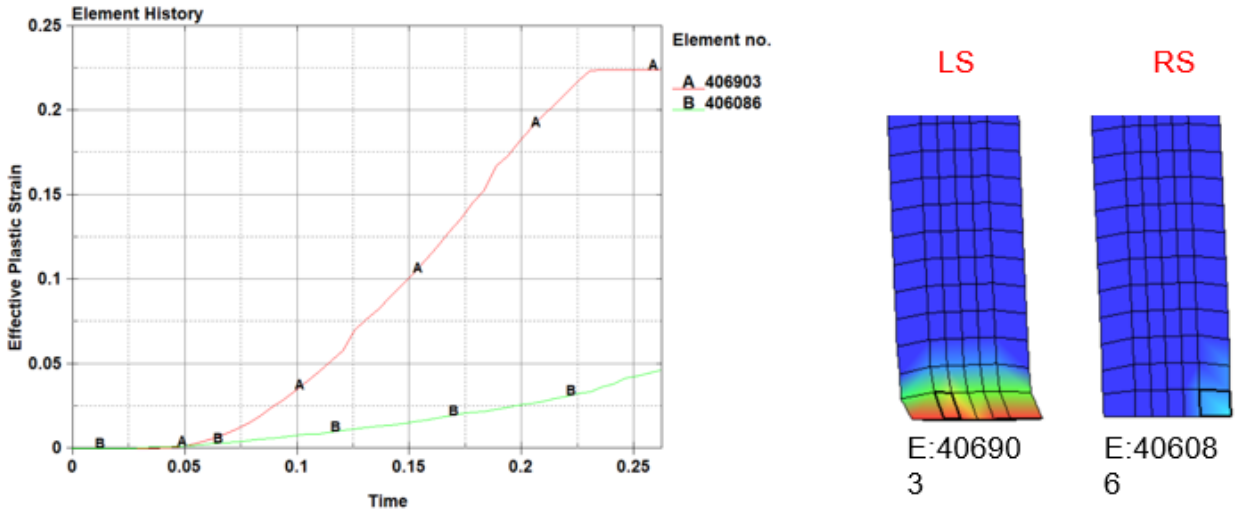

Figure 3.56 History of plastic deformation of the shear stud.

Finally, Figure 3.57 shows the plastic deformations in the shear studs and the stress contours in the concrete for the TS-IV model. Figure 3.57.a illustrates the behavior for a displacement of UX = 1.25 mm. For this displacement condition the right shear stud begins to present plastic strains of the order of 0.0023 mm/mm (Figure 3.57.a-1), as well as damage in the concrete in the shape of a cone around the shear studs (Figure 3.57.a-2). Minor damage is observed at the top and bottom of the slab (Figures 3.57.a-3-4).

For a displacement UX = 2.50 mm, the plastic strains remain low (0.0066 mm/mm) in the shear studs (Figure 3.57.b-1). Cone-shaped damage is clearly visible on the left shear stud (Figure 3.57.b-2). Damage to the top and bottom of the concrete slab is increased (Figure 3.57.b-3-4).

When the system is subjected to 75% of the imposed displacement (3.75 mm), the plastic strains increase to the order of 0.011 mm/mm (Figure 3.57.c-1). Damage is observed throughout the cross-sectional area of the concrete slab (Figure 3.57.c-2). Significant damage to the top and bottom of the concrete floors (Figures 3.57.c-3-4).

Finally, when the total displacement imposed (5 mm) is reached, the plastic strain of the shear studs is close to 0.015 mm/mm (Figure 3.57.d-1), which indicates that for this type of pushout test configuration, the shear studs do not reach large plastic deformations. The concrete suffers significant damage throughout the area affected by the studs (Figure 3.57.d-2-4). To illustrate the plastic deformation history of the shear stud, Figure 3.58 is shown. The deformation mode and the plastic deformation contours of the shear stud seem to correspond to a bending condition, however, no important geometric changes appear even for a slip magnitude of 5 mm.

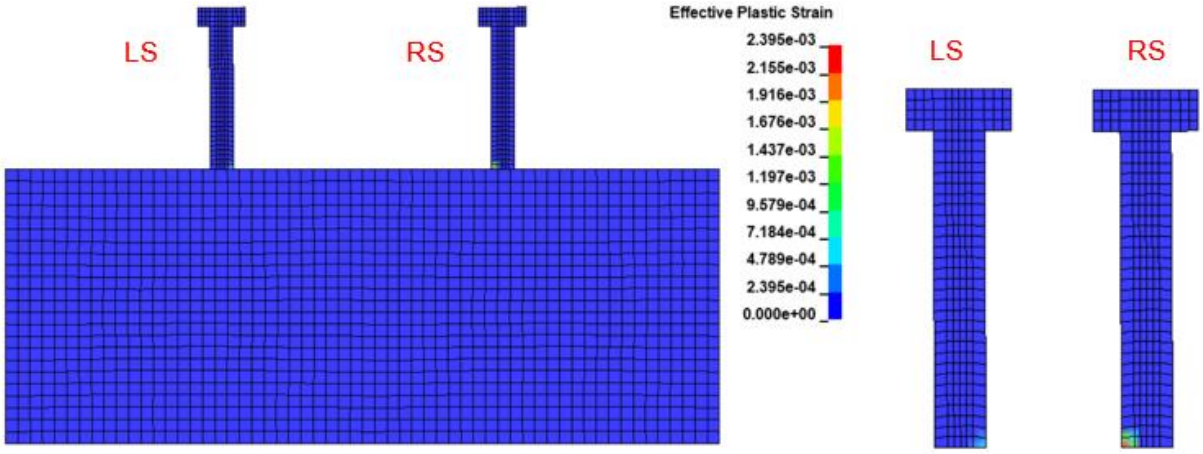

(a-1) Plastic deformation of the shear stud

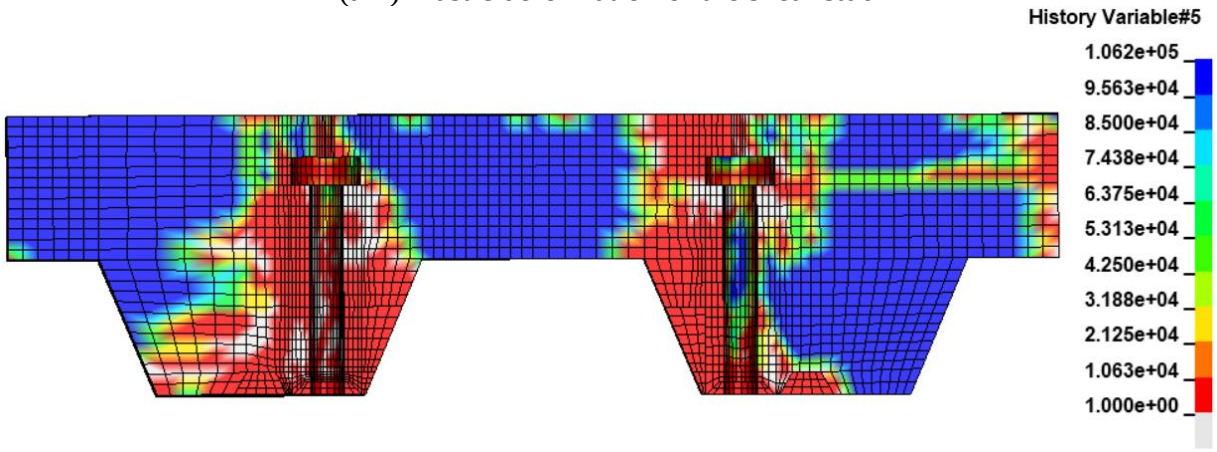

(a-2) Cross-section of the concrete slab

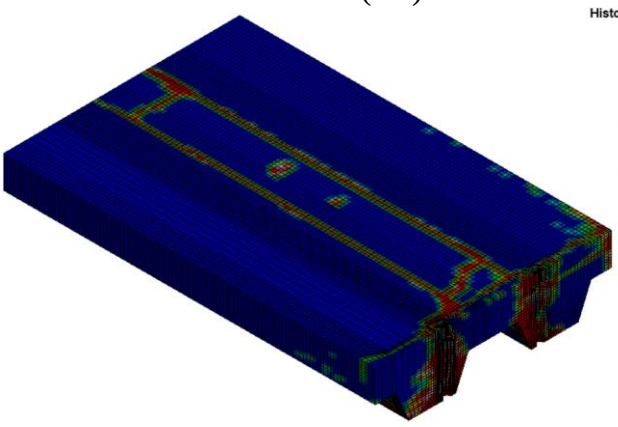

(a-3) Concrete slab top

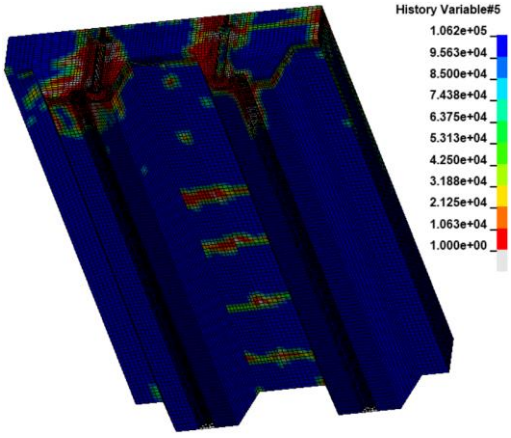

(a-4) Concrete slab bottom

(a) Percentage of applied force of 25% (UX = 1.25 mm)

Figure 3.57 Stress contours and deformed shapes.

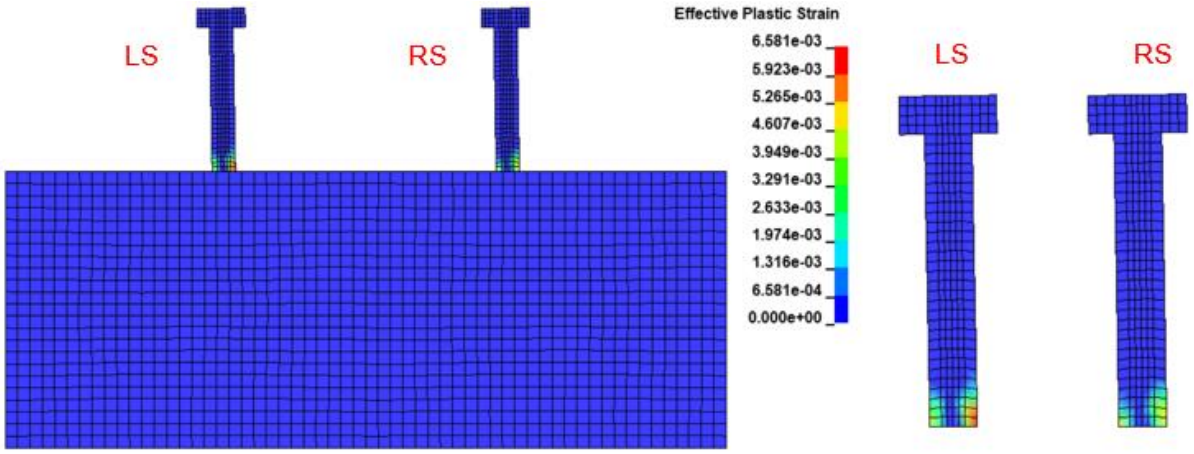

(b-1) Plastic deformation of the shear stud

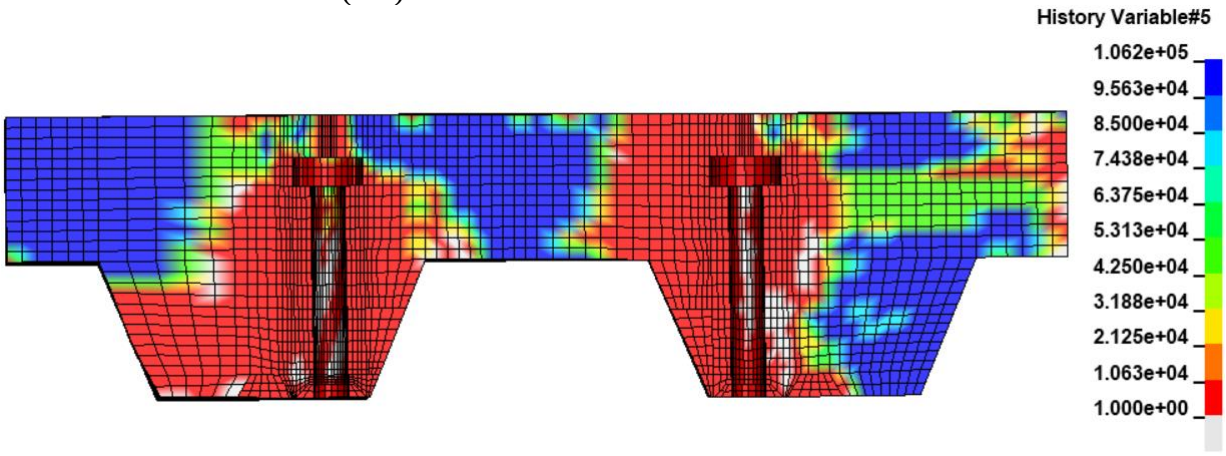

(b-2) Cross-section of the concrete slab

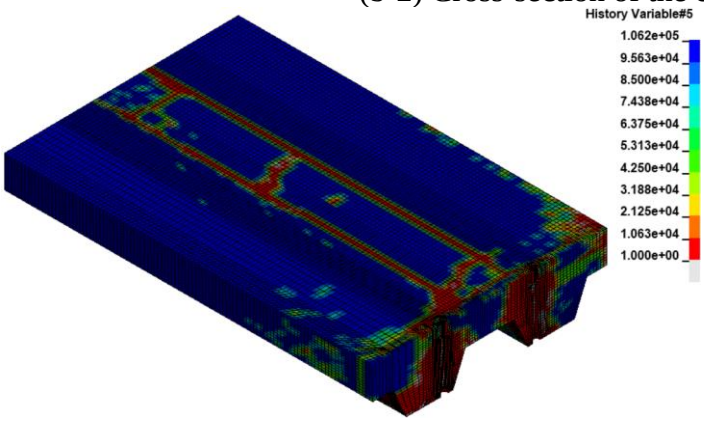

(b-3) Concrete slab top

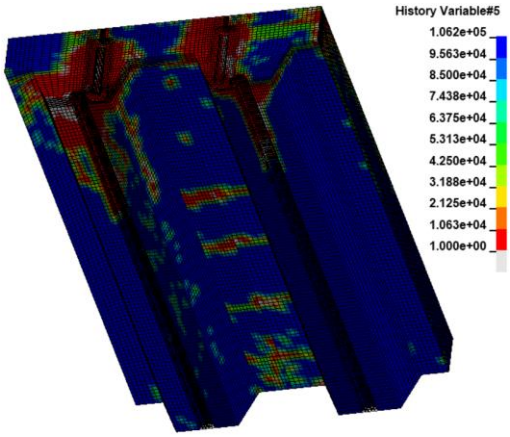

(b-4) Concrete slab bottom

(b) Percentage of applied force of 50% (UX = 2.5 mm)

Figure 3.57 Continued.

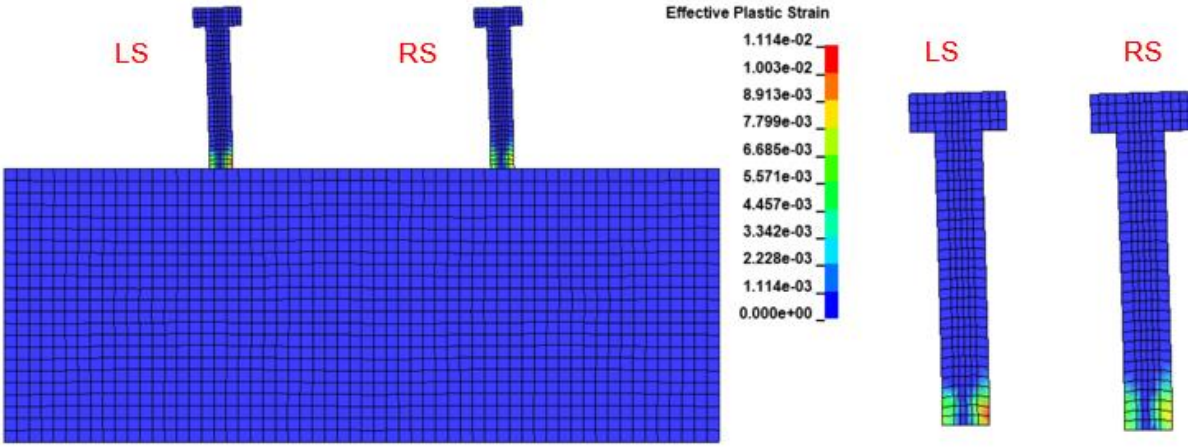

(c-1) Plastic deformation of the shear stud

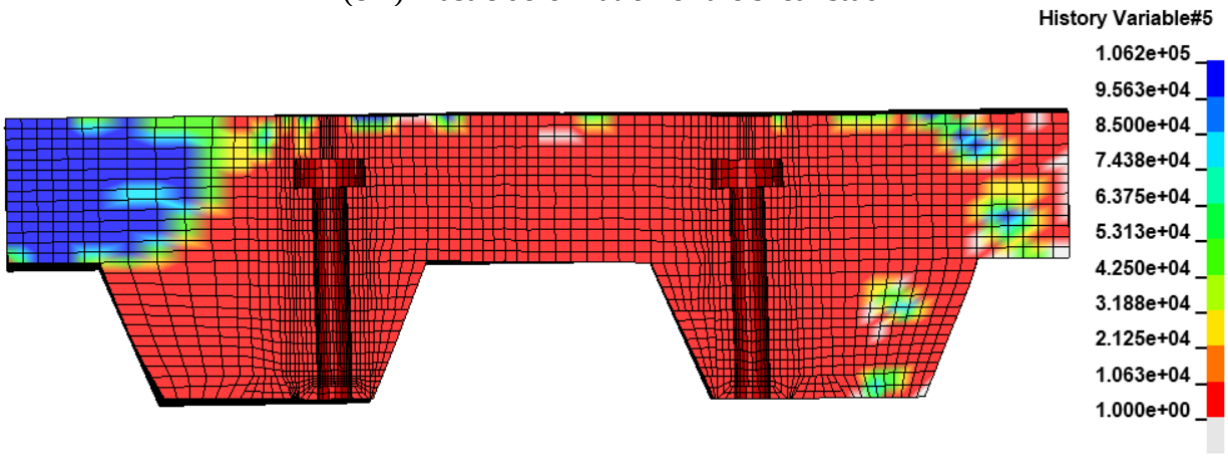

(c-2) Cross-section of the concrete slab

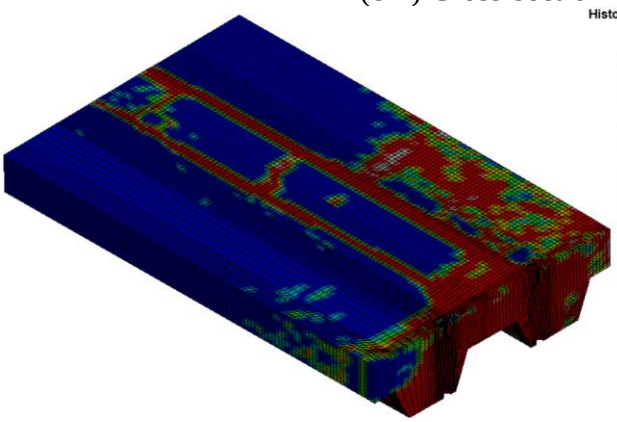

(c-3) Concrete slab top

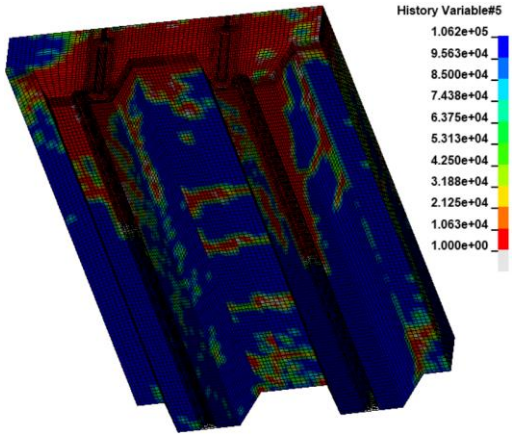

(c-4) Concrete slab bottom

(c) Percentage of applied force of 75% (UX = 2.75 mm)

Figure 3.57 Continued.

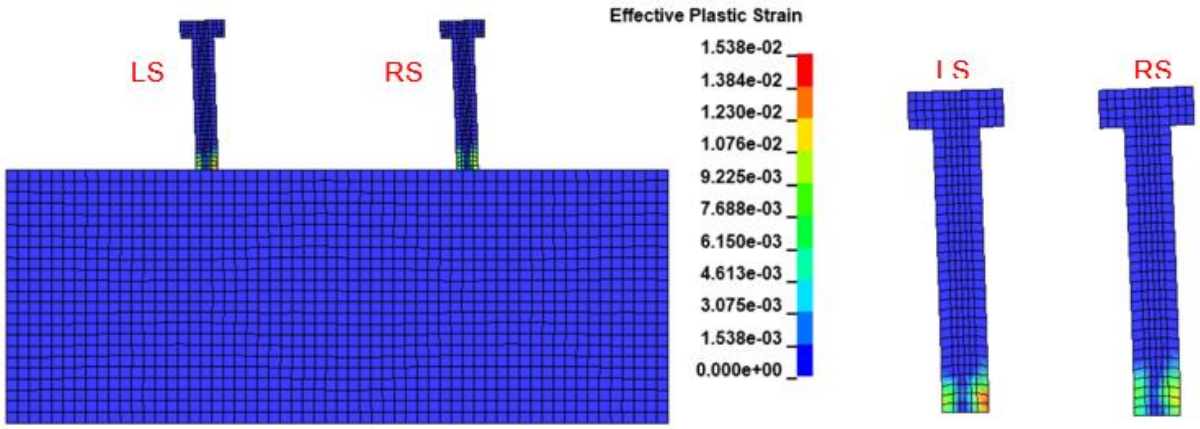

(d-1) Plastic deformation of the shear stud

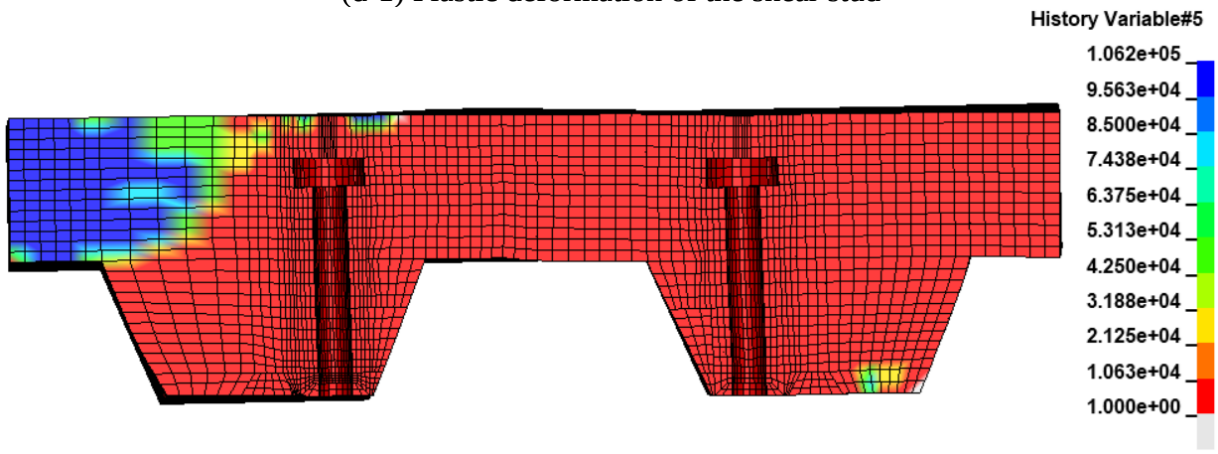

(d-2) Cross-section of the concrete slab

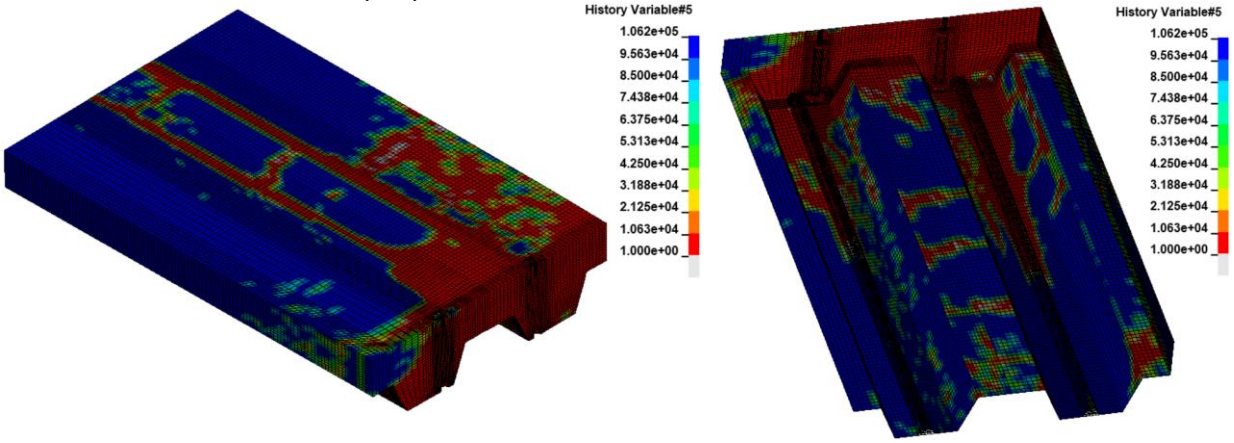

(d-3) Concrete slab top (d-4) Concrete slab bottom

(d) Percentage of applied force of 100% (UX = 5 mm)

Figure 3.57 Continued.

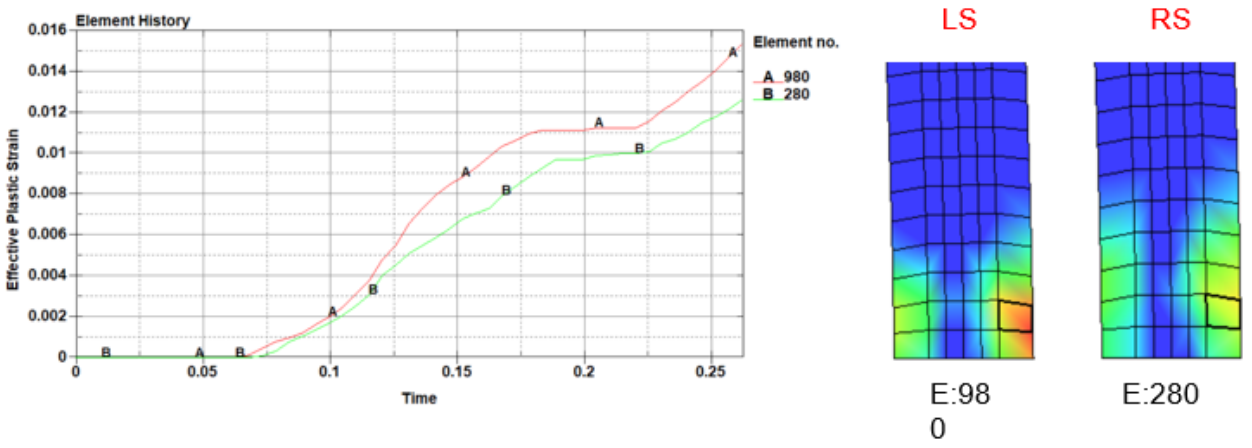

Figure 3.58 History of plastic deformation of the shear stud.

3.6.2 ***Results comparison.***

Figure 3.59 shows the comparison of the force-displacement curves for the different models, and Table 3.2 shows the different relevant parameters of each model. It is important to note that all of these cases were dominated by the failure of the concrete around the studs. Some of the variability in the results and the lack of smooth curves in Figure 3.39 can be attributed to the difficulty in tracking the concrete failure in these specimens.

Figure 3.61 shows a high variability of the behavior for each of the models, indicating that the position of the studs has a significant influence on the global behavior of the pushout tests. The TS-II.b model, which has both shear studs in a strong position with respect to the load condition in the concrete, reaches the maximum resistance (127kN) among the different models studied. This agrees with experimental findings by (Easterling, 1993). Table 3.2 shows that the weak-weak configuration supports a maximum load of 55% relative to the strong-strong configuration.

The TS-I, TS-IV and TS-III models (in order of resistance) present a combination of the strong and weak positions of the shear studs; the resistance of these models is in intermediate values to those found for the strong-strong and weak-weak configurations.

It is important to note that the plastic strains in the shear studs of conventional structures do not exceed 10%. Due to the fact that a material failure model was not defined by maximum plastic deformation, some of the numerical models studied reached deformations greater than 10%, as was the case of the TS-III and T-II.a models (Table 3.2).

Regarding the deformation modes, it was observed that the deformation patterns for the TS-II.b, TS-I and TS-IV models correspond to a bending behavior, while for the TS-III and TS-II models. a shear strain pattern is observed (Table 3.3, Figure 3.59)

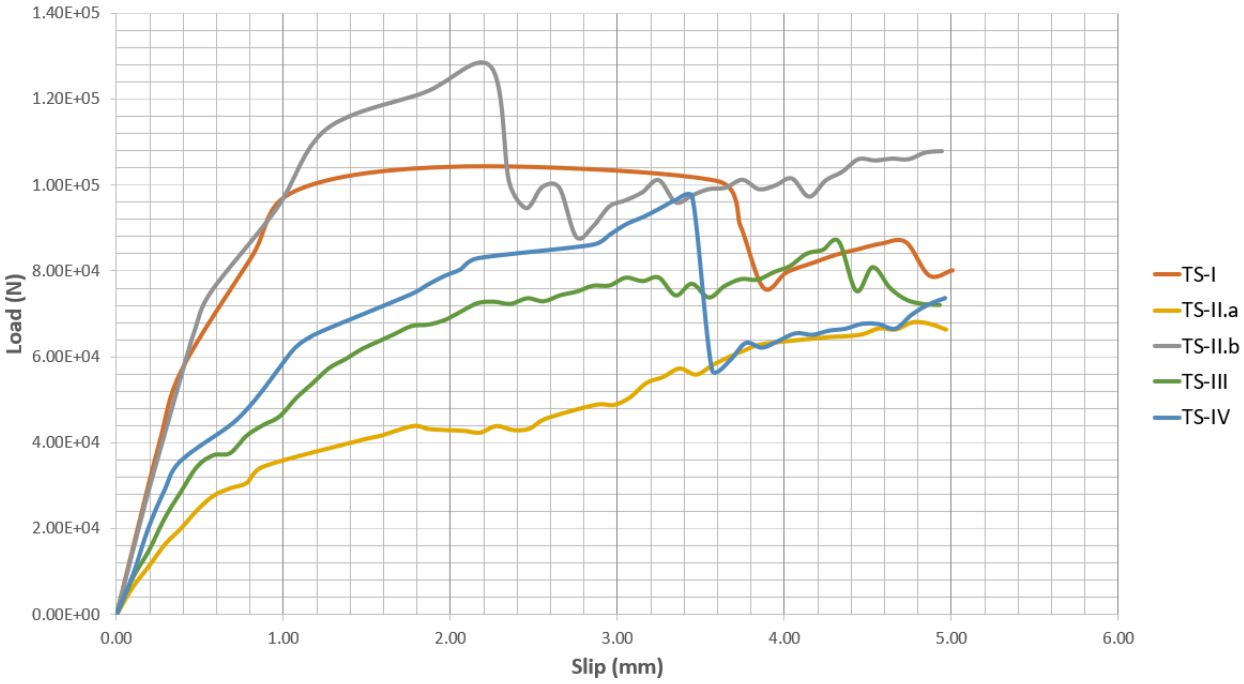

Figure 3.59 Load vs Slip comparison.

Table 3.2 Results comparison.

Model	Right Stud Position	Left Stud Position	Max. Load (KN)	Percentaje to Max Load	Stud Max. Plastic Strain	Deformation Mode for Most Deformed Stud
TS-II b	Strong	Strong	127	100%	2.05%	Bending
TS-I	Strong	Weak	105	83%	1.18%	Bending
TS-IV	Strong	Weak	97	76%	1.53%	Bending
TS-III	Weak	Strong	87	69%	23.08%	Shear
TS-II a	Weak	Weak	70	55%	12.27%	Shear

Table 3.3 Comparison of deformation modes.

Plastic Strain Contour			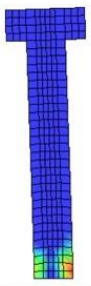	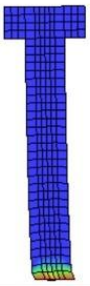	
Model	TS-II b	TS-I	TS-IV	TS-III	TS-II a
Load Direction					

3.6.3 Validation of the numerical model (FT)

To verify the numerical results and validate its behavior, the force vs displacement curve was compared with the experimental analysis for the NIST test. The displacement was measured in the vertical direction in a node in the center of the beam. The measured force corresponds to what is applied to the central actuator, considering the full geometry. The results are shown in Figure 3.60. In general, the numerical model can capture the maximum resistance of the system with 98% accuracy. However, there is a trajectory difference after the model reaches 36k N, that is, 57% of the experimental resistance. This variation in stiffness between both curves is mainly due to the non-linear behavior of the interface between the concrete and the structural steel, the presence of residual stresses, dynamic effects, the initial imperfections in the geometry of the specimen, and the boundary conditions, and the load settings. Efforts are ongoing to solve this discrepancy.

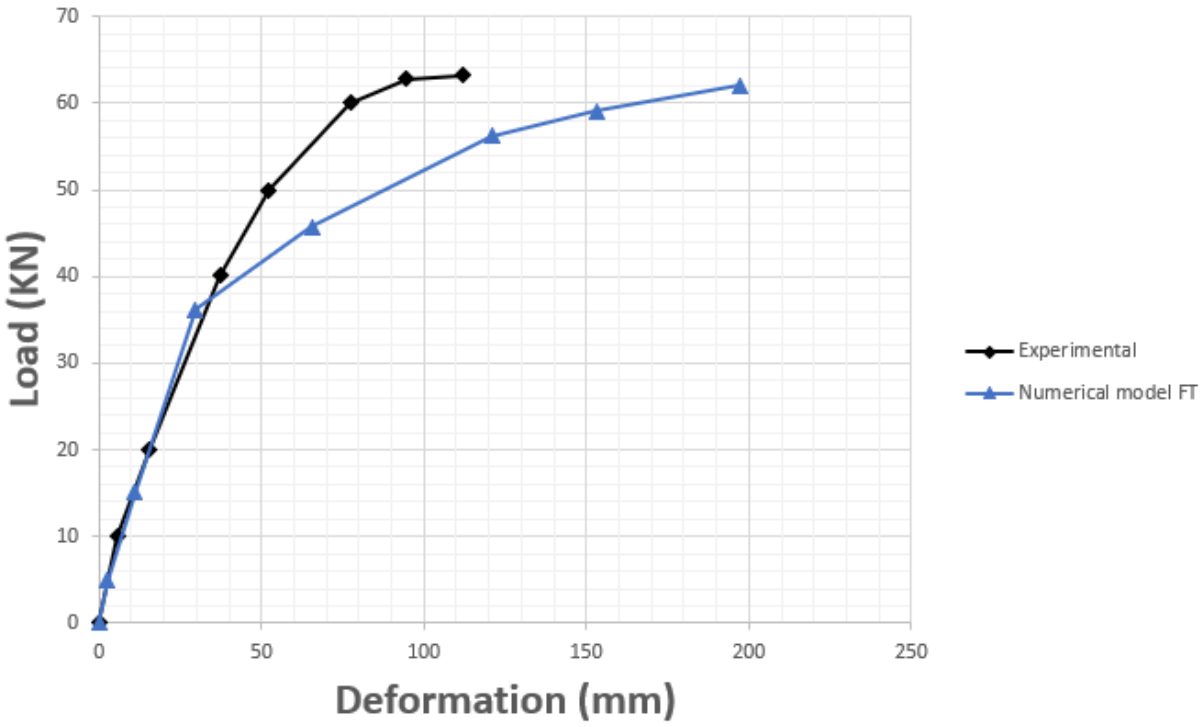

Figure 3.60 Force vs displacement results.

Figure 3.61 corresponds to the moment of sudden failure of the stud located at the end of the beam, at this moment the system has a load of 62 kN. It is observed that the stress concentrations for this instant tend to zero in Stud-3, but stress concentrations are present in stud-1 and 2 (Figure 3.62). The above can also be observed qualitatively as the Stud-3 separates from the concrete.

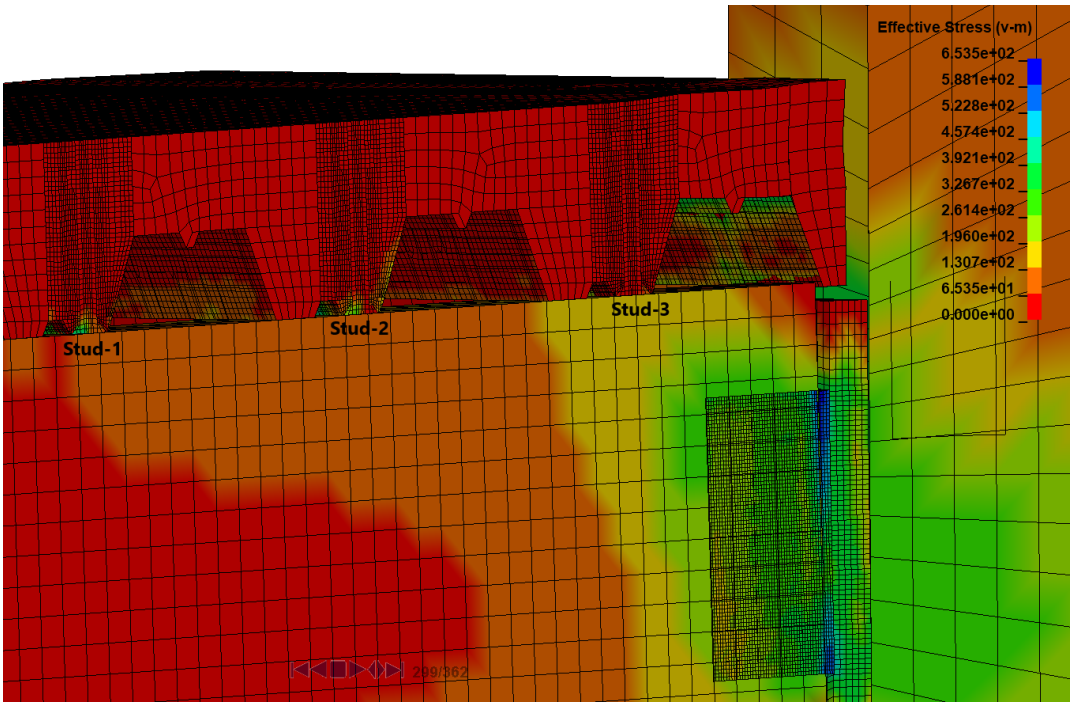

Figure 3.61 Contour of stress for a load of 62 kN.

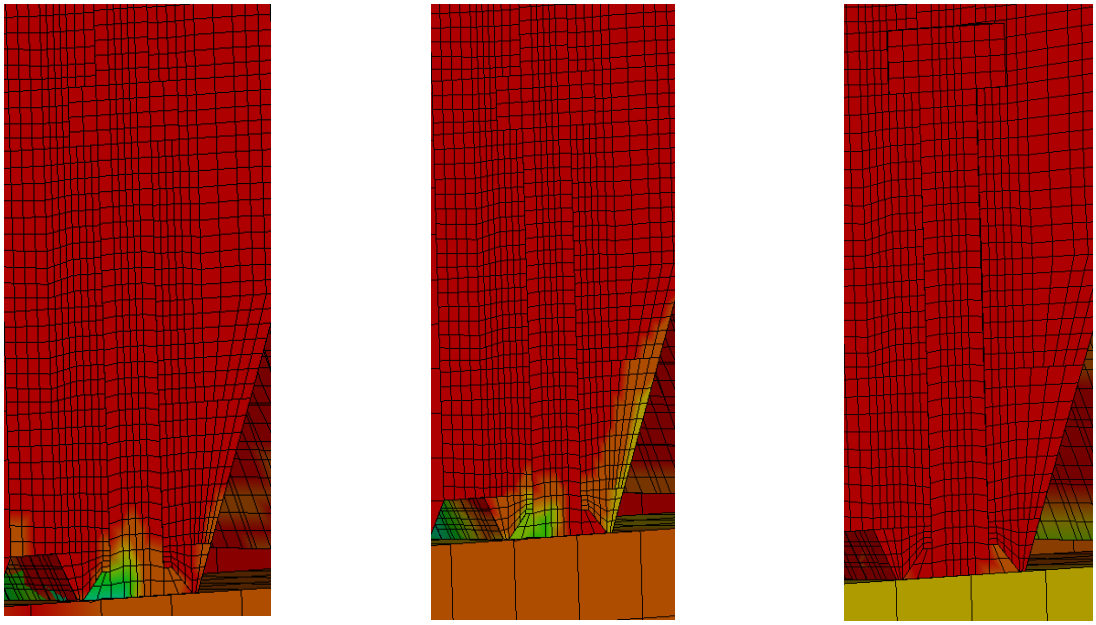

Stud-1 Stud-2 Stud-3

Figure 3.62 Contour of stress in the studs for a load of 63 kN.

The plastic strain condition over time was evaluated on the weld toe of the second and third studs, as shown in Figure 3.63. It is worth mentioning that the first stud includes a bonded contact with failure with the steel deck. It can be seen that there is no plastic straining on the first stud. This is caused by the failure of the contact before plastic strain appears, which corresponds with the brittle failure reported for the experimental analysis.

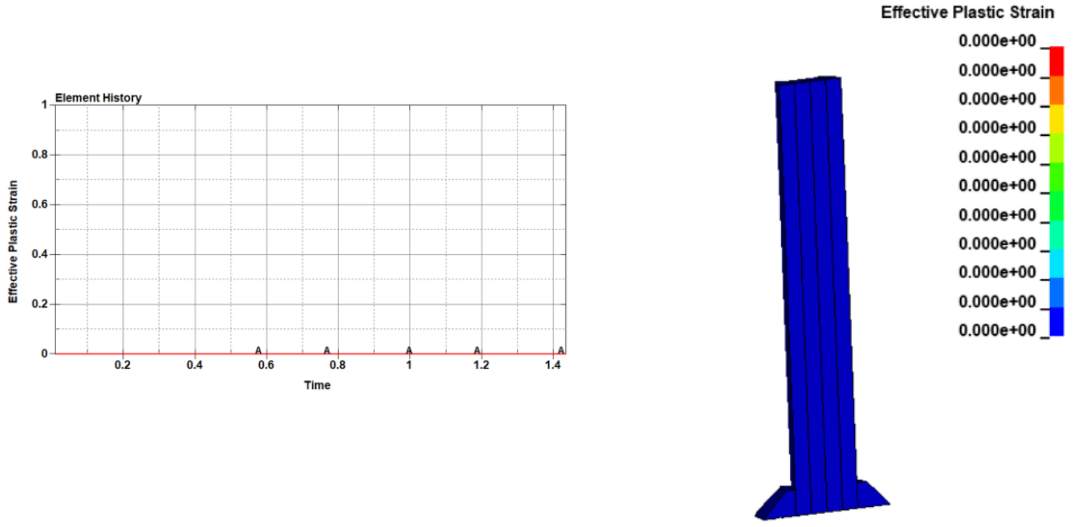

a) Plastic strain over time b) Plastic strain at the end time

Figure 3.63 Condition for Stud-3.

In contrast for the second stud, contact failure was not enabled for the stud steel-deck interface, so that larger loads can act on this stud. The plastic strain for the second stud is shown in Figure 3.64:

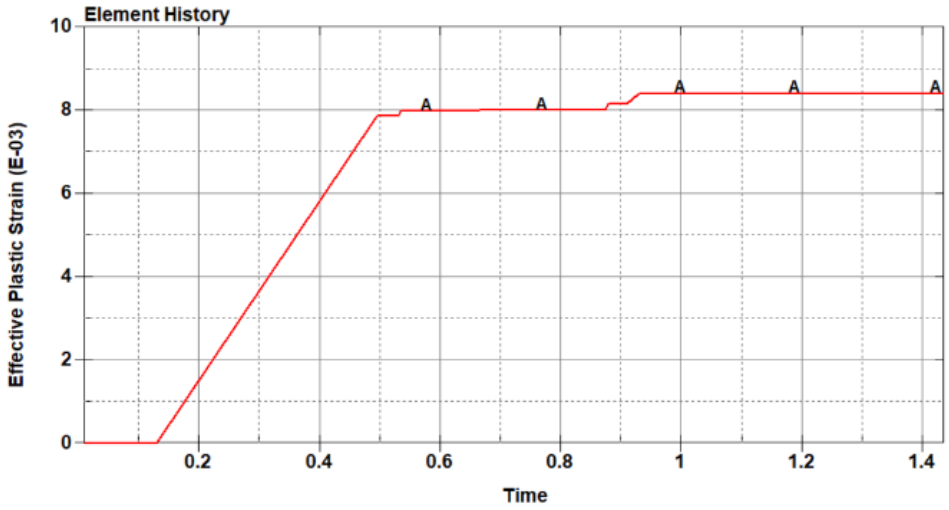

(a) History of plastic deformation of the shear stud.

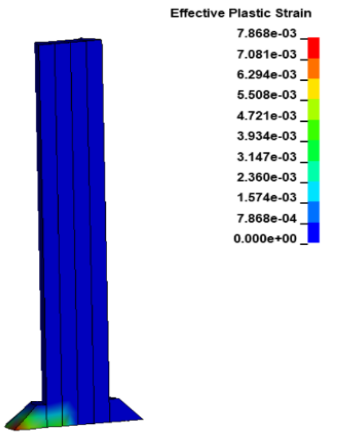

F=20 kN

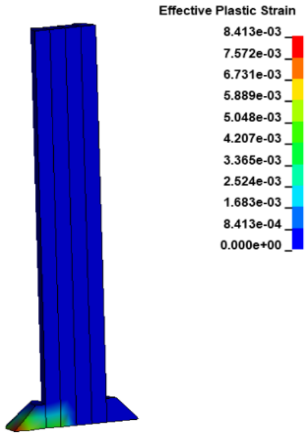

F=44 kN

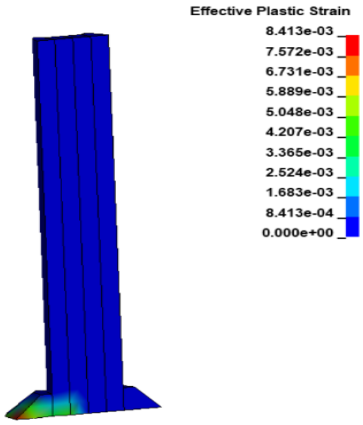

F=50 kN

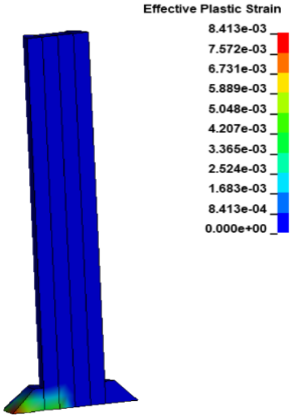

F=62 kN

(b) Plastic deformation

Figure 3.64 Condition for Stud-2.

The vertical displacement contour corresponding to a load of 60 kN is shown in Figure 3.65:

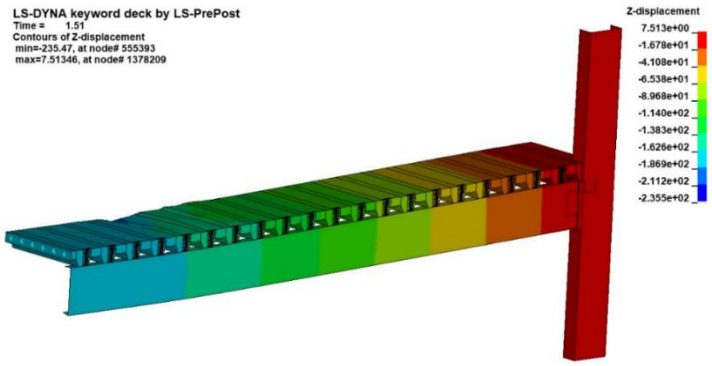

Figure 3.65 Vertical displacement of the beam for an actuator load of 60 kN.

The experimental results correspond to those the first peak obtained in the test, are shown in Figure 3.66.

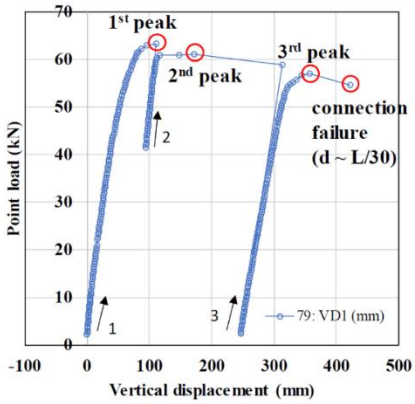

Figure 3.66 Experimental Force vs Displacement Results.

The experimental applied load on one actuator is shown in Figure 3.67.

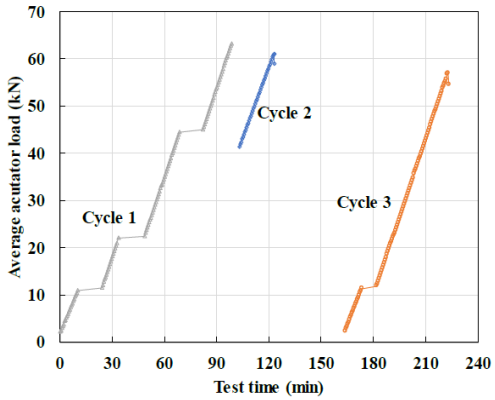

Figure 3.67 Load cycles on the actuator.

Some observations from the comparison between the experimental and the numerical model are:

- The maximum load of the beam is properly captured.

- There are some differences in stiffness between the experimental and the numerical model. Initially the numerical model seems stiffer, and it turns softer after a vertical displacement of approximately 50 mm. This could be caused by dynamic effects on the solution. The numerical model was loaded at a rate of 10 kN/s (per actuator), while the experimental panel was loaded at a rate of 2.2 kN/min (per actuator). Reducing the loading rate may allow more accurate results.

- It can be seen that the numerical model doesn't capture the reduction of the load that can be handle by the beam, there are a couple of factors that explain this behavior:

    - In the numerical model no ultimate resistance was presupposed, so the applied load is just one load cycle up to 200 kN per actuator. This way, the load will always increase so that failure will be capture as a significant reduction of the stiffness of the beam, as it can be seen on the numerical force vs displacement curve (Figure 3.68).

    - Two failure modes were identified on the experimental analysis, brittle failure of the first stud (Figure 3.68.a) and welding failure in the double angle connection (Figure 3.68.b). The authors of the report mentioned that the failure of the first stud was the cause of the reduction of the load capacity of the beam and the connection failure appears afterwards. To validate the influence of the stud failure on the general behavior of the beam, two numerical models were compared, one with a stud-steel deck contact resistance of 530 MPa and a second one with a resistance of 270 MPa. The results are shown in the Figure 3.69. It can be seen that the resistance of the connection stud – steel deck doesn't have a significant influence over the general behavior of the beam. Given the obtained results, it could be possible that the double angle connection started earlier and could be the failure mode that caused the reduction of the load capacity of the beam. The Figure 3.70 shows the stress levels on the studs, for the model with a stud-steel deck contact resistance of 530 MPa and an actuator load of 60 kN, the low stress level in the first stud shows that the contact already failed for this load level.

(a) First Stud (b) Double Angle Connection

Figure 3.68 Failures in the experimental analysis.

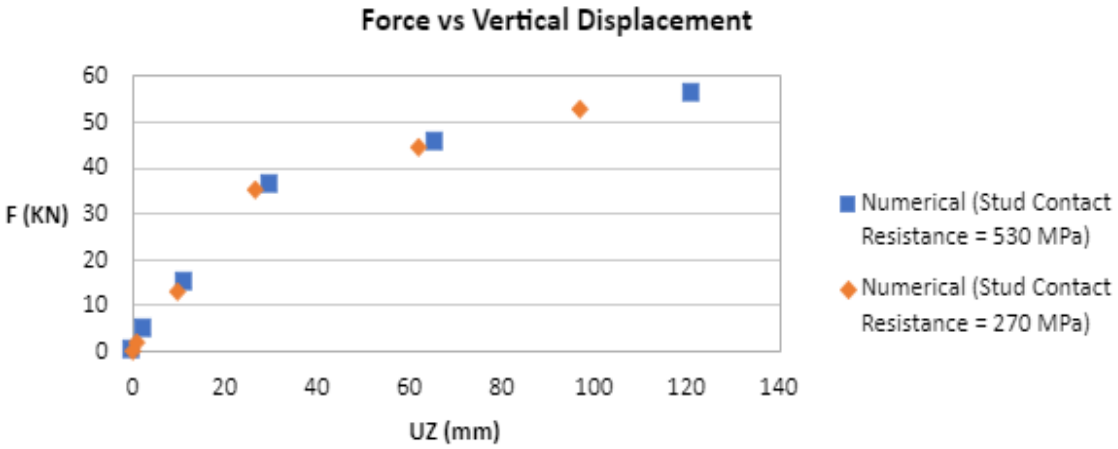

Figure 3.69 Force vs Displacement for Different Resistance of the Stud – Steel Deck Contact.

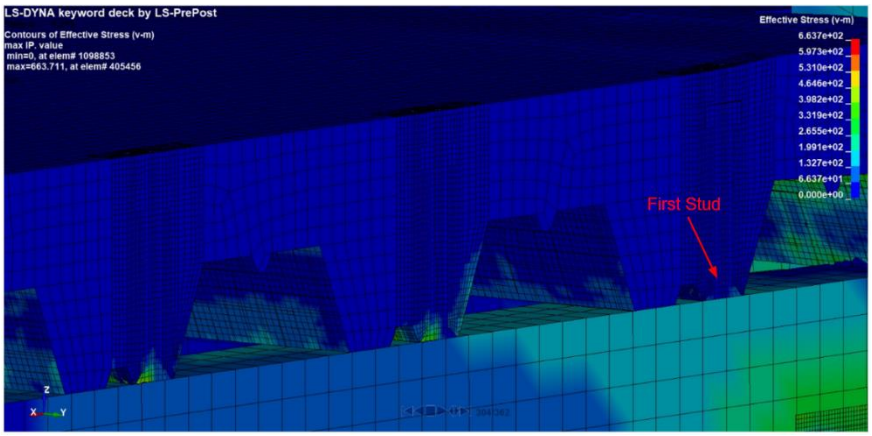

Figure 3.70 Stress Levels at the Root of the Beam.

In general, it can be seen that the numerical model is capable of capturing the maximum strength of the beam and allows to analyze complex behaviors as the failure modes bringing valuables insights of the mechanisms involved. Additional analyses could be performed in order to improve the accuracy of the results, specifically the reducing the load rate. Also, it could be valuable to include a failure model of the welding to validate the influence of this mechanism on the general behavior of the beam.

3.7. Conclusions

The chapter presents a report of rigorous investigations on the nonlinear structural behavior of composite beam systems, considering shear connectors as the main variable. These investigations have helped determine and improve design parameters, which are very difficult or cannot be determined through experimental investigations.

The results of the numerical model of the pushouts indicate that the strong or weak position of the shear determines to a large extent the structural behavior of this type of system, for which a great variability in the force-slip curves of the models was obtained. The Models can reproduce the non-linear behavior of steel and concrete materials, as well as the modes of deformation.

The TS-II.b model, which has both shear studs in a strong position with respect to the load condition in the concrete, reaches the maximum strength (127kN) among the different models studied. This agrees with the experimental results of (Easterling,1993). The predominant mode of deformation in these systems is shear stud bending.

The results of the numerical model of the beam indicate that it is capable of capturing the maximum resistance of the beam and allows the analysis of complex behaviors since the failure modes provide valuable information about the mechanisms involved.

It should be noted that the nature and extent of the damage suffered may vary due to the geometric characteristics and the load applied on the beam, that is, point or distributed load. Therefore, it is difficult to generalize the response and damage evolution of a composite beam and even more so considering the stud distribution. Detailed numerical or experimental studies are needed to realistically simulate the response and damage of a composite beam.

Chapter 4.

4. Conclusions

This research presents the development of several advances in the numerical modeling of composite steel-concrete connections, considering different structural configurations and types of loads through two specific objectives that correspond to the different chapters of this thesis:

(i) To evaluate by means of three-dimensional nonlinear finite element models the behavior of CFTs-connections.

(ii) To develop three-dimensional finite elements to study the influence of shear studs on the structural behavior of composite beams with trapezoidal profiled sheets.

Although the numerical models considered throughout this investigation are very different from each other and sensitive to the assumptions of the model, the results show that the geometry and failures observed, especially the one that occurs at the steel-concrete interface, can be represented by careful numerical models. The results show that the developed numerical models can reproduce the most important behavioral aspects observed in the tests, such as the buckling of the thin unfilled specimens, the effect of partial filling, deformation, and failure of the shear studs, and the evolution of the deformation and resistance. The ability of the models to track the transition points in the load-strain curves will also lead to the inference that the model can track the steel-concrete interaction well. The results also highlight the great advantages that connection filling provides in terms of retarding buckling and more fully utilizing the strength and stiffness of the steel.

The first objective of this dissertation (Chapter II) was addressed through a brief review of testing and analyses of concrete-filled connections, the description of a database comprising 135 tests, and the development of a numerical model capable of capturing the most relevant behavior modes up to the ultimate strength and deformation capacity of these connections. These behavioral modes include, among others, local buckling of the steel tubes and friction/contact resistance between steel and concrete. This model is calibrated against a single test and its performance is verified against three other very different tests available in the literature. The numerical models can reproduce the most important behavioral aspects observed in the tests, such as the buckling of the thin unfilled specimens, the effect of partial filling, and the evolution of deformation and resistance. The ability of the models to track the transition points in the load-strain curves will also lead to the inference that the model can track the steel-concrete interaction well. The results also highlight the great advantages that connection filling provides in terms of retarding buckling and more fully utilizing the strength and stiffness of the steel.

Finally, considering that the resistance between concrete and steel is a fundamental parameter when determining the maximum resistance of composite elements, the results show that these values seem to be in a range of 5-10% of the compressive resistance value of the concrete.

The second objective of this dissertation (Chapter III) was to develop three-dimensional finite elements to study the influence of shear studs on the structural behavior of composite beams with

trapezoidal profiled shells. These studies are achieved by comparing the numerical models developed using the best models of materials, elements, and analysis procedures available in Ansys-Ls Dyna with the experimental research carried out by the National Institute of Standards and Technology.

Chapter 3 first describes rigorous experimental investigations on the nonlinear structural behavior of composite beam systems, considering studs as the main variable. Then, Chapter III presents a detailed description of the numerical modeling of composite beams. Initially, a single-stud numerical model is developed and compared with experimental results. The numerical model managed to capture the maximum force and the damage modes presented in the experimental investigation. After this, alternative structural configurations are proposed, especially shear stud distributions according to their strong or weak position with respect to the load application in the system to model and evaluate its structural behavior. Subsequently, a validation of the beam tested by NIST was carried out considering only gravitational loads.

In summary, the developed numerical models can well track behavior reported in selected experimental investigations, including transition points in load-strain curves, ultimate strength, and maximum strain. The different numerical models incorporate non-linearity in all their elements considering shear, axial, and bending loads. For the numerical models developed in Chapters II and III, contact resistance between the steel and the concrete between 5% and 10% was assumed. Although the numerical models developed are very different in their geometric configurations and remain sensitive to the assumptions of the model, the results consistently show that the structural behavior of composite elements depends largely on the contact resistance assumed in the modeling. In addition, the numerical models were able to predict the large stress concentrations around the weld beads. However, with these numerical models, it is not possible to capture the fracture of the weld bead or the steel and concrete elements.

4.1. Impact and contributions

The present research project is distinct in several ways. Some points that make this project unique include:

- The structural behavior of different composite structural systems is evaluated considering the influence of the resistance of the steel-concrete contact.
- A base of 135 tests of composite connections is provided considering factors such as the type of connection, type of load, materiality, etc. This database can be used in the future to understand the grand challenges to evaluate the performance of other bridge design arrangements.
- The work indicates that for good modeling of composite structures it is necessary to incorporate the failure between the steel-concrete interface through a non-linear contact element.
- The work indicates that the position (strong or weak) of the studs has a significant influence on the structural behavior of composite beams.

4.2. Suggested topics for future research studies

The present research study aimed to include many of the main parameters that influence the numerical modeling of composite elements considering different structural configurations and types of loads. However, there are still some uncertainties and unexplored issues that were not included or studied in this project. The following list summarizes some of the topics that may be explored in future research studies:

• Detailed numerical or experimental studies are needed to realistically simulate the structural response and damage of composite elements under different types of loads, considering geometric configurations different from those evaluated in this research.

• Experimentally evaluate and calibrate pushout test case studies varying the position of the studs and the location of the lateral elements that confine the system. These results should be compared with those obtained in this investigation.

• Experimental and analytical determination of the influence of the impact of the steel-concrete contact resistance.

• Experimental campaigns should be carried out on the elements studied here (ie, connections, beams, etc) to analyze their structural response.

References

ACI 318-19, 2019, 2019. Building Code Requirements for Structural Concrete (ACI 318-19). American Institute Concrete.

Adhikari, S., Rassati, G., Swanson, J., and Chicchi, R., 2021. HIGH-DEFINITION MODELING OF COMPOSITE BEAMS. In M. Knobloch, U. Kuhlmann, W. Kurz, and M. Schafer (Eds.), *9th International Conference on Composite Construction in Steel and Concrete*. Stromberg, Germany.

AISC, 2010. *Specification for structural steel buildings. American Institution of Steel Construction (AISC) ANSI/AISC 360-10*. Chicago, Illinois.

AISC 360-16, 2016. Specification for Structural Steel Buildings, an American National Standard. *American Institute of Steel Construction, Chicago*, 612.

AISC 360-16, A., 2016. *Specification for Structural Steel Buildings*. Chicago, Illinois.

AISI S923-20, 2020. Test Standard for Determining the Strenght and Stiffness of Shear Connections of Composite Members. American Iron and Steel Institute (AISI).

Alsamsam, I., 1991. *SERVICEABILITY CRITERIA FOR COMPOSITE FLOOR SYSTEMS (PhD thesis)*. UNIVERSITY OF MINNESOTA.

American Institute of Steel Construction, 2001. *MANUAL of STEEL CONSTRUCTION. Load and Resistance Factor Design (Third Edition)*.

ANSYS, 2020. ANSYS Explicit Dynamics Analysis Guide. Canonsburg, PA 15317. Retrieved from http://www.ansys.com

Arizumi, Y., Hamada, S., and Tateo, K., 1981. Elastic-plastic analysis of composite beams with incomplete interaction by finite element method. *Computers and Structures*, **14**(5–6), 453–462. DOI: 10.1016/0045-7949(81)90065-1

Balasubramanian, R., and Rajaram, B., 2016. Study on behaviour of angle shear connector in steel-concrete composite structures. *International Journal of Steel Structures*, **16**(3), 807–811. DOI: 10.1007/s13296-015-0094-0

Baskar, K., Shanmugam, N. E., and Thevendran, V., 2002. Finite-Element Analysis of Steel–Concrete Composite Plate Girder. *Journal of Structural Engineering*, **128**(9), 1158–1168. DOI: 10.1061/(asce)0733-9445(2002)128:9(1158)

Chung, K. F., and Chan, C. K., 2011. Advanced finite element modelling of composite beams with high strength materials and deformable shear connectors. *Procedia Engineering*, **14**, 1114–1122. Elsevier B.V. DOI: 10.1016/j.proeng.2011.07.140

Cosenza, E., and Mazzolani, F., 1993. Linear Analysis of Composite Beams with Deformable Connectors. *Proceedings of the First Italian Workshop on Composite Structures*. University of Trento, 1993 (in Italian).

Courant, R., Friedrichs, K., and Lewy, H., 1967. On the Partial Difference Equations of Mathematical Physics. *IBM Journal*, **11**, 215–234.

Davies, C., 1969. Tests on half-scale steel–concrete composite beams with welded shear connectors. *Structural Eng.*, **47**(1), 20–40.

Easterling, W. S., Gibbings, D. R., and Murray, T. M., 1993. Strength of shear studs in steel deck on composite beams and joists. *Engineering Journal*, **30**(2), 44–54.

El-Lobody, E., and Lam, D., 2003. Finite Element Analysis of Steel-Concrete Composite Girders. *Advances in Structural Engineering*, **6**(4), 267–281. DOI: 10.1260/136943303322771655

Ellobody, E., and Young, B., 2006. Performance of shear connection in composite beams with

profiled steel sheeting. *Journal of Constructional Steel Research*, **62**(7), 682–694. DOI: 10.1016/j.jcsr.2005.11.004
EUROPEAN COMMITTEE FOR STANDARDIZATION. EN 1994-1-1, 2004. Eurocode 4: Design of composite steel and concrete structures.
Fisher, J., 1970. Design of Composite Beams With Formed Metal Deck. *Eng J Amer Inst Steel Constr* (Vol. 7, pp. 88–96).
Gautam, B. G., Xiang, Y., Liao, X., Qiu, Z., and Guo, S., 2019. Experimental Investigation of a slip in high-performance steel-concrete small box girder with different combinations of group studs. *Materials*, **12**(7), 1–18. DOI: 10.3390/ma12172781
Green, T. P., Leon, R. T., and Rassati, G. A., 2004. Bidirectional Tests on Partially Restrained, Composite Beam-to-Column Connections. *Journal Structural Engineering*, **130**(2), 320–327. DOI: 10.1061/(ASCE)0733-9445(2004)130:2(320)
Guezouli, S., and Lachal, A., 2012. Numerical analysis of frictional contact effects in push-out tests. *Engineering Structures*, **40**, 39–50. Elsevier Ltd. DOI: 10.1016/j.engstruct.2012.02.025
Hallquist, J., 2006. LS-DYNA. California. DOI: 10.1002/ima.22028
Hawkins, N. M., and Mitchell, D., 1984. Seismic Response of Composite Shear Connections. *Journal of Structural Engineering*, **110**(9), 2120–2136. DOI: 10.1061/(asce)0733-9445(1984)110:9(2120)
Heins, C. P., and Kuo, J. T. C., 1975. Ultimate Live Load Distribution Factor For Bridges. *Journal of the Structural Division, ASCE*, **101**(July), 1481–1496.
Hicks, S. J., and Smith, A. L., 2014. Stud shear connectors in composite beams that support slabs with profiled steel sheeting. *Structural Engineering International: Journal of the International Association for Bridge and Structural Engineering (IABSE)*, **24**(2), 246–253. DOI: 10.2749/101686614X13830790993122
Hirst, M. J. S., and Yeo, M. F., 1980. The analysis of composite beams using standard finite element programs. *Computers and Structures*, **11**(3), 233–237. DOI: 10.1016/0045-7949(80)90163-7
ICC, 2018. International Code Council. Retrieved from https://codes.iccsafe.org/codes
Irwan, J. M., Hanizah, A. H., Azmi, I., and Koh, H. B., 2011. Large-scale test of symmetric cold-formed steel (CFS)concrete composite beams with BTTST enhancement. *Journal of Constructional Steel Research*, **67**(4), 720–726. Elsevier Ltd. DOI: 10.1016/j.jcsr.2010.11.008
Johnson., R. P., 1970. Research on Composite Steel-Concrete Beams. *Journal of the Structural Division, ASCE*, **96**, 445–459.
Johnson, R., 1971. Composite structures of steel and concrete: beams, slabs, columns and frames for building. *Oxford: Blackwell Scientific Publications*, **1**.
Katwal, U., Tao, Z., Hassan, M. K., Uy, B., and Lam, D., 2020. Load sharing mechanism between shear studs and profiled steel sheeting in push tests. *Journal of Constructional Steel Research*, **174**, 106279. Elsevier Ltd. DOI: 10.1016/j.jcsr.2020.106279
Kostem, C. N., 1988. *Overloading behavior of steel multigirder highway bridges final report*. Bethlehem, Pennsylvania.
Lam, D., and El-Lobody, E., 2005. Behavior of Headed Stud Shear Connectors in Composite Beam. *Journal of Structural Engineering*, **131**(1), 96–107. DOI: 10.1061/(asce)0733-9445(2005)131:1(96)
Lapoujade, V., Mouteliere, C., Millecamps, A., Point, R., Ravaud, R., and Cramayel, F.-M.,

2014. Advanced MPP Decomposition of a SPH Model. *13th International LS-DYNA Users Conference*, 1–18.

Lee, M. J., Kwak, H. G., and Park, G. K., 2021. An improved calibration method of the K&C model for modeling steel-fiber reinforced concrete. *Composite Structures*, **269**(October 2020), 114010. Elsevier Ltd. DOI: 10.1016/j.compstruct.2021.114010

Leon, R. T., and Viest, I. M., 1997. Theories of Incomplete Interaction, Composite Construction in Steel and Concrete III, B. Shahrooz and D. Buckner (eds.), ASCE, New York: 858-870. In B. Shahrooz and D. Buckner (Eds.), *Composite Construction in Steel and Concrete III* (pp. 858–870). New York: ASCE.

Leskela, M. V., 2017. *Shear Conenction in Composite Flexural Members Of Steel and Concrete*.

Liu, X., Bradford, M. A., Chen, Q. J., and Ban, H., 2016. Finite element modelling of steel-concrete composite beams with high-strength friction-grip bolt shear connectors. *Finite Elements in Analysis and Design*, **108**, 54–65. Elsevier. DOI: 10.1016/j.finel.2015.09.004

M.Irwan, J., Hanizah, A. H., and Azmi, I., 2009. Test of shear transfer enhancement in symmetric cold-formed steel-concrete composite beams. *Journal of Constructional Steel Research*, **65**(12), 2087–2098. Elsevier Ltd. DOI: 10.1016/j.jcsr.2009.07.008

Maleki, S., and Bagheri, S., 2008. Behavior of channel shear connectors, Part I: Experimental study. *Journal of Constructional Steel Research*, **64**(12), 1333–1340. DOI: 10.1016/j.jcsr.2008.01.010

Malvar, L. J., Crawford, J. E., Wesevich, J. W., and Simons, D., 1997. A plasticity concrete material model for DYNA3D. *International Journal of Impact Engineering*, **19**(9–10), 847–873. DOI: 10.1016/s0734-743x(97)00023-7

Markovich, N., Kochavi, E., and Ben-Dor, G., 2009. Calibration of a Concrete Damage Material Model in LS-Dyna for a Wide Range of Concrete Strengths. *IWSRIB_2009_Haifa*.

Moffatt, K. R., and Lim, P. T. K., 1976. Finite Element Analysis of Composite Box Girder Bridges Having Complete or Incomplete Interaction. *Proc Inst Civ Eng (Lond)*, **61**(pt 2), 1–22. DOI: 10.1680/iicep.1976.3500

Mujagic, J. R. U., Easterling, W. S., Bennett, J. S., and Varma, A. H., 2015. *Assessment of Shear Connection Ductility in Composite Beams – Implications on the U.S. Design Practice* (Vol. 2016). Blacksburg, VA.

Mujagic, U., 2004. *DESIGN and BEHAVIOR of COMPOSITE STEELCONCRETE FLEXURAL MEMBERS with a FOCUS on SHEAR CONNECTORS (PhD thesis)*. Virginia Polytechnic Institute and State University.

Nelson, T., 1946. United States Patent Office - 2,402,659. San Leandro, California (USA).

Newmark, N. M., Siess, C. P., and Viest, I. M., 1951. Tests and analysis of composite beams with incomplete interaction. *Proceedings Society Experimental Stress Analysis* (pp. 75–92).

Oehlers, D. J., 1989. Splitting Induced by Shear Connectors in Composite Beams. *Journal of Structural Engineering*, **115**(2), 341–362. DOI: 10.1061/(asce)0733-9445(1989)115:2(341)

Oehlers, D. J., and Bradford, M. A., 1995. *COMPOSITE STEEL, AND CONCRETE STRUCTURAL MEMBERS. Fundamental Behaviour*. (PERGAMON, Ed.). Sidney.

Oguejiofor, E. C., and Hosain, M. U., 1997. Numerical analysis of push-out specimens with perfobond rib connectors. *Computers and Structures*, **62**(4), 617–624. DOI: 10.1016/S0045-7949(96)00270-2

Oudheusden, A. J., 1971. Composite Construction- Applications. *International Specialty Conference on Cold-Formed Steel Structures. 1.* (pp. 173–178).

Qureshi, J., 2010. *Finite element modelling of steel-concrete composite structures (PhD thesis)*.

The University of Leeds.
Rambo-Roddenberry, M. D., 2002. *BEHAVIOR AND STRENGTH OF WELDED STUD SHEAR CONNECTORS (PhD thesis)*. Virginia Polytechnic Institute and State University.
Rambo-Roddenberry, M., Lyons, J. C., Easterling, W. S., and Murray, T. M., 2002. Performance and strenght of welded shear studs. *Composite Construction in Steel and Concrete.* (pp. 458–469).
Ramesh, S., Choe, L., Seif, M., Hoehler, M., Grosshandler, W., Sauca, A., Bundy, M., et al., 2019. *Compartment Fire Experiments on Long-Span Composite-Beams with Simple Shear Connections Part 1 : Experimental Design and Beam Behavior at Ambient Temperature NIST Technical Note 2054 Compartment Fire Experiments on Long-Span Composite-Beams with Simple Sh*. DOI: 10.6028/NIST.TN.2054
Razaqpur, A. G., and Nofal, M., 1989. A finite element for modelling the nonlinear behavior of shear connectors in composite structures. *Computers and Structures*, **32**(1), 169–174. DOI: 10.1016/0045-7949(89)90082-5
Robinson, H., and Narieane, K. S., 1988. "Slip and Uplift Effects in Composite Beams," in Composite Construction. *Proceedings of an Engineering Foundation Conference, ASCE* (pp. 487–497). New York.
Roeder, C., 1984. Shear Transfer from Pushout Tests of Composite Columns. *Second U.S. – Japan Joint Seminar on Composite and Mixed Construction* (p. 339). Seattle, Washington, United States.
S. Balakrishnan., 1962. *The behavior of Composite Steel and Concrete Beams with Welded Shear Connectors*. London University.
Di Sarno, L., and Elnashai, A. S., 2005. Innovative strategies for seismic retrofitting of steel and composite structures. *Progress in Structural Engineering and Materials*, **7**(3), 115–135. DOI: 10.1002/pse.195
Selden, K. L., Varma, A. H., and Mujagic, J. R., 2015. Consideration of Shear Stud Slip in the Design of Partially Composite Beams. *Structures Congress 2015* (pp. 888–899).
Slutter, R. G., and Driscoll, G. C., 1965. Flexural Strength of Steel-Concrete Composite Beams. *Journal of the Structural Division, ASCE*, (91), 71–99.
Tahmasebinia, F., Ranzi, G., and Zona, A., 2013. Probabilistic three-dimensional finite element study on composite beams with steel trapezoidal decking. *Journal of Constructional Steel Research*, **80**, 394–411. Elsevier Ltd. DOI: 10.1016/j.jcsr.2012.10.003
Tan, E. L., and Uy, B., 2009. Experimental study on straight composite beams subjected to combined flexure and torsion. *Journal of Constructional Steel Research*, **65**(4), 784–793. Elsevier Ltd. DOI: 10.1016/j.jcsr.2008.10.006
Thevendran, V., Chen, S., Shanmugam, N. E., and Richard Liew, J. Y., 1999. Nonlinear analysis of steel-concrete composite beams curved in plan. *Finite elements in analysis and design*, **32**(3), 125–139. DOI: 10.1016/S0168-874X(99)00010-4
Thurumann, B., 1985. Composite Beams with Stud Shear Connectors. *Highway Research Board, National Academy of Science*, **174**, 18–38.
Viest, I. M., 1960. Review of Research on Composite Steel-Concrete Beams. *Journal of the Structural Division, ASCE,* 1–21.
Viest, I. M., Colaco, J. P., Furlong, R. W., Griffs, L. G., Leon, R. T., and Wyllie, L. A., 1997. *Composite Construction Design for Buildings* (McGraw-Hil.). New York.
Viest, I. M., Fountain, R. S., and Singleton, R. C., 1958. *Composite Construction In Steel And Concrete For Bridges And Buildings*. (M. Hill, Ed.).

Yanez, S. J., Pina, J. C., Saavedra-Flores, E., and Guzmán, C. F., 2018. Numerical Modeling of a New Push-Out Test Using Non-Linear Behavior of Concrete. *Proceedings of the 1st Iberic Conference on Theoretical and Experimental Mechanics and Materials / 11th National Congress on Experimental Mechanics*, (November), 759–766.

Zeng, X., Jiang, S. F., and Zhou, D., 2019. Effect of shear connector layout on the behavior of steel-concrete composite beams with interface slip. *Applied Sciences (Switzerland)*, **9**(1). DOI: 10.3390/app9010207

Zhao, H., and Leon, R. T., 2013. *Elastic Load-Defelction Behavior of Simply-Supported Composite Beams, SEM Report 13/09*. Blackburg, VA.

Appendix A

Experimental Research

Researcher	Connection type	concrete-filled. cf: concrete-filled unf: unfilled		Study parameter	Number of Specimens	Section type		Geometry (mm) Square: L - W x H x t Round: L - D x t		Material properties			Load type	Failure Mode / Ultimate strenght (Ton)
		Chord	Diagonal			Chord	Diagonal	Chord	Diagonal	Concrete - f'c (MPa)	Steel - fy (MPa) Chord	Steel - fy (MPa) Diagonal		
Sayed [17]	T	cf	unf	Stiffness of the connection, Loof solid element.	7	Circular	Circular	495.3 - 60.325 x 1.65	495.3 - 47.625 x 2.16	35	481	387	Axial	Fracture of the weld/150
	K				7			1543.8 - 73.025 x 1.65	1061.7 - 47.625 x 2.16					
Tebbett et al. [18]	T		unf	Ultimate strength, stress concentration factor.	5	Circular	Circular	2032 - 317.5 x 9.525	762 - 168.3 x 9.525	70	326	326	Axial and flexural	Punching shear / 166.9
		cf												
		unf								N.A				
Brown et al. [20]	T1, T2	unf	unf	Stress concentration factors	2	Circular	Circular	2376.4 - 914 x 32	1188.2 - 457 x 16	N.A.	400	400	Axial and Axial flexure	Deformation of the chord / N.A.
	T1G, T2G	cf	cf		2					40				
Packer [21]				Final strength, rigidity of the connection				N.A. - 127.5 x 178.1 x 4.74	N.A. - 50.9 x 51.1 x 6.32				Tension and compression axial	Deformation of the chord / 21.6
	T1	unf	unf		1	Rectangular	Rectangular			30	400	443		
	T1C	cf												Deformation of the diagonal / 24
	T2	unf							N.A. - 88.9 x 88.9 x 7.60			426		Deformation of the chord / 39.5
	T2C	cf												Deformation of the diagonal / 48.4
	T3	unf						N.A. - 127.1 x 177.9 x 7.54	N.A. - 50.9 x 51.1 x 6.32		391	443		Deformation of the chord / 32.3
	T3C	cf												Deformation of the diagonal / 31.7
	X1	unf				Rectangular	Rectangular	N.A. - 127.5 x 177.8 x 4.75	N.A. - 63.5 x 127 x 16	43.3	330	330		Web crippling of the chord walls / 39.3
	X3	cf	cf											/ 142.1
	X5													/ 90.2

	X7												/ 126.6
	X2	unf	unf		Rectangular	Square	N.A. - 127.5 x 177.8 x 4.75	N.A. - 127 x 127 x 16					Yielding of the chord face / 11.8
	X4	cf	cf										Crushing of the concrete / 72.1
	X6												/ 52.1
	X8						N.A. - 128.5 x 177.8 x 4.75						/ 66
	X9	unf	unf				N.A. - 177.8 x 127.8 x 4.75						/ 7.3
	X10	cf	cf										/ 154.9
	X12												/ 85.6
	X13												/ 144.2
	X11						N.A. - 177.8 x 127.8 x 4.75						/ 99.1
	X14												/ 78.4
	K1	unf	unf		Rectangular	Rectangular	N.A. - 127.2 x 178.1 x 4.74	N.A. - 50.9 x 51.1 x 6.32	42.7	400	443		Chord face plastification / 26.4
	K1C	cf											Punching shear / 36.8
	K1X								31.4				Punching shear / 37.1
	K2	unf					N.A. - 127.2 x 178.1 x 4.86		42.7	393			Chord face plastification / 24.7
	K2C	cf											Punching shear / 36.2
	K3	unf					N.A. - 127.2 x 178.1 x 4.74	N.A. - 88.9 x 88.3 x 7.60		400	426		Chord face plastification / 46.6
	K3C	cf											Punching shear / 82.2
	K4	unf											Chord face plastification / 55.1
	K4C	cf											Punching shear / 84.9
	K5	unf					N.A. - 127.1 x 177.9 x 7.54			391			Chord face plastification / 97.1
	K5C	cf											Compression wed / 116.6
Silva et al. [22]	1	cf	unf	Stress concentration factors	1	Circular	Circular	2148 - 406 x 9.5	1380 - 194 x 6.3	60	355	355	Reverse Loading of tension and compression	Yield of chord / 127.5
	2													Shear across splice / 99.9
	3													/ 95
	4													Yield of chord / 143

Morahan and Lalani [23]	T1, DT4, T7	cf	unf	Fatigue and ultimate strength	6	Circular	Circular	N.A. x 250 x N.A.	N.A. x 102.5 x N.A.	80	345	345	Axial compression and tension, plane flexure, out-of-plane flexure	Deformation of the diagonal / N.A.
	T5, DT2, DT5, DT8								N.A. x 167.5 x N.A.					
	T3, T9, DT3, DT6, DT9								N.A. x 250 x N.A.					
Udomworarat et al. [24]	K-I	unf	unf	Fatigue performance	1	Circular	Circular	1389.6 - 318.5 x 6.9	497.4 - 216.3 x 5.8		379	369	Tension and compression axial	Fatigue crack / 20
	K-II	cf								29.4				/ 25
	K-III		cf											/ 31
	K-IV													/ 35
Sakai et al. [25]	K1/2C	unf	unf	Maximum resistance and fatigue	1	Circular	Circular	N.A. 318.5 x 6.9	NA - 216.3 x 5.8		368	373	Tension and compression axial	Buckling of a chord member / 68
	K1/2D	cf								31				Buckling of a diagonal member / 122
	K1/2E		cf											A crack at weld of a tension diagonal / 143
	K1/2F													A crack in concrete along a dowel / 186
	A - 5													A crack at the weld of a tension diagonal / 147
	A - 3													Buckling and a crack above a gusset at a diagonal / 183
Yin et al. [26]	JD - A	cf	unf	Hysteretic behavior	1	Circular	Circular	1750 - 245 x 6	775 - 86 x 6	23.1	453.7	420.3	Tension and compression axial	Plastic tearing / 30
	JD - B													/ 35
	JD - C													Fracture and local buckling / 70
	JD - D													Plastic tearing / 63
Voth [27]	T - CB0EA	unf	unf	Skewed branch plate, connection capacity and failure modes	1	Circular	Plate	559.3 - 219.17 x 4.49	N.A. - 100 x 19	N.A.	389	326	Quasic-static and axial tension	Punching shear / 28.6
	T- CB45EA							557.8 - 219.17 x 4.49						/ 23.3
	T - CB90EA													Punching shear and tear out / 32
	T - CT0EA							559.4 - 219.17 x 4.49						/ 40.6
	T - CT45EA							559.0 - 219.17 x 4.49						Punching shear / 35.2
	T - CT90EA							557.8 - 219.17 x 4.49						Punching shear and tear out / 45.9
	T - CB0EB							558.0 - 219.17 x 4.49					Quasic-static and axial compressive	Punching shear / 25.8
	T - CB90EB							558.1 - 219.17 x 4.49						/ 31.1
	T - CT0EB							558.8 - 219.17 x 4.49						/ 38.7
	T - CT90EB							557.9 -						Punching shear and tear out / 40

								219.17 x 4.49					
	X - XB90EA							558.9 - 219.17 x 4.49				Quasic-static and axial tension	Punching shear / 22.6
	X - XB45EA							919.5 - 219.17 x 4.49					/ 25
	T - CB0FA	cf	unf					558.9 - 219.17 x 4.49					Punching shear / 32.8
	T - CB90FA							557.9 - 219.17 x 4.49					Punching shear and tear out / 33.4
	T - CT0FA							558.8 - 219.17 x 4.49					Branch failure / 93.5
	T - CT90FA							557.9 - 219.17 x 4.49					
Chen et al. [28]	CS219 - 159	cf	unf	Final strength	1	Circular	Circular	219 x 8.42	159 x 5.6	56	325	330	Plane flexure	Chord punch shear yielding and diagonal yielding / N.A.
	CS219 - 168							219 x 8.43	168 x 7.82			375		Chord puch shear yielding / N.A.
	CS219 - 203							219 x 8.42	203 x 7.79					
Roeder and Lehman [29]	CFT	N.A.	N.A.	Interactions of force, rigidity and axial load bending moment	28	Circular	N.A.	1829 - 101.6 to 508 x 6.35	N.A.	55	344	N.A.	Axial compression and cyclic lateral load	Ductile tearing / 341
	BC				26									
	B				37			1829 - 508 x 6.35 to 2.24						
Xu et al. [32]	T - 300 - 4	cf	unf	Design strengths and slenderness ratios	3	Circular	Circular	N.A. - 299.84 x 4.19	N.A. - 132.78 x 6.08	50	330	330	Axial tensile	Chord punch shear / 53.4
	Y - 300 - 4							N.A. - 300.56 x 4.18	N.A. - 132.86 x 6.09					/ 62.03
	K - 300 - 4							N.A. - 300.24 x 4.18	N.A. - 132.71 x 6.08					/ 78.5
	KT - 300 - 4							N.A. - 300.35 x 4.17	N.A. - 132.56 x 6.07					diagonal yielding / 98
	T - 300 - 4R							N.A. - 300.32 x 4.19	N.A. - 133.12 x 6.08					Chord punch shear / 54.9

	Y - 300 - 4R							N.A. - 299.67 x 4.18	N.A. - 133.32 x 6.09				/ 69.9
	K - 300 - 4R							N.A. - 300.11 x 4.18	N.A. - 133.25 x 6.08				/ 69.89
	KT - 300 - 4R							N.A. - 299.52 x 4.17	N.A. - 133.09 x 6.07				Diagonal yielding / 98
	T - 300 - 5							N.A. - 300.46 x 5.01	N.A. - 132.66 x 6.08				Chord punch shear / 66.2
	Y - 300 - 5							N.A. - 300.48 x 4.99	N.A. - 132.68 x 6.10				/ 83.61
	K - 300 - 5							N.A. - 300.32 x 5.02	N.A. - 132.98 x 6.06				/ 81.4
	KT - 300 - 5							N.A. - 300.28 x 5.01	N.A. - 133.02 x 6.09				Diagonal yielding / 98
Chen et al. [33]	TB89 x 2.5R420	unf	unf	Concave chord, final strengths	1	Circular	Circular	600 - 140 x 50	180 - 89 x 2.5	30	298	275	Axial compression	Chord plastification + Local buckling failure oc diagonal / 11.01
	TB89 x 2.5R840													/ 13.45
	TB89 x 2.5R1260													/ 14.31
	TB89 x 2.5													Chord plastification / 12.53
	TB114 x 3.0R420								180 - 114 x 3.0			310		Chord plastification + Local buckling failure of diagonal / 13.12
	TB114 x 3.0R840													/ 19.55
	TB114 x 3.0R1260													/ 18.72
	TB114 x 3.0													Chord plastification / 17.14
	TB89 x 2.5R420F	cf	unf						180 - 89 x 2.5					Local buckling failure of diagonal / 16.02
	TB89 x 2.5R840F													Material yielding failure of diagonal / 18.31
	TB89 x 2.5R1260F													/ 14.47
	TB89 x 2.5F								180 - 114 x 3.0					Local buckling failure of diagonal / 17.03
	TB114 x 3.0R420F													Material yielding failure of diagonal / 28.49
	TB114 x 3.0R840F													/ 28.71
	TB114 x 3.0R1260F													/ 27.26
	TB114 x 3.0F													/ 27.69
Huang et al. [34]	K - CHS - 6	cf	unf	Resistance and failure modes	1	Circular	Circular	2000 - 510 x 10	900 - 219 x 6.0	45	311	330	Tension and compression axial	Chord face failure / 71.7
	K - CHS - 8								900 - 219 x 8.0			325		/ 71.9
	K - CHST - 6								900 - 219 x 6.0			330		Diagonal failure / 111.5
	K - CHST - 8								900 - 219 x 8.0			325		Punching shear failure / 154.1

	K - CHST - 10								900 - 219 x 10.0			332		/ 161.2
	K - CHST - 6s*								900 - 219 x 6.0			330		Diagonal failure / 132.3
	K - CHST - 8s*								900 - 219 x 8.0			325		
	K - CHST - 10s*								900 - 219 x 10.0			322		
Xu et al. [36]	T - 300 - 4 - 133 - 6	cf	unf	Chord-wall slenderness and diameter ratio	1	Circular	Circular	2002.1 - 298.8 x 4.09	630.2 - 134.2 x 6.08	56.3	452	408	In-plane bending	Chord-wall punching shear / 8.05
	T - 300 - 5 - 133 - 6			between brace and chord.				2001.8 - 301.3 x 5.04	630.4 - 133.9 x 6.09		385	408		/ 8.09
	T - 240 - 4 - 203 - 8							2001.3 - 238.8 x 3.93	630.1 - 201.9 x 8.07		452	436		/ 17.30
	T - 240 - 5 - 203 - 8							2000.9 - 241.2 x 4.95	630.1 - 204.1 x 8.06		385	436		/ 19.83
Cheng et al. [14]	T - A1	unf	unf	Concrete filling length in chord and weld	1	Rectangular	Rectangular	1500 - 150 x 200 x 8.0	650 - 150 x 150 x 8	49.8	279.5	279.5	Axial compression and In-plane bending	Flanges recess and web heave / 51
	T - A2	cf												Web heave / 60.4
	T - A3													/ 60.6
	T - B1	unf	unf											Flanges recess, arc yield, and web heave / 55.3
	T - B2	cf												Arc yield and web heave / 65.5
	T - B3													/ 68
Musa et al. [38]	K1 - CHS - to - CFCHS	cf	unf	Stress concentration factor	1	Circular	Circular	N.A. - 273.1 x 9.3	N.A. - 101.6 x 4	40	318	336	Axial	Chord and diagonal yielding / N.A.
	K2 - CHS - to - CFCHS													
	K3 - CHS - to - CFCHS													
	K4 - CHS - to - CFCHS													
	K5 - CHS - to - CFCHS													
	K6 - CHS - to - CFCHS													
	K7 - CHS - to - CFCHS													